5-2018

Analysis of Packaged Air Conditioning System for High Temperature Climates

Ammar M. Bahman
Purdue University

Recommended Citation

Bahman, Ammar M., "Analysis of Packaged Air Conditioning System for High Temperature Climates" (2018). *Open Access Dissertations*. 1685.
https://docs.lib.purdue.edu/open_access_dissertations/1685

ANALYSIS OF PACKAGED AIR CONDITIONING SYSTEM FOR HIGH TEMPERATURE CLIMATES

A Dissertation

Submitted to the Faculty

of

Purdue University

by

Ammar M. Bahman

In Partial Fulfillment of the

Requirements for the Degree

of

Doctor of Philosophy

May 2018

Purdue University

West Lafayette, Indiana

THE PURDUE UNIVERSITY GRADUATE SCHOOL
STATEMENT OF DISSERTATION APPROVAL

Prof. Eckhard A. Groll, Chair
    School of Mechanical Engineering
Prof. James E. Braun
    School of Mechanical Engineering
Prof. Travis W. Horton
    School of Civil Engineering
Prof. Walid M. Chakroun
    School of Mechanical Engineering

Approved by:
    Prof. Jay P. Gore
        Head of the School Graduate Program

To God, the Beneficent, the Merciful.
To my father, mother, brothers, and sisters,
for their great support during my graduate studies.
To my wife, Fatemah, for providing the lovely atmosphere for my study.
I dedicate this work especially to my beloved children, Laila and Salman.
Finally, to my Major Professor Eckhard Groll,
for his immense patience and his enormous guidance.

ACKNOWLEDGMENTS

I would like to express my sincere appreciation to Professor Walid Chakroun for his generosity and commitment. Without his recommendations, I would not pursue higher education in Purdue University.

Also, I would like to thank Professor James Braun and Professor Travis Horton for being my committee members. I really appreciate their constant support and help.

My thanks extend to all the technicians and staff in Ray W. Herrick Laboratories, in particular, Frank Lee, Bob Brown and Ron Evans. With their guidance and valuable assistant, my experimental work was a success.

Special thanks all my friends and labmates for their help and support during my study in the college, namely, Davide Ziviani, Riley Barta, Domenique Lumpkin, Thomas Moesch, Harshad Inamdar, Xinye Zhang, Nelson James, Orkan Kurtulus, Christian Bach, Ian bell, Bin Yang, Stephen Caskey, Nick Czapla, Nick Salts, Alejandro Lavernia, Cai Rohleder, Vatsal Shah, Emeline Georges, Howard Cheung, Brandon Woodland, Sugi Ramaraj, Ularee Upathumchard, Anchalika Pathak, Supriya Dharkar, Andy Hjortland, Akash Patil, Jebaraj Vasudevan, Stefan Hotz, Anne Liebold, Florian Kautz, and a host of others.

TABLE OF CONTENTS

LIST OF TABLES

LIST OF FIGURES

Figure Page

Figure Page

NOMENCLATURE

SYMBOL	UNITS	DESCRIPTION
AC	-	Air Conditioning
ACHP	-	Air Conditioning Heat Pump model
ACMODEL	-	Air Conditioning Model
AHRI	-	Air Conditioning, Heating and Refrigeration Institute
ANSI	-	American National Standards Institute
ASHRAE	-	American Society of Heating, Refrigerating and Air-Conditioning Engineers
COP	-	Coefficient of Performance
COP_{sys}	-	System Coefficient of Performance
CR	-	Current Ratio
c_i	-	Compressor mapping coefficients ($i = 1, 2, ..., 11$)
c_p	kJ/kg-K	Specific heat at constant pressure
$c_{p,a}$	kJ/kg-K	Air specific heat at constant pressure
DX	-	Direct Expansion
db	°C	Dry-bulb temperature
ECU	-	Environmental Control Unit
EER	Btu/W-hr	Energy Efficiency Ratio
EES	-	Engineering Equation Solver
EVI	-	Economized Vapor Injection
EVSIM	-	Evaporator Simulation Model
EXV	-	Electronic Expansion Valve
$\dot{E}$	kW	System power consumption
$\dot{E}_{tot}$	kW	System total power consumption

SYMBOL	UNITS	DESCRIPTION
FS	-	Full Scale
GWP	-	Global Warming Potential
HCFC	-	Hydro-Chloro-Fluoro-Carbons
HFC	-	Hydro-Fluoro-Carbons
HX	-	Heat Exchanger
h	kJ/kg	Specific enthalpy
$h_{a,i}$	kJ/kg	Air enthalpy at the inlet of evaporator
$h_{a,o}$	kJ/kg	Air enthalpy at the outlet of evaporator
$h_{a,s,evap}$	kJ/kg	Saturated air enthalpy at the refrigerant evaporation temperature
$h_{amb,i}$	kJ/kg	Air enthalpy at the inlet of condenser
$h_{amb,o}$	kJ/kg	Air enthalpy at the outlet of condenser
$h_{comp,i}$	kJ/kg	Refrigerant enthalpy at the inlet of compressor
$h_{comp,inj}$	kJ/kg	Refrigerant enthalpy at the injection state of compressor
$h_{cond,o}$	kJ/kg	Refrigerant enthalpy at the outlet of condenser
$h_{econ,c,o}$	kJ/kg	Refrigerant enthalpy at the cold-side outlet of economizer
$h_{econ,h,o}$	kJ/kg	Refrigerant enthalpy at the hot-side outlet of economizer
$h_{evap,o}$	kJ/kg	Refrigerant enthalpy at the outlet of evaporator
h_{int}	kJ/kg	Refrigerant enthalpy at intermediate section
$h_{r,dis}$	kJ/kg	Refrigerant enthalpy at the discharge port
$h_{r,dis,is}$	kJ/kg	Refrigerant isentropic enthalpy at the discharge port
$h_{r,i}$	kJ/kg	Refrigerant enthalpy at the inlet of evaporator
$h_{r,inj}$	kJ/kg	Refrigerant enthalpy at the injection port
$h_{r,inj,is}$	kJ/kg	Refrigerant isentropic enthalpy at the injection port
$h_{r,inj,mix}$	kJ/kg	Refrigerant enthalpy after mixing $h_{r,inj}$ and $h_{r,inj,is}$

SYMBOL	UNITS	DESCRIPTION
$h_{r,o}$	kJ/kg	Refrigerant enthalpy at the outlet of evaporator
$h_{r,suc}$	kJ/kg	Refrigerant enthalpy at the suction port
J	-	Objective function
MAE	%	Mean Absolute Error
$\dot{m}$	kg/s	Mass flow rate
$\dot{m}_a$	kg/s	Air mass flow rate
$\dot{m}_{inj}$	kg/s	Injection mass flow rate
$\dot{m}_{inj,exp}$	kg/s	Measured injection mass flow rate
$\dot{m}_{inj,exp,i}$	kg/s	Measured injection mass flow rate at i^{th} data point
$\dot{m}_{inj,pred}$	kg/s	Estimated injection mass flow rate
$\dot{m}_{inj,pred,i}$	kg/s	Estimated injection mass flow rate at i^{th} data point
$\dot{m}_r$	kg/s	Refrigerant mass flow rate
$\dot{m}_{r,exp}$	kg/s	Measured refrigerant mass flow rate
$\dot{m}_{r,exp,i}$	kg/s	Measured refrigerant mass flow rate at i^{th} data point
$\dot{m}_{r,inj}$	kg/s	Refrigerant injection mass flow rate
$\dot{m}_{r,pred}$	kg/s	Estimated refrigerant mass flow rate
$\dot{m}_{r,pred,i}$	kg/s	Estimated refrigerant mass flow rate at i^{th} data point
$\dot{m}_{r,suc}$	kg/s	Refrigerant suction mass flow rate
$\dot{m}_{r,tot}$	kg/s	Refrigerant total mass flow rate
$\dot{m}_{suc}$	kg/s	Suction mass flow rate
$\dot{m}_{suc,exp}$	kg/s	Measured suction mass flow rate
$\dot{m}_{suc,exp,i}$	kg/s	Measured suction mass flow rate at i^{th} data point
$\dot{m}_{suc,pred}$	kg/s	Estimated suction mass flow rate
$\dot{m}_{suc,pred,i}$	kg/s	Estimated suction mass flow rate at i^{th} data point
$\dot{m}_{tot}$	kg/s	Total mass flow rate
NTU	-	Number of Thermal Units

SYMBOL	UNITS	DESCRIPTION
n	-	Number of data points
PHX	-	Plate Heat Exchanger
P	kPa	Pressure
$P_{a,i}$	kPa	Air static pressure at the inlet of evaporator
$P_{a,o}$	kPa	Air static pressure at the outlet of evaporator
P_{high}	kPa	High-side line pressure drop
P_{inj}	kPa	Injection pressure
P_{int}	kPa	Intermediate line pressure drop
P_{low}	kPa	Low-side line pressure drop
P_{suc}	kPa	Suction pressure
P^*_{high}	kPa	Effective high-side line pressure drop
P^*_{int}	kPa	Effective intermediate line pressure drop
P^*_{low}	kPa	Effective low-side line pressure drop
$\dot{Q}$	kW	Heat transfer rate
$\dot{Q}_{cond}$	kW	Condenser heat transfer rate
$\dot{Q}_{cond,a}$	kW	Condenser air-side heat transfer rate
$\dot{Q}_{cond,exp}$	kW	Measured condenser heat transfer rate
$\dot{Q}_{cond,exp,i}$	kW	Measured condenser heat transfer rate at i^{th} data point
$\dot{Q}_{cond,pred}$	kW	Estimated condenser heat transfer rate
$\dot{Q}_{cond,pred,i}$	kW	Estimated condenser heat transfer rate at i^{th} data point
$\dot{Q}_{cond,r}$	kW	Condenser refrigerant-side heat transfer rate
$\dot{Q}_{econ}$	kW	Economizer heat transfer rate
$\dot{Q}_{econ,c}$	kW	Economizer cold-side heat transfer rate
$\dot{Q}_{econ,exp}$	kW	Measured economizer heat transfer rate
$\dot{Q}_{econ,exp,i}$	kW	Measured economizer heat transfer rate at i^{th} data point
$\dot{Q}_{econ,h}$	kW	Economizer hot-side heat transfer rate

SYMBOL	UNITS	DESCRIPTION
$\dot{Q}_{econ,pred}$	kW	Estimated economizer heat transfer rate
$\dot{Q}_{econ,pred,i}$	kW	Estimated economizer heat transfer rate at i^{th} data point
$\dot{Q}_{evap}$	kW	Evaporator heat transfer rate
$\dot{Q}_{evap,a}$	kW	Evaporator air-side cooling capacity
$\dot{Q}_{evap,exp}$	kW	Measured evaporator cooling capacity
$\dot{Q}_{evap,exp,i}$	kW	Measured evaporator cooling capacity at i^{th} data point
$\dot{Q}_{evap,pred}$	kW	Estimated evaporator cooling capacity
$\dot{Q}_{evap,pred,i}$	kW	Estimated evaporator cooling capacity at i^{th} data point
$\dot{Q}_{evap,r}$	kW	Evaporator refrigerant-side cooling capacity
RT	-	Refrigeration Tons
RMSD	%	Root Mean Square Deviation
SEER	Btu/W-hr	Seasonal Energy Efficiency Ratio
SLSQ	-	Sequential Least Squares
s	kJ/kg-K	Specific entropy
TXV	-	Thermostatic Expansion Valve
T	°C	Temperature
$T_{a,i}$	°C	Air temperature at the inlet of evaporator
$T_{a,o}$	°C	Air temperature at the outlet of evaporator
$T_{a,o,exp}$	°C	Measured evaporator outlet air temperature
$T_{a,o,exp,i}$	°C	Measured evaporator outlet air temperature at i^{th} data point
$T_{a,o,pred}$	°C	Estimated evaporator outlet air temperature
$T_{a,o,pred,i}$	°C	Estimated evaporator outlet air temperature at i^{th} data point
T_{amb}	°C	Ambient temperature
$T_{amb,i}$	°C	Air temperature at the inlet of condenser

SYMBOL	UNITS	DESCRIPTION
$T_{amb,o}$	°C	Air temperature at the outlet of condenser
T_{cond}	°C (°F)	Condensation temperature
T_{dew}	°C	Refrigerant dew-point temperature
$T_{dew,inj}$	°C	Refrigerant injection dew-point temperature
T_{dis}	°C	Compressor discharge temperature
T_{dp}	°C	Air dew-point temperature
$T_{dp,i}$	°C	Air dew-point temperature at the inlet of evaporator
$T_{dp,o}$	°C	Air dew-point temperature at the outlet of evaporator
T_{evap}	°C (°F)	Evaporation temperature
T_{sub}	°C	Subcool temperature
$T_{sub,target}$	°C	Targeted subcool temperature
T_{sup}	°C	Superheat temperature
$T_{sup,inj}$	°C	Injection superheat temperature
$T_{sup,suc}$	°C	Suction superheat temperature
T^*_{cond}	°C	Effective condensing temperature
$T^*_{dew,inj}$	°C	Effective injection dew-point temperature
T^*_{evap}	°C	Effective evaporation temperature
VI	-	Vapor Injection
$\dot{V}$	m^3/s	Volumetric flow rate
$\dot{V}_{dis,th}$	m^3/s	Theoretical volumetric displacement
wb	°C	Wet-bulb temperature
$\dot{W}$	kW	Work rate
$\dot{W}_{comp}$	kW	Compressor power consumption
$\dot{W}_{comp,exp}$	kW	Measured compressor power consumption
$\dot{W}_{comp,exp,i}$	kW	Measured compressor power consumption at i^{th} data point

SYMBOL	UNITS	DESCRIPTION
$\dot{W}_{comp,pred}$	kW	Estimated compressor power consumption
$\dot{W}_{comp,pred,i}$	kW	Estimated compressor power consumption at i^{th} data point
$\dot{W}_{cond,fan}$	kW	Condenser fan power
$\dot{W}_{evap,fan}$	kW	Evaporator fan power
x	varied	Scalar variable
x_{exp}	varied	Measured scalar variable
$x_{exp,i}$	varied	Measured scalar variable at i^{th} data point
x_{pred}	varied	Estimated scalar variable
$x_{pred,i}$	varied	Estimated scalar variable at i^{th} data point
$\bar{x}$	varied	Mean value of variable x
$\bar{x}_{exp}$	varied	Mean value of measured variable x
η	%	Efficiency
η_{is}	%	Isentropic efficiency
η_v	%	Volumetric efficiency
Δ	varied	Residual term
Δ_i	varied	Residual term at i^{th} row of $\vec{\Delta}$
Δh_{int}	kJ/kg	Residual of enthalpy at intermediate section
$\vec{\Delta}$	varied	Residual vector
$\vec{\Delta}P$	kPa	Pressure drop residual vector
ΔT_{sup}	°C	Residual of superheat temperature
ϵ	-	Effectiveness
ϵ_{evap}	-	Evaporator effectiveness
ρ	kg/m^3	Density
ρ_a	kg/m^3	Air density
ρ_r	kg/m^3	Refrigerant density
$\rho_{r,suc}$	kg/m^3	Refrigerant density at suction port

ABSTRACT

Bahman, Ammar M. Ph.D., Purdue University, May 2018. Analysis of Packaged Air Conditioning System for High Temperature Climates. Major Professor: Eckhard A. Groll, School of Mechanical Engineering.

Packaged air conditioning (AC) units, called Environmental Control Units (ECUs), are being increasingly used by the U.S. military, especially in hot ambient temperature climates. The compact packaging of ECUs resembles unitary-type rooftop or room AC systems, and they are used to cool personnel and equipment in enclosed spaces such as shelters, vehicles, and containers. Despite these similarities, ECUs have distinctive features that aren't found in commercial packaged AC units. An ECU is designed to sustain harsh and extreme weather conditions up to 51.7°C (125°F) which is a design set-point by the military. As the outdoor temperature increases, both the cooling capacity and coefficient of performance (COP) of ECUs drop dramatically. In addition, the compact design degrades airflow uniformity due to air maldistribution across evaporator coil, which results in further performance degradation. Therefore, the goal of this study is to identify ways to improve the component as well as the system performance of the ECUs in the field at high ambient temperatures.

A passive solution was evaluated to compensate for the degradation in performance of ECU evaporators, known as the interleaved circuitry method. The interleaved circuitry method, where the refrigerant from a circuit with high air flow is routed to a circuit with low air flow and vice-versa, has been investigated to determine its effectiveness in reducing the air maldistribution effect. Air velocity measurements in front of the ECU's evaporator have been conducted in psychrometric chambers and the measurement locations have been defined by the log-Tchebycheff rule. The velocity profile was obtained by the Lagrange Interpolation method as percentage values. The system performance after interleaved circuitry implementation was compared to the baseline system at different operating conditions up to 51.7°C (125°F). The results showed that the interleaved circuitry method increased the superheat uniformity of the individual circuits and improved the cooling capacity and COP up to 16.6% and 12.4%, respectively. Furthermore, the tuned model predicted the evaporator cooling capacity within a mean absolute error of approximately ±10%.

Moreover, vapor injection (VI) with economization, where cool gas is injected to the compressor at an intermediate stage to absorb the heat generated during the compression process, has been experimentally and numerically assessed to significantly improve system performance. The ECU has been retrofitted with an economized vapor injection (EVI) system and experimentally characterized in side-by-side psychrometric chambers. The performance of the EVI system for superheated and saturated injection conditions were compared to the case of without injection at different operating conditions. The results showed that the EVI system reduced the compressor discharge temperature by up to 5°C, and improved the cooling capacity and COP by up to 12.7% and 3.1%, respectively. The experimental data have been used to develop, tune, and validate a detailed steady-state cycle model. The predictions of suction and injection mass flow rates, compressor power consumption, and system COP were within a mean absolute error of approximately ±5%. At last, the model has been employed to optimize the economizer geometry in order to maximize the system COP at designed ambient condition of 51.7°C (125°F). The optimization process resulted in maximum improvements in compressor discharge temperature, cooling capacity, and COP of 8.5°C, 22.3%, and 17.3%, respectively.

CHAPTER 1. INTRODUCTION

1.1 Background

Air conditioning (AC) is a process that conditions the air and then supplies it to a designated space. It provides cooling from its central plant or rooftop units. It also controls and maintains the temperature, humidity, air movement, air cleanliness, and pressure differential in a space within predefined limits for the comfort and health of the conditioned space occupants or for the purpose of product processing (Wang, 2001). Air conditioning systems can be classified based on their applications as: (1) comfort air conditioning systems used in residential, commercial, institutional, health care, and transportation sectors, or (2) process air conditioning systems for manufacturing, product storage, research and development processes. Air conditioning systems can also be classified based on their design and operating conditions as: (1) individual room air conditioning systems (*e.g.,* window-mounted room air conditioner) which allow independent air conditioning control for each room, (2) evaporative cooling air conditioning systems that utilize water to cool the air stream for energy savings, (3) desiccant-based air conditioning systems that use rotary desiccant dehumidifier specifically for latent cooling in addition to sensible cooling, (4) thermal storage air conditioning systems used to produce chilled water or ice in tanks during off-peak hours to be used later during high demand hours, (5) clean-room air conditioning systems that adjust the indoor air quality by precisely controlling temperature, relative humidity, ventilation, noise, vibration, and air pressure, (6) space conditioning air conditioning systems that supply only conditioned air using ductless fan-coil water-source heat pumps installed within the conditioned space for individual zone control, and (7) unitary packaged air conditioning systems consisting of compacted, pre-assembled, readied refrigeration units located mostly on the roof or outside the designated space area. The latter systems provide conditioned air to either a single room or multiple rooms using supply ducts.

Packaged air conditioning (AC) systems have been developed since the 1950s. Packaged systems are the dominant air conditioning system used in the United States, represented by 48% of total floor space of 5462 million m^2 (DOE, 1995). Packaged AC systems can be classified based on installation location as rooftop packaged systems, indoor packaged systems, and split packaged systems. Among these systems, the rooftop packaged systems are most widely used in commercial buildings. A typical rooftop packaged system is a vapor compression cycle which consist mainly of a casing, a compressor, DX coil (*i.e.,* an evaporator with an expansion device), a condenser, indoor and outdoor fans, filters, and controls. Additionally, the packaged system contains optional components such as an auxiliary heater, a relief or return fan (*i.e.,* included in higher capacity units), and a humidifier. The packaged AC system has many potential uses such as providing a healthy, clean, and comfortable indoor environment, as well as saving energy by developing high-efficiency equipment in residential and industrial sectors. However, none of these uses come without associated challenges. Packaged AC systems can also be operating in hot and dry climate countries, where even the indoor temperature during sleeping hours can be as low as 19.7°C (67.5°F) due to very hot outdoor temperatures (Majid et al., 2014). Moreover, design limitations and compactness that exist in tightly packaged AC systems cause constrained air flow pathways which result in highly airflow non-uniformity problems in the unit's evaporator.

The use of a packaged AC units in U.S. military applications, called Environmental Control Units (ECUs), has been increasingly growing in hot ambient temperature climates. The compact packaging of ECUs resembles unitary-type rooftop AC systems, but have distinctive features when compared to commercialized packaged AC units. An ECU is designed to sustain harsh and extreme weather conditions, and is used to cool personnel and equipment in enclosed spaces such as shelters, vehicles, and containers. The units are typically rated at an outdoor temperature of 51.7°C

(125°F) and an indoor temperature of 32.2°C (90°F) at 50% relative humidity. In climate regions that experience very high outdoor ambient temperatures, both the cooling capacity and coefficient of performance (COP) of AC units drop dramatically with an increase in the outdoor air temperature. Therefore, this work is focused on optimizing the ECU on system level as well as component level in both design and performance prospectives.

1.2 Literature Review

Typical packaged air conditioner uses a conventional vapor compression cycle, whose main components include a compressor, a condenser, an expansion valve, an evaporator, and a working fluid. This section presents a literature review on studies investigating the main components of packaged AC unit in hot ambient conditions. It also includes studies that cover system modification for performance improvement in hot climate application.

1.2.1 Miscellaneous Studies for Packaged Air Conditioning Systems

- *Design Modifications*

Bullard et al. (2006) showed that improving AC system performance at hot/dry conditions of 46°C (115°F) might be achieved with minor changes in system configuration. They fabricated micro-channel heat exchangers with an efficient compressor and tested them in an R-410A 10.5 kW split residential AC unit. Although the cooling capacity only increased by 2%, the power consumption decreased by 32%, and thus the overall Seasonal Energy Efficiency Ratio (SEER) improved 32% compared to a baseline R-410A unit with typical SEER of 12. Elbel and Hrnjak (2010) retrofitted the evaporator of an R-134a 17.5 kW packaged AC unit to be used in cooling applications at high ambient conditions. The cooling capacity per unit volume improved by 40% when used with R-744 compared to the original R-134a unit. Additionally, the COP improved approximately by 30% and 20% compared to R-134a ECU and R-410A unit, respectively. The authors recommended an ejector expansion device for further improvement.

- *Expanders and Ejectors*

An expander is used instead of a throttling device in the AC system to recover the work lost during the expansion process. Expanders were economically analyzed by Subiantoro and Ooi (2013), and they recommended them for places with high ambient temperature such as the tropics and desert regions. The cost was amortized for systems with highly efficient expanders, high cooling loads and high temperature lifts.

One type of expanders is ejector. The ejector functions to increase the suction pressure and helps to reduce the workload on the compressor to improve energy consumption. Li (2006) investigated ejector expansion device in an R-744 12 kW packaged AC unit at high outdoor temperatures. The results showed that, at typical operating conditions of residential air conditioners, the COP improved by approximately 11% and the cooling capacity by approximately 9.5%. However, at outdoor temperature greater than 48.9°C, the performance declined. The increase in outdoor temperature led to a low ejection ratio (*i.e.,* the ratio between the secondary and primary mass flow rates). This resulted in a small refrigerant mass flow rate through the evaporator, and thus reduction in system's cooling capacity relative to the conventional capacity. Lawrence and Elbel (2016) tried to solve this issue with a two-phase ejector where excess liquid was recirculated through the evaporator, known as liquid recirculation or liquid overfeed, which resulted in the potential for improved evaporator capacity and system performance. However, at ambient temperature greater than 42°C ambient temperature, the results showed that the typical ejector cycle achieved higher COP than the ejector recirculation cycle. The COP of the typical ejector cycle improved up to 11% while the COP of the ejector recirculation cycle improved only 6% compared to baseline cycle.

Overall, the ejector applied in AC system has a large potential to improve the performance, but there are some limitations such as a narrow range of operation due to the fixed geometry of the ejector (Sumeru et al., 2014).

- *Mechanical Subcoolers*

Mechanical subcooling is another method used to reduce the energy consumption due to large temperature lifts in hot climates. The aim is to further subcool the liquid refrigerant leaving the condenser using an additional vapor compression cycle. Zubair (1994) and Khan and Zubair (2000) theoretically determined the system performance as well as the exergetic performance of a refrigeration cycle combined with mechanical subcooler at high condensing temperatures up to 71.1°C (160°F). Depending on the saturation temperature at the subcooler, the COP can be improved by 23%, while the irreversibility can be reduced by 65%. Llopis et al. (2015, 2016) theoretically and experimentally investigated the combination of a R-1234yf refrigeration cycle as a mechanical subcooling cycle with a transcritical R-744 heat pump unit. The experimental results showed that at a condensing temperature of 40°C and an evaporating temperature of 0°C, the cooling capacity improved by 39.4%, while the system COP improved by 26.1% compared to baseline. However, the complexity and cost effectiveness of mechanical subcoolers might not be suitable for packaged AC systems applied in extreme and harsh ambient conditions (Qureshi and Zubair, 2013).

- *Desiccant Wheels*

A desiccant wheel is added to packaged AC systems in hot climates to remove the additional latent heat as well as improve the system performance with low operating cost (Al-alili, 2014; Jani et al., 2015; Sand and Fischer, 2005; Sheng et al., 2015). Therefore, the desiccant wheel is rarely used for hot and dry climates.

Ling et al. (2011) showed that energy savings and AC system performance improvements can be achieved when the desiccant wheel is used by dividing the condenser (or gas cooler) into two sections in the separate sensible and latent cooling unit, combined with suction line heat exchanger. The first section of the condenser provides hot air for the desiccant wheel regenerator, while the second section is for heat rejection. The COP improvement was found to be 36% and 61% for R-410A and R-744 AC systems compared to the conventional system, respectively. The desiccant wheel improved system performance because it reduced the compressor power consumption by increasing the evaporation temperature. The additional suction line heat exchanger also helped in reducing the compressor discharge temperature mainly in the R-744 unit. Despite the fact that a desiccant wheel helps to improve the performance of packaged AC system, there are not enough studies available to ensure the effectiveness of using desiccant wheel in extreme hot climates. Moreover, desiccant wheel adds complexity to the packaged AC unit.

1.2.2 Alternative Refrigerants in High Ambient Temperature Climate

A refrigerant is the working medium in the refrigeration cycle. It rejects heat to the outdoor ambient and provides cooling to the conditioned space. Due to environmental protocols, environmentally hazardous refrigerants such as HCFCs have been set on a timeline to be phased out. The Montreal protocol was amended in Kigali (2016) to include phase out schedule of high Global Warming Potential (GWP) HFCs. The option of improving the conventional vapor compression cycle becomes vital in response to these challenges. For AC systems at high temperature, researchers tried to investigate alternative refrigerants to the phased-out R-22 and those being currently used, R-410A and R-407C.

Barve and Cremaschi (2012) experimentally investigated R-32 and R-1234yf as drop-in refrigerants in an R-410A 17.6 kW residential split heat pump unit for high temperature application. The results showed that R-32 performed better than R-410A at 46.1°C (115°F). However, the discharge temperature increased significantly, which could affect the life cycle of the compressor. As for R-1234yf, the system cooling capacity and COP degraded up to 50% relative to R-410A at the extreme case.

Biswas and Cremaschi (2012) experimentally investigated two new developmental refrigerants abbreviated as DR-4 (43.5% R-32, 56.5% R-1234yf) and DR-5 (72.5% R-32, 27.5% R-1234yf) as drop-in refrigerants in an R-410A 17.6 kW residential split heat pump unit. The investigated refrigerants have low GWP, falling in the range of 300 and 500. At a high outdoor temperature of 46.1°C (115°F), the results showed that DR-5 improved cooling capacity and COP up to 4% and 22%, respectively, while DR-4 showed a COP increase of up to 16%, but a 30% lower cooling capacity in comparison with R-410A. Both examined refrigerants experienced similar compressor discharge temperatures to R-410A.

Wu et al. (2012b) experimentally and theoretically investigated R-161 in an R-22 3.5 kW residential AC system for cooling application. The simulation work compared R-161 and R-290 as alternatives to R-22. At outdoor conditions of 48/30°C (db/wb) and indoor conditions of 27/19°C (db/wb), the experimental results of R-161 showed that the cooling capacity decreased by 7% compared to R-22. However, the Energy Efficiency Ratio (EER) improved by 10% and compressor discharge temperature decreased by 5%. R-161 was also experimentally investigated by Han et al. (2012). They examined the drop-in refrigerants R-161 and R-32 to replace R-410A. The results showed that at a condensing temperature of 50°C and an evaporating temperature of 10°C, the COP of R-161 was higher by 51.85% and 40.77%, but the cooling capacity was lower by 9.47% and 11.79% than that of R-32 and R-410A, respectively. Moreover, the compressor discharge temperature of R-161 was the lowest among these refrigerants, resulting in a temperature decrease of 30% and 19.14% compared to R-32 and R-410A, respectively.

Joudi and Al-Amir (2014) tested drop-in refrigerants R-290, R-407C, and R-410A to replace R-22 in 3.51 kW and 7.03 kW residential AC split units under hot ambient conditions. The results showed that at an ambient condition of 55°C, R-407C had the closest performance to R-22, followed by R-410A. On the other hand, among the investigated refrigerants, the Total Equivalent Warming Impact (TEWI) value of

R-290 was approximately 50% less because of the low charge level compared to the other refrigerants.

For the application of packaged AC systems at high ambient temperature, Devotta et al. (2005b) experimentally and numerically investigated R-407C to replace R-22 before retrofitting the same 5.13 kW packaged AC unit and testing R-290 under the same operating conditions (Devotta et al., 2005a). The following conclusions were drawn by comparing R-290 and R-407C to R-22 at outdoor 46/24°C (db/wb) and indoor 29/19°C (db/wb): In the case of R-407C, the cooling capacity dropped by 7.9%, and the COP dropped by 13.6% as compared to R-22. In the case of R-290, although the cooling capacity dropped by 9.7%, the COP increased by 2.8% because of the low power consumed by the R-290 compressor, which was 12.4% lower compared to R-22.

Wu et al. (2012a) optimized the charge level of R-290 and R-1270 in 2.4 kW packaged AC units to replace R-22. The results of the extreme case at outdoor conditions of 40/24°C (db/wb) and indoor conditions of 27/19°C (db/wb) showed that R-1270 can increase the cooling capacity up to 14.7%, while the EER remained approximately equivalent to that of R-22. As for R-290, the cooling capacity increased up to 7.1%, while the EER decreased by 10.2%. The results also showed that the cooling capacity for R-1270 improved by 13.9% compared to R-290 when a compressor with 20% larger displacement was used.

Robinson and Groll (2001) developed a model (ACCO2) to simulate the performance of an R-744 10.6 kW packaged AC system to replace R-22 for military application in hot climates. The validated model predictions at ambient temperature of 48.9°C (120°F) showed that the COP of the system using R-744 decreased by 10% compared to R-22, while the cooling capacity almost remained the same. The authors also recommended further design modifications by implementing a 10% larger heat exchanger frontal area, and predicted that it could improve the cooling capacity and the COP by 6% and 5%, respectively. This modification is questionable, especially for compact and packaged AC units for military applications as well as operating the AC unit in supercritical mode with R-744.

Another experimental investigation on military packaged AC unit was performed by Westphalen (2006) at an extreme ambient temperature of 51.7°C (125°F). He investigated a 17.6 kW packaged AC unit with four environmentally-friendly refrigerants, namely R-1270, R-290, CARE50 (94% R-290, 6% R-12), and R-22a/502 (87% R-290, 13% R-1270) to replace R-407C. The results showed that the drop-in refrigerants performed well compared with R-407C where R-1270 showed 12% higher capacity and 10% higher COP compared to R-407C. This improvement was explained by the poor design of the packaged unit and the significant temperature glide of R-407C in the heat exchangers compared to R-1270 which is a single constituent refrigerant with no temperature glide.

Overall, the challenge with R-32, R-1234yf, R-290, R-1270 and R-161 remains with their flammability as well as concerns about their high discharge temperatures. Therefore, they may need more extensive investigations to be suitable as alternatives to existing fluorocarbon refrigerant in AC systems.

1.2.3 Condenser Improvements for High Temperature Application

A condenser is a heat exchanger that aims to reject heat from the hot refrigerant passing through it to the outdoor ambient. With the increase in outdoor air temperature, the refrigerant condenses at higher temperature, which then reduces AC system performance. Therefore, researchers investigated different approaches to reduce the temperature of air inlet to the condenser.

For hot ambient conditions, evaporative cooling is a common method to pre-cool the air before condenser inlet with sprayed water. Wang et al. (2014) evaluated an evaporative cooling unit which was located in front of the condenser for an R-410A $5.3 - 7$ kW split AC unit. The results showed that the condenser saturation temperature decreased by $2.4 - 6.6$°C when operating at outdoor conditions of $23.8 -$

44.5°C and fixed indoor condition 27/17.6°C (db/wb). Therefore, the system COP increased from 6.1% to 18% because of the increase in cooling capacity due to the increase in the mass of liquid across the evaporator, as well as due to the compressor power consumption reduction of 14.3%. Similarly, Hajidavalloo and Eghtedari (2010) combined the 5.3 kW split AC unit with evaporative cooling technology at ambient temperatures up to 49°C. The energy consumption decreased by 20.3% and the cooling capacity and COP increased by 20.1% and 50.6%, respectively.

Sawan et al. (2012) simulated evaporative cooling with the water produced from the evaporator instead of using fresh water in an R-410A 3.43 kW split AC unit. The model was validated for steady state conditions including the transient condition (*i.e.,* ON/OFF cycling the compressor) at a typical office space in Beirut, Lebanon during the months of June, August, and October. The results showed that the drained water should be sufficient in the month of October only to facilitate daily energy savings of 5.3% while 5% and 4.5% were saved in June and August, respectively. However, the recovered water was determined to last only for 6 hours in June and up to 8 hours in August.

Minh Thu and Sato (2013a,b) investigated the use of porous ceramics in evaporative cooling unit instead of spraying water. The heat transfer coefficient was found to be 4 times higher than the typical air cooled condenser. The experimental results showed improvements of up to 30% in the system performance of a 2.5 kW commercial AC system using R-410A.

Shen and Bansal (2014) developed a detailed heat pump model (HPDM) to simulate a packaged AC unit with a submerged subcooler and a slinger. The submerged subcooler was located downstream of the condenser in a water collection pan to further subcool the liquid line, while the slinger was installed on the condenser's fan to spray water (*i.e.,* from the same collection pan) into the air stream flowing over the condenser coil surface. The model was validated with an R-410A window-type AC unit with a capacity of 2.93 kW for ambient conditions up to 43.3°C (110°F). The range of EER improvement was $5 - 7\%$ compared to a conventional unit.

Martínez et al. (2016) investigated adiabatic evaporative cooling pads in an R-407C 2.5 kW split AC system. The model was validated for summer conditions in the southeast of Spain. The experimental findings showed that the optimal pad thickness of 100 mm can maximize the system COP by 10.6% in which case the cooling capacity increased by 1.8% and the compressor power decreased by 11.4%. Despite the power reduction, the adiabatic evaporative cooling pads were not found to be cost efficient and obstructed the airflow across the condenser.

The studies above show that the evaporative cooling on the condenser improves system performance to an extent. The main issue is probably the availability of fresh water. Saline water might corrode heat exchanger surfaces because of the presence of salts; fresh water might be limited in supply. In addition, water cost and system complexity might be an issue specially for AC system in arid weather conditions such as 51.7°C (125°F). The reliability of evaporative cooling with packaged AC systems in extreme hot climates is also not clear.

1.2.4 Evaporator in Packaged Air Conditioning Systems

In contrast to the condenser's work, an evaporator heat exchanger aims to remove the heat and humidity from the returned air and supply the room with conditioned air. In a packaged AC unit, the design and layout of the evaporator affects the airflow uniformity. Poor design and layout causes air maldistribution, which may result in performance degradation up to 76% compared to uniform flow (Domanski, 1991).

The degradation in evaporator effectiveness depends on the characteristics of the airflow profile. According the Blecich (2015), the degree of air maldistribution and its orientation relative to the refrigerant-side circuitry are the key factors in the degradation of evaporator effectiveness. Some researchers homogenized the airflow across the heat exchanger circuits with air guide plates (Song et al., 2012), while others optimized the refrigerant-side circuitry (Domanski and Yashar, 2007; Yashar et al., 2015). Yashar et al. (2015) developed a tube-by-tube heat exchanger model to optimize the evaporator refrigerant circuitry for an R-410A 26.5 kW AC unit. The experimental results showed improvements of 2.2% and 2.9% in cooling capacity and COP, respectively. It was also noted that future work would need to be done in the area of developing more feasible methods for mapping airflow maldistribution because of inefficient airflow measurement techniques.

Currently, two methods are investigated to compensate for the degradation of evaporator performance due to air maldistribution. The two methods are active control and passive control. The active control aims to control the exit superheat by adjusting the refrigerant mass flow rate via an expansion controller, while passive control adjusts the exit superheat by retrofitting circuit geometry or design configuration.

As for evaporator's active control, Kim et al. (2009) studied the control and placement of refrigerant flow through individual circuits in an evaporator. The validated model of a 10.55 kW R-410A residential heat pump showed that the active control can recover up to 99.99% of the lost 6% and 4% of cooling capacity and COP, respectively in the case of an air maldistribution factor of 0.4. The air maldistribution factor is a dimensionless parameter defined in the study, where 1 represents uniform flow. Similarly, Kærn et al. (2011a) compensated for the airflow maldistribution across multi-channel fin-and-tube heat exchangers by controlling the superheat traveling into each channel individually. The results showed that the cooling capacity and COP were recovered by 99.1% and 99.3%, respectively, in the case of an air maldistribution factor of 0.71. However, Mader et al. (2015a,b) showed that the superheat control technology for the individual circuits is cost effective in many cases. With that being said, in hot climate zones, the active control technology may not be quickly paid back using the same economic assumptions because the capacity delivered by the unit exceeds building demands, which results in on/off operation. Therefore, a passive control of individual evaporator circuit superheat is proposed as a viable alternative.

The arrangement of evaporator tubes also affects the heat exchanger performance, commonly seen in the case of air maldistribution, and relatively little work has been done on this passive circuitry control technique. Kærn and Tiedemann (2012) and Kærn et al. (2013) utilized fin-and-tube evaporators for residential AC system to investigate the ability of circuitry design to control individual channel superheats and thus compensate for airflow maldistribution. Interlaced and face split circuitry designs were numerically compared using both linear and computational fluid dynamic (CFD) predicted velocity profiles. The results showed that the interlaced evaporator had higher performance than the face split evaporator in cases where the air maldistribution factor is less than 0.55 because its design compensates for most of the airflow maldistribution. Bach et al. (2014) investigated the relative effects of active superheat control and passive interleaved circuitry in recovering the losses across evaporators due to air maldistribution. They numerically investigated two methods: A passive solution (interleaved circuitry) and an active solution (hybrid controls monitoring the amount of superheat at the exit of each circuit). Note that in the passive case, the evaporator circuits were interleaved independently from the air velocity profile. The simulation results show that up to 75% and 95% of the air maldistribution losses for different airflow profiles could be recovered by the interleaved circuitry and hybrid control, respectively. The results indicate that a smaller percentage of the losses can be recovered by interleaved circuitry. However, its lower implementation cost and expected reliability make it more promising than the hybrid control. Yet passive interleaved circuitry has not been experimentally investigated.

1.2.5 Compressor and Cycle Modification

The compressor is the heart of the vapor compression cycle. The cycle starts when the compressor draws in low-temperature, low-pressure refrigerant gas coming from the evaporator. The motor-driven compressors sole function is to compress the refrigerant and discharge it as a high temperature, high-pressure gas. With the increase in pressure ratio across the compressor caused by the increase in temperature lift, the efficiency of the compressor decreases and thus the system performance degrades. Therefore, researchers investigated different compressor types in several cycle configurations to be used for AC applications.

For packaged AC units, Yamamura et al. (1990) and Cho et al. (2011) recommended scroll compressors due to their high efficiency, low vibration, and low noise level. The compressor used a tip-seal mechanism, optimized axial clearance to minimize gas leakage in the compression pocket, and a driving bush design to have proper sealing force.

The scroll compressors were further developed to not only be used in single-stage AC systems, but also for two-stage or multi-stages units. When the pressure ratio or temperature lift increases, AC systems operating with a single-stage vapor compression cycle become increasingly inefficient. Thermodynamic considerations dictate the use of two-stage or multi-stages cycles. However, the complexity of those cycles and the cost of additional components increase the necessary investment.

- *Liquid Injection (Oil Flooded) with Regeneration*

One possible method to increase system performance is to flood the compressor with a significant amount of liquid (*e.g.,* oil) to achieve a quasi-isothermal compression process. The injection can be either in the suction line or in the chamber during the compression process. As a result, the rise in compressor discharge temperature can be limited despite significant elevation in the temperature lift. In addition, using a regenerator in the cycle increases refrigerant subcooling, and thus increases cooling capacity.

Bell et al. (2011), James et al. (2016), and Ramaraj et al. (2016) showed that the effectiveness of compressor flooding and regeneration increases as the temperature lift of the system increases. They performed an in-depth examination on the oil flooding with regeneration technology for low ambient conditions while Yang et al. (2014) and Luo (2016) investigated the cooling mode. Yang et al. (2014) experimentally tested an R-410A 17.6 kW split heat pump unit in air conditioning mode based on Standard (2008a). The unit was retrofitted with an oil injected compressor, integrated oil cooler, and regenerator. They explored the effect of different oil flooding mass fractions on system performance. According to the results, the optimal oil flooding mass fraction varied relative to operating conditions. The optimal oil mass fraction was in the range of $10 - 30\%$. A system COP improvement of up to 8% was observed compared to the baseline unit. Later, Luo (2016) simulated oil flooded compression with a regenerator aiming to improve the performance of an R-32 air conditioner. He developed a single stage oil flooded compressor model to evaluate system-level performance improvement. According to the results, the improvement of system COP in cooling mode was relatively lower than that in the heating mode. At a condensing temperature of 50°C, the COP increased only 8.7%. In cooling mode, less compression heat was produced during the compression process because of the lower compression ratio.

A relatively small improvement in system performance with liquid (or oil) injection comes at cost of an additional oil separator, adding complexity to the system and introducing the possibility of it affecting the cooling performance in the cases of incomplete separation. The liquid (or oil) injection with a regenerator is mostly used to reduce the discharge temperature. In AC systems, however, Xu et al. (2011) explained that the benefit of excess subcooling surpass the reduction in discharge temperature. Therefore, vapor injection with economizing steps in to increase the cooling capacity, despite the modest system performance improvement at ambient temperature greater than 35°C.

- *Vapor Injection with Economization*

Vapor injection with an economizer shares the same concept of liquid injection with regeneration. It aims to cool the refrigerant during the compression process by injecting cool refrigerant gas at an intermediate stage within the compressor. Therefore, the compressor discharge temperature is reduced. The economizer can be either a flash tank or a plate heat exchanger (PHX) which allows for excess liquid going to the evaporator, and thus improves the system performance. Currently, vapor injected compression with economization dominates in heat pump applications because of its performance, and because it enables operation of a two-stage cycle with only a single compressor. The ability to regulate its capacity between single-stage and two-stage modes contributes to its reliability as well (Park et al., 2015). For example, a single compressor with multi-port injection eliminates the need for multiple compressors and thereby lowers the cost significantly (Mathison et al., 2011).

The economized vapor injection (EVI) system shows significant system performance improvement in low ambient conditions (Bertsch and Groll, 2008; Xu et al., 2011). However, the benefit can be extended for extremely hot summer conditions where peak temperatures occur for a small period during the day. In such cases, Ding et al. (2004) showed that the cooling capacity was more important than the COP. The cooling capacity of the R-22 heat pump unit increased 9.7% when the condensing temperature was 60°C and the evaporating temperature was 2°C. In addition, the compressor discharge temperature decreased by 5°C, which would enhance the compressor performance in hot summer weather.

Scroll compressors are implemented in EVI systems because of their suitability among all types of compressors for refrigerant injection. This is on account of the ability of scroll compressors to tolerate small amounts of liquid (or two-phase) injection. Two-phase injection has been investigated to some degree. For the cooling application, Qv et al. (2017) optimized the duration of single-phase and two-phase injection in a split heat pump unit with a flash tank operating under ambient temperature ranges from 28°C to 39°C. Two-phase injection instantaneously decreased the compressor discharge temperature and cooling capacity compared to single-phase injection, and consequently an optimal injection duration of 8 seconds was obtained to avoid severe performance degradation. The results showed that the capacity and the EER of the two-phase injection cycle with a flash tank economizer were 25% and 32% higher compared to AC system without injection, respectively. Despite the performance improvement, the flash tank might be not suitable as an economizer for cooling applications due to the longer capacity recovery period.

Wang et al. (2009) conducted experimental study on an 11 kW R-410A residential split AC unit to investigate vapor injection cycle with both a flash tank and a PHX. The flash tank and plate heat exchanger (PHX) as economizers showed a performance improvement over the non-injection system. When operating at maximum cooling mode, the cooling capacity and COP were improved by 14% and 4%, respectively, at an ambient temperature of 46.1°C. According to the results of Wang et al. (2009) and Heo et al. (2011), although a flash tank economizer was more favorable in terms of the system performance improvement and the relatively low cost, the PHX as an economizer was more favorable as it could achieve a wider injection operating range and it also allowed easy control of the injection mass flow rate.

Using a PHX as an economizer in a vapor injection cycle developed sufficient cooling COP and capacity for summer application as demonstrated by Bertsch and Groll (2008) and Tello-Oquendo et al. (2016). Cho et al. (2016) studied the vapor injection with a PHX by varying the outdoor temperature and injection ratio in a 28 kW split unit using R-410A and R-32. At the optimum injection ratio, the results showed $2.1 - 6.3\%$ higher cooling capacity than those without vapor injection for an ambient temperature of 35°C. To the best of our knowledge, vapor injection compression with economization technology has not been investigated in a packaged AC unit under arid weather conditions such as 51.7°C (125°F).

1.3 Motivation

Most packaged AC systems installed in arid regions experience low performance. The degradation in performance of packaged AC units due to high ambient temperatures is a well known problem faced by industry. Developing a better understanding of the component and cycle performance of packaged AC units is the primary motivation behind this work. An evaluation of energy performance of packaged AC is also a driving factor behind this study. The compactness and design limitations of such packaged units motivates the use of a passive solution to improve heat exchanger effectiveness and compensate for airflow maldistribution. A continuing motivation behind this work is to integrate the benefit of novel cycle technologies into packaged AC units to enhance performance when applied in high temperature conditions. To the extent of our knowledge, passive interleaved circuitry and novel compression technology such as vapor injection with economization have not been investigated in packaged AC units at extreme hot weather conditions up to 51.7°C (125°F).

1.4 Objectives

The objectives of this study are to develop a better understanding of component- and system-level performance of a packaged AC unit at high ambient temperature conditions up to 51.7°C (125°F), experimentally evaluate the passive solution of interleaved circuitry to compensate airflow maldistribution in a packaged AC unit, develop and validate interleaved circuitry model, experimentally investigate novel cycle technology such as vapor injection (VI) with economization to be integrated in a packaged AC unit, develop a detailed cycle model for the economized vapor injection (EVI) system, and optimize the model for such extreme weather conditions.

The effectiveness of interleaved circuitry is evaluated in Chapter 2 for a packaged AC unit to compensate for airflow maldistribution at extreme hot weather conditions. Extensive experiments are conducted on three different evaporator circuitries using an R-407C Environmental Control Unit (ECU) with a capacity of 5 tons of refrigeration. To account for air maldistribution across the evaporator, air velocity profiles are regressed from the local air velocity measurements. The cooling capacity, COP and evaporator superheat of the interleaved circuitry are evaluated and compared to the original circuitry configuration at different steady-state operating conditions up to 51.7°C (125°F). An implicit model of an interleaved circuitry evaporator is developed and validated by tuning the evaporator heat transfer parameters using the experimental data.

The effectiveness of EVI technology is assessed in Chapter 3 for a packaged air conditioner to improve the overall system performance at extreme high temperature conditions. The same R-407C ECU was retrofitted with a plate heat exchanger (PHX) as an economizer and additional expansion device to examine superheated and saturated injections at different steady-state operating conditions in side-by-side psychrometric chambers. The cooling capacity, COP, and compressor discharge temperature of the EVI system are evaluated and compared to a baseline case without injection. An implicit cycle model for the EVI system is developed and validated by using the experimental results. The accuracy of the model is further improved by tuning heat transfer and pressure drop correlations. Finally, the validated model was employed to numerically investigate an alternative VI compressor with an optimized PHX design to maximize the system COP at an outdoor temperature of 51.7°C (125°F) and an indoor temperature of 32.2°C (90°F) with 50% relative humidity.

CHAPTER 2. APPLICATION OF INTERLEAVED CIRCUITRY TO IMPROVE EVAPORATOR EFFECTIVENESS AND COP

2.1 Introduction

Of all of the components affected by compactness design of the packaged AC unit, the evaporator suffers the most. Bahman and Groll (2016) showed higher irreversibility associated with the evaporator of the ECU. This is mainly due to the packaged design of the ECU that causes significant air maldistribution across the evaporator coil. In this chapter, interleaved circuitry is evaluated to compensate for air maldistribution. Experiments on three different evaporator circuitries were conducted using an R-407C ECU with 17.6 kW cooling capacity at a variety of steady-state operating conditions inside psychrometric chambers up to 51.7°C (125°F). An air velocity profile was fitted from local air velocity measurements that accounted for the air maldistribution across the evaporator coil. The interleave procedure was based on the air velocity percentage contribution of each circuit. The cooling capacity, COP and evaporator superheat of the interleaved circuitry were evaluated and compared to the original circuitry configuration. An implicit model of an interleaved circuitry evaporator was validated by tuning the evaporator heat transfer parameters using experimental data.

2.1.1 Background

The ECU performance can be enhanced by adopting, for instance, a high efficiency scroll compressors or high efficiency fan. However, the design and layout of ECU components often cause air maldistribution within them, as shown in Figure 2.1. Of all of the components affected by air maldistribution, the evaporator suffers the most (Chunlu and Jie, 2014). In some cases, the heat transfer performance in the

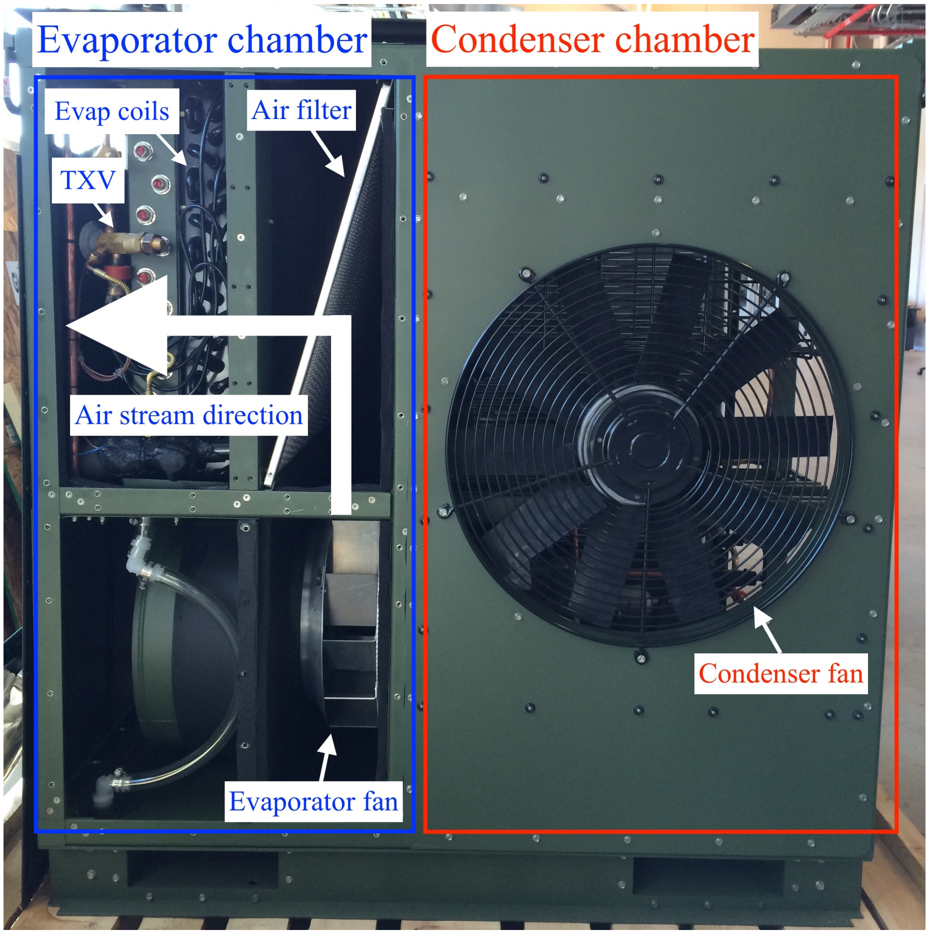

Figure 2.1. Layout and compactness of the Environmental Control Unit (ECU) resulted in air maldistribution in the evaporator chamber.

evaporator can be up to 35% lower than an evaporator exposed to a uniform air flow distribution (Aganda et al., 2000). Extensive research has been conducted on the impact of non-uniform airflow on such heat exchangers—both experimentally (Gong et al., 2008; Payne and Domanski, 2003) and numerically (Domanski, 1991; Kærn et al., 2011b; Lee and Domanski, 1997). Domanski (1991) showed that non-uniform airflow affected the exit superheat and resulted in cooling capacity of 76% of the capacity obtained from uniform airflow. The degradation is associated with uneven refrigerant superheat at the outlet of different circuits. According to the results from Gong et al. (2008), the airflow maldistribution primarily attributes in the thermostatic expansion valve hunting in the fin-and-tube evaporators. In contrast, two studies opposed that conclusion: Timoney and Foley (1994) and Kirby et al. (1998) found that air maldistribution across heat exchangers led to improvement in thermal performance relative to units with uniform airflows. These papers found higher evaporator capacity as a result of higher overall heat transfer coefficient caused by the intensity of airflow turbulence. However, the increase in evaporator capacity of approximately $3-4\%$ compared to uniform airflow was not particularly significant.

The degradation in evaporator effectiveness depends on the characteristics of the airflow profile. According to Blecich (2015), the degree of air maldistribution and its orientation relative to the refrigerant-side circuitry are the key factors in the degradation of evaporator effectiveness. Some researchers homogenized the airflow across the heat exchanger circuits with air guide plates (Song et al., 2012), while others optimized the refrigerant-side circuitry (Domanski and Yashar, 2007; Yashar et al., 2015). Yashar et al. (2015) developed and implemented an algorithm for optimizing evaporator circuitry on a rooftop unit. The measurements of the airflow maldistribution over the evaporator were performed to characterize the performance of the evaporator using Particle Image Velocimetry (PIV) and a tube-by-tube heat exchanger model. An algorithm was then used to determine the optimum placement of the re-worked circuitry, which was then physically implemented and experimentally tested in a prototype evaporator. Using a 7.5-ton unit with R-410A, improvements of 2.2% and 2.9% in capacity and COP, respectively, were found over the manufacturers design. It was also noted that the practicality of their in-depth and time consuming measurement techniques needed to be considered and that future research would need to be done in the area of developing more feasible methods for mapping airflow maldistribution.

Currently, the degradation of evaporator performance due to air maldistribution is being compensated for by active control or passive control of individual evaporator circuit superheat as shown in Figure 2.2. The active control aims to control the exit superheat by adjusting the refrigerant mass flow rate via an expansion controller, while passive control adjusts the exit superheat by retrofitting circuit geometry or design configuration. As for active control, Mader et al. (2015a,b) showed that the superheat control technology for the individual circuits is cost effective in many cases. However, in hot climate zones, the active control technology may not be quickly paid back using the same economic assumptions as in cold climates because the capacity delivered by the unit exceeds building demands, which results in cyclic on/off operations. Therefore, a passive control of individual evaporator circuit superheat is proposed as a viable alternative.

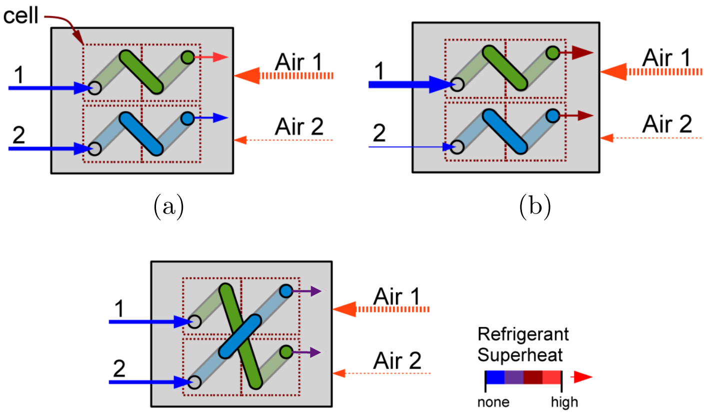

(a) (b)

(c)

Figure 2.2. 2-Circuit evaporator with (a) original, (b) active and (c) passive control circuitries to compensate for airflow maldistribution (Bach et al., 2014).

The evaporator tube arrangements also affect the heat exchanger performance, but relatively little work has been done on passive circuitry control. Kaga et al. (2009) numerically investigated the air maldistribution condition in an evaporator by varying the length of downstream circuitry. The results showed that when the downstream circuitry length increased, the loss in cooling capacity improved from 6% to less than 1% with applied air maldistribution. However, the increase in circuitry length increased the overlap between the evaporator tubes up to 60%. Kærn and Tiedemann (2012) and Kærn et al. (2013) utilized A-shaped fin-and-tube evaporators for residential air-conditioning to investigate the ability of circuitry design to control individual channel superheats and thus compensate for airflow maldistribution. A numerical comparison between interlaced (interchanged circuitry) and face split (non-intersected circuitry) circuitry designs was conducted using both linear and CFD-predicted velocity profiles. The results showed that the interlaced evaporator had higher performance than the face split evaporator at airflow distribution parameter values below 0.55, where a value of 1 represents uniform flow, because its design compensates for most of the airflow maldistribution. Bach et al. (2014) investigated the relative effects of active superheat control and passive interleaved circuitry in recovering the losses across evaporators due to variable airflow maldistribution. Both passive (interleaved circuitry) and active (hybrid controls monitoring the amount of superheat at the exit of each circuit) solutions were considered and modeled. According to simulation predictions, up to 75% and 95% of the flow maldistribution losses could be recovered by the interleaved circuitry and hybrid control, respectively, for different airflow profiles. Note that Bach et al. (2014) interleaved the evaporator circuits without direct consideration of the air velocity profile. The results indicate that a smaller percentage of the losses can be recovered by interleaved circuitry. However, its lower implementation cost and expected reliability is more promising than the hybrid control. Therefore, it was concluded that the interleaved circuitry would be the better approach for the study herein.

2.2 Experimental Methodology

2.2.1 Experimental Setup

Three evaporators designated as baseline, modified and interleaved configurations were tested in an Environmental Control Unit (ECU) under the same operating conditions in side-by-side psychrometric chambers to evaluate the evaporator effectiveness and coefficient of performance (COP) of the unit. The ECU setup in the psychrometric chambers is schematically shown in Figure 2.3. The ECU uses R-407C as a refrigerant and has a rated capacity of 17.6 kW (60,000 Btu/hr). Figure 2.4 illustrates the system schematic. The compressor type is a hermetic scroll with a volumetric displacement rate of 19.53 m^3/h. The condenser is based on a micro-channel design made of aluminum and treated with corrosion resistant clad material. The throttling device is an externally equalized thermostatic expansion valve. The evaporator is a fin-and-tube type heat exchanger, and made of copper pipes E-coated for corrosion protection. The fins are made of aluminum and E-coated as well. The indoor blower is placed in front of evaporator coil due to military restriction of contamination infiltration, which ensures that no exterior air can be leaked into the occupied space. There is also a hot-gas bypass circuit that allows the system to continue to run even if the thermostat is satisfied. The isolation ball valves are used to deactivate the hot-gas and the de-superheating valves and therefore, only four components are active all times. The unit was charged with 2.98 kg (6.56 lb), 3.18 kg (7.01 lb) and 3.41 kg (7.51 lb) of refrigerant for baseline, modified and interleaved configurations, respectively, to overcome the additional pipe length and ensure consistent subcooling of 5°C in the liquid line.

Two psychrometric chambers were used to conduct the system performance tests. These chambers supply uniform air flow with temperature and humidity maintained within ±0.55°C and ±0.5%, respectively, of their set-points as shown in Figure 2.3. The following parameters were measured: temperatures and pressures at the inlet and outlet of all components, refrigerant flow rate in the liquid line, air humidity at the inlet and outlet of the evaporator, and the power consumption of the fans, compressor, and total for the unit. In addition, surface temperatures were measured with 6 T-type thermocouples at the evaporator inlet and outlet circuits. A nozzle box built according to ASHRAE standard 41.2 (Standard, 1987) was used to measure the total airflow of the evaporator. On the air side, a grid with 9 T-type thermocouples were installed at the air inlet and outlet of both evaporator and condenser. All measuring instrumentation conformed to the requirements of ANSI/AHRI Standard 210/240 (Standard, 2008a). The mounting position of each measuring instrumentation is shown in Figure 2.4, and the respective accuracy of these instruments are stated in

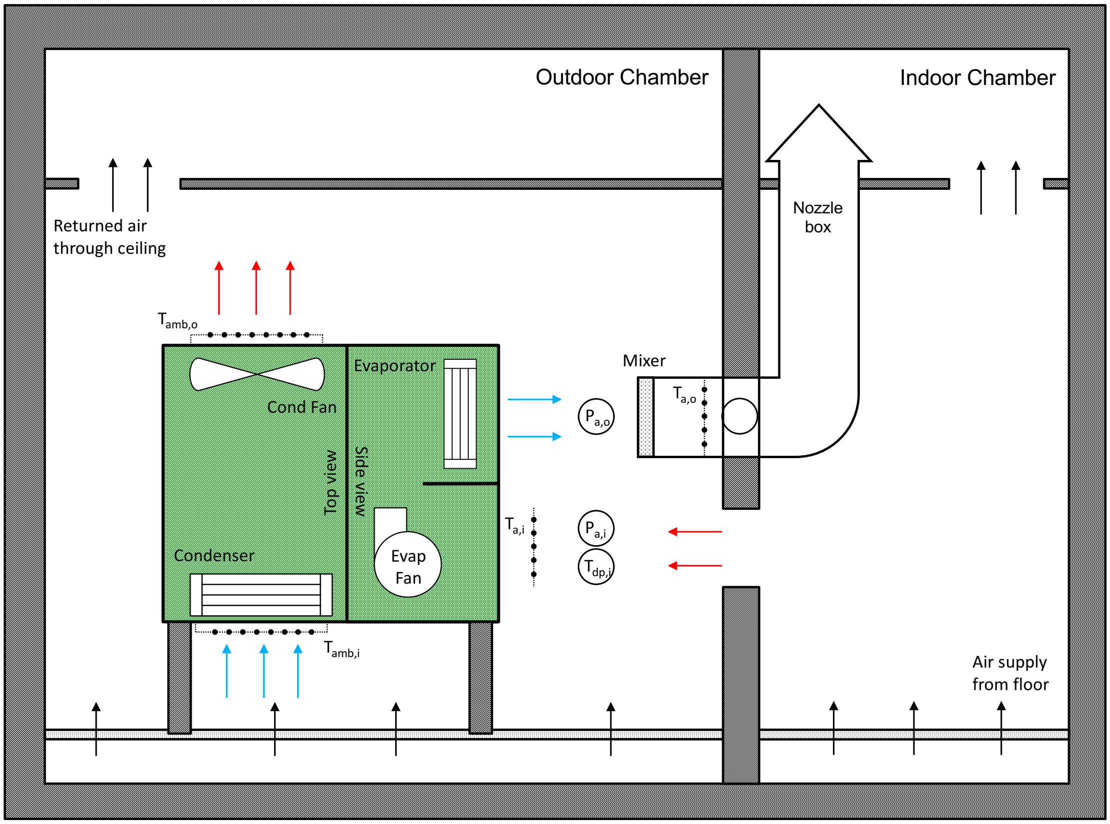

Figure 2.3. Schematic of the test facility used to conduct the experimental investigation of the 17.6 kW R-407C ECU.

Table 2.1. Due to the compactness of the unit, it is assumed that the refrigerant pressure in the suction line is constant.

The compactness and the layout of the unit result in air maldistribution in the evaporator chamber as shown in Figure 2.1. Figure 2.1 shows that the air stream in the evaporator chamber turned 90 degrees from the fan to the evaporator surface. In order to adequately account for air maldistribution across the face of the evaporator, the velocity of air was measured at 42 points with a hot-wire anemometer. The measurement locations have been defined by the log-Tchebycheff rule, which is recommended by ASHRAE Standard 111 (Standard, 2008b) as shown in Figure 2.5. The log-Tchebycheff rule requires that a minimum of 25 readings must be taken

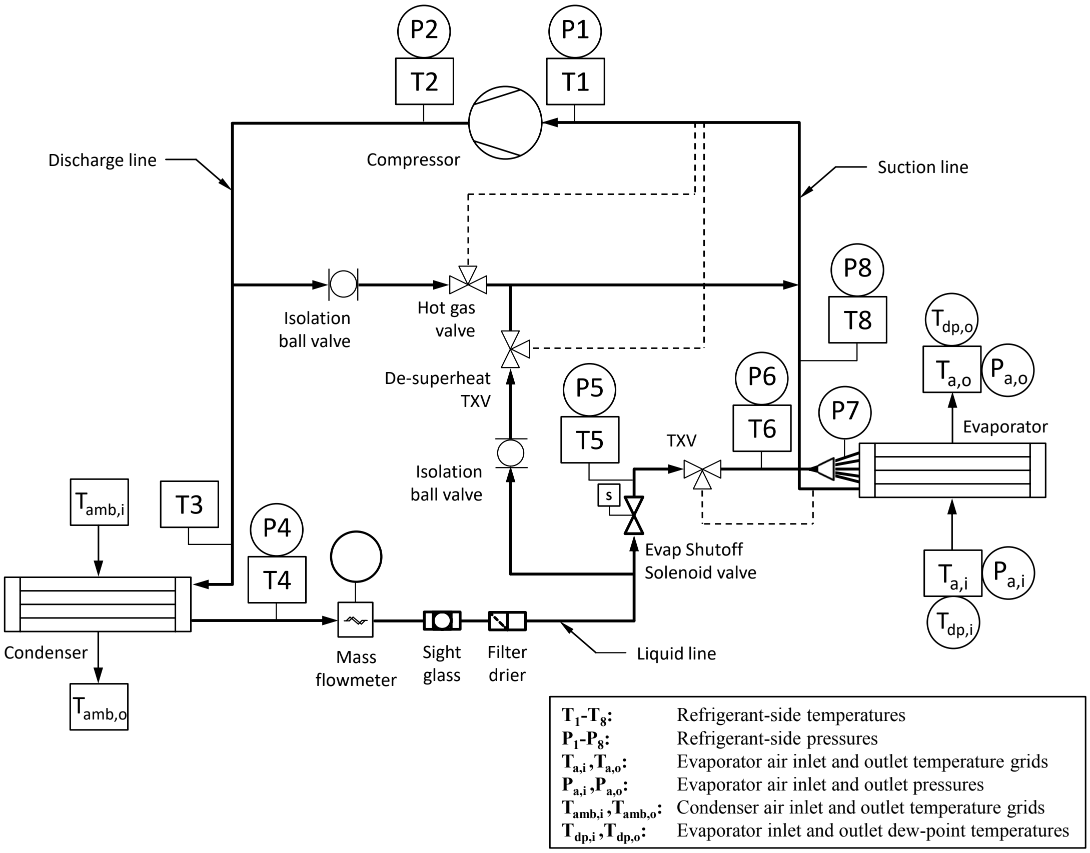

Figure 2.4. Measured points of the system.

Table 2.1. Measurement instrumentation and accuracy for the system.

Physical parameter	Instrument	Range	Accuracy
In-line temperature	Thermocouple stainless steel T-type	−250 − 350°C	±1.1°C
Surface temperature	Thermocouple wire T-type	−250 − 350°C	±1.1°C
Refrigerant pressure	Pressure transducer	0 − 1750, 0 − 3500, 0 − 7000 kPa	±0.08% FS
Air humidity	Hygrometer chilled mirror	−20 − 85°C, 0 − 95%	±0.2°C
Air pressure	Static pressure transducer	0 − 5 inH$_2$O	±1.0% FS
Air velocity	Portable anemometer	0 − 25 m/s	±1.5% FS
Air flow rate	ASHRAE nozzle box	2188 − 5107 m^3/hr	±6.66 m^3/hr
Refrigerant flow rate	Coriolis flow meter	0 − 2720 kg/hr	±0.2% ±0.87 kg/hr
Unit total power	Power transducer	0 − 40 kW	±0.5% FS
	Current transformer	100 : 5 CR	±1.5% FS
Compressor power	Power transducer	0 − 45 kW	±0.25% FS
	Current transformer	1000 : 1 CR	±0.3% FS
Fans power	Power transducer	0 − 2 kW	±0.04% FS

across a traverse plane. For rectangular ducts, the number of measurements along each side of the duct depends on how wide that side is. The log-Tchebycheff rule defines the location of the traverse planes by multiplying the side length with several multipliers. Holes had been drilled in the cover of the unit to reach these locations. The holes were just slightly bigger than the used testing probe. To avoid air leakage, the holes were tightly sealed. The portable anemometer device had a range of $0 - 25$ m/s, with ±1.5% full scale accuracy. Across these 42 local air velocity points, an average air velocity of 3.72 m/s was calculated. The accuracy of these measurements can be stated to be reasonably accurate due to the fact that the average velocity was 3.62 m/s based on the air flow rate measurement. Note that the local air velocities were measured inside of the psychometric chambers with an open lab environment temperature (*i.e.,* 26°C) where only the evaporator fan was operating.

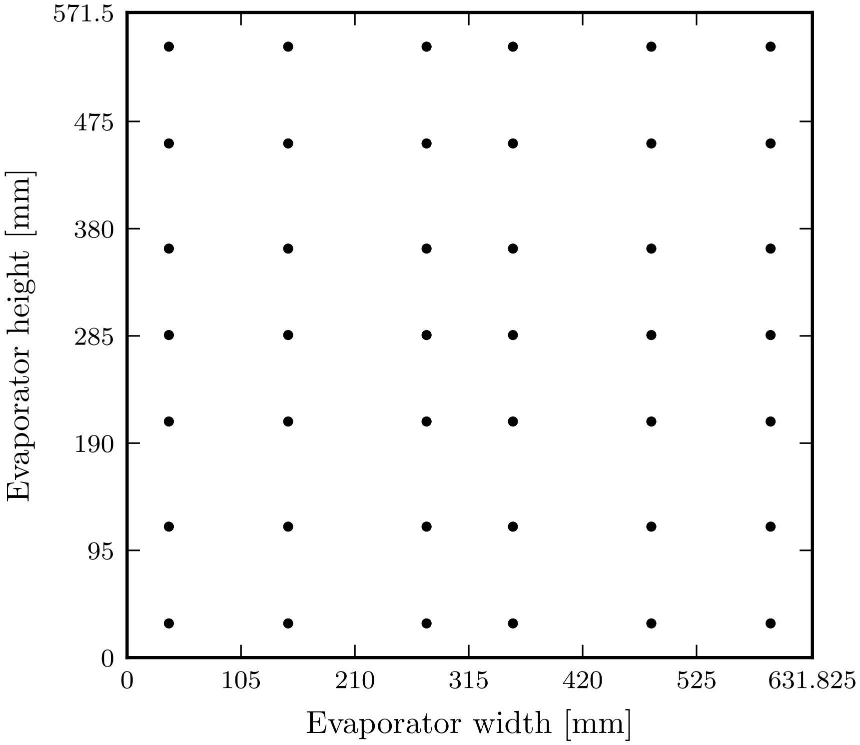

Figure 2.5. Local air velocity measurement locations as defined by the log-Tchebycheff rule.

2.2.2 Experimental Methods

The experiments were conducted in a pair of psychrometric chambers that simulate indoor and outdoor conditions, with the ECU positioned in the outdoor chamber. The test conditions are shown in Table 2.2. The ECU was charged under the same condition of Test 4/A for testing the three evaporators (*i.e.,* baseline, modified and interleaved evaporator configurations). Note that Test Conditions 4/A, B and C conformed to ASHRAE Standard 210/240 (Standard, 2008a), while Test Conditions 1 and 2 present extremely high ambient temperatures. Upon running the ECU for more than one hour and having reached steady state, data measurements were taken every two seconds for 20 minutes. The averaged values of the measured data were used in Section 2.3 to quantify the benefit of interleaving circuitry application in the improvement of cooling capacity and COP as well as evaporator's superheat. The superheat of the individual circuits was calculated by subtracting the outlet temperature measured on the tube surface from the inlet temperature measured on the tube surface. In each test, the energy balance between the air-side and refrigerant-side was within 6% per ANSI/AHRI Standard 210/240 (Standard, 2008a). Each test for the different evaporator configurations (*i.e.,* baseline, modified and interleaved) was carefully performed at the same temperatures in the outdoor and indoor psychrometric chambers to increase the reliability of the test results.

Because the local air velocity measurements do not represent real air velocities for each circuit, these results cannot be used for the simulation work, which needs the air velocity for each circuit of the evaporator as a simulation input. Therefore, it is necessary to obtain a continuous air velocity profile for the whole evaporator based on the known local air velocities measurements. Then, the continuous velocity profile can be divided into several sections, and the number of sections will be the same as the number of circuits. Here, the Lagrange interpolation method (Lagrange, 1877) is used to obtain the continuous air velocity profile based on the known local air velocity measurements.

Table 2.2. Testing conditions in psychrometric chamber.

Test No.	Outdoor condition				Indoor condition				Description
	Dry-bulb		Wet-bulb		Dry-bulb		Wet-bulb		
	°C	°F	°C	°F	°C	°F	°C	°F	
1	51.7	125	29.4	85	32.2	90	23.9	75	steady, wet coil
2	46.1	115	22.2	72	29.4	85	17.2	63	steady, dry coil
3	40.6	105	22.8	73	29.4	85	17.2	63	steady, dry coil
4/A	35	95	23.9	75	26.7	80	19.4	67	steady, wet coil
5	29.4	85	17.2	63	23.9	75	13.9	57	steady, dry coil
6	23.9	75	17.2	63	25	77	13.9	57	steady, dry coil
B	27.8	82	18.3	65	26.7	80	19.4	67	steady, wet coil
C	27.8	82	18.3	65	26.7	80	13.9	57	steady, dry coil

2.2.3 Data Reduction

The main cycle performance quantification parameters, cooling capacity and coefficient of performance (COP), were calculated based on the refrigerant enthalpy method. The refrigerant enthalpies were calculated using thermodynamic property functions in the Engineering Equation Solver (EES) software (Klein and Alvarado, 2016). The local pressure and temperature measurements were used to determine refrigerant enthalpies. However, the refrigerant enthalpy of a two-phase mixture state cannot be determined with the available measurements. Therefore, it is assumed that the enthalpy across the expansion valve is constant. It is also assumed that the local pressure at the condenser inlet is equal to the compressor's discharge pressure. This is valid since the tube between the condenser inlet and compressor's discharge point is short, thus the pressure drop is negligible. Hence, the total cooling capacity of the evaporator air coil measured on the refrigerant side is determined by

$$\dot{Q}_{evap,r} = \dot{m}_r(h_{r,o} - h_{r,i}) \tag{2.1}$$

and the cooling coefficient of performance (COP) is calculated by

$$\mathrm{COP}_{sys} = \frac{\dot{Q}_{evap,r}}{\dot{E}_{tot}} \tag{2.2}$$

where $\dot{E}_{tot}$ is the total power input, which includes the compressor, the fans and the power used by the controllers.

The overall heat transfer effectiveness on the air-side of the evaporator is defined as the ratio of the available heat transfer rate over the maximum possible heat rate which is determined by

$$\epsilon_{evap} = \frac{h_{a,i} - h_{a,o}}{h_{a,i} - h_{a,s,evap}} \tag{2.3}$$

where $h_{a,s,evap}$ is the saturated air enthalpy at the refrigerant evaporation temperature.

2.3 Results and Discussion

Figure 2.6 illustrates the air velocity contours generated using the measurements of local air velocity at the face of the ECU's evaporator. Figure 2.7 presents the continuous air velocity profile fitted using the experimental measurements. Figure 2.8 shows the air velocity percentages contributed by the individual evaporator circuit to provide guidance for the interleaving arrangement design. Figure 2.9 shows the proposed interleave circuitry configuration as well as the original baseline and the modified evaporator circuits. Figure 2.10 compares the superheat distribution for the three evaporator circuitry configurations based on the measured data given in Appendix A. Figure 2.11 illustrates pressure-enthalpy and temperature-entropy diagrams of the vapor compression refrigeration cycle of each evaporator circuitry configuration. Those diagrams were generated by computing the thermodynamic state properties from the performance test data available in Appendix B. In addition, an uncertainty analysis of the performance results was carried out according to the Taylor and Kuyatt (1994) method using the EES software (Klein and Alvarado, 2016). The resulting uncertainties are listed with the performance results in Appendix C. Figure 2.12 compares the overall heat transfer effectiveness of the air-side for the different circuitry arrangements for all test conditions. Figure 2.13 shows the percentage improvements in cooling capacity and COP when the interleaved circuitry was implemented. The following sections discuss the experimental results for the three evaporator circuitry configurations that are based on Figures 2.6 to 2.13.

2.3.1 Air Velocity Profile

The air velocity contours at the face of the ECU's evaporator were created using the local air velocity measurements as shown in Figure 2.6. Figure 2.6 shows that the air velocities are higher at the middle part and the upper part of the evaporator. The velocity trend behavior is due to the air stream direction inside the evaporator chamber, which has to take a 90 degree bend from the evaporator fan to the evaporator surface. Therefore, a significant air maldistribution occurred.

Figure 2.7 shows the average air velocity measurements across the surface of the ECU's evaporator. As a result, a continuous air velocity profile (*i.e.,* one dimension) is generated. The air velocity profile was generated using the Lagrange interpolation polynomial (Lagrange, 1877) and compared with cubic polynomial fit. It can be noticed from Figure 2.7 that the continuous velocity profile is akin to the air velocity contour in Figure 2.6. The measured air velocity profile justifies the assumption of air maldistribution across the evaporator.

The air velocity profile was used to calculate the fraction of total air flow seen by each circuit of the evaporator as shown in Figure 2.8. Note that the air velocity distribution is the same as the air flow rate distribution because the area occupied by each circuit in the cross-section of air flow passage is the same. Figure 2.8 helps in the circuit interleaving decision. For instance, the highest air velocity is observed for circuit number 3 and therefore, it is interleaved with the circuit that has the lowest air velocity percentage, which is circuit number 5 in this case. This process was repeated

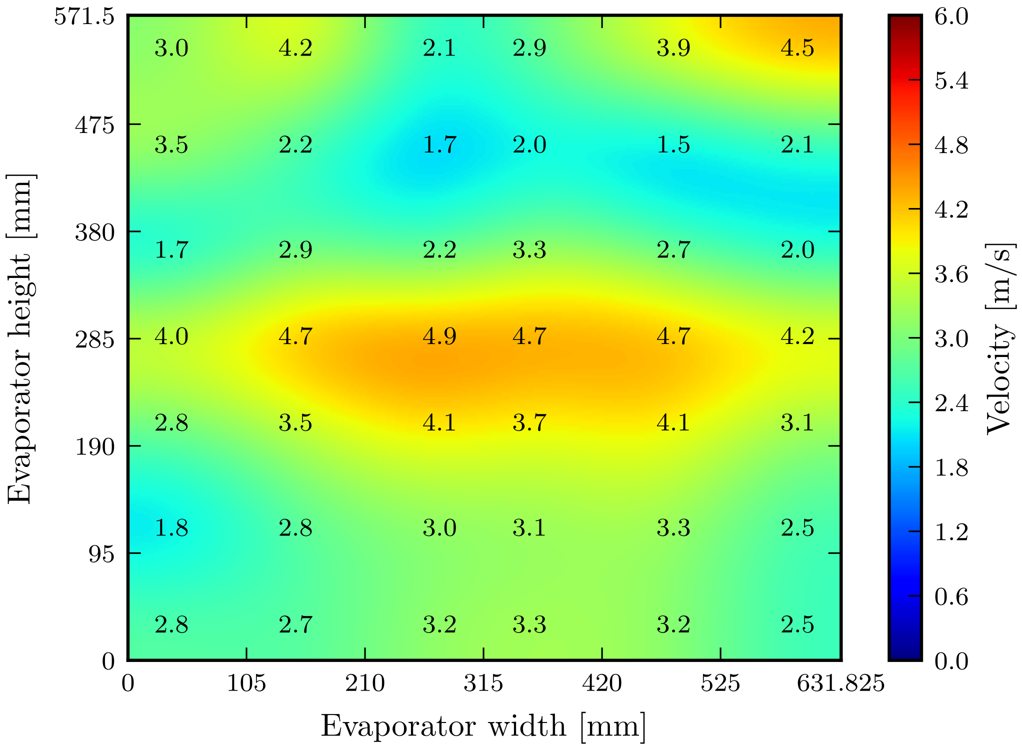

Figure 2.6. The contours of air velocity at the face of evaporator generated from the measured local air velocities (±0.375 m/s).

for the rest of the other circuits. The interleaved circuitry configuration was used in the experimental and simulation work.

Figure 2.9 shows the proposed interleaved circuitry as well as the baseline and the modified (or parallel) evaporator circuits. The baseline evaporator in Figure 2.9a had a complex circuitry arrangement that might have caused problems when interleaving its circuits, and therefore it was retrofitted to parallel configuration as shown in Figure 2.9b. The interleaved evaporator in Figure 2.9c was retrofitted based on the results in Figure 2.8. Due to the space limitation inside the evaporator chamber, the interleaved evaporator header had to be extended 76.2 mm (3 in) out of the unit. However, an insulated metal case was designed to seal the extended area to avoid any air leakage. Another effect of the modifications was the extra pipe length due to

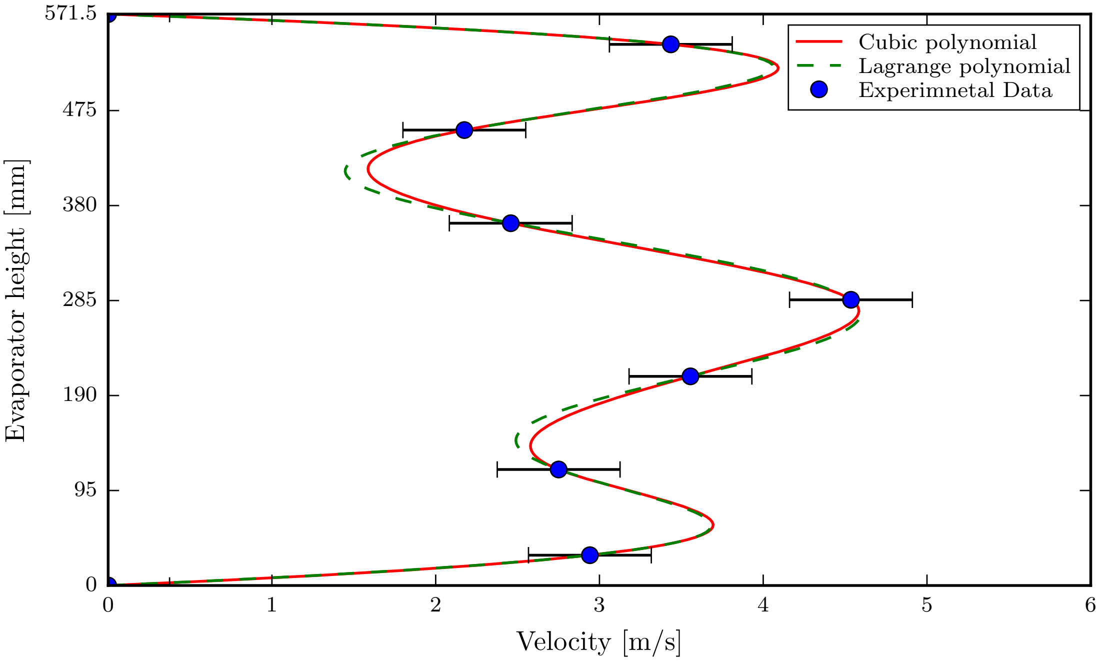

Figure 2.7. Air velocity profile correlated from experimental measurements.

the circuits rearrangements, which caused additional pressure drop in the evaporator. The average increase in pressure drop was estimated to be 5.54 and 19.66 kPa for the modified and interleaved arrangements, respectively.

2.3.2 Superheat Improvement

The air maldistribution affects the superheat for each individual circuit. Figure 2.10 compares the superheat distribution for the baseline, modified and interleaved evaporator circuitry for different test conditions. Figure 2.10a shows uneven superheat distribution across the baseline evaporator circuits, where the maximum superheat of 14°C (Test Condition C) occurred at circuit number 2, while the minimum superheat of 4°C (Test Condition 2) occurred at circuit number 6 with a difference of approximately 5 to 12°C. On the other hand, the parallel circuitry arrangement in the modified evaporator deteriorated the superheat distribution as shown in Figure 2.10b.

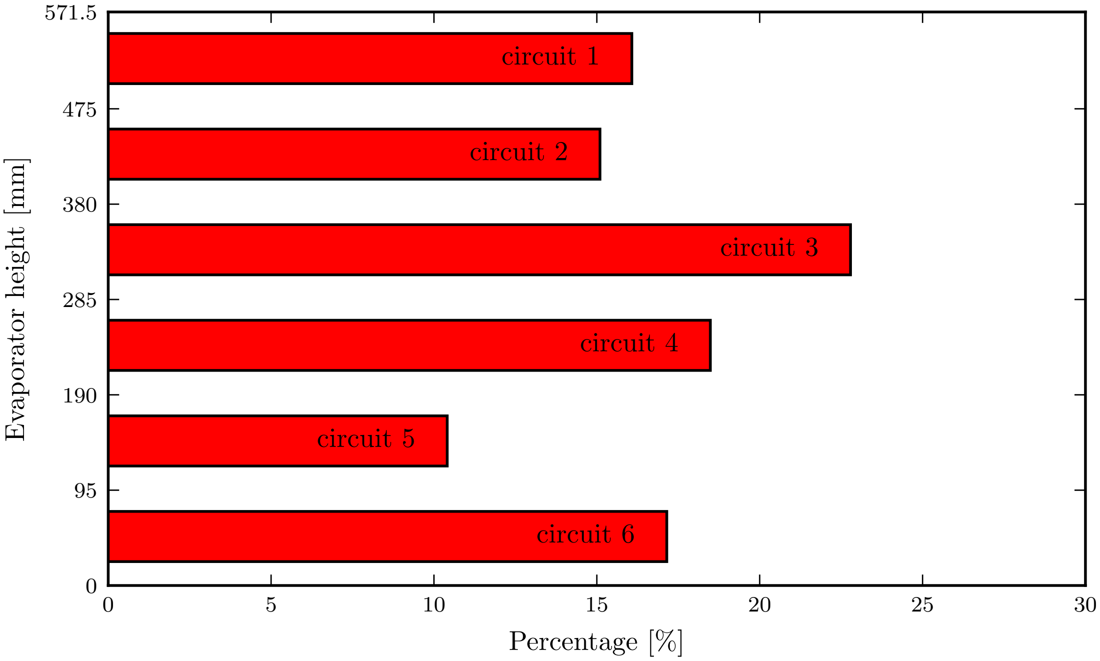

Figure 2.8. The percentage of accumulated air flow rate for the individual circuits based on the resulting continuous air velocity profile.

The superheat difference was approximately 9 to 14°C. The maximum and minimum superheats still occurred at circuits numbers 2 and 6 with values of 16 and 2°C, respectively. Figure 2.10c illustrated the improvement in superheat distribution with interleave circuitry configuration. Compared to the other circuitry arrangements, the superheat distribution was relatively uniform across the interleaved evaporator circuits. The superheat difference was approximately 1 to 5°C. Note that the superheat distribution was not sensitive to the change of testing conditions, even though the unit had different circuit arrangements.

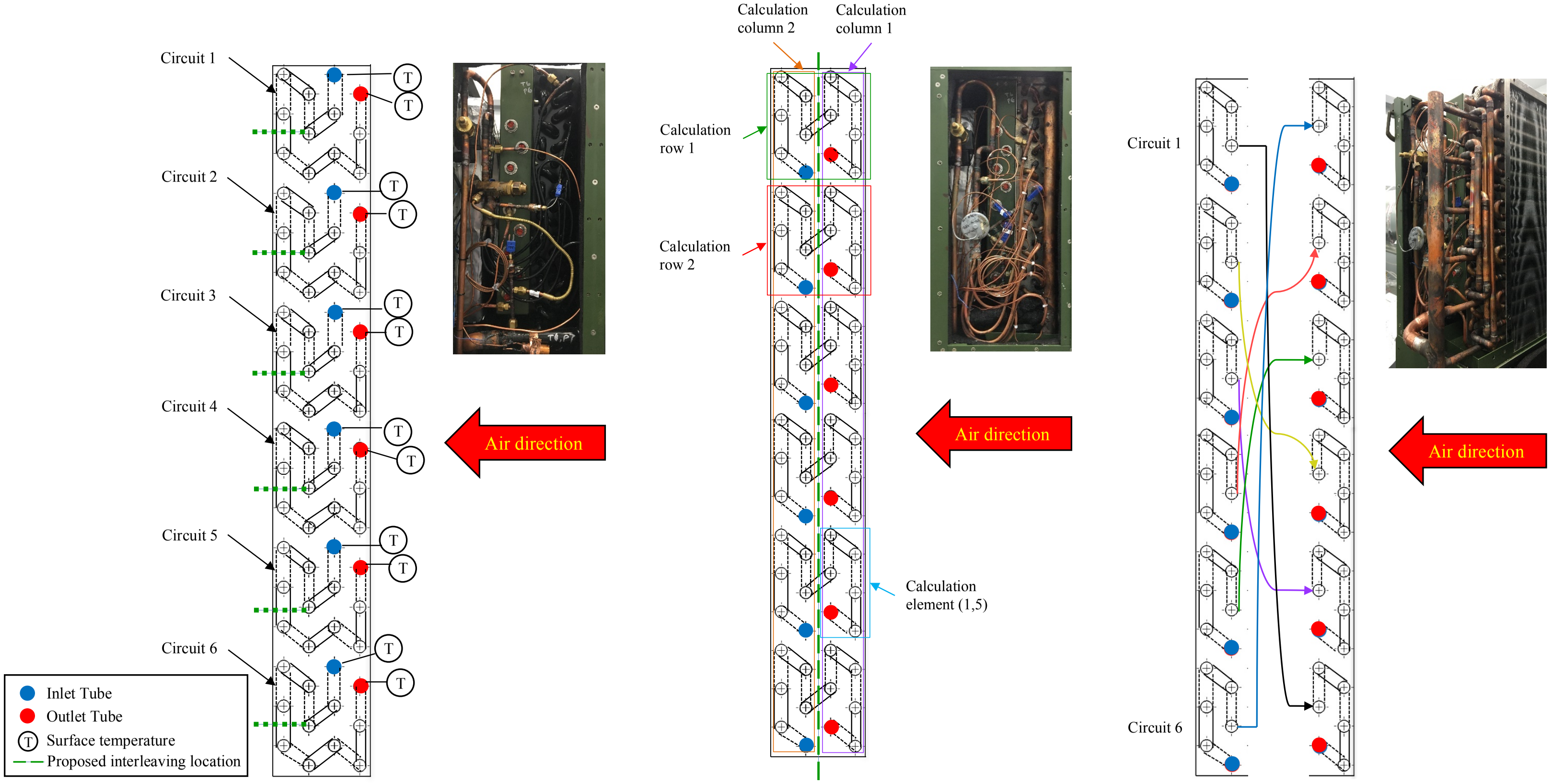

(a) (b) (c)

Figure 2.9. Arrangement configurations for (a) baseline, (b) modified, and (c) interleaved ECU evaporator circuitries where interleaved circuitry configured as circuit 3 to circuit 5, circuit 4 to circuit 2 and circuit 6 to circuit 1.

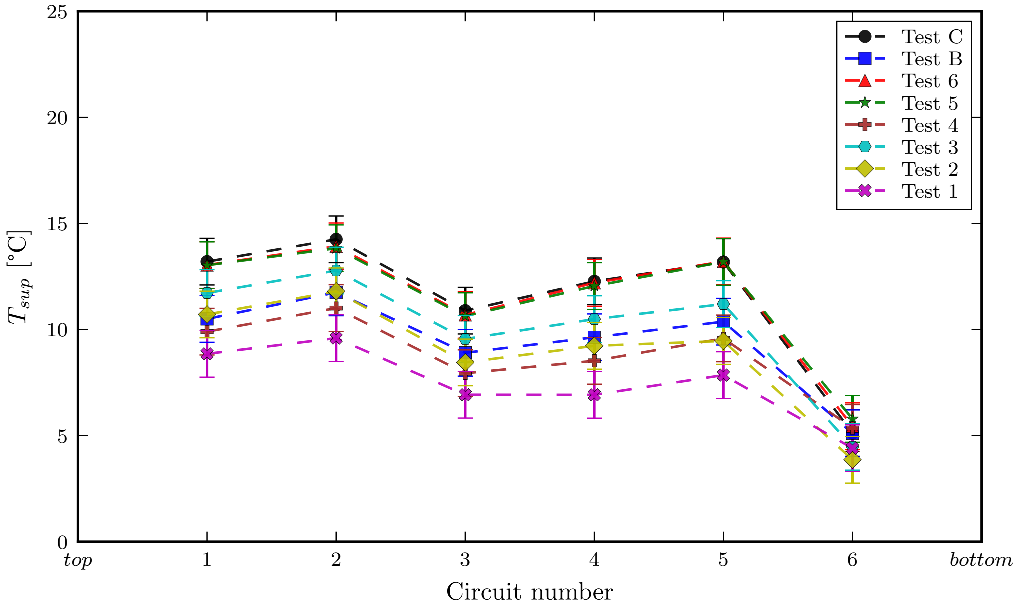

(a)

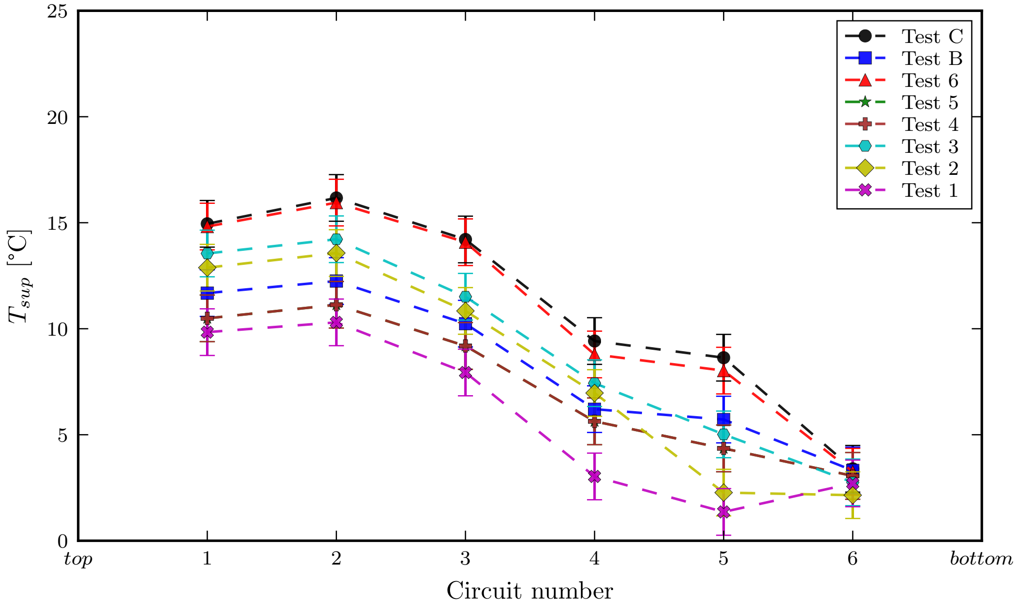

(b)

Figure 2.10. Superheat temperature across the tested (a) baseline, (b) modified, and (c) interleaved evaporator circuitry configurations at different testing conditions.

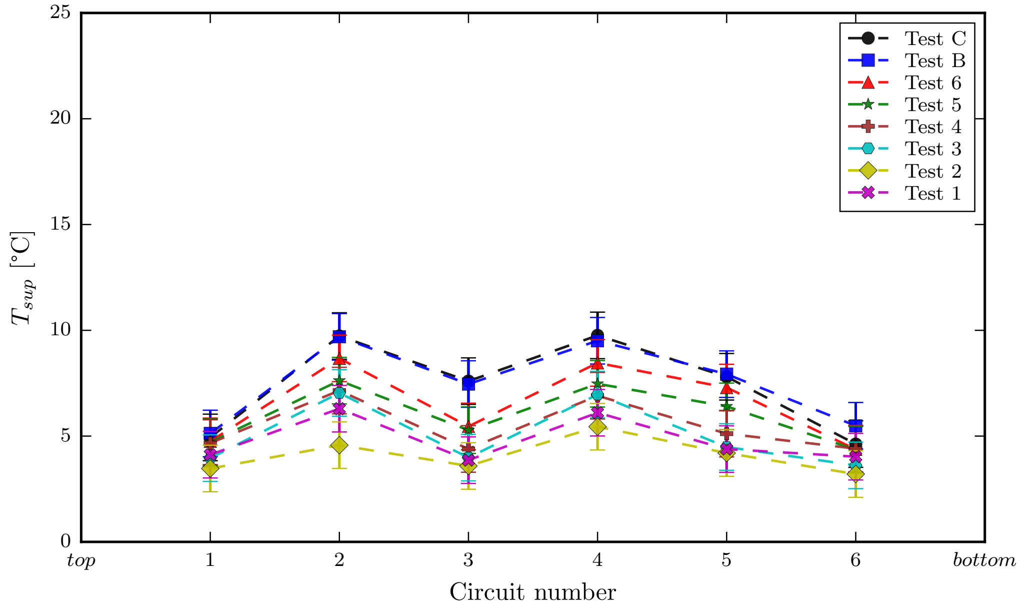

(c)

Figure 2.10. Continued.

2.3.3 Effectiveness and Performance Improvement

Air maldistribution affects the evaporator effectiveness and consequently the overall performance of the ECU. Figure 2.11 compares the refrigeration cycle of the ECU for the three evaporator circuitry arrangements. Figures 2.11a and 2.11b indicate that the interleaved circuitry arrangement exhibited a relatively higher evaporating pressure and temperature than that of the other two evaporator configurations. The interleaved circuitry configuration reduced the air maldistribution effect and enhanced the heat transfer on the air side. The heat transfer effect on the air side was increased by interleaving the higher air flow rate circuit with the lower one, reducing the difference between the evaporating temperature and the return air and thus, increasing the cooling capacity. In other words, the interleaved circuitry leads to an increase in the evaporating pressure as shown in Figures 2.11a and 2.11b. This leads to a reduction in the pressure ratio across the compressor and thus, an increase in the mass flow rate and cooling capacity. Note that no significant improvement on unit performance was observed when the parallel circuitry arrangement (*i.e.,* modified arrangement) was tested.

Figure 2.12 shows the overall heat transfer effectiveness on the air-side of the evaporator with the different circuitry configurations at all test conditions. It can be seen from Figure 2.12 that the heat transfer effect on the air side was relatively increased using the interleaved circuitry arrangement compared to the other two arrangements. The interleaved circuitry compensates for the air maldistribution and therefore, more heat transfer on the air side was obtained. Also, there is no significant improvement in the heat transfer effectiveness that can be noticed between the baseline and the modified arrangements.

The cooling capacity and COP were improved as a result of interleaving the evaporator circuits. Figure 2.13 shows that for different testing conditions, the improvement in cooling capacity ranged from 5.4% to 16.6%, while the improvement in COP ranged from 1% to 12.4%. Note that the lowest improvements were observed at Test Condition B because the unit was working at an off-design point. Otherwise, the minimum cooling capacity and COP improvements were 5.3% and 4.5%, respectively.

2.4 Model Development

The interleaved circuity model was initially developed by Bach (2014) using the evaporator model from Bell (2015). More specific details about the evaporator model can be found in *Evaporator Model* section in Appendix F. This model is modified here to interleave evaporator circuits based on the actual air velocity profile. The interleaved evaporator is shown in Figure 2.9c. The refrigerant from the circuit that has highest air flow is redirected to the circuit that has the lowest air flow, and so on for the remaining circuits. This leads to a decrease in the difference of exit superheat between individual circuits on the refrigerant-side and thus, the air maldistribution effect is compromised. Note that knowing the air velocity profile is essential to interleaving the circuits accordingly. Here, the air velocity results from Section 2.3.1 were

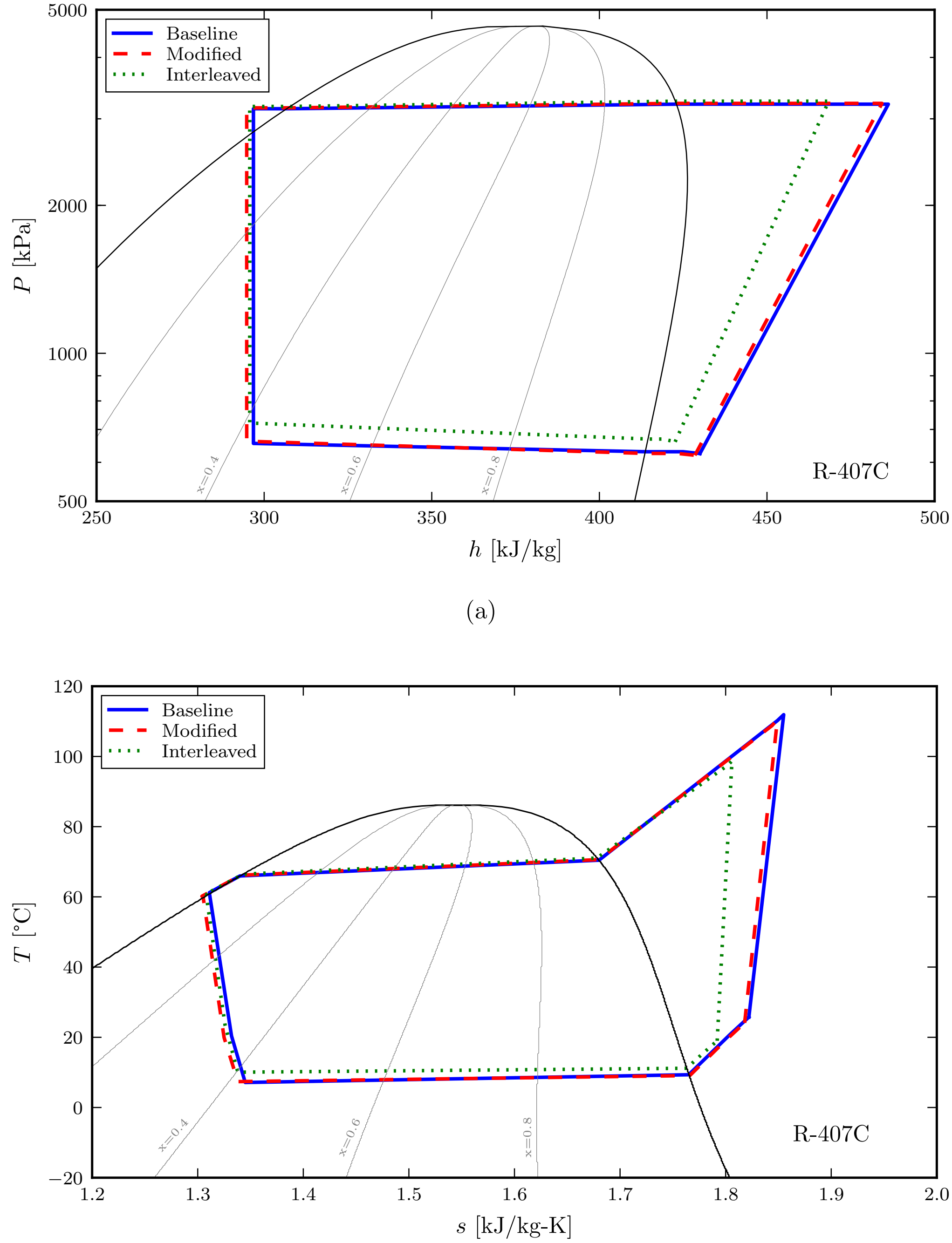

(a)

(b)

Figure 2.11. Diagrams of (a) pressure-enthalpy and (b) temperature-entropy to compare baseline, modified and interleaved evaporator circuitry arrangements at Test Condition 1.

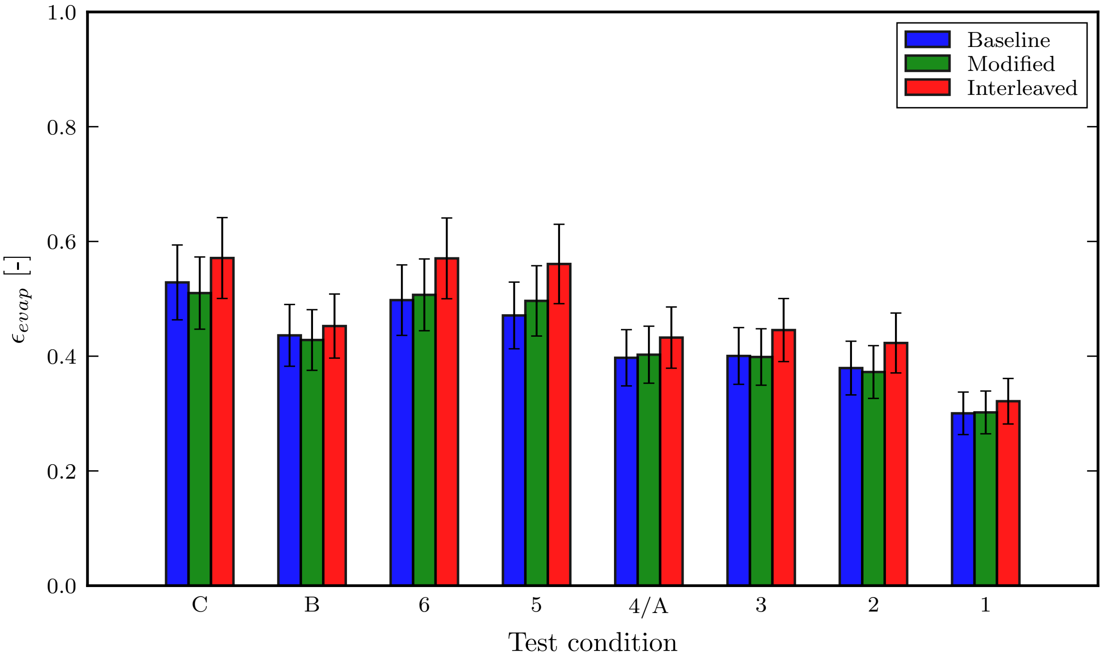

Figure 2.12. Air-side overall heat transfer effectiveness improvement using interleaved circuitry arrangement at different testing conditions.

used in the simulation work. In addition, there is a slight increase in pressure drop because of extended return bends in some circuits.

2.4.1 Evaporator Model

The evaporator model of Bell (2015) was constructed using a moving boundary method, which divides the evaporator according to the phases of refrigerant flow as shown in Figure 2.14. Each section of the heat exchanger in Figure 2.14 is simulated using the ϵ-NTU method (Bergman et al., 2011) as separate crossflow heat exchangers, assuming constant refrigerant pressure equal to the saturation pressure.

To accurately estimate the behavior of the heat transfer from the air to the refrigerant side of the evaporator, the partial-wet partial-dry method (Braun, 1988) is utilized in explaining the air side sensible and latent heat transfer when the surface

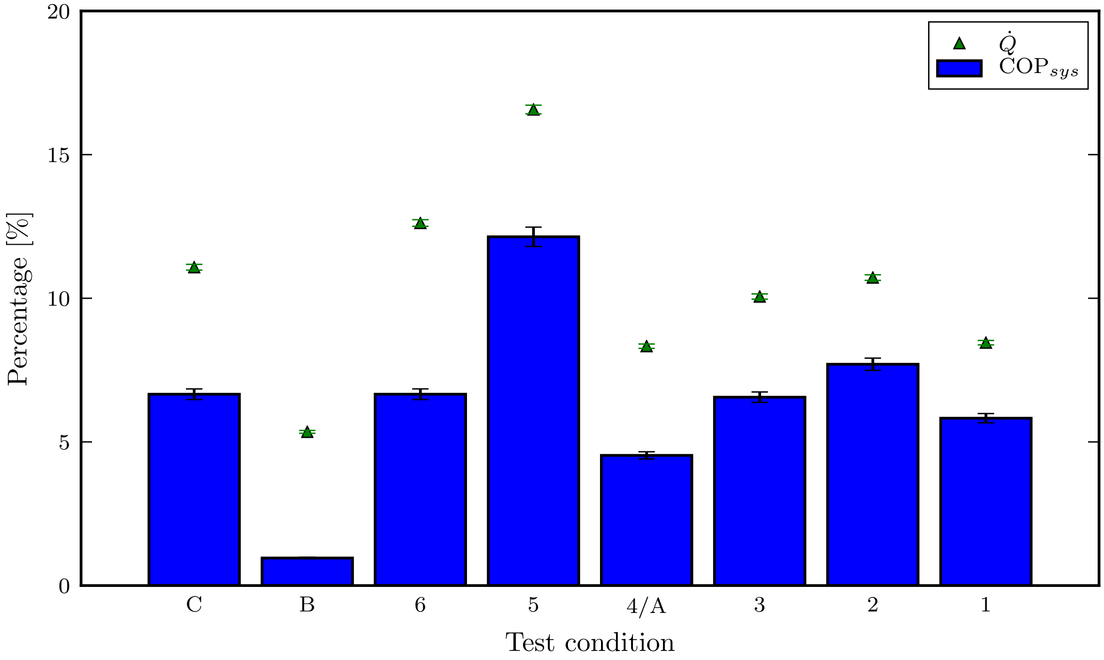

Figure 2.13. COP and cooling capacity improvements using interleaved circuitry arrangement at different testing conditions.

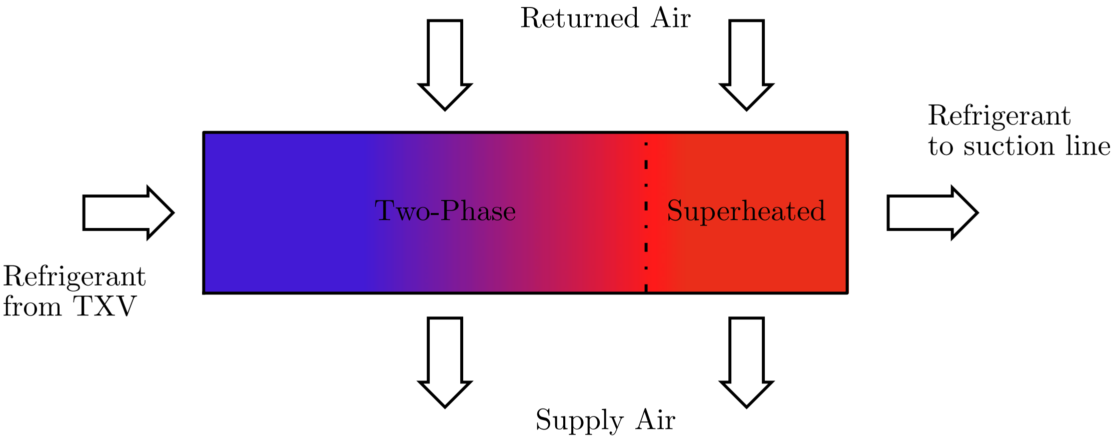

Figure 2.14. Schematic of evaporator model simulated by moving boundary method.

temperature of the coil falls below the dew-point of air at the inlet of the evaporator. A model schematic is shown in Figure 2.15. The evaporator in Figure 2.15 is solved by separating the heat exchanger into two sections. The section with surface temperatures higher than the dew-point is solved by a completely dry analysis, while the other section is solved assuming a completely wet analysis.

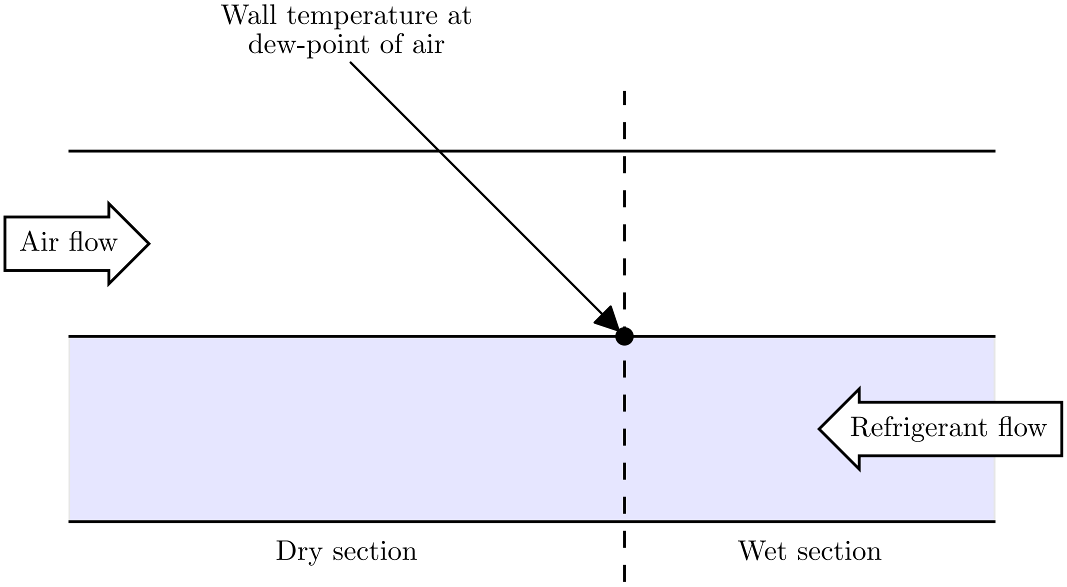

Figure 2.15. Schematic of evaporator model simulated by partial-wet-partial-dry method.

The correlations used to solve the heat transfer coefficients and friction factors in the evaporator model are presented in Table 2.3, while the geometrical parameters shown in Table 2.4 are used.

Table 2.3. Heat transfer and pressure drop correlations in evaporator model.

		Single-phase	Two-phase
Refrigerant-side	Heat transfer	Gnielinski (1976)	Shah (1976)
	Pressure drop	Churchill (1977)	Lockhart and Martinelli (1949)
Air-side	Heat transfer	Wang et al. (1998)	
	Fin efficiency	Schmidt (1945) modified by Hong and Webb (1996)	

Table 2.4. Simplified geometry of the ECU evaporator.

Number of tubes per bank (per element)	3
Number of banks (per element)	2
Number of circuits (per element)	1
Length of tubes [mm]	631.825
Outer diameter of tubes [mm]	12.7
Inner diameter of tubes [mm]	11.7348
Longitudinal distance between tubes [mm]	27.4828
Transverse distance between tubes [mm]	131.75
Fins per inch	12
Fin waviness [mm]	0.79375
Half-wavelength of fin wave [mm]	6.35
Fin thickness [mm]	0.1905
Conductivity of fins [W/m-K]	237

2.4.2 Interleaved Circuitry Model

The ACHP evaporator model (Bell, 2015) is used in the analysis of the interleaved circuitry evaporator. In this particular analysis, each evaporator element is treated as an equivalent to an individual ACHP evaporator. 12 elements with 6 tubes in each element were used in the evaporator as shown in Figure 2.9. The inlet and outlet state conditions for each element were computed iteratively with respect to the known inlet state conditions to the overall evaporator.

The flow chart in Figure 2.16 shows the algorithm used in the evaporator solver. To simulate the experimental scenarios, the implicit evaporator model was structured as shown in Figure 2.16. Measurements include indoor dry-bulb temperature and humidity, fan air flow rate and power consumption, inlet refrigerant saturation pressure and quality (or enthalpy), targeted exit superheat temperature and an initial value for refrigerant mass flow rate, all of which were input to the model. A non-linear numerical solver (Moré et al., 1980) was used to satisfy the convergence by adjusting the independent variables (*i.e.,* h_{int} and $\dot{m}_r$) to minimize the residuals (*i.e.,* Δh_{int}

and ΔT_{sup}). The main outputs include the refrigerant and air state conditions for every circuit as well as the cooling capacity.

Note that each element in the evaporator model does not separate superheat section and two-phase section air outlet temperatures. However, the overall outlet air temperature and humidity is calculated for each section. As a result of this methodology, the relationship of heat transfer to the air inlet temperature is slightly nonlinear. Therefore, the simulation work and tuning process were related to the ECU system that has an evaporator of 6 circuits and uses R-407C as a refrigerant. For model simplification, other factors are not evaluated such as cross fin conduction, air and refrigerant side fouling, the mixing and equalization of the air flow across the heat exchanger, and manufacturing tolerances. Refrigerant distribution across the different circuits was assumed to be uniform.

2.4.3 Model Tuning

There was a systematic bias between the simulation results and experimental observations due to simplifications and imperfect information related to the evaporator. To eliminate the bias, two tuning multipliers were used: A multiplier for the air-side heat transfer coefficient and another multiplier for the refrigerant-side heat transfer coefficient of the evaporator. Note that only the refrigerant-side heat transfer coefficient of the two-phase region is corrected because the cooling capacity in the evaporator is dominated by the heat transfer rate in the two-phase region.

The estimation of the multipliers was conducted in a computational process as shown in Figure 2.17. The tuning process in Figure 2.17 eliminated the estimation bias in the refrigerant mass flow rate, the evaporator heat transfer rate, and supply air temperature by minimizing the objective function (Equation (2.4)), which calculates the sum of squares of the difference between measurement and estimation at the i^{th}

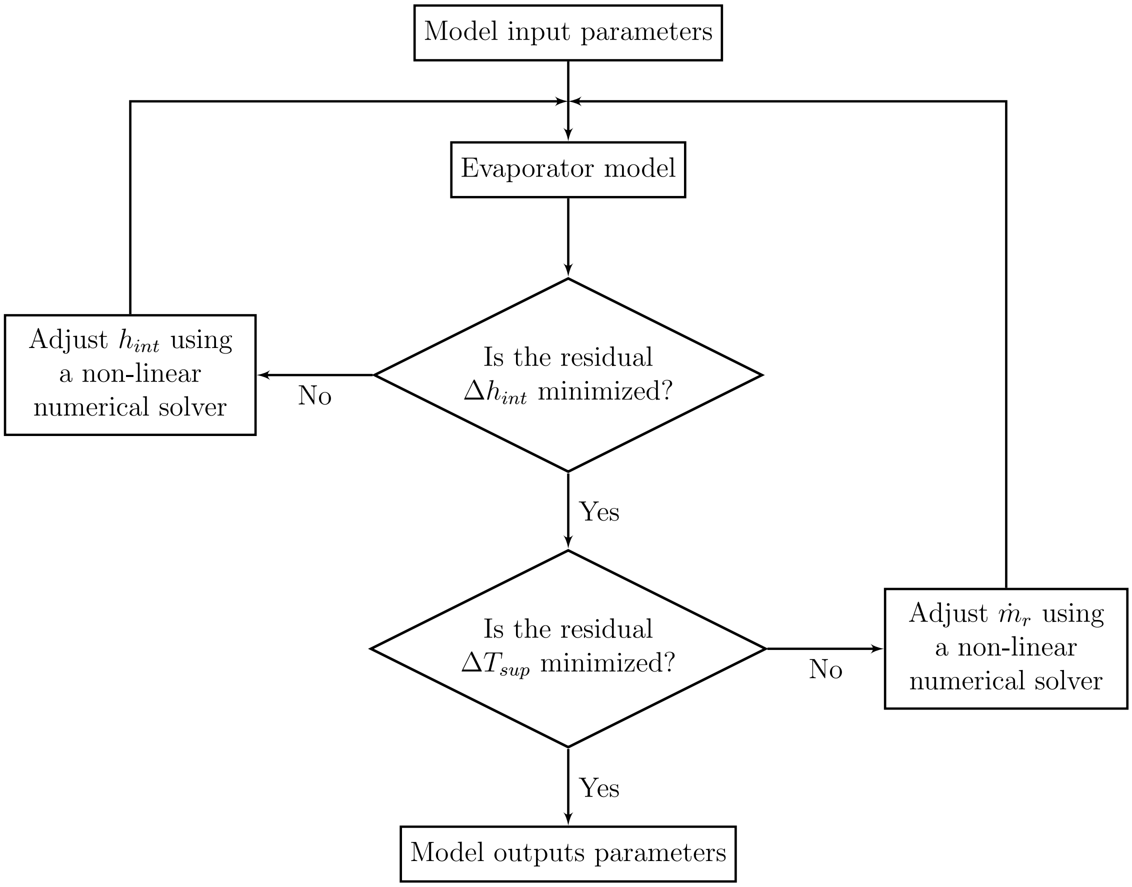

Figure 2.16. Flowchart of evaporator interleaved circuitry solver.

data point of the baseline experimental results. The optimization problem was solved with sequential least squares method (Kraft, 1988),

$$J = \sum_i \left(\frac{\dot{m}_{r,pred,i} - \dot{m}_{r,exp,i}}{\dot{m}_{r,exp,i}}\right)^2 + \left(\frac{\dot{Q}_{evap,pred,i} - \dot{Q}_{evap,exp,i}}{\dot{Q}_{evap,exp,i}}\right)^2 + \left(\frac{T_{a,o,pred,i} - T_{a,o,exp,i}}{T_{a,o,exp,i}}\right)^2 \quad (2.4)$$

The tuning multipliers results are shown in Table 2.5. Those factors were used for interleaved circuitry simulation and validation. It can be noticed from Table 2.5 that the air-side multiplier is relatively low because of the differences between the predicted outlet air temperatures and the measured one which is mainly a result of the influence of the air leakage around the evaporator in the experimental measurements.

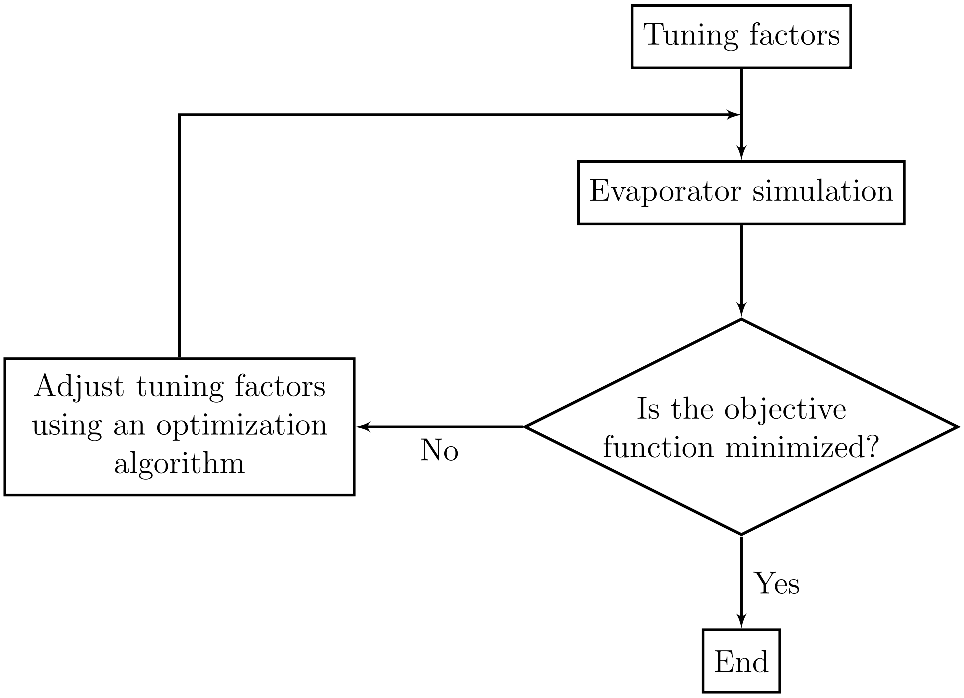

Figure 2.17. Flowchart of evaporator tuning process.

In addition, the multiplier accounts for all discrepancy in the simplified model input parameters.

Table 2.5. Evaporator tuning multipliers.

Air-side heat transfer	0.176
Refrigerant-side heat transfer	0.7

2.4.4 Model Validation

Since the model simulates cases with different indoor/outdoor conditions and air velocity profiles, only the 8 tests conducted with the ECU were used for validation. The comparison of the refrigerant mass flow rate and the cooling capacity between the tuned simulation and experimental results for baseline and interleaved circuitry models are normalized based on the average experimental values and plotted in Figures 2.18 and 2.19, respectively. The percentage error between the predicted and experimental values is calculated by the mean absolute method and the root mean square deviation method given in Equations (2.5) and (2.6), respectively,

$$\mathrm{MAE} = \frac{100}{n} \sum\nolimits_{i=1}^{n} \left| \frac{x_{pred,i} - x_{exp,i}}{x_{exp,i}} \right| \tag{2.5}$$

$$\mathrm{RMSD} = \frac{100}{\bar{x}_{exp}} \sqrt{\sum\nolimits_{i=1}^{n} \frac{\left(x_{pred,i} - x_{exp,i}\right)^2}{n}} \tag{2.6}$$

Figure 2.18 shows that the refrigerant mass flow rate and cooling capacity for the tuned baseline model were estimated within approximately 10% and 13% for MAE and RMSD, respectively, without significant bias. However, only the results of one condition (*i.e.,* Test Condition 5) were over-predicted because the heat transfer has a nonlinear behavior while the tuning factors were chosen to be constant values.

Using the same tuning factors from the baseline model, Figure 2.19 shows the predicted refrigerant mass flow rate and cooling capacity for interleaved circuitry configuration. Figure 2.19 shows that the refrigerant mass flow rate and cooling capacity for the interleaved circuitry model were predicted within approximately 10% and 11% for MAE and RMSD, respectively.

2.5 Summary

This chapter presented an application of interleaved circuitry in a packaged air-conditioner to compensate for airflow maldistribution. The effectiveness of interleaved circuitry was evaluated in a 17.6 kW R-407C Environmental Control Unit (ECU) based on air velocity measurements. The interleaved circuitry arrangement was based on the air velocity percentage attributed to each of the evaporator circuits, where the refrigerant from the circuit that had the highest air flow was redirected to the circuit that has the lowest air flow, and so on for the remaining circuits. The interleaved evaporator was experimentally investigated at extreme testing conditions up to 51.7°C (125°F) and comparisons of cooling capacity, COP and evaporator superheat were

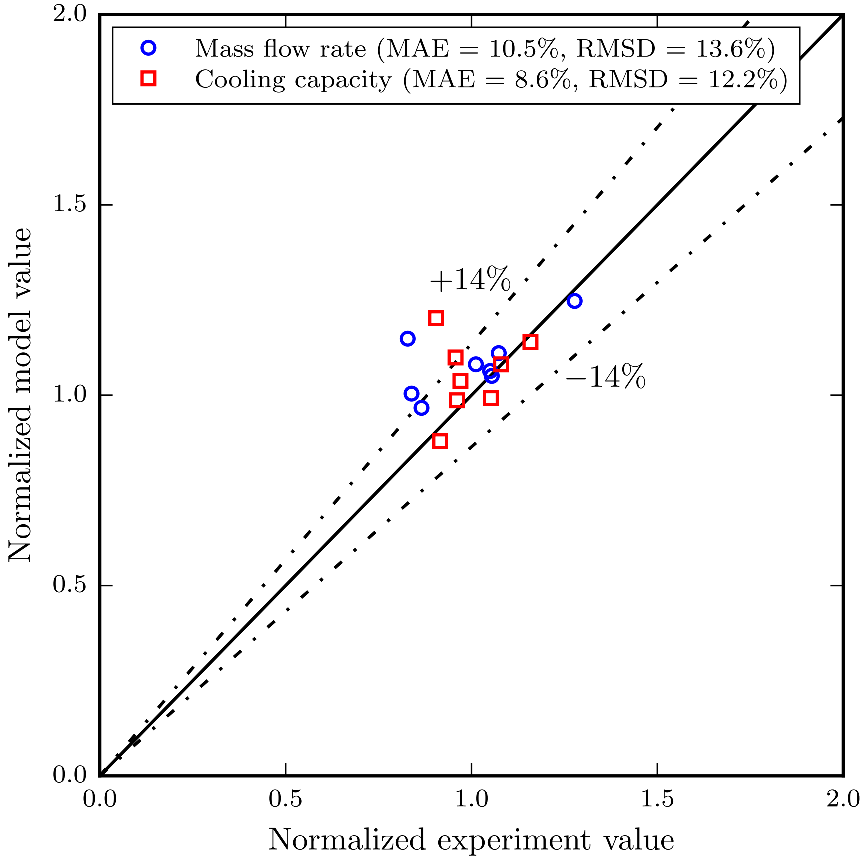

Figure 2.18. Comparison of experimental and predicted mass flow rate and cooling capacity for baseline model (normalized with average experimental value).

evaluated with respect to the original evaporator circuitry. An interleaved circuitry model was developed and validated using the experimental data. The results yielded the following conclusions:

- The local air velocity measurements were fitted using Lagrange interpolation polynomial to generate a continuous air velocity profile on the face of the ECU evaporator.
- Despite the increase of approximately 20 kPa in refrigerant-side pressure drop across interleaved evaporator circuitry compared to original circuitry, the su-

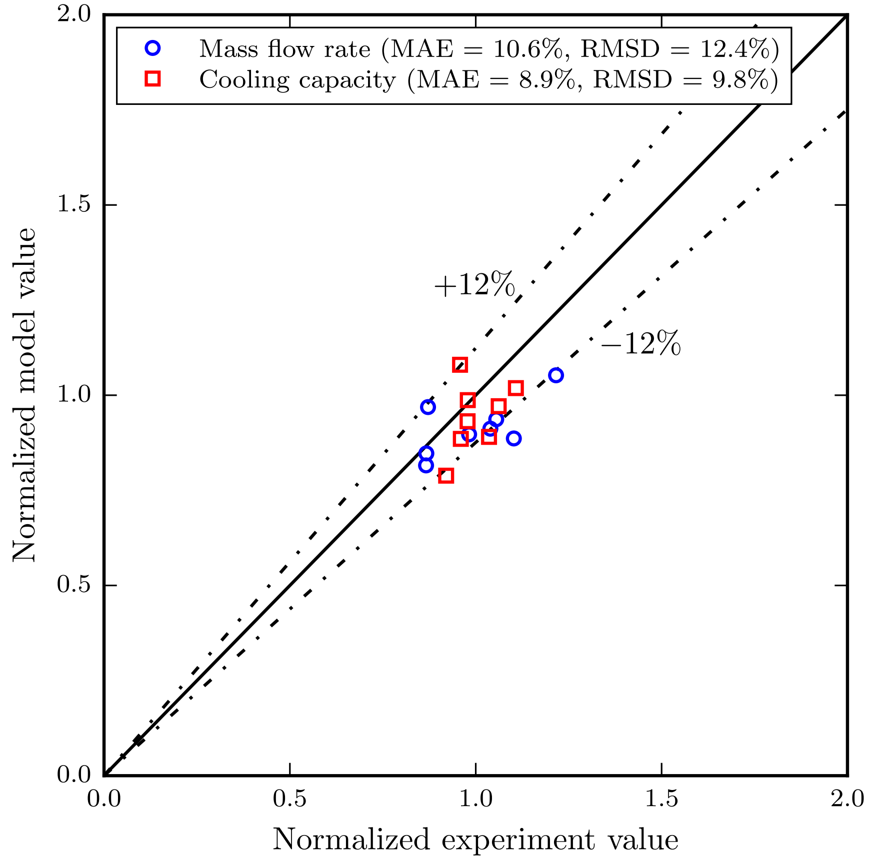

Figure 2.19. Comparison of experimental and predicted mass flow rate and cooling capacity for interleaved model (normalized with average experimental value).

perheat distribution improved for the interleaved circuitry with a difference of $1 - 5$°C.

- The interleaved circuitry arrangement improved the cooling capacity and COP within $5.3 - 16.6\%$ and $4.5 - 12.4\%$, respectively.
- An implicit evaporator model based on the moving boundary method was developed, tuned and then validated within a mean absolute error of approximately ±10% of mass flow rate and cooling capacity predictions.

CHAPTER 3. APPLICATION OF VAPOR INJECTED COMPRESSION WITH ECONOMIZING IN HIGH TEMPERATURE CONDITIONS

3.1 Introduction

For the application in hot ambient temperatures, the system performance of a packaged air conditioning (AC) unit degrades significantly. Bahman et al. (2014) showed that vapor injection (VI) with economization was superior to liquid (*e.g.,* oil) flooding with regeneration at ambient temperatures greater than 35°C. In this chapter, the aim is to assess the application of economized vapor injection (EVI) system in a packaged AC unit to improve the performance at extreme ambient conditions. To evaluate the effectiveness of EVI in a packaged air conditioner, an R-407C Environmental Control Unit (ECU) with 17.6 kW cooling capacity was retrofitted with a single-port VI scroll compressor, a plate heat exchanger (PHX) economizer and an additional expansion device to examine superheated and saturated injections at different steady-state operating conditions up to 51.7°C (125°F) in side-by-side psychrometric chambers. The cooling capacity, COP, and compressor discharge temperature of the EVI system were evaluated and compared to the case without injection (baseline case). An implicit cycle model of an EVI system was developed and validated by using the experimental results. The accuracy of the model was further improved by tuning heat transfer and pressure drop correlations. Finally, the validated model was employed to numerically investigate an alternative VI compressor with an optimized PHX design to maximize the system COP at outdoor temperature of 51.7°C (125°F) and indoor temperature of 32.2°C (90°F) with 50% relative humidity.

3.1.1 Background

The majority of research conducted on ECU systems focuses on system-level overall performance (Elbel and Hrnjak, 2010; Elbel et al., 2012; Hwang et al., 2001; Li, 2006; Li and Groll, 2006; Manzione and Calkins, 2002; Robinson and Groll, 2001). However, the packaged AC unit performance can be enhanced by employing specific components, such as high efficiency scroll compressors. For instance, Yamamura et al. (1990) and Cho et al. (2011) recommended scroll compressors due to their high efficiency, low vibration, and low noise level. The compressor featured a tip-seal mechanism, optimized axial clearance to minimize gas leakage in the compression pocket, and a driving bush design to have proper sealing force.

The scroll compressors were further developed to be used in single-stage AC systems as well as in two-stage or multi-stage units. When the pressure ratio or temperature lift increases, AC systems using single-stage vapor compression cycles become increasingly inefficient. Thermodynamic considerations dictate the use of two-stage or multi-stages cycles. However, the complexity of those cycles and the cost of additional components increase the necessary investment.

One possible method to increase system performance is to flood the compressor with a significant amount of liquid (*e.g.,* oil) to achieve a quasi-isothermal compression process. The injection can occur either in the suction line or directly into the working chambers during the compression process. As a result, the rise in compressor discharge temperature can be limited despite a significant increase of the temperature lift of the system. In addition, by including an internal regenerator in the cycle, the refrigerant subcooling can be increased along with the cooling capacity. Bell et al. (2011), James et al. (2016), and Ramaraj et al. (2016) showed that the effectiveness of flooded compression and internal regeneration increases as the temperature lift of the system increases. They conducted in-depth analyses on the benefits of oil flooding with regeneration technology in cold climate applications. Whereas, Yang et al. (2014) and Luo (2016) investigated the cooling mode.

A relatively small improvement in system performance with liquid (or oil) injection comes at the cost of an additional oil separator and oil cooler, adding complexity to the system and introducing the possibility of it affecting the cooling performance in the case of incomplete separation. The liquid (or oil) injection with a regenerator is mostly used to reduce the discharge temperature. However, in AC systems, Xu et al. (2011) explained that the benefits of excess subcooling surpass the benefits from a reduction in discharge temperature. Therefore, vapor injection with economizing can be beneficial to increase the cooling capacity, despite the modest system performance improvement at ambient temperatures greater than 35°C.

Vapor injection (VI) with an economizer shares the same goal of liquid injection with regeneration, as shown in Figure 3.1. It aims to cool the refrigerant during the compression process by injecting refrigerant gas at an intermediate stage into the compressor. Therefore, the compressor discharge temperature is reduced, and the compressor operating range is extended to larger temperature lifts. The economizer can be either a flash tank or a plate heat exchanger (PHX), which allows the refrigerant to enter the evaporator at lower quality, and thus improves the system performance. Currently, the economized vapor injection (EVI) system shown in Figure 3.1 dominates the market in heat pump applications because of its performance and due to the fact that it enables a quasi-two-stage cycle operation with a single compressor. Moreover, the ability to modulate the capacity between single-stage and two-stage modes results in improved reliability (Park et al., 2015). For example, a single compressor with multi-port injection eliminates the need for multiple compressors thereby lowering the cost significantly (Mathison et al., 2011).

The vapor injection (VI) with economizing shows significant system performance improvement in cold climates (Bertsch and Groll, 2008; Navarro et al., 2013; Xu et al., 2011). However, the benefit can be extended to extremely hot summer conditions where peak temperatures occur for a small period during the day. In such cases, Ding et al. (2004) showed that the cooling capacity was more important than the COP. The cooling capacity of a R-22 heat pump unit increased by 9.7% when the condensing

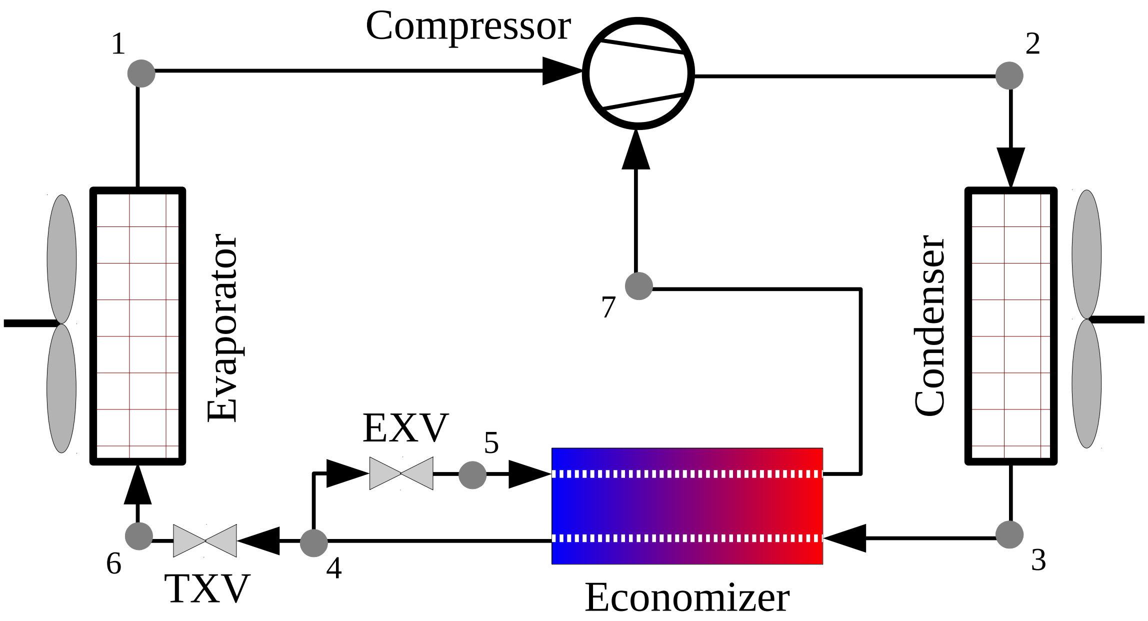

Figure 3.1. Vapor injection (VI) system diagram with plate heat exchanger (PHX) economizer.

and evaporating temperatures were 60°C and 2°C, respectively. Furthermore, the compressor discharge temperature decreased by 5°C, which enhanced the compressor performance in hot summer weather. Wang et al. (2009) conducted an experimental study on an 11 kW R-410A residential AC split unit to investigate vapor injection cycle with both a flash tank and a PHX as economizers. The flash tank and PHX economizers showed a performance improvement over the non-injected system. When operating at maximum cooling mode, the cooling capacity and COP were improved by 14% and by 4% at an ambient temperature of 46.1°C, respectively. According to the results of Wang et al. (2009) and Heo et al. (2011), although a flash tank economizer was more favorable in terms of the system performance improvement and the relatively low cost, the PHX economizer was more suitable as it allowed to achieve a wider range of injection conditions as well as easier control of the injection mass flow rate. Using a PHX economizer in a vapor injection cycle developed sufficient cooling COP and capacity for summer application as demonstrated by Bertsch and Groll (2008) and Tello-Oquendo et al. (2016). Cho et al. (2016) studied the vapor injection with PHX cycle by varying the outdoor temperature and injection ratio in a 28 kW split unit using R-410A and R-32. At the optimum injection ratio, the results showed 2.1 to 6.3% higher cooling capacity than those without vapor injection for an ambient temperature of 35°C. To the best of the author's knowledge, vapor injection with PHX economizing technology has not been investigated in a packaged AC unit under extremely hot weather conditions such as 51.7°C (125°F) or higher.

3.2 Experimental Methodology

3.2.1 Experimental Setup and Procedures

An Environmental Control Unit (ECU) was retrofitted with economized vapor injection (EVI) system, as shown in Figure 3.2, and tested under the same operating conditions in side-by-side psychrometric chambers to assess the implementation of vapor injection and unit's performance improvement. A schematic of the ECU setup installed inside the psychrometric chambers is shown in Figure 2.3. The ECU has a rated cooling capacity of 17.6 kW (60,000 Btu/hr) and uses R-407C as a working fluid. Figure 3.3 illustrates the original ECU system schematic as black solid lines and the retrofitted parts as colored lines. The compressor type is a hermetic scroll compressor with a single-port injection and a volumetric displacement rate of 14.1 m^3/h. More details about the setup can be found in Section 2.2.

To integrate the vapor-injected system, the ECU was retrofitted with an economizer and an electronic expansion valve (EXV) as illustrated with colors in Figure 3.3. The economizer is a brazed plate heat exchanger (PHX) which was over-sized for the purpose of this study. After the PHX, a stepper motor-driven electronic expansion valve (EXV) is installed to facilitate and control the down-stream injection to the compressor. The EXV has been selected based on the nominal capacity of the PHX

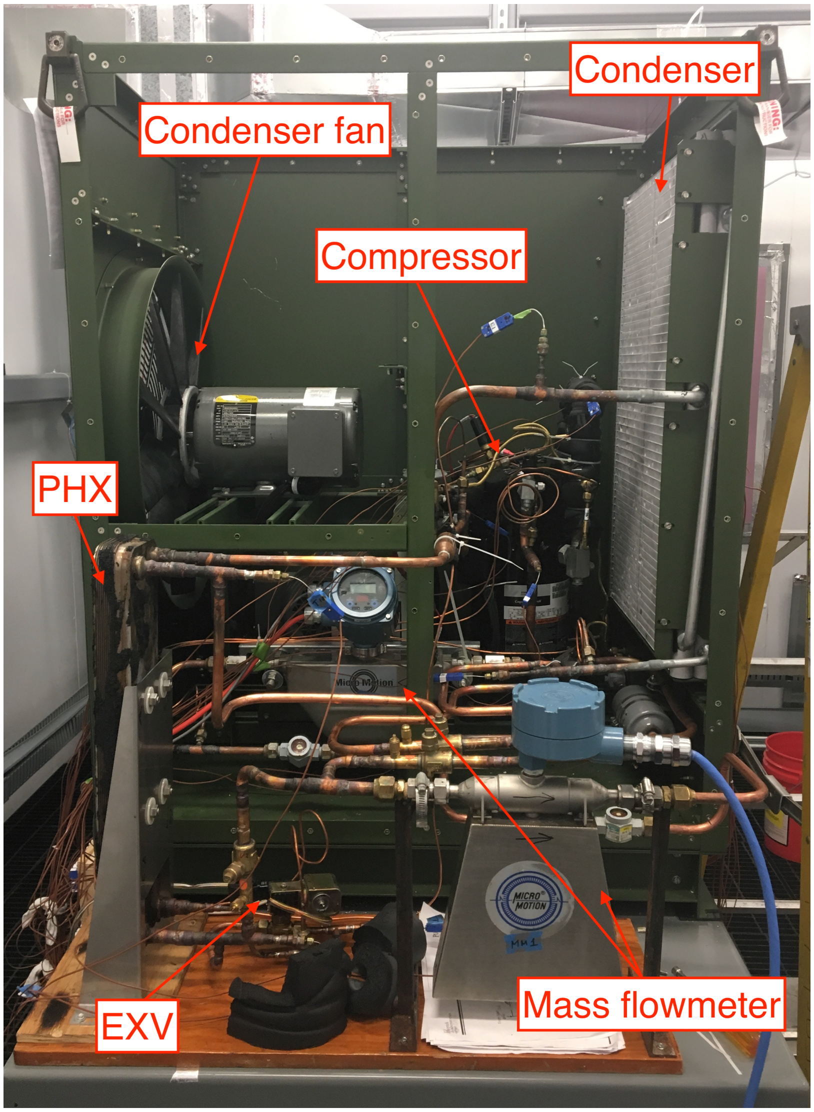

Figure 3.2. Layout of the Environmental Control Unit (ECU) retrofitted with VI compressor, economizer (PHX), EXV and mass flow meters.

to control the injection flow. The EXV control is based on the injection superheat that resulted from the temperature and pressure measurements at the injection port. To be noted is that all the retrofitted parts are fully insulated to avoid any heat loss during testing. Moreover, Figure 3.3 shows the mounting position of each measuring instrumentation, while the respective accuracies of these instruments are listed in Table 3.1. The following parameters were measured: temperatures and pressures at the

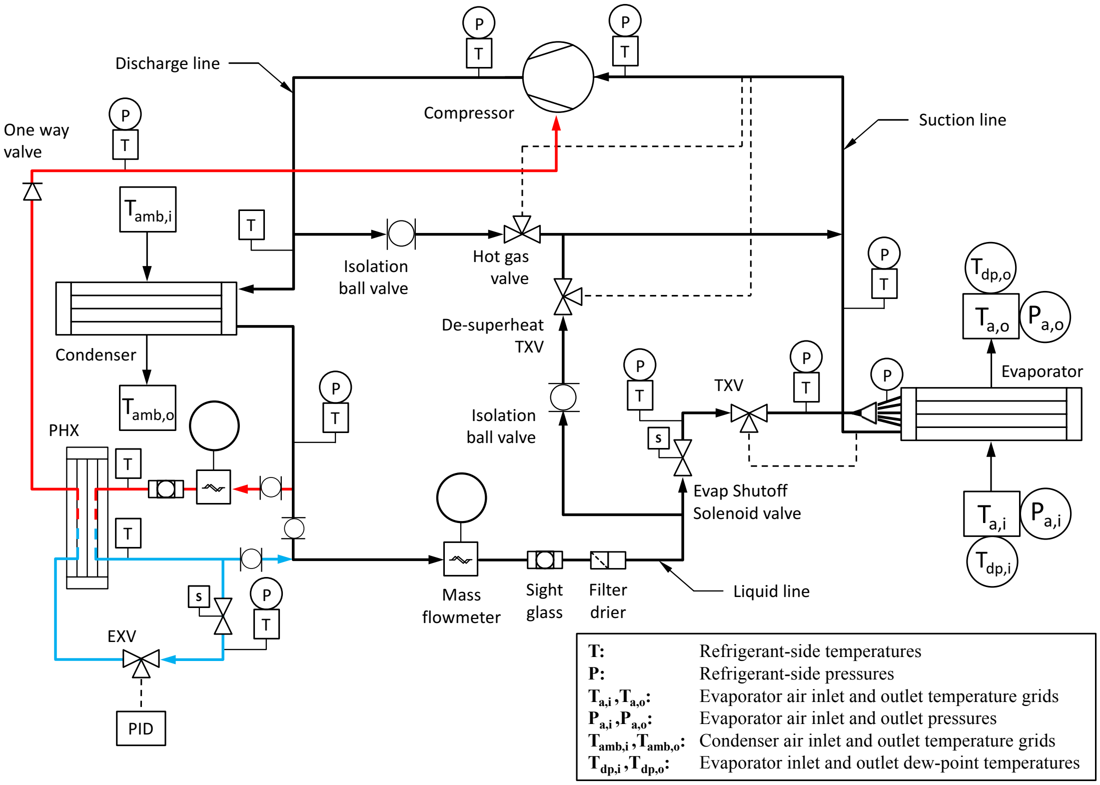

Figure 3.3. Measured points of the EVI system.

inlet and outlet of all the components, total refrigerant flow rate after the condenser, injection refrigerant flow rate after the PHX, air humidity at the inlet and outlet of the evaporator, and the power consumption of the fans, compressor, and total power of the unit. The unit was charged with 5.01 kg (11.05 lb) of refrigerant to overcome the additional pipe length and to maintain injection superheat of 7°C and ensure consistent subcooling of 5°C in the liquid line.

3.2.2 Experimental Methods

The experimental tests were performed in a pair of psychrometric chambers that simulate indoor and outdoor conditions, with the unit located in the outdoor cham-

Table 3.1. Measurement instrumentation and accuracy for the EVI system.

Physical parameter	Instrument	Range	Accuracy
In-line temperature	Thermocouple stainless steel T-type	−250–350°C	±1.1°C
Surface temperature	Thermocouple wire T-type	−250–350°C	±1.1°C
Refrigerant pressure (low/high)	Pressure transducer	0–1750, 0–3500, 0–7000 kPa	±0.08% FS
Refrigerant pressure (intermediate)	Pressure transducer	0–3447 kPa	±0.13% FS
Air humidity	Hygrometer chilled mirror	−20–85°C, 0–95%	±0.2°C
Air pressure	Static pressure transducer	0–5 inH_2O	±1.0% FS
Air velocity	Portable anemometer	0–25 m/s	±1.5% FS
Air flow rate	ASHRAE nozzle box	2188–5107 m^3/hr	±6.66 m^3/hr
Refrigerant flow rate (total)	Coriolis flow meter	0–2720 kg/hr	±0.2% ±0.87 kg/hr
Refrigerant flow rate (suction)	Coriolis flow meter	0–680 kg/hr	±0.15% ±0.18 kg/hr
Unit total power	Power transducer	0–40 kW	±0.5% FS
	Current transformer	100 : 5 CR	±1.5% FS
Compressor power	Power transducer	0–45 kW	±0.25% FS
	Current transformer	1000 : 1 CR	±0.3% FS
Fans power	Power transducer	0–2 kW	±0.04% FS

ber, as shown in Figure 2.3. The test conditions are reported in Table 2.2. The ECU was charged under the same operating condition of Test 4/A for testing the economized vapor injection (EVI) system with no-injection (baseline), superheated-injection ($T_{sup} = 7°C$) and saturated-injection ($T_{sup} = 0°C$). To be noted is that Test Conditions 4/A, B and C are compliant with ASHRAE Standard 210/240 (Standard, 2008a), while Test Conditions 1 and 2 represent extreme ambient temperatures. After ensuring that the ECU reached steady-state conditions (typically after a run time of at least an hour), measurements were recorded every two seconds for 20 minutes. The average values of the data measurements were used in Section 3.3 to assess the EVI on improving the cooling capacity and COP as well as the reduction of compressor discharge temperature.

3.2.3 Data Reduction

The cooling capacity and coefficient of performance (COP) were determined based on the air and the refrigerant enthalpy methods. Both methods were determined using thermodynamic property feature in the Engineering Equation Solver (EES) software (Klein and Alvarado, 2016) and compared to agree with each other within 6% per ANSI/AHRI Standard 210/240 (Standard, 2008a). The measured dry-bulb and dew-point temperatures, and the atmospheric pressure at a corresponding location were used to determine the air enthalpies, whereas the local temperature and pressure measurements were used to calculate the refrigerant enthalpies. Because the available measurements cannot be used to calculate the refrigerant property at a two-phase mixture state, it was assumed a constant refrigerant enthalpy across the expansion valve. Since the tube between the compressor discharge port and the condenser inlet is relatively short, the pressure drop is neglected. Hence, the total cooling capacity measured on the refrigerant-side and the air-side is determined by Equations (3.1) and (3.2), respectively. The cooling coefficient of performance (COP) is calculated by Equation (3.3) where $\dot{E}_{tot}$ is the total power input, which includes the compressor, the fans, and the power used by the controllers,

$$\dot{Q}_{evap,r} = \dot{m}_{r,suc}(h_{r,o} - h_{r,i}) \tag{3.1}$$

$$\dot{Q}_{evap,a} = \dot{m}_{a}(h_{a,i} - h_{a,o}) + \dot{W}_{evap,fan} \tag{3.2}$$

$$\text{COP}_{sys} = \frac{\dot{Q}_{evap,a}}{\dot{E}_{tot}} \tag{3.3}$$

The volumetric efficiency is defined as the ratio of the actual compressor suction volume flow rate to the maximum theoretical compressor suction volume flow rate as shown in Equation (3.4),

$$\eta_v = \frac{\dot{m}_{r,suc}}{\rho_{r,suc}\dot{V}_{disp,th}} \tag{3.4}$$

The overall isentropic efficiency is defined as the ratio of the actual compressor power consumption to the power consumption needed for an adiabatic and reversible process from the suction port to the discharge port as expressed by Equation (3.5). The term $h_{r,inj,mix}$ in Equation (3.5) is defined as the specific enthalpy of the refrigerant vapor after mixing with the intermediate pressure flow and the partially compressed flow at state $h_{r,inj,is}$, which is determined by Equation (3.6),

$$\eta_{is} = \frac{\dot{m}_{r,suc}\left(h_{r,inj,is} - h_{r,suc}\right) + \dot{m}_{r,tot}\left(h_{r,dis,is} - h_{r,inj,mix}\right)}{\dot{W}_{comp}} \tag{3.5}$$

$$h_{r,inj,mix} = \frac{\dot{m}_{r,suc} h_{r,inj,is} + \dot{m}_{r,inj} h_{r,inj}}{\dot{m}_{r,tot}} \tag{3.6}$$

This definition of the overall isentropic efficiency was used by Lumpkin et al. (2018) and it is documented in ASHRAE Standard 23.1 (Standard, 2015) for a single-port multi-stage system with vapor injection and an economizer.

3.3 Results and Discussion

The following sections discuss the experimental results for the economized vapor injection (EVI) system based on the calculated performance results provided in Appendix D. In addition, an uncertainty analysis of the performance results was carried out according to the Taylor and Kuyatt (1994) method using the EES software (Klein and Alvarado, 2016). The analysis considered devices accuracies and propagation of sensors accuracies through calculated properties. The resulting uncertainties are listed with the performance results in Appendix E.

3.3.1 Discharge Temperature Improvement

The economized vapor injection (EVI) reduces the discharge temperature of the compressor due to the injection of cooler refrigerant during the compression process. Figure 3.4 shows the absolute improvement to the compressor discharge temperature of the EVI system with respect to the baseline conditions (no-injection). Figure 3.4 shows that the compressor discharge temperatures had limited improvements when injecting the compressor with superheated vapor of 7°C. In fact, the maximum improvement was found during Test Condition 2 with a decrease of 1.7°C compared to baseline. On the contrary, significant improvements were achieved when injecting saturated vapor that further helped in reducing the compressor discharge temperature in all test conditions, as shown in Figure 3.4. The saturated EVI led to a maximum improvement of 5°C under Test Condition 2. In addition, the improvement increases toward the extreme condition (*i.e.,* Test Condition 1) because of the increase in injected mass flow rate that absorbs more heat generated during the compression process. Note that Test Conditions 6 and C show no significant improvement because the unit was working at low temperature-lift conditions.

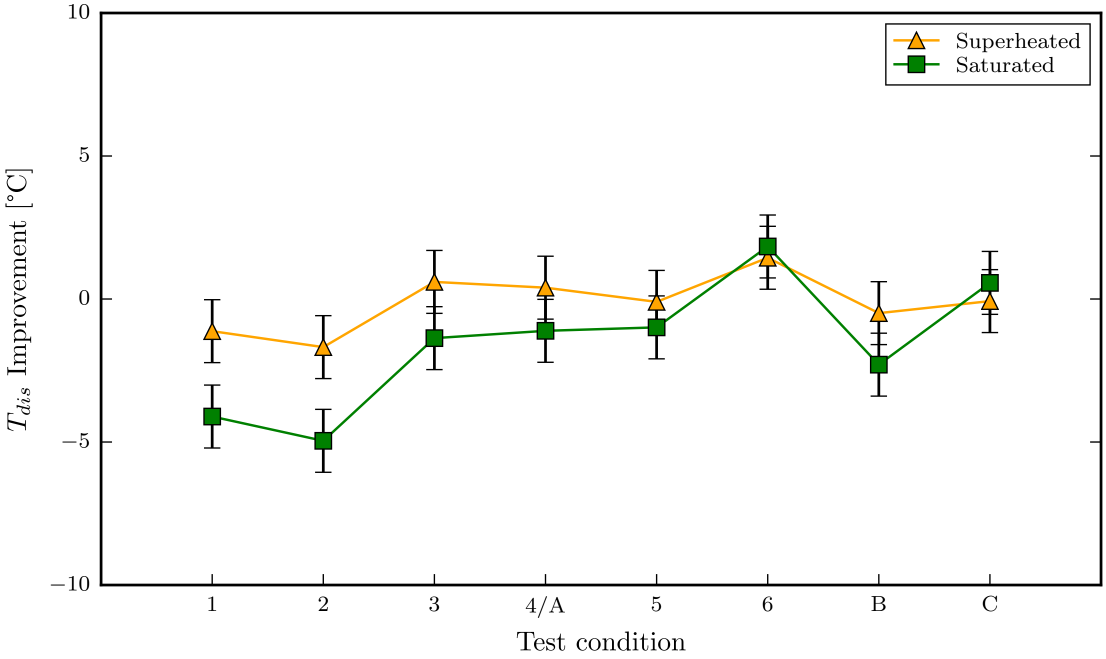

Figure 3.4. Comparison of compressor discharge temperature improvement using superheated ($T_{sup} = 7$°C) and saturated ($T_{sup} = 0$°C) economized vapor injections (EVIs) at different testing conditions.

3.3.2 Cooling Capacity Improvement

The cooling capacity of the economized vapor injection (EVI) system improved as a result of the increased subcooling in the economizer compared to the baseline vapor compression cycle without injection. Figure 3.5 shows that, for different testing conditions, the improvements in cooling capacity ranged from 5.9% to 12.7% for the superheated-injection condition, while the improvements for the saturated-injection condition ranged from 4% to 11.8% compared to baseline conditions (no-injection). The slightly lower cooling capacity in the saturated-injection condition is attributed to an increase in injected mass flow rate into the compressor that reduced the evaporator's mass flow rate. To be noted is that the lowest improvements in the cooling capacity were observed at Test Condition 6 because the unit was working at a low temperature-lift condition.

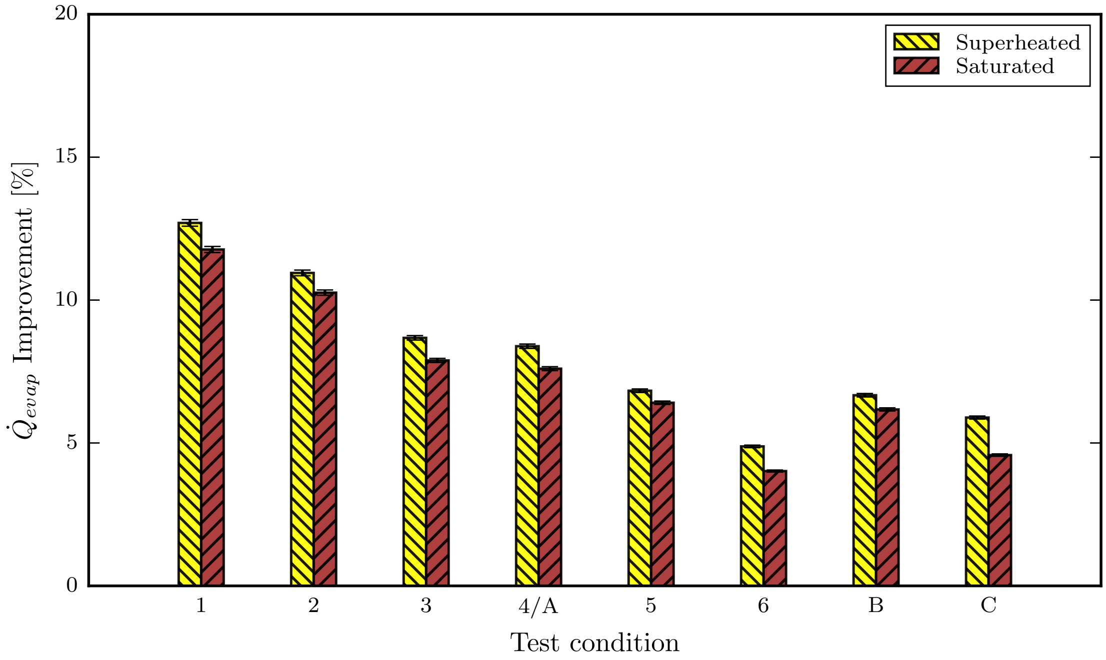

Figure 3.5. Comparison of Cooling capacity improvements using superheated (T_{sup} = 7°C) and saturated (T_{sup} = 0°C) economized vapor injections (EVIs) at different testing conditions.

3.3.3 Performance Improvement

Economized vapor injection (EVI) affects the compressor performance and consequently the overall performance of the ECU. Figure 3.6 compares the refrigeration cycle of the ECU for baseline (no-injection), superheat and saturated EVIs at the extreme case (*i.e.,* Test Condition 1). Figures 3.6a and 3.6b indicate that the EVI systems (superheated and saturated) exhibited a significant increase in the subcooling degree relative to the baseline system. Therefore, the cooling capacity increased due to the increase in enthalpy of vaporization across the evaporator. The EVI enhanced the heat recovery during the compression process. This leads to a decrease in discharge temperature of the compressor and thus, a decrease in the condensing pressure and temperature as shown in Figures 3.6a and 3.6b. However, the EVI also slightly decreased the evaporation pressure and temperature, which may increase the compressor's work load, and hence may affect the overall system COP.

The EVI deviates the system COP due to the increase in compressor power consumption as shown in Figure 3.7. Figure 3.7 compares the system COP improvement for the superheat-injection and saturated-injection cases with the baseline (no-injection) case at different testing conditions. The system COP improved for the EVI system, in which the maximum improvement of 3.1% was observed at Test Condition 1 for superheated EVI, while the maximum improvement of 1.3% was observed at Test Condition 2 for saturated EVI. Note that the compressor electrical current exceeded the design limit when tested at higher outdoor conditions (*i.e.,* Test Conditions 1 through 3). Therefore, the VI compressor was not optimized for air conditioning applications. Rather, it was designed for refrigeration applications which explains the reduction in system COP among most of the testing conditions. This stipulates a potential for system optimization at high temperature conditions.

3.4 Model Development

The retrofitted Environmental Control Unit (ECU) with economized vapor injection (EVI) system can be described as a vapor-compression system that works as an air conditioner (AC) with additional components to account for the EVI part. Besides the four major components (*i.e.,* a compressor, a condenser, an expansion valve, and an evaporator), there are an economizer and an additional expansion valve, as shown in Figure 3.1. The components in Figure 3.1 are modeled in an object-oriented fashion by using the programming language Python (2016). The thermo-physical properties of the refrigerant (R-407C) were obtained using CoolProp (Bell et al., 2014). Due to

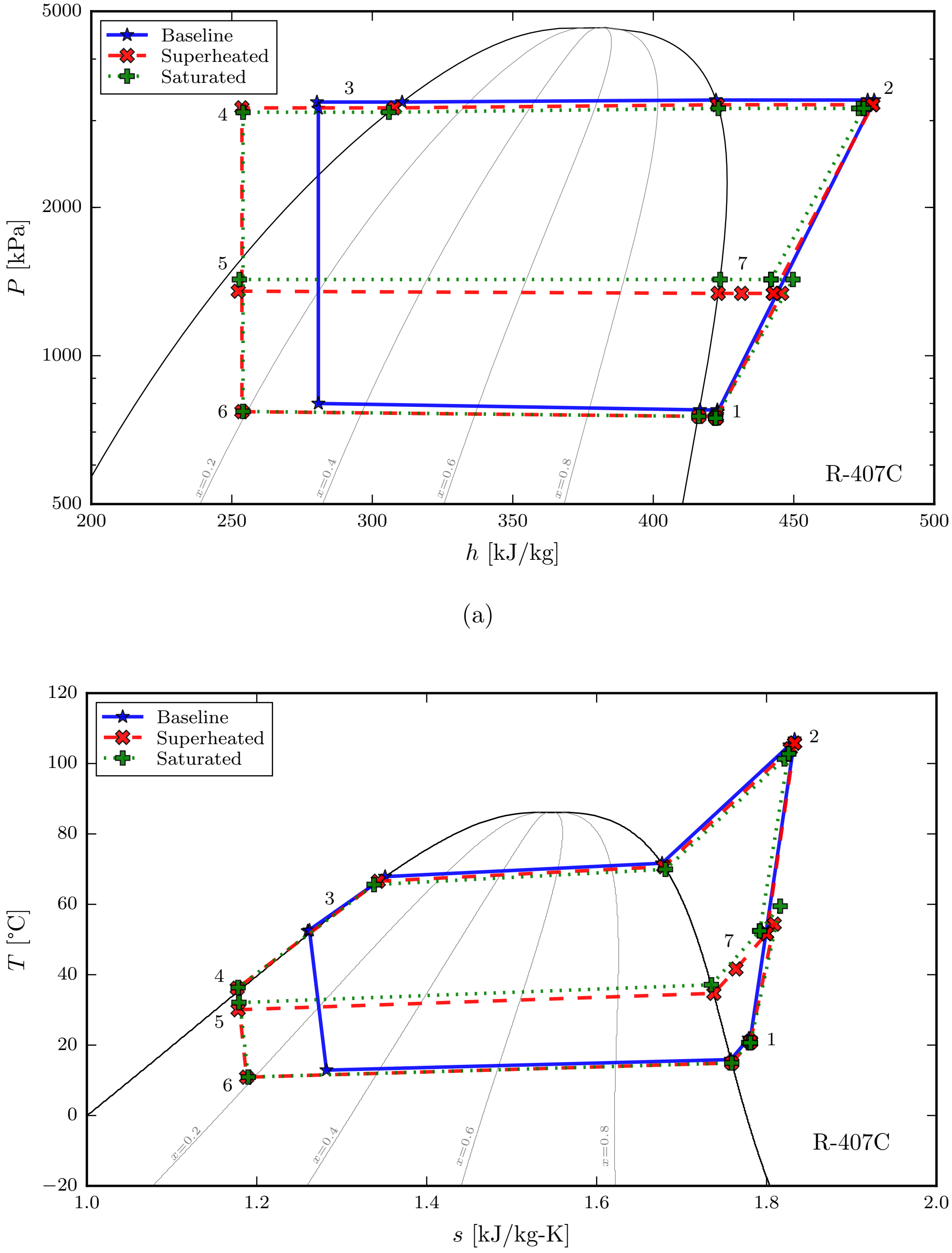

(a)

(b)

Figure 3.6. Diagrams of (a) pressure-enthalpy and (b) temperature-entropy to compare baseline (no-injection), superheated ($T_{sup} = 7$°C) and saturated ($T_{sup} = 0$°C) economized vapor injection (EVI) at Test Condition 1.

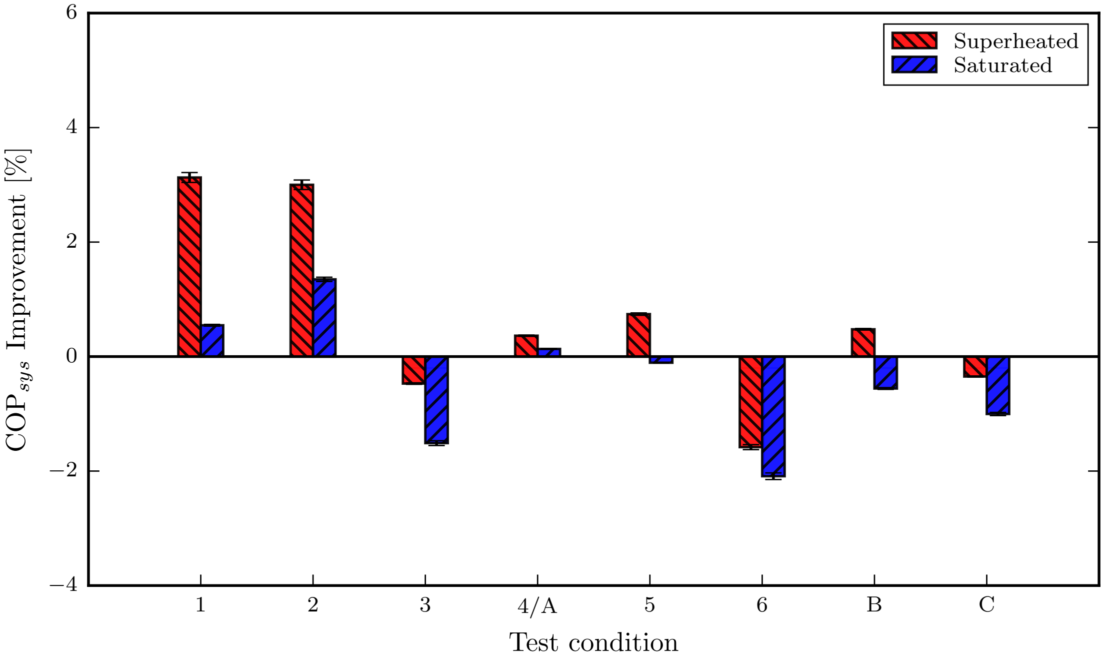

Figure 3.7. Comparison of system COP improvements using superheated (T_{sup} = 7°C) and saturated (T_{sup} = 0°C) economized vapor injections (EVIs) at different testing conditions.

the compactness of the ECU, suction line, discharge line and liquid line are excluded in the model. Each component model is explained in the following sections. However, more specific details about the models can be found in Appendix F.

3.4.1 Compressor Model

The single-port vapor-injection (VI) compressor model described by Tello-Oquendo et al. (2017) was used and is expressed in Equations (3.7) to (3.9),

$$\begin{aligned}\dot{W}_{comp} = c_1 + c_2 T_{evap} + c_3 T_{cond} + c_4 T_{evap}^2 + c_5 T_{evap} T_{cond} + c_6 T_{cond}^2 \\ + c_7 T_{evap}^3 + c_8 T_{cond} T_{evap}^2 + c_9 T_{cond}^2 T_{evap} + c_{10} T_{cond}^3 + c_{11} T_{dew,inj}\end{aligned} \tag{3.7}$$

$$\begin{aligned}\dot{m}_{suc} = c_1 + c_2 T_{evap} + c_3 T_{cond} + c_4 T_{evap}^2 + c_5 T_{evap} T_{cond} + c_6 T_{cond}^2 \\ + c_7 T_{evap}^3 + c_8 T_{cond} T_{evap}^2 + c_9 T_{cond}^2 T_{evap} + c_{10} T_{cond}^3\end{aligned} \tag{3.8}$$

$$\frac{\dot{m}_{inj}}{\dot{m}_{suc}} = c_1 + c_2 \frac{P_{inj}}{P_{suc}} \tag{3.9}$$

Lumpkin et al. (2018) extensively tested the same R-407C VI compressor in a calorimetric test bench; their experimental measurements were mapped herein. The coefficients of the suction mass flow rate, the injection mass flow ratio, and the power consumption correlations are estimated by minimizing the sum of squares of the difference between measurement and estimation at every data point. The estimated compressor model coefficients are listed in Table F.2 along with the R^2 values.

The refrigerant state at the compressor outlet is calculated using the overall isentropic efficiency (*i.e.,* Equation (3.5)) by assuming adiabatic mixing at the injection state, and including the compression heat loss fraction from experimental results.

3.4.2 Condenser Model

The condenser model from Bell (2015) was modified to account for multi-louvered micro-channel design geometry. The condenser model was formulated using a moving boundary method, which divides the condenser according to the phases of refrigerant flow as shown in Figure 3.8. Each section of the condenser in Figure 3.8 is simulated using the ϵ-NTU method as separate crossflow multi-louvered micro-channel heat exchangers (Lee, 2010), assuming constant refrigerant pressure equal to the inlet pressure.

The correlations used to estimate the heat transfer coefficients and friction factors in the micro-channel condenser model are summarized in Table 3.2, while the geometrical parameters used are listed in Table 3.3.

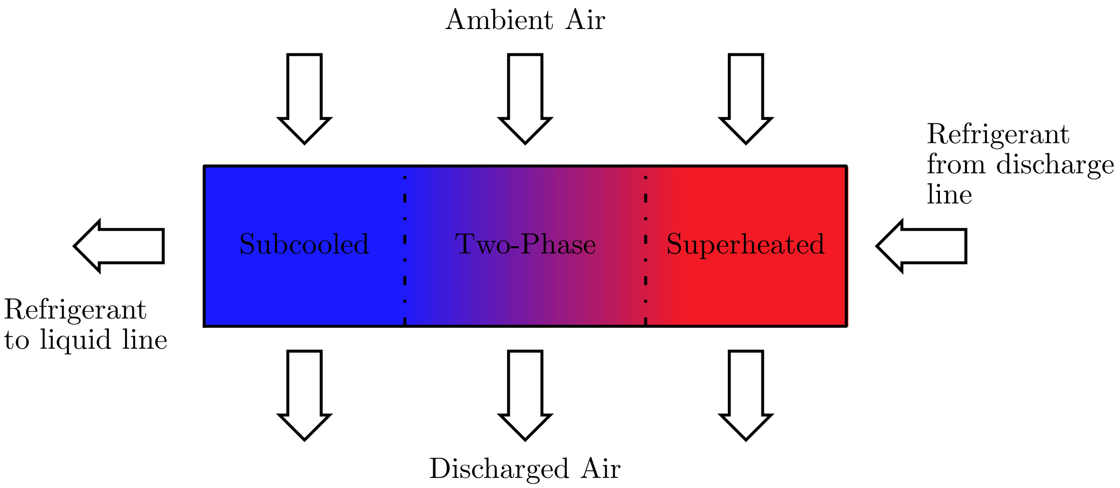

Figure 3.8. Schematic of crossflow condenser model simulated by moving boundary method.

Table 3.2. Heat transfer and pressure drop correlations in microchannel condenser model.

		Single-phase	Two-phase
Refrigerant-side	Heat transfer	Gnielinski (1976)	Kim and Mudawar (2013)
	Pressure drop	Churchill (1977)	Kim and Mudawar (2012)
Air-side	Heat transfer	Kim and Bullard (2002)	
	Friction factor	Chang et al. (2000)	

3.4.3 Economizer Model

The plate heat exchanger (PHX) model proposed by (Bell et al., 2015) was considered herein. The model was constructed with robust steady-state, counterflow, moving-boundary model. The model accounts for any phase condition for both hot and cold streams. In addition, the model efficiently utilizes internal and external pinching points, allowing for the possibility of mixed phase combinations in both refrigerant streams. For instance, Figure 3.9 illustrates the most general case of the counterflow moving-boundary PHX model where both streams enter with single-phase

Table 3.3. Simplified geometry of the ECU micro-channel condenser.

Number of tubes per slab	52
Number of passes per slab	2
Number of slabs	2
Number of ports (channels)	11
Length of tubes [mm]	540
Width of tubes [mm]	25.4
Height of tubes (major diameter) [mm]	1.8288
Wall thickness of tubes [mm]	0.381
Wall thickness of ports [mm]	0.4064
Aspect ratio of ports	1.7675
Fins per inch	14
Fin height [mm]	12.3952
Fin thickness [mm]	0.1143
Louver height [mm]	25.4
Louver pitch [mm]	1.12
Louver angle [degree]	25
Conductivity of fins [W/m-K]	117

states, undergo complete phase change, and exit with single-phase states. There are five separate zones as shown in Figure 3.9, in which each zone is defined by the phase boundary of each one of the streams. Note that the PHX exhibits no heat loss with the surroundings.

The heat transfer coefficients and friction factors correlations of the economizer model are listed in Table 3.4, and the geometrical parameters of the PHX are provided in Table 3.5.

Table 3.4. Heat transfer and pressure drop correlations in economizer model.

		Single-phase	Two-phase
Hot-side	Heat transfer Pressure drop	Martin (2010)	Longo (2010, 2011); Longo et al. (2004) Lockhart and Martinelli (1949)
Cold-side	Heat transfer Pressure drop	Martin (2010)	Cooper (1984) Lockhart and Martinelli (1949) modified by Claesson (2004)

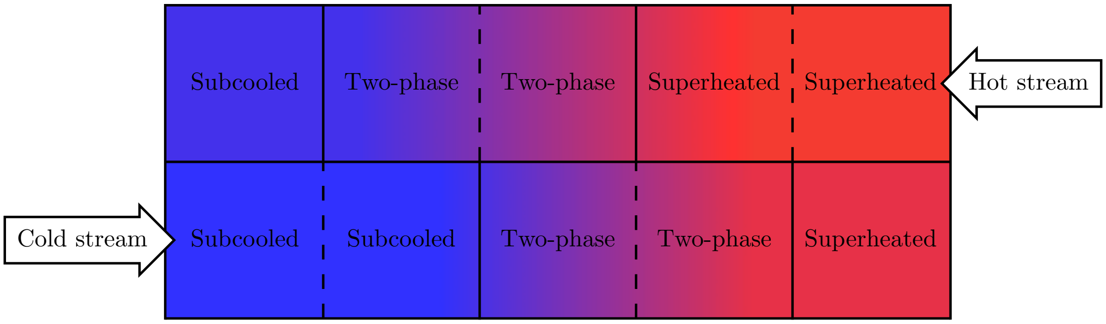

Figure 3.9. Schematic of counterflow economizer model simulated by moving boundary method showing phase boundaries (solid lines) and zone boundaries (dash lines).

Table 3.5. Simplified geometry of the ECU economizer (PHX).

Number of plates	10
Length of plates [mm]	457.2
Width of plates [mm]	73.025
Thickness of plates [mm]	0.3
Wavelength of plates [mm]	6.26
Amplitude of corrugation [mm]	1
Chevron angle [degree]	65
Conductivity of plates [W/m-K]	15

3.4.4 Expansion Valve Model

The expansion valve works as a constant enthalpy throttling valve. The expansion valve neither receives nor produces work, and does not exchange heat with its surroundings. It is assumed that the expansion process is steady-state, and the changes in kinetic and potential energies are neglected. The same concept can be applied for thermal expansion valve (TXV).

3.4.5 Evaporator Model

The evaporator model of Bell (2015) was constructed using a moving boundary method, which divides the evaporator according to the phases of refrigerant flow as shown in Figure 2.14. Each section of the heat exchanger in Figure 2.14 is simulated using the ϵ-NTU method (Bergman et al., 2011) as separate crossflow fin-and-tube heat exchangers, assuming constant refrigerant pressure is equal to the saturation pressure.

To accurately estimate the behavior of the heat transfer from the air to the refrigerant side of the evaporator, the partially-wet and partially-dry method (Braun, 1988) is utilized in predicting the air side sensible and latent heat transfer when the surface temperature of the coil falls below the dew-point of air at the inlet of the evaporator. A model schematic is shown in Figure 2.15. The evaporator in Figure 2.15 is solved by separating the heat exchanger into two sections. The section with surface temperatures higher than the dew-point is solved by a completely dry analysis, while the other section is solved assuming a completely wet analysis.

The correlations used to solve the heat transfer coefficients and friction factors in the evaporator model are presented in Table 2.3, while the geometrical parameters shown in Table 3.6 are used.

3.4.6 Fan Model

The evaporator fan ran at fixed-speed during the experiments, while the condenser fan had two operation modes. The average airflow rate and power consumption for the evaporator fan were obtained from the experiment and were equal to 0.8023 m^3/s and 0.77 kW, respectively. The airflow across the condenser fan was not measured, but estimated from the manufacturer data. In particular, the airflow rate was equal to 1.746 and 1.18 m^3/s for high and low operation modes, corresponding to average measured power consumption of 1.032 kW and 0.396 kW, respectively. In the model, both fans were modeled by using these values for steady-state operation.

Table 3.6. Simplified geometry of the ECU evaporator.

Number of tubes per bank	18
Number of banks	4
Number of circuits	6
Length of tubes [mm]	631.825
Outer diameter of tubes [mm]	12.7
Inner diameter of tubes [mm]	11.7348
Longitudinal distance of tubes [mm]	27.4828
Transverse distance of tubes [mm]	131.75
Fins per inch	12
Fin waviness [mm]	0.79375
Half-wavelength of fin wave [mm]	6.35
Fin thickness [mm]	0.1905
Conductivity of fins [W/m-K]	237

3.4.7 Pre-Conditioner Model

The pre-conditioner model from Bell (2015) was modified in order to obtain good initial guesses for the main cycle solver; namely, refrigerant dew-point temperatures in evaporator, condenser, and economizer (cold-side). The pre-conditioner model duplicates the main cycle to be solved with simplified models for condenser, evaporator and economizer, as shown in Figure 3.10.

Figure 3.10 shows the pre-conditioner algorithm. In the compressor submodel, for a given input set of independent variables (*i.e.,* T_{evap}, T_{cond}, and $T_{dew,inj}$) and known suction and injection superheats (*i.e.,* $T_{sup,suc}$ and $T_{sup,inj}$), the inlet, outlet and injection pressures can be computed. Hence, the compressor map from Section 3.4.1 is used to predict the suction and injection mass flow rates as well as the compressor power.

In the condenser submodel, by imposing the subcooling degree, the heat transfer rate on the refrigerant-side is calculated, and then compared with the air-side to check for consistency by the employed numerical solver. It is assumed that the condenser's air-side had the minimum capacitance rate, and the limiting condenser's air-side

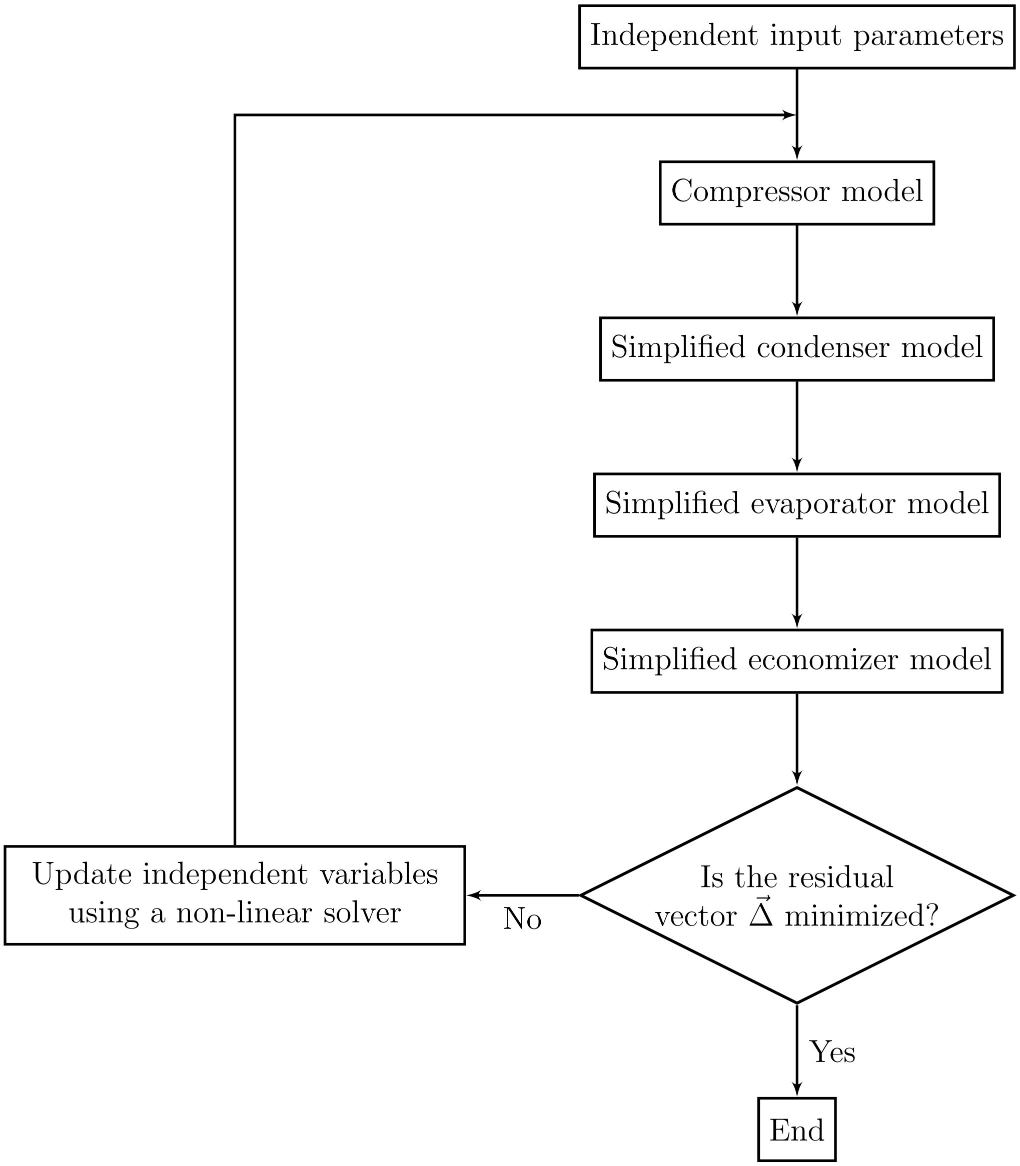

Figure 3.10. Flowchart of pre-conditioner model solver.

outlet state is the refrigerant condensing temperature T_{cond}; just to get approximate initial guesses.

In the evaporator submodel, a fully dry analysis is first considered to determine the inlet and outlet surface temperatures of the evaporator. The surface temperatures are compared with the air dew-point to check if the evaporator is fully-dry or fully-wet. In the cases where the air dew-point is between the surface inlet and outlet temperatures, the heat transfer rate is calculated using a simple weighted mix of the fully-dry and the fully-wet heat transfer rates. Note that the effectiveness of all heat exchangers is assumed to be constant (*i.e.*, $\epsilon = 0.96$) as well as the air specific heat and density (*i.e.*, $\rho_a = 1.2$ kg/m^3, and $c_{p,a} = 1.005$ kJ/kg-K).

An energy balance is then performed on the evaporator to determine the states on the economizer (*i.e.*, cold-side inlet and hot-side outlet). Considering the assumption of adiabatic economizer and isenthalpic expansion process, the economizer's hot-side and cold-side heat transfer rates are calculated, and then compared to check for consistency by the employed numerical solver.

Finally, to minimize the residual vector (Equation (3.10)), the independent variables (*i.e.*, T_{evap}, T_{cond}, and $T_{dew,inj}$) are iterated by the mean of *fsolve* function (Moré et al., 1980) to attain convergence,

$$\vec{\Delta} = \begin{bmatrix} \dot{W}_{comp} + \dot{Q}_{evap} - \dot{Q}_{cond} - \dot{Q}_{econ,h} \\ \dot{Q}_{cond,a} - \dot{Q}_{cond,r} \\ \dot{Q}_{econ,h} - \dot{Q}_{econ,c} \end{bmatrix} \tag{3.10}$$

3.4.8 System-Level Model

To simulate the ECU, the implicit economized vapor injection (EVI) system model was assembled, as shown in Figure 3.11. The required input parameters to the overall system model included the geometry data of the components, indoor and outdoor dry-bulb temperature and humidity, fans air flow rate and power consumption, targeted suction and injection superheats, and subcooling degree. The main system solver is initialized by a set of guess values for the independent parameters (*i.e.*, T_{evap}, T_{cond}, and $T_{dew,inj}$), as shown in Figure 3.11.

The flow chart in Figure 3.11 shows the algorithm used in the system-level solver. At first, the pre-conditioner model is solved to obtain approximate initial guesses for the independent variables, so that the evaporation, condensing, and injection pressures can be computed. Then, the compressor model is activated with the pressures

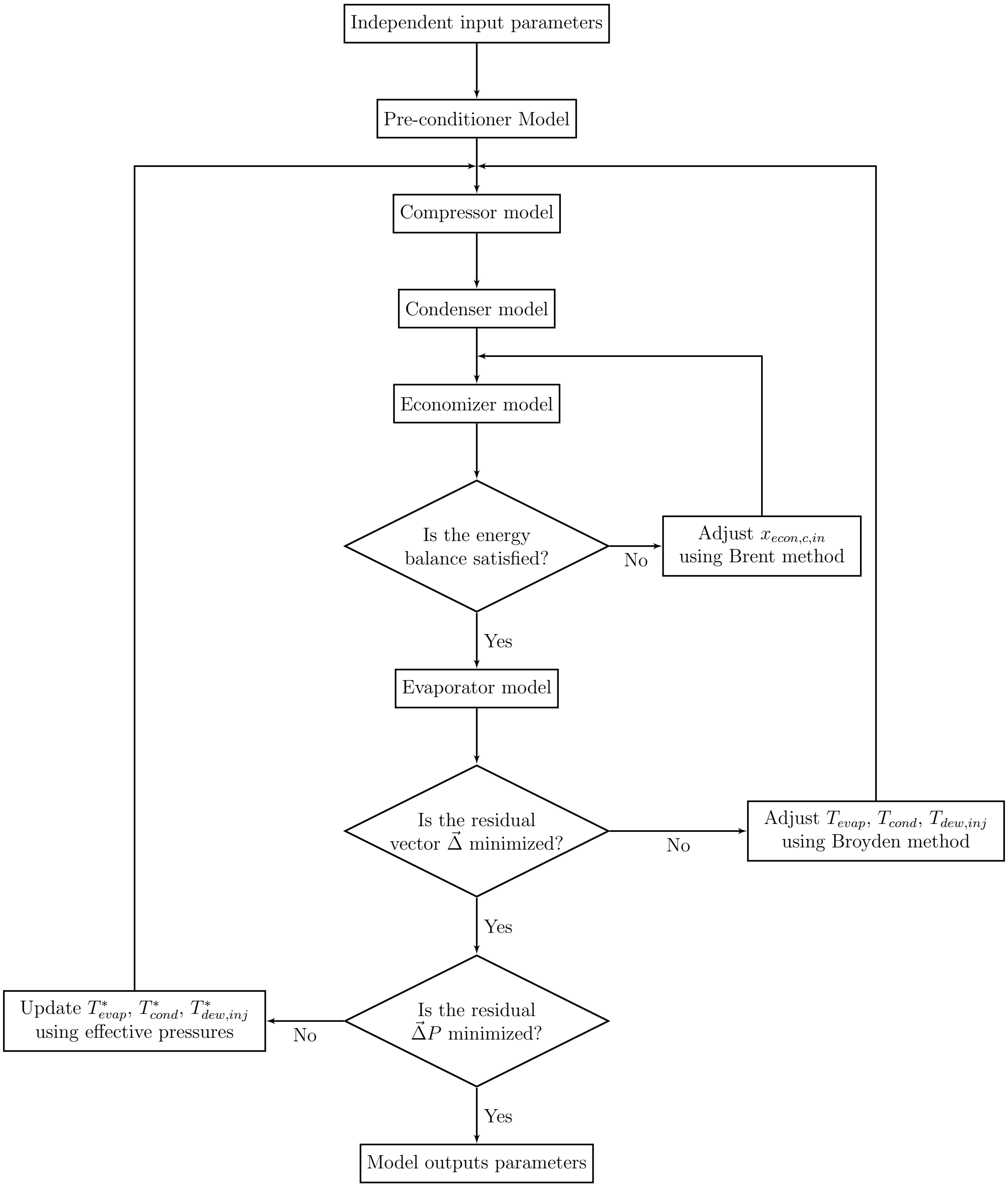

Figure 3.11. Flowchart of EVI system model solver.

and the known suction and injection superheats. Once the suction and injection mass flow rates from the compressor model are known, the condenser and economizer models are solved. The condenser subcooling degree is calculated, and successively compared with the targeted subcooling value to ensure cycle convergence (*i.e.,* Δ_1 in Equation (3.12)).

Due to the fact that the economizer model needs the information of the inlets on both hot and cold sides, the inlet quality of the cold-side is iterated to ensure the energy balance on the economizer, as show in Equation (3.11). Equation (3.11) is driven to zero by the mean of Brent (1973) method. Upon economizer's convergence, the outlet enthalpy (cold-side) is compared with the compressor injection enthalpy to check for system convergence (*i.e.,* Δ_2 in Equation (3.12)),

$$\dot{m}_{tot} h_{cond,o} - \dot{m}_{suc} h_{econ,h,o} - \dot{m}_{inj} h_{econ,c,o} = 0 \tag{3.11}$$

The evaporator is the last component model to be computed. The evaporator outlet enthalpy is compared with the compressor inlet enthalpy to check for consistency by the employed numerical solver (*i.e.,* Δ_3 in Equation (3.12)).

The system model then checks the overall residual vector (Equation (3.12)). A multi-dimensional Broyden (1965) solver is used to drive the residual vector to zero by adjusting the independent variables (*i.e.,* T_{evap}, T_{cond}, and $T_{dew,inj}$),

$$\vec{\Delta} = \begin{bmatrix} T_{sub} - T_{sub,target} \\ h_{econ,c,o} - h_{comp,inj} \\ h_{evap,o} - h_{comp,i} \end{bmatrix} \tag{3.12}$$

Once the residual vector is minimized, the model checks for the pressure drop residual, as shown in Equation (3.13). The pressure drops are considered after the cycle iteration completed to avoid numerical difficulties. The high, low, and intermediate pressure drops (*i.e.,* P_{high}, P_{low}, and P_{int}) correspond to the pressure drops in condenser with hot-side of economizer, evaporator, and cold-side of economizer, respectively. These pressure drops are employed to shift the saturation temperatures used in the compressor map in order to yield less refrigerant mass flow rate and a higher compressor power consumption. Hence, new effective saturation temperatures

($i.e.$, T^*_{cond}, T^*_{evap}, and $T^*_{dew,inj}$) are calculated, and iterated in the cycle model until the updated effective pressure drop ($i.e.$, P^*_{high}, P^*_{low}, and P^*_{int}) are equal to the pressure drop terms calculated from the converged cycle model ($i.e.$, P_{high}, P_{low}, and P_{int}). In other words, it means driving the pressure drop residual (Equation (3.13)) to zero,

$$\vec{\Delta} P = \begin{bmatrix} P^*_{high} - P_{high} \\ P^*_{low} - P_{low} \\ P^*_{int} - P_{int} \end{bmatrix} \tag{3.13}$$

The main outputs of the EVI system model are obtained at last and include the inlet and outlet states for each component as well as the main performance parameters such as cooling capacity, power consumption, and system COP.

A number of simplifications are introduced within the model such as cross fin conduction, air and refrigerant side fouling, the mixing and equalization of the air flow across the heat exchanger, and manufacturing tolerances. Therefore, to eliminate the bias due to such simplifications and imperfect information related to the EVI system, a set of tuning parameters need to be identified based on the experimental data discussed in Section 3.2.

3.4.9 Model Tuning

There was a systematic bias between the simulation and experimental results due to simplifications and imperfect information related to the economized vapor injection (EVI) system components. To minimize the bias, 9 tuning multipliers were introduced to adjust heat transfer coefficients and pressure drop on both air-side and refrigerant-side for the condenser and evaporator model as well as the cold-side and hot-side in the economizer model. It should be noted that on the refrigerant-side, only the heat transfer coefficient of the two-phase region has been corrected in the heat exchangers because the heat transfer rate in the two-phase region is dominant.

The estimation of the multipliers was conducted by means of an iterative scheme, as shown in Figure 3.12. The tuning process eliminates the discrepancy in the estimations of the suction and injection mass flow rates, the condenser, evaporator and economizer heat transfer rates, and the compressor power consumption by minimizing an objective function. In particular, the objective function is given by Equation (3.14) and represents the sum of squares of the difference between measurement and estimation at the i^{th} data point of the superheated EVI experimental results ($T_{sup} =$ 7°C). The optimization problem was solved with a bounded sequential least squares (SLSQ) method (Kraft, 1988),

$$\begin{aligned} J = \sum\nolimits_i & \left(\frac{\dot{m}_{suc,pred,i} - \dot{m}_{suc,exp,i}}{\dot{m}_{suc,exp,i}}\right)^2 + \left(\frac{\dot{m}_{inj,pred,i} - \dot{m}_{inj,exp,i}}{\dot{m}_{inj,exp,i}}\right)^2 \\ & + \left(\frac{\dot{Q}_{cond,pred,i} - \dot{Q}_{cond,exp,i}}{\dot{Q}_{cond,exp,i}}\right)^2 + \left(\frac{\dot{Q}_{evap,pred,i} - \dot{Q}_{evap,exp,i}}{\dot{Q}_{evap,exp,i}}\right)^2 \\ & + \left(\frac{\dot{Q}_{econ,pred,i} - \dot{Q}_{econ,exp,i}}{\dot{Q}_{econ,exp,i}}\right)^2 + \left(\frac{\dot{W}_{comp,pred,i} - \dot{W}_{comp,exp,i}}{\dot{W}_{comp,exp,i}}\right)^2 \end{aligned} \tag{3.14}$$

The tuning multipliers results are reported in Table 3.7. Those factors were used for EVI system simulation and validation. The multipliers account for all discrepancy in the EVI model input parameters.

Table 3.7. EVI system-level tuning multipliers.

Condenser air-side convection heat transfer coefficient	0.71
Condenser refrigerant-side convection coefficient	0.71
Condenser refrigerant-side pressure drop correlation	0.71
Evaporator air-side convection heat transfer coefficient	1.5
Evaporator refrigerant-side convection coefficient	0.654
Evaporator refrigerant-side pressure drop correlation	0.645
Economizer cold-side convection coefficient	1.5
Economizer hot-side pressure drop correlation	0.61
Economizer cold-side pressure drop correlation	1.26

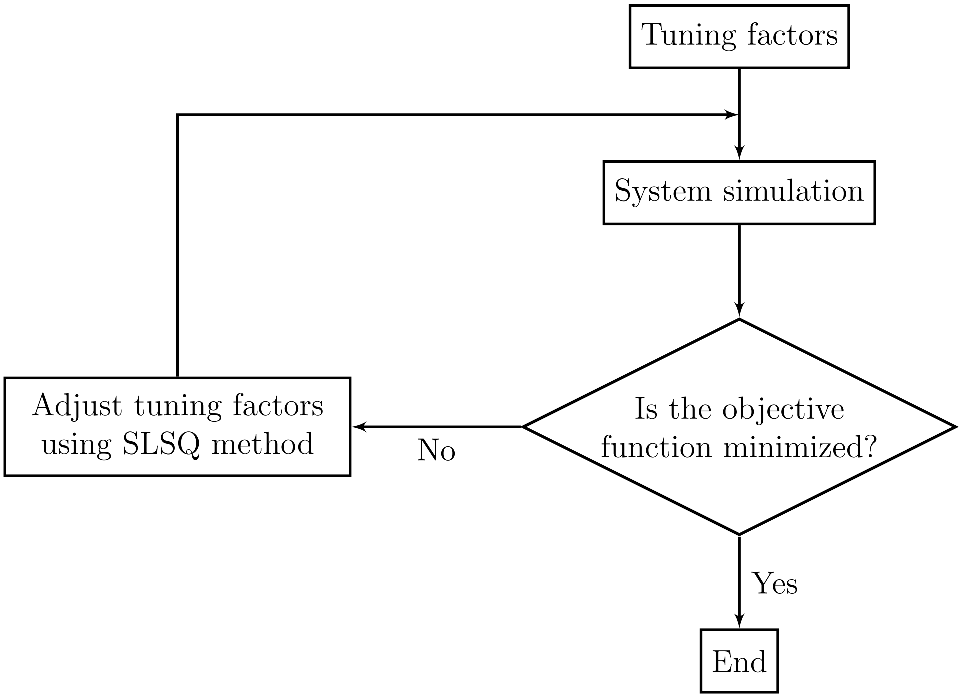

Figure 3.12. Flowchart of EVI system-level tuning process.

3.4.10 Model Validation

Since the model simulates cases with different indoor/outdoor conditions, the validation is carried out with only the 8 test conditions conducted with the retrofitted ECU, as shown in Figure 3.13. The comparisons of the refrigerant suction mass flow rate, the injection mass flow rate, the VI compressor power and the system COP between the model simulations (pre-tuned and post-tuned) and the experimental results are illustrated in Figure 3.13a through Figure 3.13h. The percentage error between the predicted and experimental values is calculated by the Mean Absolute Error (MAE) and the Root Mean Square Deviation (RMSD) given in Equations (2.5) and (2.6), respectively. The cycle model was also assessed for superheated and saturated injections scenarios with respect to MAE for the main cycle parameters, as shown in Figure 3.14.

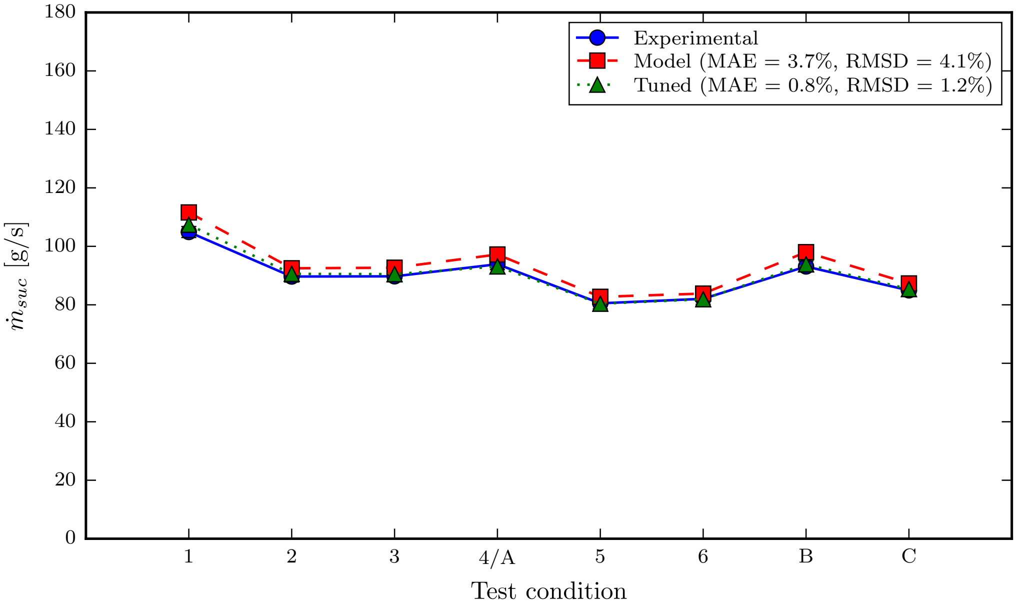

(a)

Figure 3.13. Comparison of model simulation results with experimental data for superheated ($T_{sup} = 7°C$) economized vapor injection (EVI) at different testing conditions for (a) suction mass flow rate, (b) injection mass flow rate, (c) economizer heat transfer rate, (d) condenser heat transfer rate, (e) cooling capacity, (f) compressor power consumption, (g) total power consumption, and (h) system COP.

Figure 3.13 shows that the model captured the system and component performances quite reasonably and within the experimental uncertainties, even without tuning. Maximum MAE and RMSD of approximately 12% and 11% occurred in the predictions of the economizer heat transfer rate and injection mass flow rate. All other MAEs and RMSDs were below 10%. After tuning the system model, the MAE and RMSD values were reduced significantly for all parameters. The maximum post-tuning MAE and RMSD of 4.1% and 4.6% were associated with the predictions of the system COP. Otherwise, the MAEs of all the other parameters fell below 4%, while the RMSDs were less than 7%. To be noted is that the model slightly deviates when predicting the compressor and total powers for Test Condition 3 through Test Condition 1, which represents the extreme ambient case. This behavior occurs

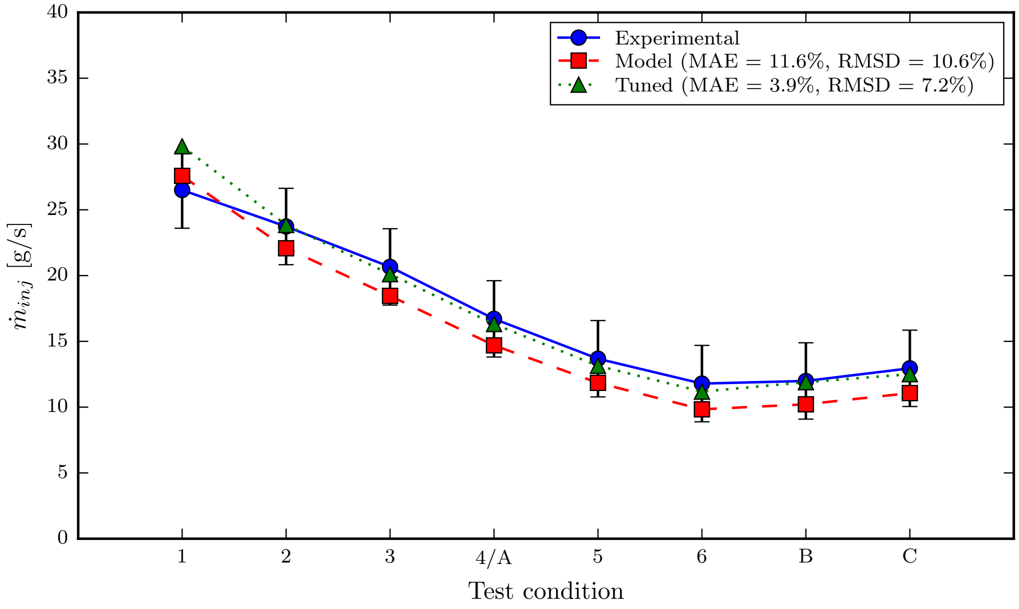

(b)

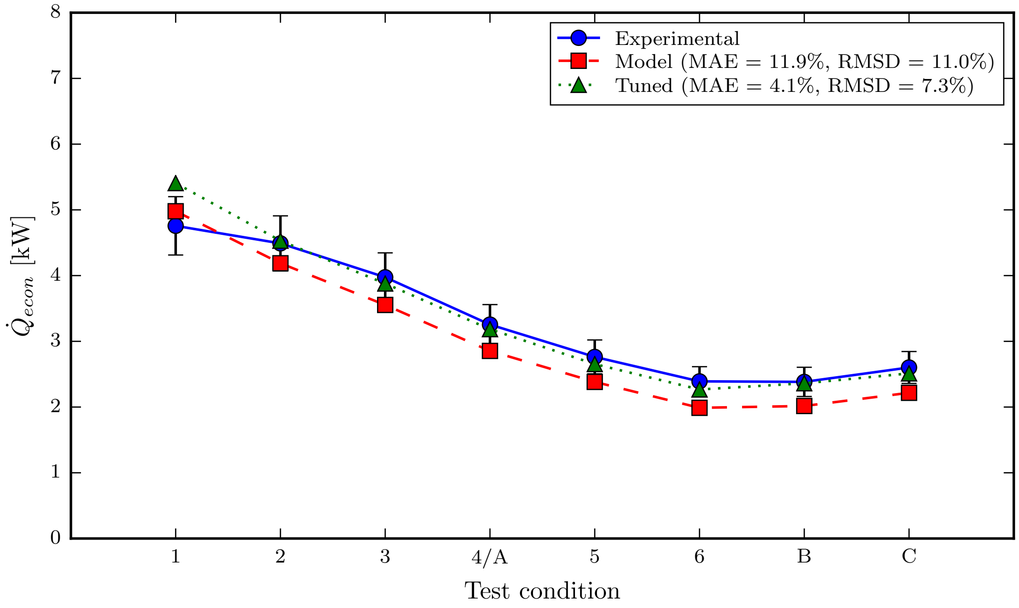

(c)

Figure 3.13. Continued.

because the VI compressor was overloaded and pushed outside its envelope, which resulted in slightly under-predicted compressor power, and therefore under-predict

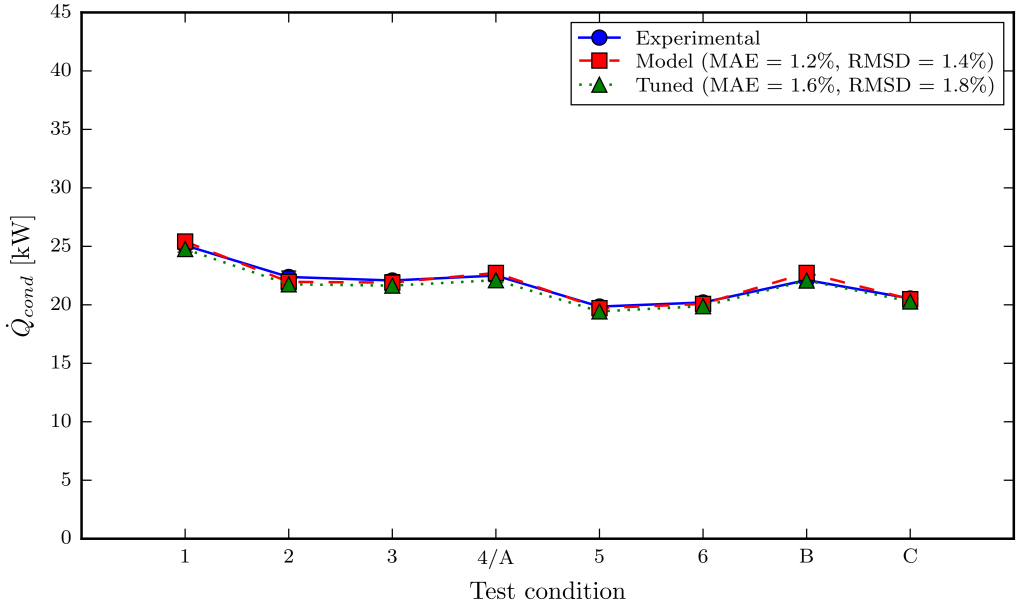

(d)

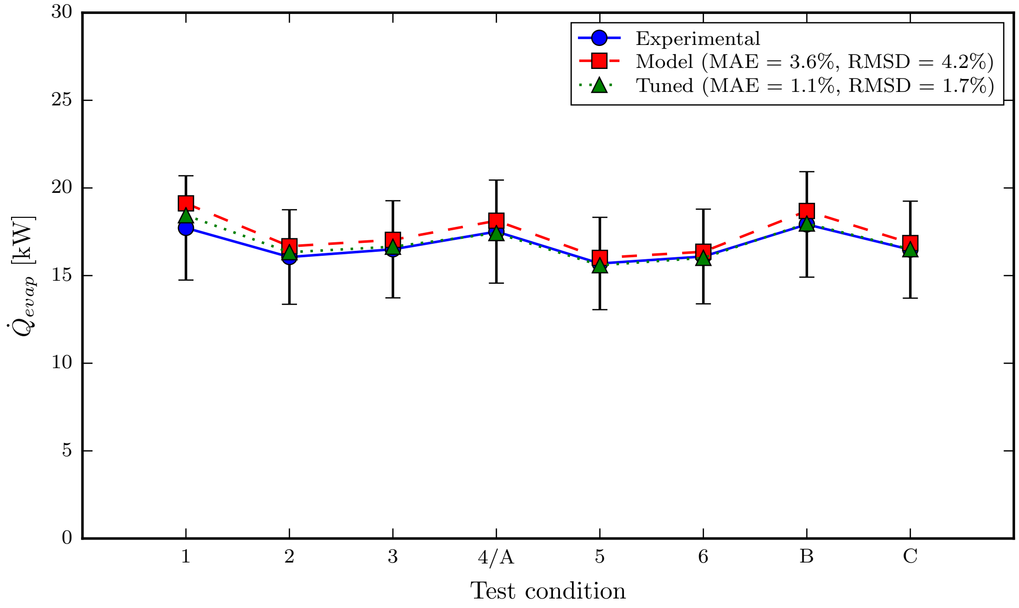

(e)

Figure 3.13. Continued.

total power consumptions at those particular testing conditions. Again, this compressor was designed for refrigeration applications. Therefore, the ECU system needs

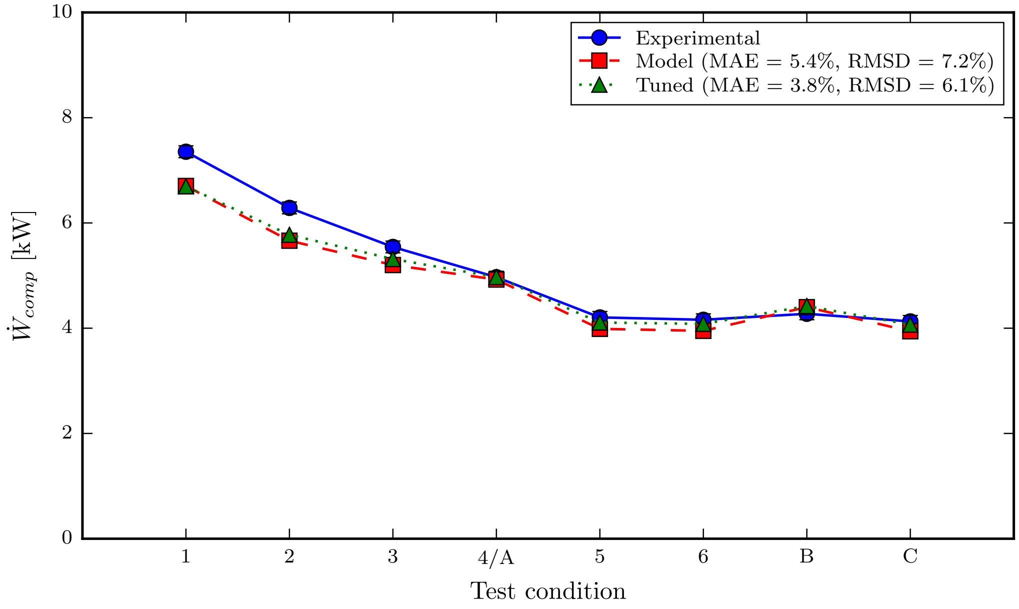

(f)

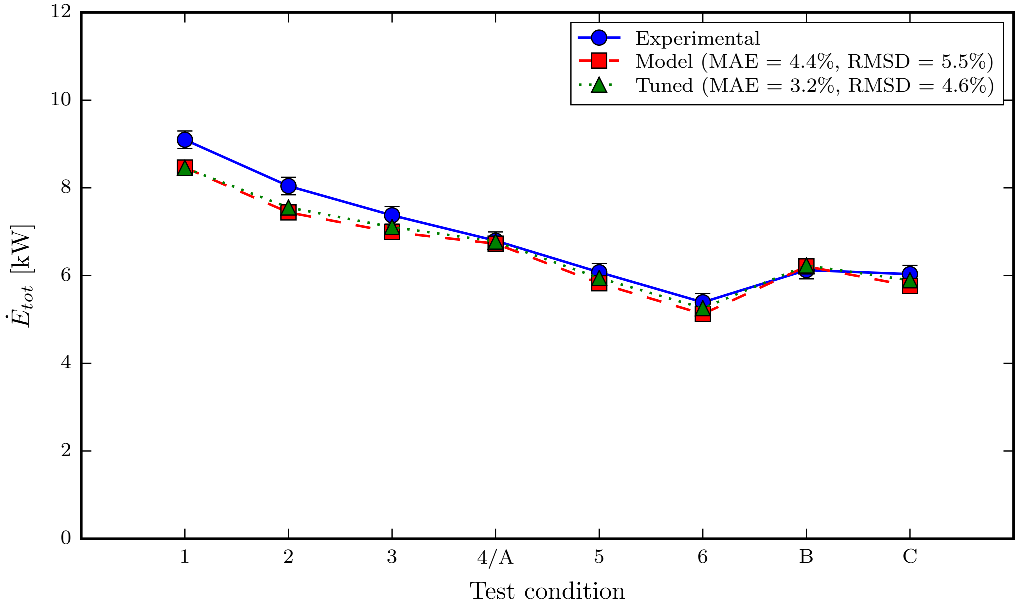

(g)

Figure 3.13. Continued.

to be optimized for air conditioning application at high ambient temperatures and it is object of discussion in the next section.

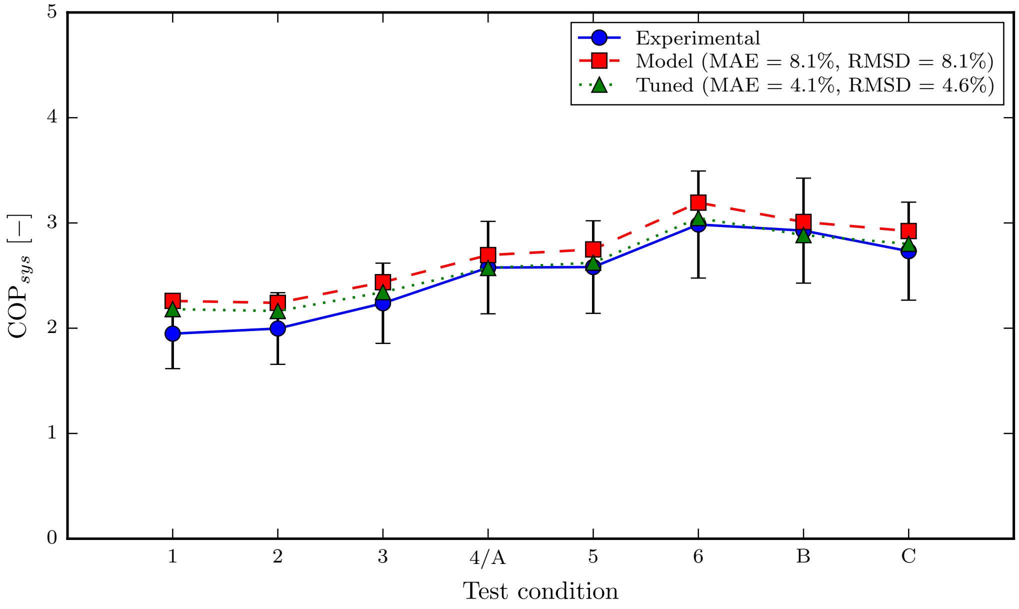

(h)

Figure 3.13. Continued.

The EVI cycle model with no tuning has been exercised to predict the experimental performance of the system with two different injection scenarios (*i.e.,* superheated- and saturated-injection conditions). In particular, the accuracy of the model has been assessed in terms of the mean absolute error (MAE) between measured and predicted values of the compressor discharge temperature, injection mass flow rate, suction mass flow rate, compressor power consumption, and system COP for both injection scenarios. The results are shown in Figure 3.14. To be noted is that the model is able to predict the experimental results with similar error trends for both the superheated-injection and saturated-injection cases. However, for saturated-injection case, the model consistently under-predicts the injection mass flow rate resulting in a higher MAE of 17.5% compared to superheated-injection case where the MAE is 11.6%. This is attributed to the fact that the compressor map was calibrated only on the experimental data for vapor injection. Thus, in the case of saturated injection, there might be some liquid injected to the compressor, and therefore the current model is no longer viable.

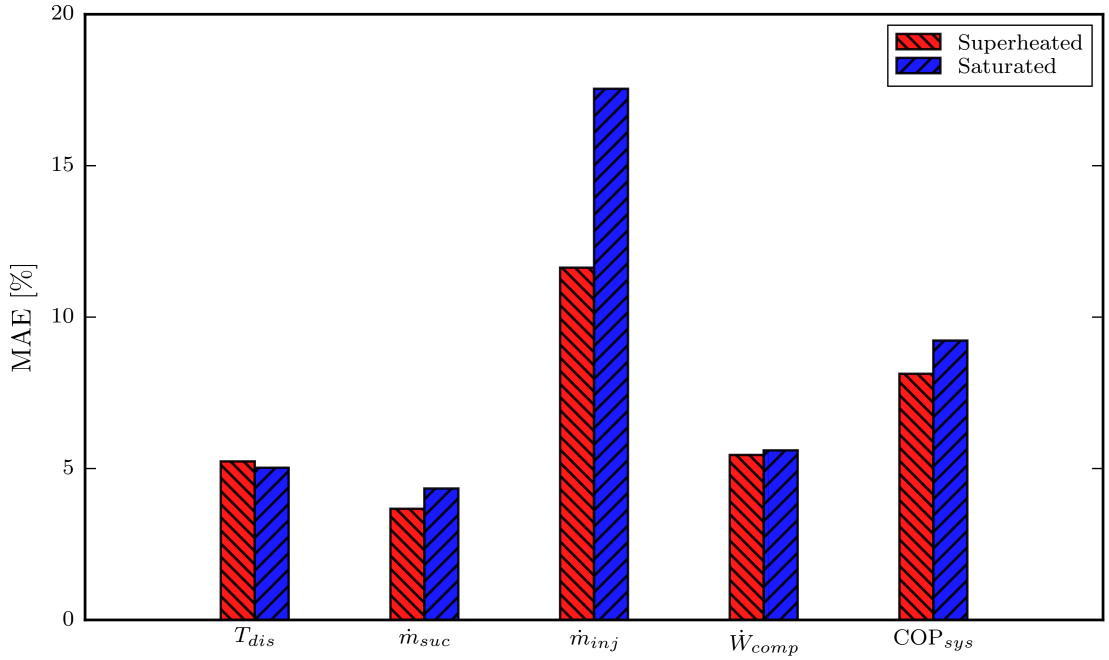

Figure 3.14. Comparison of mean absolute error (MAE) for model simulation results with experimental data for superheated ($T_{sup} = 7°\text{C}$) and saturated ($T_{sup} = 0°\text{C}$) injections.

3.5 System Optimization

The simulation work and the experimental results showed that the current vapor-injected (VI) compressor operates with limitations at high ambient conditions. In addition, the optimal injection state of the economized vapor injection (EVI) system is a strong function of sizing of the economizer because the injection state is directly linked to the heat transfer in the economizer. Therefore, a new VI compressor and a properly sized economizer have been simulated to maximize the system COP for air conditioning (AC) application at extreme ambient condition.

3.5.1 Objective Function

In order to optimize the COP of the Environmental Control Unit (ECU), the VI compressor from Tello-Oquendo et al. (2017) was selected because it featured a larger compressor envelope and it was designed for higher condensing temperatures. The VI compressor mapped coefficients to be used in the optimization process are reported in Table F.3. With respect to the geometry parameters of the plate heat exchanger (PHX) acting as an economizer, the same parameters reported in the economizer model (Section 3.4.3) were modified.

The estimation of the PHX variables was performed by using the iterative scheme shown in Figure 3.15. The optimization process illustrated in Figure 3.15 simulates the cycle with superheated injection ($T_{sup} = 7$°C) using the proposed VI compressor at outdoor temperature of 51.7°C (125°F) and indoor temperature of 32.2°C (90°F) with 50% relative humidity (*i.e.,* Test Condition 1). At first, the system COP is calculated at this operating condition. Then the PHX geometry parameters are varied using a bounded optimization solver by the mean of sequential least squares (SLSQ) method (Kraft, 1988) until the system COP is maximized.

The optimized PHX geometry parameters are shown in Table 3.8 and were further employed to exercise the EVI system model. The optimized parameters account for EVI system COP improvement.

Table 3.8. Geometry of the optimized economizer (PHX).

Number of plates	10
Length of plates [mm]	508
Width of plates [mm]	38.1
Thickness of plates [mm]	0.2
Wavelength of plates [mm]	5
Amplitude of corrugation [mm]	0.9
Chevron angle [degree]	76

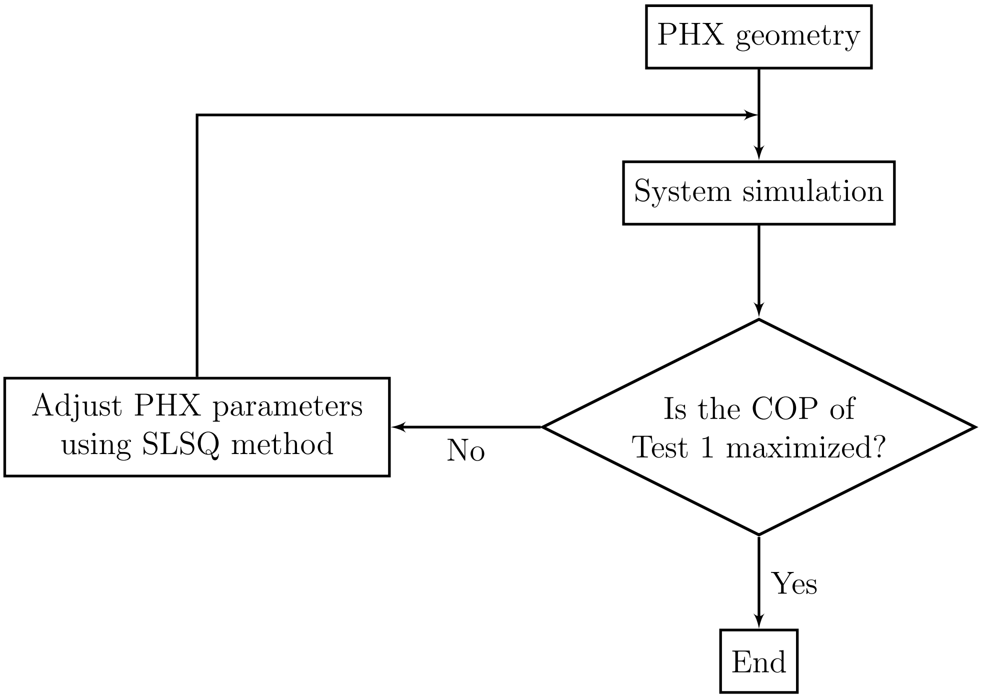

Figure 3.15. Flowchart of system COP optimization.

3.5.2 Optimization Results

The optimized plate heat exchanger (PHX) and the new VI compressor model were simulated inside the cycle model for superheated injection condition (T_{sup} = 7°C). The predictions showed significant enhancements of the system and the component performance, as shown in Figure 3.16 through Figure 3.18. Figures 3.16, 3.17, and 3.18 illustrate the comparisons between the optimized simulation results and the experimental data (*i.e.,* superheated EVI) at different testing conditions for compressor discharge temperature, cooling capacity, and system COP, respectively.

The compressor discharge temperatures were reduced as a result of changing the VI compressor as well as optimizing the economizer sizing (*i.e.,* PHX geometries) and the injection state (Navarro et al., 2013). Significant improvements to the compressor discharge temperatures were obtained for all testing conditions, as reported in Figure 3.16. In particular, for the case of extreme ambient conditions (*i.e.,* Test Condition 1), the discharge temperature was reduced by 6.9°C. Whereas in the case of ANSI/AHRI rating condition (*i.e.,* Test Condition 4/A), the discharge temperature decreased by 5.8°C. Furthermore, the maximum improvement to the discharge temperature of 8.5°C was achieved at Test Condition B, while the minimum improvement 4.5°C was found at Test Condition 2.

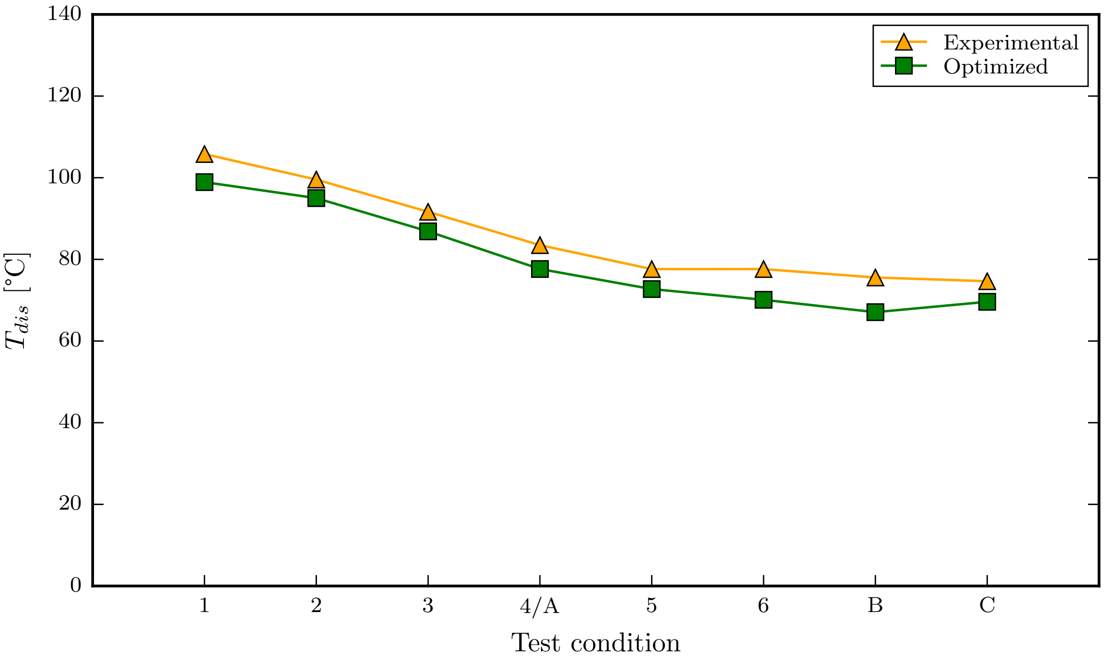

Figure 3.16. Comparison between optimized compressor discharge temperature and experimental results for superheated-injection (T_{sup} = 7°C) at different testing conditions.

The system optimization resulted in higher cooling capacity due to the larger volumetric displacement of the new VI compressor that helped to increase the suction refrigerant mass flow rate. Figure 3.17 shows that for different testing conditions, the relative improvement in cooling capacity ranged from 16.7% to 22.3%. To be noted is that the lowest improvement of 16.7% was obtained at Test Condition C, which was an off-design operating point. The maximum cooling capacity improvement of 22.3% was attained at Test Condition 1.

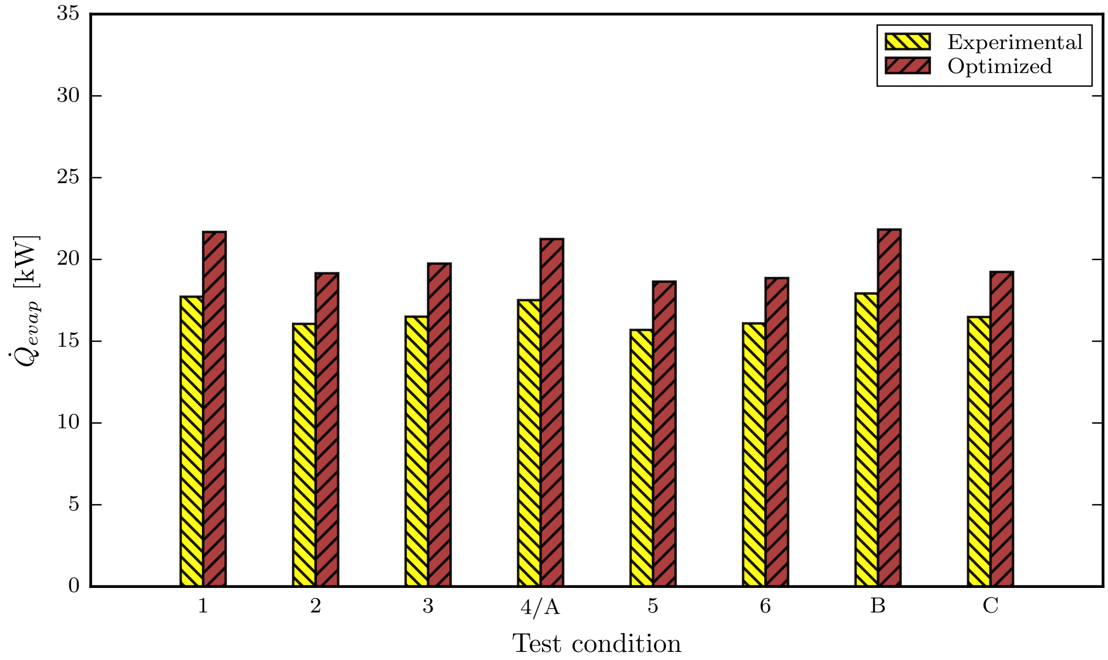

Figure 3.17. Comparison between optimized cooling capacity and experimental results for superheated-injection (T_{sup} = 7°C) at different testing conditions.

The significant increase in cooling capacity and the optimized economizer sizing enhanced the system COP, as it can be seen in Figure 3.18. In particular, Figure 3.18 shows that, for different testing conditions, the increase in system COP ranged from 5.7% to 17.3%. The maximum improvement of 17.3% was achieved at Test Condition B, while the minimum improvement of 5.7% was found at Test Condition 2. The higher temperature lift that caused higher power consumption resulted in a relatively small improvement in system COP at the extreme conditions (*i.e.,* Test Condition 4 back to Test Condition 1). However, the system COP still improved by 11.3% at the extreme case of Test Condition 1.

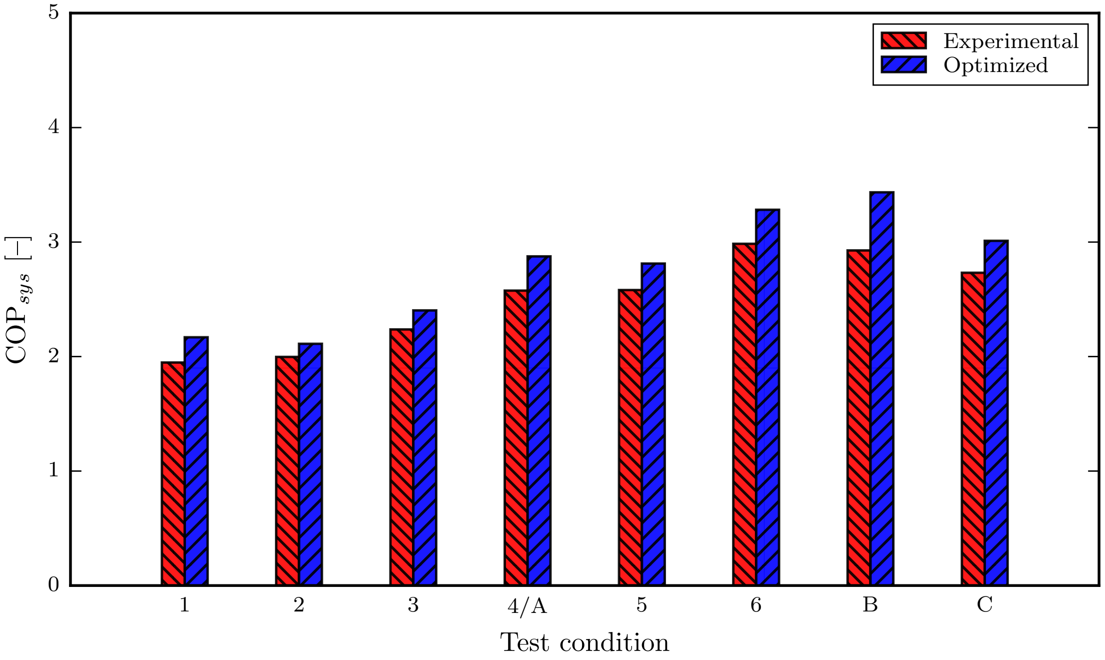

Figure 3.18. Comparison between optimized system COP and experimental results for superheated-injection (T_{sup} = 7°C) at different testing conditions.

3.6 Summary

This chapter presented an assessment of vapor injection with economization in a packaged air conditioning (AC) unit to improve the performance under high temperature ambient conditions. The effectiveness of economized vapor injection (EVI) system was investigated in a 17.6 kW Environmental Control Unit (ECU) with R-407C as working fluid. The ECU was retrofitted with a plate heat exchanger (PHX) as an economizer, and an additional expansion device to experimentally evaluate superheated and saturated injections at extreme testing conditions. Comparisons of cooling capacity, COP, and compressor discharge temperature were analyzed with respect to the case of no injection. An EVI cycle model was developed and validated using the experimental data. Moreover, the EVI's vapor injection (VI) compressor and economizer were optimized for maximize system COP using the validated model. The results yielded the following conclusions:

- Despite a lack of improvement in the compressor discharge temperature at off-design conditions, the EVI system reduced the compressor discharge temperature by up to 1.7°C and 5°C for superheated and saturated injection conditions, respectively.
- The EVI system improved the cooling capacity for the superheated injection condition by up to 12.7%, while the improvement for the saturated injection case was up to 11.8% because of the excess in evaporator's mass flow rate.
- Due to the design limitations of the VI compressor for AC applications, the relative improvements in EVI system COP were 3.1% and 1.3% for superheated and saturated injection conditions, respectively.
- An implicit detailed EVI cycle model was developed, tuned, and then validated within a mean absolute error of approximately ±5% for predictions of suction and injection mass flow rates, compressor power consumption, and system COP.
- An alternative VI compressor and an optimized PHX geometry were simulated to maximize the system COP at designed ambient condition of 51.7°C (125°F). The optimization process resulted in maximum improvements in compressor discharge temperature, cooling capacity and COP of 8.5°C, 22.3%, and 17.3%, respectively.

CHAPTER 4. SUMMARY AND RECOMMENDATIONS

4.1 Summary

The study presented here evaluates packaged air conditioning (AC) system at high ambient conditions. The packaged AC unit is characterized by an Environmental Control Unit (ECU) to cool military shelters and equipment. Due to design limitations and airflow maldistribution in the packaged AC units, the evaluation of interleaving evaporator circuity was discussed in Chapter 2. To compensate for air maldistribution, experimental air velocity measurements were conducted on a 5 RT packaged ECU with R-407C as working fluid. The interleaved circuitry arrangement was based on the airflow percentage contributed for each of the evaporator circuits. In this arrangement, the refrigerant from the circuit that has highest air flow was redirected to the circuit that has the lowest air flow, and so on for the remaining circuits. The interleaved evaporator was experimentally investigated at extreme testing conditions up to 51.7°C (125°F) and compared with the baseline circuitry with respect to cooling capacity, COP and evaporator superheat. The experimental data was then used to validate an interleaved circuitry model. The results showed that despite a small increase in pressure drop across the interleaved evaporator circuitry compared to original circuitry, the superheat distribution improved by $1 - 5$°C. In addition, the cooling capacity and COP of the interleaved unit improved by 16.6% and 12.4% compared to the baseline unit. Moreover, the tuned model can predict the mass flow rate and cooling capacity for the interleaved arrangement within a mean absolute error of approximately ±10%.

Operating the packaged AC units at extremely high temperature ambient conditions resulted in severe performance degradation. Chapter 3 presented an assessment of vapor injection (VI) with economization to improve the system performance under high ambient temperature conditions. This technology reduced the heat generated during the compression process by injecting cool gas to the compressor chamber at an intermediate stage. The effectiveness of economized vapor injection (EVI) system was investigated in the same 5 RT ECU. The ECU was retrofitted with a plate heat exchanger (PHX) as an economizer, and an additional expansion device to experimentally evaluate superheated and saturated injections at extreme testing conditions up to 51.7°C (125°F) and compared with the case of no injection with respect to cooling capacity, COP, and compressor discharge temperature. The experimental data was then used to develop, tune, and validate a detailed steady-state cycle model. The results showed that the EVI system reduced the compressor discharge temperature by up to 5°C, and improved the cooling capacity and COP by up to 12.7% and 3.1%, respectively. The implicit EVI cycle model predicted suction and injection mass flow rates, compressor power consumption, and system COP within a mean absolute error of approximately ±5%. Moreover, the EVI's VI compressor and economizer were optimized for maximize system COP at an outdoor design set-point of 51.7°C (125°F) using the validated model. The optimization approach resulted in maximum improvements in compressor discharge temperature, cooling capacity and COP of 8.5°C, 22.3%, and 17.3%, respectively.

4.2 Recommendations

In Chapter 2, the evaporator tubes were modeled using a simple ϵ-NTU method. Therefore, the future work should consider a discrete heat exchanger model for accuracy such as EVSIM (Lee et al., 2003) or ACMODEL (Shen, 2006). Ideally, the future work should also consider the conduction across the evaporator fins as it is utilized in EVAP5 model (Payne and Domanski, 2003). In addition, the interleaved evaporator should be exercised in system level simulations.

In Chapter 3, the EVI system was simulated by imposing the subcooling. Therefore, future work should consider the system charge as an input to the model using available methods such as Shen et al. (2009) to estimate the subcooling. Furthermore, a fully mechanistic cycle model with expansion valve models could also be developed to resemble the real system operation. In addition, the optimized PHX design and the proposed VI compressor should be experimentally tested to validate the numerical predictions.

REFERENCES

REFERENCES

A. A. Aganda, J. E. R. Coney, and C. G. W. Sheppard. Airflow maldistribution and the performance of a packaged air conditioning unit evaporator. *Applied Thermal Engineering*, 20(6):515–528, 2000. ISSN 13594311. doi: 10.1016/S1359-4311(99) 00038-1.

A. Al-alili. Experimental Investigation of a Hybrid Air Conditioner for Hot and Humid Climates. *ASHRAE Transactions*, 120:1–9, 2014.

C. K. Bach. *Refrigerant side compensation for air-side maldistribution of evaporators and its effects on system performance*. PhD thesis, Purdue University, 2014.

C. K. Bach, E. A. Groll, J. E. Braun, and W. T. Horton. Mitigation of air flow maldistribution in evaporators. *Applied Thermal Engineering*, 73(1):877–885, 2014. ISSN 13594311. doi: 10.1016/j.applthermaleng.2014.08.010.

A. Bahman, E. Groll, T. Horton, and J. Braun. Technologies to Improve the Performance of A/C Systems in Hot Climate Regions. *15th International Refrigeration and Air Conditioning Conference at Purdue*, 2014. URL `https://docs.lib.purdue.edu/iracc/1431/`.

A. M. Bahman and E. A. Groll. Second-Law Analysis to Improve the Energy Efficiency of Environmental Control Unit. *16th International Refrigeration and Air Conditioning Conference at Purdue*, 2016. URL `http://docs.lib.purdue.edu/iracc/1706/`.

A. Barve and L. Cremaschi. Drop-in Performance of Low GWP Refrigerants in a Heat Pump System for Residential Applications. *International Refrigeration and Air Conditioning Conference*, pages 1–10, 2012.

I. H. Bell. Air conditioning and heat pump model (achp) source code version 1.5, 2015. URL `https://github.com/TSTK/ACHP`. [Online; accessed 30-Sep-2016].

I. H. Bell, E. A. Groll, and J. E. Braun. Performance of vapor compression systems with compressor oil flooding and regeneration. *International Journal of Refrigeration*, 34(1):225–233, 2011. doi: 10.1016/j.ijrefrig.2010.09.004.

I. H. Bell, J. Wronski, S. Quoilin, and V. Lemort. Pure and pseudo-pure fluid thermophysical property evaluation and the open-source thermophysical property library CoolProp version 6.1.0. *Industrial & Engineering Chemistry Research*, 53(6):2498–2508, 2014. doi: 10.1021/ie4033999.

I. H. Bell, S. Quoilin, E. Georges, J. E. Braun, E. A. Groll, W. T. Horton, and V. Lemort. A generalized moving-boundary algorithm to predict the heat transfer rate of counterflow heat exchangers for any phase configuration. *Applied Thermal Engineering*, 79:192–201, 2015. ISSN 13594311. doi: 10.1016/j.applthermaleng.2014.12.028.

T. L. Bergman, F. P. Incropera, D. P. DeWitt, and A. S. Lavine. *Fundamentals of heat and mass transfer.* John Wiley & Sons, 7th edition, 2011.

S. S. Bertsch and E. A. Groll. Two-stage air-source heat pump for residential heating and cooling applications in northern U.S. climates. *International Journal of Refrigeration*, 31(7):1282–1292, 2008. ISSN 01407007. doi: 10.1016/j.ijrefrig.2008.01.006.

A. Biswas and L. Cremaschi. Performance and Capacity Comparison of Two New LGWP Refrigerants Alternative to R410A in Residential Air Conditioning Applications. *International Refrigeration and Air conditioning conference*, pages 1–10, 2012.

P. Blecich. Experimental investigation of the effects of airflow nonuniformity on performance of a fin-and-tube heat exchanger. *International Journal of Refrigeration*, 59:65–74, 2015. ISSN 01407007. doi: 10.1016/j.ijrefrig.2015.06.029.

J. E. Braun. *Methodologies for the design and control of central cooling plant.* PhD thesis, University of Wisconsin - Madison, 1988.

R. P. Brent. *Algorithms for minimization without derivatives.* Englewood Cliffs, NJ: Prentice-Hall, 1973.

C. G. Broyden. A class of methods for solving nonlinear simultaneous equations. *Mathematics of computation*, 19(92):577–593, 1965.

C. W. Bullard, J. Proctor, J. Brezner, K. B. Mercer, and R. A. Davis. Modeling and testing of a utility peak reducing residential hot/dry air conditioner (HDAC) using microchannel heat exchangers. *ASHRAE Transactions*, 112 PART 1:162–170, 2006. ISSN 00012505.

Y.-J. Chang, K.-C. Hsu, Y.-T. Lin, and C.-C. Wang. A generalized friction correlation for louver fin geometry. *International Journal of Heat and Mass Transfer*, 43(12):2237–2243, 2000. ISSN 00179310. doi: 10.1016/S0017-9310(99)00289-6.

I. Y. Cho, H. J. Seo, D. Kim, and Y. Kim. Performance comparison between R410A and R32 multi-heat pumps with a sub-cooler vapor injection in the heating and cooling modes. *Energy*, 112:179–187, 2016. ISSN 03605442. doi: 10.1016/j.energy.2016.06.069. URL `http://dx.doi.org/10.1016/j.energy.2016.06.069`.

Y.-H. Cho, B. Lee, and J.-K. Lee. Development of high efficiency scroll compressor for Packane Air Conditioners. *International Conference on Compressors and their Systems*, pages 323–328, 2011. doi: 10.1533/9780857095350.9.469. URL `http://dx.doi.org/10.1533/9780857095350.9.469`.

Z. Chunlu and G. Jie. Robust Design of Fin-and-tube Heat Exchanger's Refrigerant Circuitry Subject to Different Air Maldistributions. *Journal of Tongji University*, 42(1):103–8, 2014.

S. W. Churchill. Friction-factor equation spans all fluid-flow regimes. *Chemical engineering*, 84(24):91–92, 1977.

J. Claesson. *Thermal and Hydraulic Performance of Compact Brazed Plate Heat Exchangers Operating as Evaporators in Domestic Heat Pumps.* PhD thesis, KTH, 2004.

M. G. Cooper. Heat Flow Rates in Saturated Nucleate Pool Boiling-A Wide-Ranging Examination Using Reduced Properties. *Advances in Heat Transfer*, 16:157–239, 1984. ISSN 0065-2717. doi: https://doi.org/10.1016/S0065-2717(08)70205-3.

S. Devotta, A. S. Padalkar, and N. K. Sane. Performance assessment of HC-290 as a drop-in substitute to HCFC-22 in a window air conditioner. *International Journal of Refrigeration*, 28(4):594–604, 2005a. ISSN 01407007. doi: 10.1016/j.ijrefrig.2004.09.013.

S. Devotta, A. S. Padalkar, and N. K. Sane. Performance assessment of HCFC-22 window air conditioner retrofitted with R-407C. *Applied Thermal Engineering*, 25(17-18):2937–2949, 2005b. ISSN 13594311. doi: 10.1016/j.applthermaleng.2005.03.002.

Y. Ding, Q. Chai, G. Ma, and Y. Jiang. Experimental study of an improved air source heat pump. *Energy Conversion and Management*, 45(15-16):2393–2403, 2004. ISSN 01968904. doi: 10.1016/j.enconman.2003.11.021.

U. S. DOE. (EIA) US Department of Energy/ Energy Information Administration, 1993. *Household Energy Consumption and Expenditures 1993*, (Part I: National Data, DOE/EIA-0321 Washington, DC), 1995.

P. Domanski. Simulation of an evaporator with nonuniform one-dimensional air distribution. *ASHRAE Transactions*, 97:793–802, 1991.

P. A. Domanski and D. Yashar. Optimization of finned-tube condensers using an intelligent system. *International Journal of Refrigeration*, 30(3):482–488, 2007. ISSN 01407007. doi: 10.1016/j.ijrefrig.2006.08.013.

S. Elbel and P. Hrnjak. Design , Build-up , And Performance Investigation Of A 35 kW (10 Ton) Military Environmental Control Unit Using Transcritical R744 Technology. *International Refrigeration and Air Conditioning Conference at Purdue*, 2010. URL `http://docs.lib.purdue.edu/iracc/1049`.

S. Elbel, C. D. Bowers, M. Reichle, J. M. Cristiani, and P. Hrnjak. Vapor Jet Ejector Used To Generate Free Waste Heat Driven Cooling In Military Environmental Cooling Units. *International Refrigeration and Air Conditioning Conference at Purdue*, 2012. URL `http://docs.lib.purdue.edu/iracc/1191`.

V. Gnielinski. New equations for heat and mass-transfer in turbulent pipe and channel flow. *International chemical engineering*, 16(2):359–368, 1976.

J. Gong, T. Gao, X. Yuan, and D. Huang. Effects of air flow maldistribution on refrigeration system dynamics of air source heat pump chiller under frosting conditions. *Energy Conversion and Management*, 49(6):1645–1651, 2008. ISSN 01968904. doi: 10.1016/j.enconman.2007.11.004.

E. Hajidavalloo and H. Eghtedari. Performance improvement of air-cooled refrigeration system by using evaporatively cooled air condenser. *International Journal of Refrigeration*, 33(5):982–988, 2010. ISSN 01407007. doi: 10.1016/j.ijrefrig.2010.02.001. URL `http://dx.doi.org/10.1016/j.ijrefrig.2010.02.001`.

X. H. Han, Y. Qiu, P. Li, Y. J. Xu, Q. Wang, and G. M. Chen. Cycle performance studies on HFC-161 in a small-scale refrigeration system as an alternative refrigerant to HFC-410A. *Energy and Buildings*, 44(1):33–38, 2012. ISSN 03787788. doi: 10.1016/j.enbuild.2011.10.004. URL `http://dx.doi.org/10.1016/j.enbuild.2011.10.004`.

J. Heo, M. W. Jeong, C. Baek, and Y. Kim. Comparison of the heating performance of air-source heat pumps using various types of refrigerant injection. *International Journal of Refrigeration*, 34(2):444–453, 2011. ISSN 01407007. doi: 10.1016/j.ijrefrig.2010.10.003. URL `http://dx.doi.org/10.1016/j.ijrefrig.2010.10.003`.

K. T. Hong and R. L. Webb. Calculation of fin efficiency for wet and dry fins. *HVAC&R Research*, 2(1):27–41, 1996. doi: 10.1080/10789669.1996.10391331.

Y. Hwang, H.-J. Huff, M. Preissner, and R. Radermacher. CO2 transcritical cycles for high temperature applications. *ASME International Mechanical Engineering Congress and Exposition*, 41(2001):255–260, 2001.

N. A. James, J. E. Braun, E. A. Groll, and W. T. Horton. Semi-empirical modeling and analysis of oil flooded R410A scroll compressors with liquid injection for use in vapor compression systems. *International Journal of Refrigeration*, 66:50–63, 2016. ISSN 01407007. doi: 10.1016/j.ijrefrig.2015.12.011. URL `http://dx.doi.org/10.1016/j.ijrefrig.2015.12.011`.

D. B. Jani, M. Mishra, and P. K. Sahoo. Performance studies of hybrid solid desiccant-vapor compression air-conditioning system for hot and humid climates. *Energy and Buildings*, 102:284–292, 2015. ISSN 03787788. doi: 10.1016/j.enbuild.2015.05.055. URL `http://dx.doi.org/10.1016/j.enbuild.2015.05.055`.

K. A. Joudi and Q. R. Al-Amir. Experimental Assessment of residential split type air-conditioning systems using alternative refrigerants to R-22 at high ambient temperatures. *Energy Conversion and Management*, 86:496–506, 2014. ISSN 01968904. doi: 10.1016/j.enconman.2014.05.036. URL `http://dx.doi.org/10.1016/j.enconman.2014.05.036`.

M. R. Kærn and T. Tiedemann. Compensation of Airflow Maldistribution in Fin-and-Tube Evaporators. *International Refrigeration and Air Conditioning Conference at Purdue*, 2012. URL `http://docs.lib.purdue.edu/iracc/1198`.

M. R. Kærn, W. Brix, B. Elmegaard, and L. F. S. Larsen. Compensation of flow maldistribution in fin-and-tube evaporators for residential air-conditioning. *International Journal of Refrigeration*, 34(5):1230–1237, 2011a. ISSN 01407007. doi: 10.1016/j.ijrefrig.2011.03.011.

M. R. Kærn, W. Brix, B. Elmegaard, and L. F. S. Larsen. Performance of residential air-conditioning systems with flow maldistribution in fin-and-tube evaporators. *International Journal of Refrigeration*, 34(3):696–706, 2011b. ISSN 01407007. doi: 10.1016/j.ijrefrig.2010.12.010.

M. R. Kærn, B. Elmegaard, and L. F. S. Larsen. Comparison of fin-and-tube interlaced and face split evaporators with flow maldistribution and compensation. *International Journal of Refrigeration*, 36(1):203–214, 2013. ISSN 01407007. doi: 10.1016/j.ijrefrig.2012.10.006.

K. Kaga, S. Kotoh, T. Ogushi, and H. Yoshida. Influence of air-flow imbalance and refrigerant flow path pattern on an evaporator's performance. *Heat Transfer-Asian Research*, 38(6):385–399, 9 2009. ISSN 10992871. doi: 10.1002/htj.20260.

J.-U.-R. Khan and S. M. Zubair. Design and rating of dedicated mechanical- sub-cooling vapour compression refrigeration systems. *Proc Instn Mech Engrs*, 214, 2000.

J.-H. Kim, J. E. Braun, and E. A. Groll. A hybrid method for refrigerant flow balancing in multi-circuit evaporators: Upstream versus downstream flow control. *International Journal of Refrigeration*, 32(6):1271–1282, 2009. ISSN 01407007. doi: 10.1016/j.ijrefrig.2009.01.013.

M. H. Kim and C. W. Bullard. Air-side thermal hydraulic performance of multi-louvered fin aluminum heat exchangers. *International Journal of Refrigeration*, 25(3):390–400, 2002. ISSN 01407007. doi: 10.1016/S0140-7007(01)00025-1.

S. M. Kim and I. Mudawar. Universal approach to predicting two-phase frictional pressure drop for adiabatic and condensing mini/micro-channel flows. *International Journal of Heat and Mass Transfer*, 55(11-12):3246–3261, 2012. ISSN 00179310. doi: 10.1016/j.ijheatmasstransfer.2012.02.047.

S. M. Kim and I. Mudawar. Universal approach to predicting heat transfer coefficient for condensing mini/micro-channel flow. *International Journal of Heat and Mass Transfer*, 56(1-2):238–250, 2013. ISSN 00179310. doi: 10.1016/j.ijheatmasstransfer.2012.09.032.

E. S. Kirby, C. W. Bullard, and W. E. Dunn. Effect of airflow nonuniformity on evaporator performance. *ASHRAE Transactions: Symposia*, 104:755–762, 1998.

S. Klein and F. Alvarado. Engineering equation solver, academic professional version 10.092-3d. *F-Chart Software, Madison, WI*, 2016.

D. Kraft. A software package for sequential quadratic programming. 1988. URL `http://www.opengrey.eu/item/display/10068/147127`.

J. L. Lagrange. *Leçons élémentaires sur les Mathématiques, données à l'École normale, en 1795*, pages 183–287. Gauthier-Villars, Paris, 1877.

N. Lawrence and S. Elbel. Experimental investigation on the effect of evaporator design and application of work recovery on the performance of two-phase ejector liquid recirculation cycles with R410A. *Applied Thermal Engineering*, 100:398–411, 2016. ISSN 13594311. doi: 10.1016/j.applthermaleng.2016.01.079. URL `http://dx.doi.org/10.1016/j.applthermaleng.2016.01.079`.

H. S. Lee. *Thermal design: heat sinks, thermoelectrics, heat pipes, compact heat exchangers, and solar cells.* John Wiley & Sons, 2010.

J. Lee and P. A. Domanski. Impact of air and refrigerant maldistributions on the performance of finned-tube evaporators with R-22 and R-407C. Technical report, The Air-Conditioning and Refrigeration Technology Institute, 1997.

J. Lee, Y. C. Kwon, and M. H. Kim. An improving method for analyzing a fin and tube evaporator containing a zeotropic mixture refrigerant with air maldistribution. *International Journal of Refrigeration*, 26(6):707–720, 2003. ISSN 01407007. doi: 10.1016/S0140-7007(03)00023-9.

D. Li. *Investigation of an ejector-expansion device in a transcritical carbon dioxide cycle for military ECU applications.* PhD thesis, Purdue University, 2006.

D. Li and E. A. Groll. Theoretical Performance Evaluation of a Carbon Dioxide based Environmental Control Unit (ECU) with Microchannel Heat Exchangers. *International Refrigeration and Air Conditioning Conference at Purdue*, 2006.

J. Ling, O. Kuwabara, Y. Hwang, and R. Radermacher. Enhancement Options for Separate Sensible and Latent Cooling Air-Conditioning Systems. *International Refrigeration and Air Conditioning Conference at Purdue*, pages 1–8, 2011.

R. Llopis, R. Cabello, D. Sánchez, and E. Torrella. Energy improvements of CO2 transcritical refrigeration cycles using dedicated mechanical subcooling. *International Journal of Refrigeration*, 55:129–141, 2015. ISSN 01407007. doi: 10.1016/j.ijrefrig.2015.03.016.

R. Llopis, L. Nebot-Andrés, R. Cabello, D. Sánchez, and J. Catalán-Gil. Experimental evaluation of a CO2 transcritical refrigeration plant with dedicated mechanical subcooling. *International Journal of Refrigeration*, 69:361–368, 2016. ISSN 0140-7007. doi: 10.1016/j.ijrefrig.2016.06.009. URL `http://dx.doi.org/10.1016/j.ijrefrig.2016.06.009`.

R. Lockhart and R. Martinelli. Proposed correlation of data for isothermal two-phase, two-component flow in pipes. *Chemical Engineering Progress*, 45(1):39–48, 1949.

G. A. Longo. Heat transfer and pressure drop during HFC refrigerant saturated vapour condensation inside a brazed plate heat exchanger. *International Journal of Heat and Mass Transfer*, 53(5-6):1079–1087, 2010. ISSN 00179310. doi: 10.1016/j.ijheatmasstransfer.2009.11.003.

G. A. Longo. The effect of vapour super-heating on hydrocarbon refrigerant condensation inside a brazed plate heat exchanger. *Experimental Thermal and Fluid Science*, 35(6):978–985, 2011. ISSN 08941777. doi: 10.1016/j.expthermflusci.2011.01.018.

G. A. Longo, A. Gasparella, and R. Sartori. Experimental heat transfer coefficients during refrigerant vaporisation and condensation inside herringbone-type plate heat exchangers with enhanced surfaces. *International Journal of Heat and Mass Transfer*, 47(19-20):4125–4136, 2004. ISSN 00179310. doi: 10.1016/j.ijheatmasstransfer.2004.05.001.

D. R. Lumpkin, A. M. Bahman, and E. A. Groll. Two-phase injected and vapor-injected compression: Experimental results and mapping correlation for a R-407C scroll compressor. *International Journal of Refrigeration*, 86:449–462, 2018. ISSN 01407007. doi: 10.1016/j.ijrefrig.2017.11.009.

B. Luo. Theoretical study of R32 in an oil flooded compression cycle with a scroll machine. *International Journal of Refrigeration*, 70:269–279, 2016. doi: 10.1016/j.ijrefrig.2016.06.002. URL `http://linkinghub.elsevier.com/retrieve/pii/S0140700716301505`.

G. Mader, B. Palm, and B. Elmegaard. Maldistribution in air-water heat pump evaporators. Part 1: Effects on evaporator, heat pump and system level. *International Journal of Refrigeration*, 50:207–216, 2015a. ISSN 01407007. doi: 10.1016/j.ijrefrig.2014.07.006.

G. Mader, B. Palm, and B. Elmegaard. Maldistribution in air-water heat pump evaporators. Part 2: Economic analysis of counteracting technologies. *International Journal of Refrigeration*, 50:217–226, 2015b. ISSN 01407007. doi: 10.1016/j.ijrefrig.2014.07.005.

N. H. A. Majid, N. Takagi, S. Hokoi, S. N. N. Ekasiwi, and T. Uno. Field survey of air conditioner temperature settings in a hot, dry climate (Oman). *HVAC&R Research*, 20(7):751–759, 2014. doi: 10.1080/10789669.2014.953845. URL `http://www.scopus.com/inward/record.url?eid=2-s2.0-84907858030&partnerID=tZOtx3y1`.

J. A. Manzione and F. E. Calkins. Evaluation of transcritical CO2 using an automotive compressor in an Automotive Compressor in a Packaged-Unitary Military ECU. *ASHRAE Transactions: Symposia*, 108:937–943, 2002.

H. Martin. *VDI Heat Atlas*, chapter B6: Pressure Drop and and Heat Transfer in Plate Heat Exchangers. Springer Berlin Heidelberg, Berlin, Heidelberg, 2nd edition, 2010. ISBN 978-3-540-77876-9. doi: 10.1007/978-3-540-77877-6.

P. Martínez, J. Ruiz, C. G. Cutillas, P. J. Martínez, A. S. Kaiser, and M. Lucas. Experimental study on energy performance of a split air-conditioner by using variable thickness evaporative cooling pads coupled to the condenser. *Applied Thermal Engineering*, 105:1041–1050, 2016. doi: 10.1016/j.applthermaleng.2016.01.067.

M. M. Mathison, J. E. Braun, and E. A. Groll. Performance limit for economized cycles with continuous refrigerant injection. *International Journal of Refrigeration*, 34(1):234–242, 2011. doi: 10.1016/j.ijrefrig.2010.09.006. URL `http://dx.doi.org/10.1016/j.ijrefrig.2010.09.006`.

H. T. Minh Thu and H. Sato. Proposal of an eco-friendly high-performance air-conditioning system. Part 1. Possibility of improving existing air-conditioning system by an evapo-transpiration condenser. *International Journal of Refrigeration*, 36(6):1589–1595, 2013a. doi: 10.1016/j.ijrefrig.2013.04.004. URL `http://dx.doi.org/10.1016/j.ijrefrig.2013.04.004`.

H. T. Minh Thu and H. Sato. Proposal of an eco-friendly high-performance air-conditioning system part 2. Application of evapo-transpiration condenser to residential air-conditioning system. *International Journal of Refrigeration*, 36(6):1596–1601, 2013b. doi: 10.1016/j.ijrefrig.2013.04.006. URL `http://dx.doi.org/10.1016/j.ijrefrig.2013.04.006`.

J. Moré, B. Garbow, and K. Hillstrom. User guide for MINPACK-1. 1980. URL `http://cds.cern.ch/record/126569/files/CM-P00068642.pdf`.

E. Navarro, A. Redón, J. Gonzálvez-Macia, I. Martinez-Galvan, and J. Corberán. Characterization of a vapor injection scroll compressor as a function of low, intermediate and high pressures and temperature conditions. *International Journal of Refrigeration*, 36(7):1821–1829, 2013. doi: 10.1016/j.ijrefrig.2013.04.022.

C. Park, H. Lee, Y. Hwang, and R. Radermacher. Recent advances in vapor compression cycle technologies. *International Journal of Refrigeration*, 60:118–134, 2015. ISSN 01407007. doi: 10.1016/j.ijrefrig.2015.08.005. URL `http://dx.doi.org/10.1016/j.ijrefrig.2015.08.005`.

W. V. Payne and P. A. Domanski. Potential benefits of smart refrigerant distributors. *Air-Conditioning and Refrigeration Technology Institute*, 2003.

S. F. Python. Python language reference, version 2.7.13, 2016. URL `http://www.python.org`.

B. A. Qureshi and S. M. Zubair. Cost optimization of heat exchanger inventory for mechanical subcooling refrigeration cycles. *International Journal of Refrigeration*, 36(4):1243–1253, 2013. ISSN 01407007. doi: 10.1016/j.ijrefrig.2013.02.011.

D. Qv, B. Dong, L. Cao, L. Ni, J. Wang, R. Shang, and Y. Yao. An experimental and theoretical study on an injection-assisted air- conditioner using R32 in the refrigeration cycle. *Applied Energy*, 185:791–804, 2017. ISSN 0306-2619. doi: 10.1016/j.apenergy.2016.10.100. URL `http://dx.doi.org/10.1016/j.apenergy.2016.10.100`.

S. Ramaraj, J. E. Braun, E. A. Groll, and W. T. Horton. Performance analysis of liquid flooded compression with regeneration for cold climate heat pumps. *International Journal of Refrigeration*, 68:50–58, 2016. ISSN 01407007. doi: 10.1016/j.ijrefrig.2016.04.017. URL `http://dx.doi.org/10.1016/j.ijrefrig.2016.04.017`.

D. M. Robinson and E. A. Groll. Theoretical performance comparison of CO2 transcritical cycle technology versus HCFC-22 technology for a military packaged air conditioner application. *ASHRAE Transactions*, 6(4):325–348, 2001. ISSN 00012505. doi: 10.1080/10789669.2000.10391420.

J. R. Sand and J. C. Fischer. Active desiccant integration with packaged rooftop HVAC equipment. *Applied Thermal Engineering*, 25(17-18):3138–3148, 2005. ISSN 13594311. doi: 10.1016/j.applthermaleng.2005.04.007.

R. Sawan, K. Ghali, and M. Al-Hindi. Use of condensate drain to pre-cool the inlet air to the condensers: A technique to improve the performance of split air-conditioning units. *HVAC&R Research*, 9669(March 2015):37–41, 2012. ISSN 10789669. doi: 10.1080/10789669.2012.619395. URL `http://www.tandfonline.com/doi/abs/10.1080/10789669.2012.619395`.

T. Schmidt. *La production calorifique des surfaces munies dailettes.* 1945.

M. M. Shah. A new correlation for heat transfer during boiling flow through pipes. *ASHRAE Transactions*, 82:66–86, 1976.

B. Shen. *Improvement and validation of unitary air conditioner and heat pump simulation models at off -design conditions.* PhD thesis, Purdue University, 2006.

B. Shen and P. Bansal. Assessment of Environmentally Friendly Refrigerants for Window Air Conditioners. *International Refrigeration and Air Conditioning Conference at Purdue*, pages 1–8, 2014.

B. Shen, J. E. Braun, and E. A. Groll. Improved methodologies for simulating unitary air conditioners at off-design conditions. *International Journal of Refrigeration*, 32(7):1837–1849, 2009. ISSN 01407007. doi: 10.1016/j.ijrefrig.2009.06.009.

Y. Sheng, Y. Zhang, and G. Zhang. Simulation and energy saving analysis of high temperature heat pump coupling to desiccant wheel air conditioning system. *Energy*, 83:583–596, 2015. ISSN 03605442. doi: 10.1016/j.energy.2015.02.068. URL `http://dx.doi.org/10.1016/j.energy.2015.02.068`.

X. Song, D. Huang, X. Liu, and Q. Chen. Effect of non-uniform air velocity distribution on evaporator performance and its improvement on a residential air conditioner. *Applied Thermal Engineering*, 40:284–293, 2012. ISSN 13594311. doi: 10.1016/j.applthermaleng.2012.02.024.

A. Standard. Standard 41.2-1987, standard methods for laboratory airflow measurement. *American Society of Heating, Refrigerating and Air-Conditioning Engineers, Inc., Atlanta, GA*, 1987.

A. Standard. ANSI/AHRI Standard 210/240. *Performance rating of unitary A/C and air-source heat pump equipment*, 2008a.

A. Standard. Standard 111-2008, practices for measurement, testing, adjusting, and balancing of building, heating, ventilation, air-conditioning and refrigeration systems. *American Society of Heating, Refrigerating and Air-Conditioning Engineers, Inc., Atlanta, GA*, 2008b.

A. Standard. ANSI/ASHRAE Standard 23.1 (Working Draft 13). *Method of Testing for Rating the Performance of Positive Displacement Refrigerant Compressor and Condensing Units that Operate at Subcritical Temperatures of the Refrigerant*, 2015.

A. Subiantoro and K. T. Ooi. Economic analysis of the application of expanders in medium scale air-conditioners with conventional refrigerants, R1234yf and CO2. *International Journal of Refrigeration*, 36(5):1472–1482, 2013. ISSN 01407007. doi: 10.1016/j.ijrefrig.2013.03.010. URL `http://dx.doi.org/10.1016/j.ijrefrig.2013.03.010`.

K. Sumeru, S. Sulaimon, H. Nasution, and F. N. Ani. Numerical and experimental study of an ejector as an expansion device in split-type air conditioner for energy savings. *Energy and Buildings*, 79:98–105, 2014. ISSN 03787788. doi: 10.1016/j.enbuild.2014.04.043. URL `http://dx.doi.org/10.1016/j.enbuild.2014.04.043`.

B. Taylor and C. Kuyatt. Nist technical note 1279: Guidelines for evaluating and expressing the uncertainty of nist measurements results. *National Institute of Standards and Technology, Washington DC*, 1994.

F. M. Tello-Oquendo, E. Navarro-Peris, J. Gonzálvez-Maciá, and J. M. Corberán. Performance of a scroll compressor with vapor-injection and two-stage reciprocating compressor operating under extreme conditions. *International Journal of Refrigeration*, 63:144–156, 2016. ISSN 01407007. doi: 10.1016/j.ijrefrig.2015.10.035. URL `http://dx.doi.org/10.1016/j.ijrefrig.2015.10.035`.

F. M. Tello-Oquendo, E. Navarro-Peris, and J. Gonzálvez-Maciá. New characterization methodology for vapor-injection scroll compressors. *International Journal of Refrigeration*, 74:528–539, 2017. ISSN 01407007. doi: 10.1016/j.ijrefrig.2016.11.019.

D. J. Timoney and P. J. Foley. Some effects of air flow maldistribution on performance of a compact evaporator with R134a. *Heat Recovery Systems and CHP*, 14(5):517–523, 1994. ISSN 08904332. doi: 10.1016/0890-4332(94)90054-X.

C.-C. Wang, Y.-M. Tsai, and D.-C. Lu. Comprehensive study of convex-louver and wavy fin-and-tube heat exchangers. *Journal of Thermophysics and Heat Transfer*, 12(3):423–430, 1998. doi: 10.2514/2.6354.

S. K. Wang. *Handbook of air conditioning and refrigeration*. McGraw-Hill New York, second edi edition, 2001. ISBN 0-07-068167-8. URL `http://www.academia.edu/download/34024926/Handbook_of_Air_Conditioning_and_Refrigeration.pdf`.

T. Wang, C. Sheng, and A. G. A. Nnanna. Experimental investigation of air conditioning system using evaporative cooling condenser. *Energy and Buildings*, 81:435–443, 2014. ISSN 03787788. doi: 10.1016/j.enbuild.2014.06.047. URL `http://dx.doi.org/10.1016/j.enbuild.2014.06.047`.

X. Wang, Y. Hwang, and R. Radermacher. Two-stage heat pump system with vapor-injected scroll compressor using R410A as a refrigerant. *International Journal of Refrigeration*, 32(6):1442–1451, 2009. ISSN 01407007. doi: 10.1016/j.ijrefrig.2009.03.004. URL `http://dx.doi.org/10.1016/j.ijrefrig.2009.03.004`.

D. Westphalen. Converting a Military Environmental Control Unit to Propylene Refrigerant. *International Refrigeration and Air Conditioning Conference at Purdue*, 2006. URL `http://docs.lib.purdue.edu/iracc/840`.

J. H. Wu, L. D. Yang, and J. Hou. Experimental performance study of a small wall room air conditioner retrofitted with R290 and R1270. *International Journal of Refrigeration*, 35(7):1860–1868, 2012a. ISSN 01407007. doi: 10.1016/j.ijrefrig.2012.06.004.

Y. Wu, X. Liang, X. Tu, and R. Zhuang. Study of R161 Refrigerant for Residential Air- conditioning Applications. *International Refrigeration and Air Conditioning Conference at Purdue*, pages 1–7, 2012b.

X. Xu, Y. Hwang, and R. Radermacher. Refrigerant injection for heat pumping/air conditioning systems: Literature review and challenges discussions. *International Journal of Refrigeration*, 34(2):402–415, 2011. ISSN 01407007. doi: 10.1016/j.ijrefrig.2010.09.015. URL `http://dx.doi.org/10.1016/j.ijrefrig.2010.09.015`.

M. Yamamura, S. Muramatsu, Y. Kojima, S. Yamamoto, S. Kawahara, and N. Ishi. Compact Type Scroll Compressor for Air Conditioners. *International Compressor Engineering Conference*, 1990.

B. Yang, T. N. Blatchley, C. K. Bach, J. E. Braun, and W. T. Horton. Application Of Oil Flooded Compression With Regeneration To A Packaged Heat Pump System. *International Refrigeration and Air Conditioning Conference at Purdue*, 2014.

D. A. Yashar, S. Lee, and P. A. Domanski. Rooftop air-conditioning unit performance improvement using refrigerant circuitry optimization. *Applied Thermal Engineering*, 83:81–87, 2015. ISSN 13594311. doi: 10.1016/j.applthermaleng.2015.03.012.

S. M. Zivi. Estimation of steady-state steam void-fraction by means of the principle of minimum entropy production. *Journal of Heat Transfer*, 86(2):247–251, 1964.

S. M. Zubair. Thermodynamics of a vapor-compression refrigeration cycle with mechanical subcooling. *Energy*, 19(6):707–715, 1994.

APPENDICES

APPENDIX A. CIRCUITRY SUPERHEAT TEMPERATURE MEASURED FOR BASELINE, MODIFIED AND INTERLEAVED EVAPORATOR CIRCUITRY

Table A.1. Superheat temperature across the circuitry of baseline evaporator at different testing conditions (±1.1°C).

Test No.		Circuit number						
	top	1	2	3	4	5	6	*bottom*
1		8.86	9.60	6.93	6.92	7.85	4.41	
2		10.71	11.80	8.45	9.23	9.46	3.86	
3		11.72	12.78	9.55	10.49	11.20	4.47	
4/A		9.90	11.01	7.94	8.53	9.58	5.36	
5		13.03	13.83	10.63	12.05	13.19	5.79	
6		13.04	13.92	10.69	12.20	13.21	5.44	
B		10.50	11.75	8.90	9.63	10.37	5.11	
C		13.20	14.25	10.89	12.27	13.18	5.13	

Table A.2. Superheat temperature across the circuitry of modified evaporator at different testing conditions (±1.1°C).

Test No.		Circuit number						
	top	1	2	3	4	5	6	*bottom*
1		9.84	10.30	7.94	3.03	1.36	2.71	
2		12.88	13.57	10.84	6.97	2.27	2.15	
3		13.55	14.22	11.51	7.43	5.02	2.75	
4/A		10.49	11.13	9.19	5.63	4.36	3.06	
5		10.49	11.13	9.19	5.63	4.36	3.06	
6		14.82	15.95	14.08	8.79	8.03	3.26	
B		11.68	12.25	10.24	6.21	5.72	3.32	
C		14.95	16.17	14.21	9.42	8.63	3.39	

Table A.3. Superheat temperature across the circuitry of interleaved evaporator at different testing conditions (±1.1°C).

Test No.		Circuit number						
	top	1	2	3	4	5	6	*bottom*
1		4.12	6.30	3.86	6.11	4.39	4.03	
2		3.47	4.57	3.59	5.44	4.20	3.20	
3		3.96	7.04	3.98	6.96	4.48	3.62	
4/A		4.67	7.15	4.39	6.91	5.12	4.41	
5		4.72	7.62	5.28	7.47	6.41	4.36	
6		4.75	8.67	5.46	8.46	7.30	4.37	
B		5.12	9.69	7.46	9.51	7.93	5.49	
C		4.94	9.73	7.60	9.76	7.80	4.62	

APPENDIX B. THERMODYNAMIC PROPERTIES MEASURED AND CALCULATED FOR BASELINE, MODIFIED AND INTERLEAVED EVAPORATOR CIRCUITRY

Table B.1. Thermodynamic properties measured and calculated at various state points for Test Condition 1.

Configuration	State	Pressure kPa	Temperature °C	Enthalpy kJ/kg	Entropy kJ/kg-K	Specific volume m^3/kg	Description
Baseline	1	625.3	25.75	430	1.822	0.04121	Compressor inlet
	2	3213	111.9	486.2	1.855	0.008957	Compressor outlet
	3	3213	110.2	484	1.849	0.008862	Condenser inlet
	4	3145	61.2	296.8	1.311	0.001052	Condenser outlet
	5	3097	61.19	296.8	1.311	0.001053	Expansion valve inlet
	6	990.4	20.4	296.8	1.332	0.009118	Expansion valve outlet
	7	655.6	7.122	296.8	1.345	0.01606	Evaporator inlet
	8	630.6	20.75	425	1.804	0.03977	Evaporator outlet
Modified	1	620.2	24.11	428.5	1.818	0.04125	Compressor inlet
	2	3225	110.5	484.3	1.849	0.008835	Compressor outlet
	3	3225	108.8	482.1	1.844	0.008739	Condenser inlet
	4	3158	60.18	294.7	1.304	0.001043	Condenser outlet
	5	3109	60.17	294.8	1.305	0.001044	Expansion valve inlet
	6	977.6	19.9	294.8	1.325	0.009048	Expansion valve outlet
	7	662.3	7.372	294.8	1.338	0.01551	Evaporator inlet
	8	625.6	18.84	423.3	1.799	0.03972	Evaporator outlet
Interleaved	1	660.6	19.01	422.6	1.792	0.03734	Compressor inlet
	2	3258	98.74	468.4	1.806	0.008021	Compressor outlet
	3	3258	97.48	466.7	1.802	0.007942	Condenser inlet
	4	3179	60.67	295.7	1.307	0.001046	Condenser outlet
	5	3118	60.65	295.7	1.308	0.001048	Expansion valve inlet
	6	1079	23.32	295.7	1.326	0.007904	Expansion valve outlet
	7	721.4	10.05	295.7	1.338	0.01399	Evaporator inlet
	8	669.2	15.56	419	1.779	0.03606	Evaporator outlet

Table B.2. Thermodynamic properties measured and calculated at various state points for Test Condition 2.

Configuration	State	Pressure kPa	Temperature °C	Enthalpy kJ/kg	Entropy kJ/kg-K	Specific volume m^3/kg	Description
Baseline	1	496.5	19.71	427	1.832	0.05178	Compressor inlet
	2	3001	112.5	489.5	1.868	0.009837	Compressor outlet
	3	3001	110.4	486.8	1.861	0.009715	Condenser inlet
	4	2950	56.01	287.2	1.282	0.001014	Condenser outlet
	5	2917	56	287.2	1.282	0.001015	Expansion valve inlet
	6	787.2	12.56	287.2	1.305	0.01121	Expansion valve outlet
	7	522	0.05578	287.2	1.319	0.01947	Evaporator inlet
	8	501	14.9	422.4	1.815	0.05006	Evaporator outlet
Modified	1	480.5	19.45	427.1	1.835	0.05363	Compressor inlet
	2	2980	113.8	491.2	1.873	0.009994	Compressor outlet
	3	2980	111.5	488.5	1.866	0.009868	Condenser inlet
	4	2932	54.79	285	1.276	0.001006	Condenser outlet
	5	2900	54.81	285	1.276	0.001007	Expansion valve inlet
	6	753.1	11.09	285	1.299	0.01161	Expansion valve outlet
	7	512.4	−0.5389	285	1.312	0.01948	Evaporator inlet
	8	484.7	14	421.9	1.816	0.05171	Evaporator outlet
Interleaved	1	569.5	14.45	420.4	1.797	0.04321	Compressor inlet
	2	3093	92.54	462.5	1.794	0.008242	Compressor outlet
	3	3093	91.34	460.9	1.79	0.008161	Condenser inlet
	4	3025	60.67	295.9	1.308	0.00105	Condenser outlet
	5	2974	60.54	295.8	1.308	0.001051	Expansion valve inlet
	6	975.2	19.85	295.8	1.329	0.009199	Expansion valve outlet
	7	629	5.828	295.8	1.343	0.01676	Evaporator inlet
	7	577.6	10.82	416.6	1.783	0.04166	Evaporator outlet

Table B.3. Thermodynamic properties measured and calculated at various state points for Test Condition 3.

Configuration	State	Pressure kPa	Temperature °C	Enthalpy kJ/kg	Entropy kJ/kg-K	Specific volume m^3/kg	Description
Baseline	1	460.4	18.99	427.1	1.839	0.05609	Compressor inlet
	2	2584	103.1	483.1	1.863	0.01131	Compressor outlet
	3	2584	100.9	480.5	1.856	0.01117	Condenser inlet
	4	2531	48.61	274.4	1.244	0.000973	Condenser outlet
	5	2501	48.61	274.4	1.244	0.0009735	Expansion valve inlet
	6	713.6	9.088	274.4	1.263	0.01086	Expansion valve outlet
	7	485.5	−2.39	274.4	1.274	0.01855	Evaporator inlet
	8	465	13.95	422.3	1.821	0.05414	Evaporator outlet
Modified	1	453.7	18.53	426.8	1.839	0.05688	Compressor inlet
	2	2560	102.8	483	1.863	0.01142	Compressor outlet
	3	2560	100.6	480.4	1.857	0.01128	Condenser inlet
	4	2508	47.98	273.3	1.241	0.0009697	Condenser outlet
	5	2479	47.98	273.3	1.241	0.0009701	Expansion valve inlet
	6	696.8	8.317	273.3	1.26	0.01107	Expansion valve outlet
	7	484.3	−2.495	273.3	1.27	0.01837	Evaporator inlet
	8	458.1	13.19	421.8	1.821	0.05483	Evaporator outlet
Interleaved	1	525.5	12.36	419.4	1.801	0.04682	Compressor inlet
	2	2692	85.91	460.2	1.798	0.009577	Compressor outlet
	3	2692	84.61	458.5	1.793	0.009482	Condenser inlet
	4	2622	53.17	282.4	1.269	0.001	Condenser outlet
	5	2577	53.04	282.2	1.268	0.001	Expansion valve inlet
	6	872.8	15.76	282.2	1.285	0.008998	Expansion valve outlet
	7	576.8	2.837	282.2	1.297	0.01617	Evaporator inlet
	8	533.2	8.868	415.9	1.787	0.04518	Evaporator outlet

Table B.4. Thermodynamic properties measured and calculated at various state points for Test Condition 4/A.

Configuration	State	Pressure kPa	Temperature °C	Enthalpy kJ/kg	Entropy kJ/kg-K	Specific volume m^3/kg	Description
Baseline	1	480	19.52	427.2	1.835	0.0537	Compressor inlet
	2	2251	91.41	473.6	1.848	0.01262	Compressor outlet
	3	2251	89.36	471.2	1.842	0.01248	Condenser inlet
	4	2183	43.28	265.6	1.218	0.0009482	Condenser outlet
	5	2152	43.23	265.5	1.218	0.0009484	Expansion valve inlet
	6	725.2	9.336	265.5	1.231	0.009224	Expansion valve outlet
	7	507.5	−1.383	265.5	1.24	0.01561	Evaporator inlet
	8	485.2	14.3	422.2	1.817	0.05172	Evaporator outlet
Modified	1	492	18.77	426.2	1.83	0.05206	Compressor inlet
	2	2255	89.72	471.5	1.842	0.01247	Compressor outlet
	3	2255	87.79	469.3	1.836	0.01233	Condenser inlet
	4	2184	43.41	265.8	1.218	0.0009489	Condenser outlet
	5	2150	43.39	265.8	1.218	0.0009492	Expansion valve inlet
	6	734.9	9.759	265.8	1.232	0.009075	Expansion valve outlet
	7	525.3	−0.3805	265.8	1.24	0.01493	Evaporator inlet
	8	497	13.73	421.4	1.812	0.05021	Evaporator outlet
Interleaved	1	535.9	12.67	419.5	1.799	0.04587	Compressor inlet
	2	2359	79.46	457.5	1.8	0.011	Compressor outlet
	3	2359	78.07	455.8	1.795	0.01089	Condenser inlet
	4	2274	46.35	270.7	1.234	0.0009635	Condenser outlet
	5	2231	46.28	270.6	1.233	0.0009637	Expansion valve inlet
	6	841.3	14.22	270.6	1.246	0.007938	Expansion valve outlet
	7	583.9	2.869	270.6	1.255	0.01375	Evaporator inlet
	8	543.4	9.573	416.3	1.787	0.04439	Evaporator outlet

Table B.5. Thermodynamic properties measured and calculated at various state points for Test Condition 5.

Configuration	State	Pressure kPa	Temperature °C	Enthalpy kJ/kg	Entropy kJ/kg-K	Specific volume m^3/kg	Description
Baseline	1	340.9	11.81	423.2	1.852	0.07521	Compressor inlet
	2	1799	84.93	472.3	1.862	0.01612	Compressor outlet
	3	1799	82.3	469.3	1.854	0.0159	Condenser inlet
	4	1750	33.21	249.4	1.167	0.0009064	Condenser outlet
	5	1732	33.14	249.3	1.167	0.0009063	Expansion valve inlet
	6	509.8	−1.719	249.3	1.181	0.0121	Expansion valve outlet
	7	361.5	−11.22	249.3	1.189	0.01992	Evaporator inlet
	8	345.6	7.627	419.4	1.837	0.07269	Evaporator outlet
Modified	1	366.5	14.06	424.6	1.851	0.07029	Compressor inlet
	2	1805	84.1	471.3	1.859	0.01598	Compressor outlet
	3	1805	81.63	468.5	1.851	0.01577	Condenser inlet
	4	1751	33.44	249.7	1.168	0.0009074	Condenser outlet
	5	1732	33.43	249.7	1.168	0.0009075	Expansion valve inlet
	6	533.9	−0.3683	249.7	1.181	0.01135	Expansion valve outlet
	7	391.4	−9.072	249.7	1.188	0.01795	Evaporator inlet
	8	371.1	8.894	419.9	1.833	0.0677	Evaporator outlet
Interleaved	1	422.2	7.064	417	1.811	0.05821	Compressor inlet
	2	1896	71.78	455.9	1.811	0.014	Compressor outlet
	3	1896	70.13	453.9	1.806	0.01385	Condenser inlet
	4	1824	36.62	254.8	1.184	0.0009202	Condenser outlet
	5	1797	36.5	254.6	1.184	0.0009199	Expansion valve inlet
	6	641.6	5.237	254.6	1.195	0.00926	Expansion valve outlet
	7	458.5	−4.579	254.6	1.203	0.01543	Evaporator inlet
	8	429	3.599	413.7	1.798	0.05616	Evaporator outlet

Table B.6. Thermodynamic properties measured and calculated at various state points for Test Condition 6.

Configuration	State	Pressure kPa	Temperature °C	Enthalpy kJ/kg	Entropy kJ/kg-K	Specific volume m^3/kg	Description
Baseline	1	349	14.02	425	1.856	0.07407	Compressor inlet
	2	1743	84.54	472.6	1.866	0.01671	Compressor outlet
	3	1743	82.22	470	1.859	0.01651	Condenser inlet
	4	1690	28.62	242.2	1.144	0.0008891	Condenser outlet
	5	1672	28.66	242.3	1.144	0.0008893	Expansion valve inlet
	6	500.7	−2.442	242.3	1.155	0.01094	Expansion valve outlet
	7	369.3	−10.85	242.3	1.162	0.01739	Evaporator inlet
	8	353.9	8.543	420	1.837	0.07115	Evaporator outlet
Modified	1	351.9	13.24	424.2	1.853	0.07316	Compressor inlet
	2	1724	82.7	470.8	1.862	0.01678	Compressor outlet
	3	1724	80.5	468.4	1.855	0.01659	Condenser inlet
	4	1669	28.5	242	1.143	0.0008888	Condenser outlet
	5	1651	28.6	242.2	1.144	0.0008892	Expansion valve inlet
	6	498.5	−2.567	242.2	1.155	0.011	Expansion valve outlet
	7	374.5	−10.48	242.2	1.161	0.01702	Evaporator inlet
	8	356.4	8.669	420.1	1.837	0.07064	Evaporator outlet
Interleaved	1	415.9	6.31	416.5	1.811	0.05896	Compressor inlet
	2	1862	69.96	454.3	1.808	0.01417	Compressor outlet
	3	1862	68.52	452.6	1.803	0.01404	Condenser inlet
	4	1788	33.68	250.1	1.169	0.0009081	Condenser outlet
	5	1761	33.57	250	1.169	0.0009078	Expansion valve inlet
	6	622.1	4.163	250	1.179	0.00891	Expansion valve outlet
	7	450.6	−5.202	250	1.186	0.01473	Evaporator inlet
	8	423	3.067	413.3	1.798	0.05689	Evaporator outlet

Table B.7. Thermodynamic properties measured and calculated at various state points for Test Condition B.

Configuration	State	Pressure kPa	Temperature °C	Enthalpy kJ/kg	Entropy kJ/kg-K	Specific volume m^3/kg	Description
Baseline	1	459	18.3	426.5	1.837	0.05609	Compressor inlet
	2	1815	79.44	465.9	1.844	0.01548	Compressor outlet
	3	1815	77.31	463.5	1.837	0.0153	Condenser inlet
	4	1733	34.00	250.6	1.171	0.0009098	Condenser outlet
	5	1705	33.95	250.6	1.171	0.0009098	Expansion valve inlet
	6	665.1	6.217	250.6	1.18	0.008055	Expansion valve outlet
	7	485.4	−3.085	250.6	1.186	0.01332	Evaporator inlet
	8	464.9	13.92	422.3	1.821	0.05415	Evaporator outlet
Modified	1	465.5	17.33	425.4	1.832	0.05497	Compressor inlet
	2	1819	77.88	464.1	1.838	0.0153	Compressor outlet
	3	1819	75.88	461.8	1.832	0.01513	Condenser inlet
	4	1736	34.39	251.3	1.173	0.0009114	Condenser outlet
	5	1706	34.39	251.3	1.173	0.0009117	Expansion valve inlet
	6	662.2	6.103	251.3	1.183	0.008235	Expansion valve outlet
	7	496.2	−2.439	251.3	1.189	0.01304	Evaporator inlet
	8	471.3	13.22	421.5	1.817	0.05314	Evaporator outlet
Interleaved	1	498.7	13.14	420.8	1.81	0.04987	Compressor inlet
	2	1908	73.56	457.8	1.816	0.01405	Compressor outlet
	3	1908	71.83	455.7	1.811	0.0139	Condenser inlet
	4	1816	35.56	253.1	1.179	0.0009157	Condenser outlet
	5	1781	35.53	253.1	1.179	0.0009159	Expansion valve inlet
	6	722.7	8.864	253.1	1.188	0.007346	Expansion valve outlet
	7	537.2	−0.09379	253.1	1.193	0.01191	Evaporator inlet
	8	506.1	8.617	416.4	1.793	0.04788	Evaporator outlet

Table B.8. Thermodynamic properties measured and calculated at various state points for Test Condition C.

Configuration	State	Pressure kPa	Temperature °C	Enthalpy kJ/kg	Entropy kJ/kg-K	Specific volume m^3/kg	Description
Baseline	1	366.5	15.55	426	1.855	0.07075	Compressor inlet
	2	1728	82.92	471	1.862	0.01675	Compressor outlet
	3	1728	80.35	468.1	1.854	0.01653	Condenser inlet
	4	1673	31.24	246.3	1.157	0.0008991	Condenser outlet
	5	1653	31.24	246.3	1.157	0.0008993	Expansion valve inlet
	6	531.9	−0.5821	246.3	1.169	0.01073	Expansion valve outlet
	7	387.7	−9.428	246.3	1.176	0.01728	Evaporator inlet
	8	370.9	9.896	420.8	1.836	0.06804	Evaporator outlet
Modified	1	362.6	14.94	425.5	1.855	0.07139	Compressor inlet
	2	1697	81.69	470.1	1.861	0.01701	Compressor outlet
	3	1697	79.11	467.2	1.853	0.01678	Condenser inlet
	4	1640	30.92	245.8	1.156	0.0008981	Condenser outlet
	5	1621	30.93	245.8	1.156	0.0008983	Expansion valve inlet
	6	520.6	−1.213	245.8	1.168	0.011	Expansion valve outlet
	7	386.9	−9.502	245.8	1.174	0.01721	Evaporator inlet
	8	367.3	10.13	421.1	1.838	0.06885	Evaporator outlet
Interleaved	1	424	7.876	417.7	1.813	0.05817	Compressor inlet
	2	1808	71.88	457.4	1.82	0.0149	Compressor outlet
	3	1808	70.09	455.3	1.814	0.01474	Condenser inlet
	4	1733	34.07	250.8	1.171	0.0009101	Condenser outlet
	5	1706	33.97	250.6	1.171	0.0009099	Expansion valve inlet
	6	626.7	4.407	250.6	1.181	0.008914	Expansion valve outlet
	7	458.2	−4.715	250.6	1.188	0.01452	Evaporator inlet
	8	430.5	4.036	414	1.799	0.05607	Evaporator outlet

APPENDIX C. PERFORMANCE TESTING RESULTS FOR BASELINE, MODIFIED AND INTERLEAVED EVAPORATOR CIRCUITRY

Table C.1. Performance testing results for baseline circuitry configuration at different testing conditions.

Test No.	$\dot{m}_r$ g/s	ϵ_{evap} –	$\dot{Q}_{evap}$ kW	$\dot{W}_{comp}$ kW	$\dot{E}_{tot}$ kW	COP$_{sys}$ –
1	143.3 ± 2.866	0.3 ± 0.0371	18.38 ± 0.46	9.096 ± 0.1125	10.75 ± 0.2	1.709 ± 0.04734
2	118.3 ± 2.366	0.379 ± 0.0468	16 ± 0.4	8.439 ± 0.1125	10.23 ± 0.2	1.564 ± 0.04332
3	113.5 ± 2.27	0.4 ± 0.0494	16.79 ± 0.42	7.221 ± 0.1125	9.025 ± 0.2	1.86 ± 0.05152
4/A	120.4 ± 2.408	0.397 ± 0.0490	18.86 ± 0.472	6.338 ± 0.1125	8.21 ± 0.2	2.298 ± 0.06365
5	92.92 ± 1.858	0.471 ± 0.0581	15.81 ± 0.395	5.115 ± 0.1125	7.018 ± 0.2	2.252 ± 0.06238
6	94.08 ± 1.882	0.498 ± 0.0614	16.72 ± 0.418	4.978 ± 0.1125	6.215 ± 0.2	2.691 ± 0.07454
B	117.8 ± 2.356	0.4363 ± 0.0538	20.24 ± 0.506	5.21 ± 0.1125	7.03 ± 0.2	2.879 ± 0.07975
C	97.09 ± 1.942	0.529 ± 0.0652	16.95 ± 0.424	4.947 ± 0.1125	6.824 ± 0.2	2.483 ± 0.06878

Table C.2. Performance testing results for modified circuitry configuration at different testing conditions.

Test No.	$\dot{m}_r$ g/s	ϵ_{evap} –	$\dot{Q}_{evap}$ kW	$\dot{W}_{comp}$ kW	$\dot{E}_{tot}$ kW	COP$_{sys}$ –
1	144.8 ± 2.896	0.302 ± 0.0373	18.6 ± 0.465	9.196 ± 0.1125	10.91 ± 0.2	1.705 ± 0.04722
2	115.4 ± 2.308	0.372 ± 0.0460	15.79 ± 0.395	8.441 ± 0.1125	10.21 ± 0.2	1.547 ± 0.04284
3	112.7 ± 2.254	0.399 ± 0.0492	16.73 ± 0.418	7.204 ± 0.1125	9.002 ± 0.2	1.858 ± 0.05148
4/A	124 ± 2.480	0.403 ± 0.0497	19.3 ± 0.483	6.382 ± 0.1125	8.195 ± 0.2	2.355 ± 0.06524
5	97.83 ± 1.957	0.496 ± 0.0613	16.65 ± 0.416	5.157 ± 0.1125	7.011 ± 0.2	2.375 ± 0.06578
6	95.11 ± 1.902	0.507 ± 0.0626	16.92 ± 0.423	4.944 ± 0.1125	6.14 ± 0.2	2.756 ± 0.07633
B	120.5 ± 2.410	0.428 ± 0.0528	20.51 ± 0.513	5.233 ± 0.1125	7.091 ± 0.2	2.892 ± 0.08012
C	97.55 ± 1.951	0.510 ± 0.0629	17.1 ± 0.428	4.889 ± 0.1125	6.782 ± 0.2	2.521 ± 0.06984

Table C.3. Performance testing results for interleaved circuitry configuration at different testing conditions.

Test No.	$\dot{m}_r$ g/s	ϵ_{evap} –	$\dot{Q}_{evap}$ kW	$\dot{W}_{comp}$ kW	$\dot{E}_{tot}$ kW	COP$_{sys}$ –
1	161.7 ± 3.234	0.322 ± 0.0397	19.93 ± 0.498	9.3 ± 0.1125	11.02 ± 0.2	1.808 ± 0.05008
2	146.6 ± 2.932	0.423 ± 0.0522	17.71 ± 0.443	8.722 ± 0.1125	10.51 ± 0.2	1.685 ± 0.04667
3	138.2 ± 2.764	0.446 ± 0.0550	18.47 ± 0.462	7.552 ± 0.1125	9.321 ± 0.2	1.982 ± 0.05490
4/A	140.3 ± 2.806	0.432 ± 0.0534	20.43 ± 0.511	6.677 ± 0.1125	8.508 ± 0.2	2.402 ± 0.06654
5	115.9 ± 2.318	0.561 ± 0.0692	18.43 ± 0.461	5.439 ± 0.1125	7.296 ± 0.2	2.526 ± 0.06997
6	115.3 ± 2.306	0.571 ± 0.0704	18.83 ± 0.471	5.35 ± 0.1125	6.562 ± 0.2	2.87 ± 0.07950
B	130.6 ± 2.612	0.453 ± 0.0558	21.32 ± 0.533	5.488 ± 0.1125	7.336 ± 0.2	2.907 ± 0.08052
C	115.2 ± 2.304	0.571 ± 0.0705	18.82 ± 0.471	5.257 ± 0.1125	7.106 ± 0.2	2.649 ± 0.07338

APPENDIX D. THERMODYNAMIC PROPERTIES MEASURED AND CALCULATED FOR BASELINE, SUPERHEATED AND SATURATED VAPOR INJECTION WITH ECONOMIZATION

Table D.1. Thermodynamic properties measured and calculated at various state points for Test Condition 1.

Configuration	State	Pressure kPa	Temperature °C	Enthalpy kJ/kg	Entropy kJ/kg-K	Specific volume m^3/kg	Description
Baseline (no-injection)	1	769.4	21.87	422.9	1.781	0.03173	Compressor inlet
	2	3303	106.9	478.6	1.833	0.008348	Compressor outlet
	3	3303	105.2	476.3	1.827	0.008247	Condenser inlet
	4	3272	52.41	280.3	1.26	0.000985	Condenser outlet
	5	3174	52.61	280.8	1.262	0.0009876	TXV inlet
	6	955.2	18.71	280.8	1.278	0.007657	TXV outlet
	7	800	12.89	280.8	1.282	0.01004	Evaporator inlet
	8	776.4	21.91	422.8	1.779	0.03139	Evaporator outlet
	9	3257	52.47	280.5	1.261	0.0009856	PHX inlet
	10	3257	52.18	279.9	1.259	0.0009838	PHX outlet
	11	-	-	-	-	-	EXV inlet
	12	-	-	-	-	-	Compressor injection
Superheated ($T_{sup} = 7$°C)	1	747.4	20.87	422.4	1.781	0.03265	Compressor inlet
	2	3231	105.8	478.1	1.833	0.008542	Compressor outlet
	3	3231	104.2	476.1	1.828	0.008453	Condenser inlet
	4	3184	55.13	285.3	1.276	0.001004	Condenser outlet
	5	3090	36.13	253.6	1.177	0.0009081	TXV inlet
	6	861.1	14.48	253.6	1.186	0.005375	TXV outlet
	7	770	10.88	253.6	1.188	0.006633	Evaporator inlet
	8	753.4	21.07	422.5	1.781	0.03237	Evaporator outlet
	9	3164	55.16	285.3	1.276	0.001004	PHX inlet
	10	3149	35.28	252.2	1.172	0.0009043	PHX outlet
	11	3149	35.37	252.3	1.172	0.0009046	EXV inlet
	12	1338	41.64	431.4	1.764	0.01808	Compressor injection
Saturated ($T_{sup} = 0$°C)	1	746.7	20.66	422.2	1.781	0.03264	Compressor inlet
	2	3176	102.8	474.9	1.826	0.008572	Compressor outlet
	3	3176	101.3	473.1	1.821	0.008485	Condenser inlet
	4	3120	57.81	290.3	1.291	0.001024	Condenser outlet
	5	3024	36.37	254	1.178	0.0009095	TXV inlet
	6	862.3	14.54	254	1.188	0.005412	TXV outlet
	7	770.8	10.92	254	1.19	0.006678	Evaporator inlet
	8	753.2	20.67	422.1	1.779	0.03231	Evaporator outlet
	9	3099	57.75	290.2	1.291	0.001024	PHX inlet
	10	3099	35.41	252.4	1.173	0.0009052	PHX outlet
	11	3099	35.61	252.7	1.174	0.000906	EXV inlet
	12	1428	37.14	423.8	1.735	0.01596	Compressor injection

Table D.2. Thermodynamic properties measured and calculated at various state points for Test Condition 2.

Configuration	State	Pressure kPa	Temperature °C	Enthalpy kJ/kg	Entropy kJ/kg-K	Specific volume m^3/kg	Description
Baseline (no-injection)	1	661.8	18.55	422.2	1.79	0.03717	Compressor inlet
	2	2873	101.2	477.1	1.839	0.009733	Compressor outlet
	3	2873	99.21	474.6	1.832	0.009607	Condenser inlet
	4	2846	46.99	271.4	1.234	0.0009599	Condenser outlet
	5	2773	47.13	271.7	1.235	0.0009616	TXV inlet
	6	815.3	13.24	271.7	1.25	0.008491	TXV outlet
	7	687.7	7.86	271.7	1.254	0.01101	Evaporator inlet
	8	667.9	18.5	422	1.789	0.03676	Evaporator outlet
	9	2833	47.02	271.4	1.234	0.0009602	PHX inlet
	10	2833	46.78	271	1.233	0.000959	PHX outlet
	11	-	-	-	-	-	EXV inlet
	12	-	-	-	-	-	Compressor injection
Superheated ($T_{sup} = 7$°C)	1	630.4	16.76	421.1	1.791	0.03893	Compressor inlet
	2	2783	99.55	476.2	1.839	0.01005	Compressor outlet
	3	2783	97.76	474	1.833	0.009934	Condenser inlet
	4	2740	50.03	276.7	1.251	0.0009784	Condenser outlet
	5	2673	28.46	241.8	1.139	0.0008824	TXV inlet
	6	718.4	8.346	241.8	1.148	0.005664	TXV outlet
	7	648.9	5.206	241.8	1.149	0.006903	Evaporator inlet
	8	635.6	16.62	420.9	1.789	0.03853	Evaporator outlet
	9	2725	49.91	276.5	1.25	0.0009779	PHX inlet
	10	2717	27.25	239.9	1.133	0.000878	PHX outlet
	11	2717	27.48	240.3	1.134	0.0008788	EXV inlet
	12	1150	36.18	429.4	1.77	0.02118	Compressor injection
Saturated ($T_{sup} = 0$°C)	1	626.8	16.82	421.3	1.792	0.03921	Compressor inlet
	2	2738	96.28	472.8	1.831	0.01006	Compressor outlet
	3	2738	94.63	470.7	1.825	0.009954	Condenser inlet
	4	2689	52.15	280.5	1.263	0.0009925	Condenser outlet
	5	2620	29.16	242.8	1.143	0.0008852	TXV inlet
	6	718.5	8.382	242.8	1.152	0.00583	TXV outlet
	7	646.6	5.128	242.8	1.153	0.007134	Evaporator inlet
	8	632.6	16.71	421	1.79	0.03876	Evaporator outlet
	9	2673	52.06	280.3	1.262	0.0009921	PHX inlet
	10	2673	28.06	241.2	1.137	0.000881	PHX outlet
	11	2673	28.31	241.5	1.138	0.0008819	EXV inlet
	12	1206	30.93	422	1.742	0.01916	Compressor injection

Table D.3. Thermodynamic properties measured and calculated at various state points for Test Condition 3.

Configuration	State	Pressure kPa	Temperature °C	Enthalpy kJ/kg	Entropy kJ/kg-K	Specific volume m^3/kg	Description
Baseline (no-injection)	1	648.7	17.71	421.6	1.79	0.03786	Compressor inlet
	2	2487	91.06	469.9	1.83	0.01107	Compressor outlet
	3	2487	89.12	467.5	1.824	0.01093	Condenser inlet
	4	2453	42.4	263.9	1.212	0.000941	Condenser outlet
	5	2382	42.53	264.2	1.213	0.0009424	TXV inlet
	6	790	12.01	264.2	1.225	0.007853	TXV outlet
	7	674.1	7.028	264.2	1.228	0.01011	Evaporator inlet
	8	655.3	17.4	421.2	1.788	0.03736	Evaporator outlet
	9	2442	42.2	263.6	1.211	0.0009401	PHX inlet
	10	2442	42.01	263.3	1.21	0.0009392	PHX outlet
	11	-	-	-	-	-	EXV inlet
	12	-	-	-	-	-	Compressor injection
Superheated (T_{sup} = 7°C)	1	615.6	16.51	421.2	1.793	0.03996	Compressor inlet
	2	2457	91.66	471	1.834	0.01129	Compressor outlet
	3	2457	89.85	468.8	1.828	0.01116	Condenser inlet
	4	2409	45.25	268.7	1.227	0.0009559	Condenser outlet
	5	2343	25.43	237.2	1.125	0.000874	TXV inlet
	6	697.8	7.31	237.2	1.132	0.005273	TXV outlet
	7	633.9	4.363	237.2	1.133	0.006418	Evaporator inlet
	8	620.6	16.4	421	1.792	0.03957	Evaporator outlet
	9	2395	45.1	268.5	1.226	0.0009553	PHX inlet
	10	2389	24.24	235.4	1.119	0.0008698	PHX outlet
	11	2389	24.53	235.8	1.12	0.0008707	EXV inlet
	12	1079	33.93	428.5	1.772	0.02262	Compressor injection
Saturated (T_{sup} = 0°C)	1	613.6	16.54	421.3	1.794	0.04012	Compressor inlet
	2	2434	89.69	469	1.829	0.01129	Compressor outlet
	3	2434	87.97	466.9	1.824	0.01117	Condenser inlet
	4	2381	47.11	271.9	1.237	0.0009664	Condenser outlet
	5	2315	26.04	238.1	1.128	0.0008762	TXV inlet
	6	698.6	7.372	238.1	1.135	0.005409	TXV outlet
	7	633.4	4.365	238.1	1.137	0.00659	Evaporator inlet
	8	619.5	16.34	421	1.792	0.03963	Evaporator outlet
	9	2367	46.86	271.5	1.236	0.0009652	PHX inlet
	10	2367	24.83	236.3	1.122	0.0008719	PHX outlet
	11	2367	25.09	236.7	1.123	0.0008727	EXV inlet
	12	1118	28.23	421.2	1.745	0.02076	Compressor injection

Table D.4. Thermodynamic properties measured and calculated at various state points for Test Condition 4/A.

Configuration	State	Pressure kPa	Temperature °C	Enthalpy kJ/kg	Entropy kJ/kg-K	Specific volume m^3/kg	Description
Baseline (no-injection)	1	645.3	17.28	421.3	1.79	0.038	Compressor inlet
	2	2207	83.1	464.4	1.824	0.01233	Compressor outlet
	3	2207	81.17	462.1	1.818	0.01218	Condenser inlet
	4	2168	37.18	255.6	1.186	0.0009197	Condenser outlet
	5	2098	37.3	255.8	1.187	0.0009208	TXV inlet
	6	773.9	11.1	255.8	1.196	0.006895	TXV outlet
	7	670.3	6.606	255.8	1.199	0.008811	Evaporator inlet
	8	652	16.83	420.7	1.787	0.03745	Evaporator outlet
	9	2158	36.84	255	1.184	0.0009183	PHX inlet
	10	2158	36.68	254.8	1.183	0.0009177	PHX outlet
	11	-	-	-	-	-	EXV inlet
	12	-	-	-	-	-	Compressor injection
Superheated ($T_{sup} = 7$°C)	1	628.4	16.37	420.8	1.79	0.03899	Compressor inlet
	2	2185	83.49	465.2	1.827	0.01252	Compressor outlet
	3	2185	81.69	463	1.821	0.01238	Condenser inlet
	4	2130	39.6	259.5	1.199	0.0009309	Condenser outlet
	5	2063	23.3	234	1.115	0.0008684	TXV inlet
	6	708.3	7.682	234	1.121	0.004605	TXV outlet
	7	647.7	4.925	234	1.122	0.005606	Evaporator inlet
	8	634.5	16.18	420.5	1.788	0.03852	Evaporator outlet
	9	2118	39.36	259.1	1.197	0.0009299	PHX inlet
	10	2119	22.2	232.4	1.109	0.0008646	PHX outlet
	11	2119	22.53	232.9	1.111	0.0008657	EXV inlet
	12	1037	32.57	428	1.773	0.02356	Compressor injection
Saturated ($T_{sup} = 0$°C)	1	624.4	17.08	421.6	1.793	0.03944	Compressor inlet
	2	2151	81.99	463.9	1.825	0.01266	Compressor outlet
	3	2151	80.22	461.8	1.819	0.01252	Condenser inlet
	4	2092	41.25	262.2	1.207	0.0009391	Condenser outlet
	5	2025	23.86	234.9	1.118	0.0008705	TXV inlet
	6	706.5	7.628	234.9	1.124	0.004766	TXV outlet
	7	645	4.824	234.9	1.125	0.005801	Evaporator inlet
	8	630.8	16.68	421.1	1.791	0.03889	Evaporator outlet
	9	2080	40.8	261.5	1.205	0.000937	PHX inlet
	10	2080	22.63	233	1.112	0.0008662	PHX outlet
	11	2080	22.9	233.4	1.113	0.0008671	EXV inlet
	12	1061	26.4	420.5	1.747	0.02193	Compressor injection

Table D.5. Thermodynamic properties measured and calculated at various state points for Test Condition 5.

Configuration	State	Pressure kPa	Temperature °C	Enthalpy kJ/kg	Entropy kJ/kg-K	Specific volume m^3/kg	Description
Baseline (no-injection)	1	555.5	14.71	420.9	1.801	0.04452	Compressor inlet
	2	1867	77.72	463.2	1.834	0.0148	Compressor outlet
	3	1867	75.47	460.6	1.826	0.01461	Condenser inlet
	4	1831	31.95	247.4	1.16	0.0009008	Condenser outlet
	5	1781	32.03	247.5	1.161	0.0009015	TXV inlet
	6	659.5	5.868	247.5	1.169	0.00766	TXV outlet
	7	577	1.845	247.5	1.172	0.009618	Evaporator inlet
	8	561.8	14.18	420.3	1.798	0.04382	Evaporator outlet
	9	1825	31.45	246.6	1.158	0.0008989	PHX inlet
	10	1825	31.33	246.4	1.157	0.0008984	PHX outlet
	11	-	-	-	-	-	EXV inlet
	12	-	-	-	-	-	Compressor injection
Superheated ($T_{sup} = 7$°C)	1	532.7	13.07	419.9	1.801	0.04628	Compressor inlet
	2	1844	77.62	463.4	1.835	0.01502	Compressor outlet
	3	1844	75.52	461	1.828	0.01484	Condenser inlet
	4	1797	33.82	250.3	1.17	0.0009085	Condenser outlet
	5	1750	17.11	224.8	1.085	0.0008507	TXV inlet
	6	594.6	2.081	224.8	1.089	0.004981	TXV outlet
	7	548.3	-0.3157	224.8	1.09	0.005977	Evaporator inlet
	8	537.5	12.88	419.6	1.799	0.04576	Evaporator outlet
	9	1789	33.56	249.9	1.169	0.0009076	PHX inlet
	10	1788	15.89	223	1.078	0.0008469	PHX outlet
	11	1788	16.3	223.6	1.08	0.0008481	EXV inlet
	12	873.6	26.76	425.6	1.779	0.02805	Compressor injection
Saturated ($T_{sup} = 0$°C)	1	530.3	13.63	420.5	1.804	0.04665	Compressor inlet
	2	1827	76.73	462.7	1.834	0.01512	Compressor outlet
	3	1827	74.65	460.3	1.827	0.01494	Condenser inlet
	4	1775	34.97	252.2	1.176	0.0009135	Condenser outlet
	5	1728	17.42	225.3	1.086	0.0008517	TXV inlet
	6	595	2.113	225.3	1.091	0.005059	TXV outlet
	7	547.9	-0.3254	225.3	1.092	0.006079	Evaporator inlet
	8	536.3	13.18	419.9	1.801	0.04595	Evaporator outlet
	9	1768	34.53	251.5	1.174	0.0009117	PHX inlet
	10	1768	16.13	223.4	1.08	0.0008477	PHX outlet
	11	1768	16.5	223.9	1.081	0.0008488	EXV inlet
	12	898.8	20.71	418.5	1.753	0.02606	Compressor injection

Table D.6. Thermodynamic properties measured and calculated at various state points for Test Condition 6.

Configuration	State	Pressure kPa	Temperature °C	Enthalpy kJ/kg	Entropy kJ/kg-K	Specific volume m^3/kg	Description
Baseline (no-injection)	1	559.9	13.92	420.1	1.798	0.04393	Compressor inlet
	2	1856	76.19	461.6	1.83	0.01479	Compressor outlet
	3	1856	74.29	459.4	1.823	0.01462	Condenser inlet
	4	1816	28.2	241.5	1.141	0.0008867	Condenser outlet
	5	1766	28.32	241.7	1.142	0.0008875	TXV inlet
	6	655.3	5.504	241.7	1.149	0.006771	TXV outlet
	7	580.7	1.866	241.7	1.151	0.008434	Evaporator inlet
	8	566.6	13.52	419.5	1.795	0.04324	Evaporator outlet
	9	1811	27.92	241.1	1.139	0.0008857	PHX inlet
	10	1811	27.89	241	1.139	0.0008856	PHX outlet
	11	-	-	-	-	-	EXV inlet
	12	-	-	-	-	-	Compressor injection
Superheated ($T_{sup} = 7$°C)	1	540.5	13.42	420.1	1.8	0.04561	Compressor inlet
	2	1846	77.63	463.4	1.835	0.01501	Compressor outlet
	3	1846	75.8	461.3	1.829	0.01485	Condenser inlet
	4	1796	31.1	246	1.156	0.0008977	Condenser outlet
	5	1749	16.25	223.5	1.08	0.0008481	TXV inlet
	6	600.3	2.329	223.5	1.085	0.00464	TXV outlet
	7	556.2	0.06918	223.5	1.085	0.005546	Evaporator inlet
	8	546	13.09	419.6	1.798	0.045	Evaporator outlet
	9	1789	30.68	245.4	1.154	0.0008962	PHX inlet
	10	1787	15.12	221.9	1.074	0.0008446	PHX outlet
	11	1787	15.48	222.4	1.076	0.0008457	EXV inlet
	12	860	26.2	425.3	1.779	0.02849	Compressor injection
Saturated ($T_{sup} = 0$°C)	1	533.9	15.28	422	1.808	0.0467	Compressor inlet
	2	1822	78.03	464.2	1.839	0.01529	Compressor outlet
	3	1822	76.14	462.1	1.832	0.01513	Condenser inlet
	4	1769	31.93	247.3	1.16	0.0009011	Condenser outlet
	5	1724	16.28	223.6	1.08	0.0008483	TXV inlet
	6	595	2.065	223.6	1.085	0.004748	TXV outlet
	7	550.6	-0.2287	223.6	1.086	0.005682	Evaporator inlet
	8	540.2	14.81	421.4	1.805	0.04597	Evaporator outlet
	9	1763	31.42	246.5	1.158	0.0008992	PHX inlet
	10	1763	15.1	221.8	1.074	0.0008447	PHX outlet
	11	1763	15.46	222.4	1.076	0.0008457	EXV inlet
	12	875.6	19.84	418.2	1.754	0.02677	Compressor injection

Table D.7. Thermodynamic properties measured and calculated at various state points for Test Condition B.

Configuration	State	Pressure kPa	Temperature °C	Enthalpy kJ/kg	Entropy kJ/kg-K	Specific volume m^3/kg	Description
Baseline (no-injection)	1	620.2	18.51	423.1	1.799	0.04006	Compressor inlet
	2	1854	76.05	461.5	1.829	0.01479	Compressor outlet
	3	1854	73.96	459.1	1.822	0.01461	Condenser inlet
	4	1809	30.34	244.8	1.152	0.0008947	Condenser outlet
	5	1747	30.51	245.1	1.153	0.0008958	TXV inlet
	6	725.5	8.753	245.1	1.16	0.006072	TXV outlet
	7	644	5.076	245.1	1.161	0.007578	Evaporator inlet
	8	627.7	18.14	422.6	1.796	0.03942	Evaporator outlet
	9	1802	29.99	244.3	1.15	0.0008934	PHX inlet
	10	1802	29.91	244.2	1.15	0.0008931	PHX outlet
	11	-	-	-	-	-	EXV inlet
	12	-	-	-	-	-	Compressor injection
Superheated (T_{sup} = 7°C)	1	613.5	17.03	421.8	1.796	0.04023	Compressor inlet
	2	1848	75.56	461	1.828	0.0148	Compressor outlet
	3	1848	73.66	458.8	1.822	0.01464	Condenser inlet
	4	1789	32.61	248.4	1.164	0.0009037	Condenser outlet
	5	1726	20.02	229.1	1.099	0.0008597	TXV inlet
	6	685.3	6.513	229.1	1.104	0.004169	TXV outlet
	7	633.4	4.105	229.1	1.104	0.005025	Evaporator inlet
	8	619.9	17.02	421.6	1.794	0.03975	Evaporator outlet
	9	1779	32.39	248.1	1.163	0.0009029	PHX inlet
	10	1780	19.07	227.7	1.094	0.0008565	PHX outlet
	11	1780	19.45	228.3	1.096	0.0008576	EXV inlet
	12	953.3	29.68	426.8	1.776	0.02567	Compressor injection
Saturated (T_{sup} = 0°C)	1	614.4	16.71	421.5	1.794	0.0401	Compressor inlet
	2	1822	73.75	459.3	1.825	0.01492	Compressor outlet
	3	1822	71.89	457.2	1.818	0.01476	Condenser inlet
	4	1756	34.6	251.6	1.174	0.0009121	Condenser outlet
	5	1692	20.68	230.1	1.103	0.0008619	TXV inlet
	6	689.3	6.724	230.1	1.107	0.004267	TXV outlet
	7	636	4.256	230.1	1.108	0.005149	Evaporator inlet
	8	621.7	16.38	421	1.792	0.03948	Evaporator outlet
	9	1746	34.12	250.8	1.172	0.0009102	PHX inlet
	10	1746	19.61	228.5	1.097	0.0008583	PHX outlet
	11	1746	19.95	229	1.099	0.0008593	EXV inlet
	12	987.8	23.92	419.7	1.749	0.02364	Compressor injection

Table D.8. Thermodynamic properties measured and calculated at various state points for Test Condition C.

Configuration	State	Pressure kPa	Temperature °C	Enthalpy kJ/kg	Entropy kJ/kg-K	Specific volume m^3/kg	Description
Baseline (no-injection)	1	577.7	15.33	421	1.798	0.04271	Compressor inlet
	2	1810	74.72	460.6	1.829	0.01513	Compressor outlet
	3	1810	72.56	458.2	1.822	0.01494	Condenser inlet
	4	1768	30.56	245.2	1.153	0.0008958	Condenser outlet
	5	1714	30.63	245.3	1.154	0.0008965	TXV inlet
	6	681.1	6.798	245.3	1.161	0.006875	TXV outlet
	7	600	2.946	245.3	1.163	0.008616	Evaporator inlet
	8	584.8	14.87	420.4	1.795	0.04201	Evaporator outlet
	9	1762	30.14	244.5	1.151	0.0008943	PHX inlet
	10	1762	30.05	244.4	1.151	0.000894	PHX outlet
	11	-	-	-	-	-	EXV inlet
	12	-	-	-	-	-	Compressor injection
Superheated ($T_{sup} = 7$°C)	1	560.2	13.93	420.1	1.797	0.0439	Compressor inlet
	2	1780	74.65	461	1.831	0.01544	Compressor outlet
	3	1780	72.67	458.8	1.825	0.01527	Condenser inlet
	4	1726	32.95	249	1.166	0.0009055	Condenser outlet
	5	1673	17.88	225.9	1.089	0.0008533	TXV inlet
	6	624.2	3.571	225.9	1.093	0.004632	TXV outlet
	7	576.9	1.214	225.9	1.094	0.005555	Evaporator inlet
	8	565.2	13.92	420	1.796	0.04346	Evaporator outlet
	9	1717	32.73	248.6	1.165	0.0009047	PHX inlet
	10	1715	16.84	224.4	1.083	0.00085	PHX outlet
	11	1715	17.21	225	1.085	0.0008511	EXV inlet
	12	897	27.59	425.9	1.778	0.02728	Compressor injection
Saturated ($T_{sup} = 0$°C)	1	549.8	15.83	422.1	1.806	0.04531	Compressor inlet
	2	1765	75.28	461.9	1.835	0.01566	Compressor outlet
	3	1765	73.21	459.6	1.828	0.01548	Condenser inlet
	4	1709	33.58	250	1.169	0.0009083	Condenser outlet
	5	1659	17.82	225.9	1.088	0.0008532	TXV inlet
	6	615.8	3.159	225.9	1.093	0.004771	TXV outlet
	7	568.3	0.7673	225.9	1.094	0.005727	Evaporator inlet
	8	556.4	15.4	421.6	1.803	0.0446	Evaporator outlet
	9	1702	33.1	249.2	1.167	0.0009064	PHX inlet
	10	1702	16.58	224	1.082	0.0008493	PHX outlet
	11	1702	16.95	224.6	1.084	0.0008504	EXV inlet
	12	907.3	21.03	418.6	1.752	0.02581	Compressor injection

APPENDIX E. PERFORMANCE TESTING RESULTS FOR BASELINE, SUPERHEATED AND SATURATED VAPOR INJECTION WITH ECONOMIZATION

Table E.1. Performance testing results for baseline (no-injection) economized vapor injection (EVI) at different testing conditions.

Test No.	$\dot{m}_{tot}$ g/s	$\dot{m}_{suc}$ g/s	T_{dis} °C	$\dot{Q}_{cond}$ kW	$\dot{Q}_{econ}$ kW	$\dot{Q}_{evap}$ kW	$\dot{W}_{comp}$ kW	$\dot{E}_{tot}$ kW	η_v %	η_{is} %	COP$_{sys}$ –
1	–	110.7 ± 2.213	106.9 ± 1.1	22.13 ± 0.5197	–	15.72 ± 0.4005	6.555 ± 0.1125	8.324 ± 0.2	87.09 ± 1.842	61.13 ± 1.679	1.888 ± 0.06614
2	–	96.31 ± 1.926	101.2 ± 1.1	19.93 ± 0.4591	–	14.48 ± 0.3568	5.612 ± 0.1125	7.465 ± 0.2	88.8 ± 1.871	63.67 ± 1.862	1.939 ± 0.0706
3	–	96.7 ± 1.934	91.06 ± 1.1	20.02 ± 0.4583	–	15.18 ± 0.3667	4.924 ± 0.1125	6.754 ± 0.2	90.81 ± 1.914	66.61 ± 2.081	2.248 ± 0.08591
4/A	–	97.94 ± 1.959	83.1 ± 1.1	20.52 ± 0.4657	–	16.15 ± 0.382	4.462 ± 0.1125	6.292 ± 0.2	92.33 ± 1.946	67.97 ± 2.245	2.567 ± 0.1017
5	–	84.98 ± 1.7	77.72 ± 1.1	18.34 ± 0.4105	–	14.68 ± 0.3405	3.824 ± 0.1125	5.73 ± 0.2	93.85 ± 1.974	68.84 ± 2.5	2.562 ± 0.1074
6	–	86.28 ± 1.726	76.19 ± 1.1	19 ± 0.4225	–	15.34 ± 0.3522	3.81 ± 0.1125	5.058 ± 0.2	94.03 ± 1.98	68.92 ± 2.51	3.033 ± 0.1387
B	–	94.71 ± 1.894	76.05 ± 1.1	20.53 ± 0.4587	–	16.8 ± 0.3871	3.901 ± 0.1125	5.769 ± 0.2	94.11 ± 1.979	67.91 ± 2.436	2.913 ± 0.1213
C	–	88.9 ± 1.778	74.72 ± 1.1	19.14 ± 0.4281	–	15.56 ± 0.3595	3.769 ± 0.1125	5.677 ± 0.2	94.19 ± 1.982	68.5 ± 2.513	2.741 ± 0.1155

Table E.2. Performance testing results for superheated (T_{sup} = 7°C) economized vapor injection (EVI) at different testing conditions.

Test No.	$\dot{m}_{tot}$ g/s	$\dot{m}_{suc}$ g/s	T_{dis} °C	$\dot{Q}_{cond}$ kW	$\dot{Q}_{econ}$ kW	$\dot{Q}_{evap}$ kW	$\dot{W}_{comp}$ kW	$\dot{E}_{tot}$ kW	η_v %	η_{is} %	COP$_{sys}$ –
1	131.4 ± 2.628	104.9 ± 2.098	105.8 ± 1.1	25.08 ± 0.5962	4.357 ± 0.3567	17.72 ± 0.4153	7.353 ± 0.1125	9.097 ± 0.2	84.93 ± 1.796	59.62 ± 1.347	1.948 ± 0.0626
2	113.4 ± 2.268	89.67 ± 1.793	99.55 ± 1.1	22.38 ± 0.5217	4.146 ± 0.3004	16.06 ± 0.3679	6.286 ± 0.1125	8.042 ± 0.2	86.63 ± 1.825	61.7 ± 1.499	1.997 ± 0.06753
3	110.4 ± 2.208	89.74 ± 1.795	91.66 ± 1.1	22.08 ± 0.5094	3.652 ± 0.2847	16.5 ± 0.3749	5.544 ± 0.1125	7.374 ± 0.2	88.94 ± 1.874	64.31 ± 1.677	2.237 ± 0.07917
4/A	110.6 ± 2.212	93.89 ± 1.878	83.49 ± 1.1	22.5 ± 0.5134	2.957 ± 0.2762	17.51 ± 0.3964	4.969 ± 0.1125	6.795 ± 0.2	90.79 ± 1.914	65.45 ± 1.83	2.576 ± 0.09569
5	94.19 ± 1.884	80.51 ± 1.61	77.62 ± 1.1	19.85 ± 0.4458	2.535 ± 0.2299	15.69 ± 0.3502	4.205 ± 0.1125	6.076 ± 0.2	92.45 ± 1.945	66.73 ± 2.091	2.581 ± 0.1027
6	93.85 ± 1.877	82.06 ± 1.641	77.63 ± 1.1	20.2 ± 0.451	2.207 ± 0.2256	16.09 ± 0.3588	4.16 ± 0.1125	5.391 ± 0.2	92.87 ± 1.954	67.17 ± 2.123	2.985 ± 0.1292
B	105.1 ± 2.102	93.11 ± 1.862	75.56 ± 1.1	22.12 ± 0.4968	2.141 ± 0.2543	17.92 ± 0.4024	4.274 ± 0.1125	6.125 ± 0.2	92.9 ± 1.956	65.56 ± 2.031	2.927 ± 0.116
C	97.89 ± 1.958	84.94 ± 1.699	74.65 ± 1.1	20.54 ± 0.4614	2.371 ± 0.2378	16.48 ± 0.3686	4.129 ± 0.1125	6.033 ± 0.2	92.51 ± 1.948	65.69 ± 2.087	2.732 ± 0.1093

Table E.3. Performance testing results for saturated (T_{sup} = 0°C) economized vapor injection (EVI) at different testing conditions.

Test No.	$\dot{m}_{tot}$ g/s	$\dot{m}_{suc}$ g/s	T_{dis} °C	$\dot{Q}_{cond}$ kW	$\dot{Q}_{econ}$ kW	$\dot{Q}_{evap}$ kW	$\dot{W}_{comp}$ kW	$\dot{E}_{tot}$ kW	η_v %	η_{is} %	COP$_{sys}$ –
1	137.3 ± 2.746	104.5 ± 2.09	102.8 ± 1.1	25.09 ± 0.6097	5.189 ± 0.3838	17.57 ± 0.4125	7.517 ± 0.1125	9.253 ± 0.2	84.62 ± 1.789	57.5 ± 1.292	1.899 ± 0.0606
2	117.4 ± 2.348	89.57 ± 1.791	96.28 ± 1.1	22.33 ± 0.5285	4.6 ± 0.3173	15.96 ± 0.3662	6.316 ± 0.1125	8.121 ± 0.2	87.12 ± 1.835	60.83 ± 1.734	1.965 ± 0.06616
3	113.0 ± 2.26	89.56 ± 1.791	89.69 ± 1.1	22.02 ± 0.513	3.978 ± 0.2954	16.38 ± 0.3728	5.583 ± 0.1125	7.398 ± 0.2	89.12 ± 1.877	63.33 ± 1.694	2.214 ± 0.07824
4/A	112.2 ± 2.244	93.34 ± 1.867	81.99 ± 1.1	22.39 ± 0.514	3.197 ± 0.2829	17.38 ± 0.3938	4.958 ± 0.1125	6.762 ± 0.2	91.31 ± 1.923	64.85 ± 1.952	2.57 ± 0.09577
5	95.23 ± 1.905	80.26 ± 1.605	76.73 ± 1.1	19.82 ± 0.4468	2.677 ± 0.2337	15.63 ± 0.349	4.208 ± 0.1125	6.104 ± 0.2	92.88 ± 1.954	66.19 ± 2.116	2.56 ± 0.1015
6	93.36 ± 1.867	80.67 ± 1.613	78.03 ± 1.1	20.05 ± 0.4478	2.306 ± 0.2254	15.96 ± 0.3551	4.136 ± 0.1125	5.374 ± 0.2	93.48 ± 1.963	66.92 ± 2.126	2.97 ± 0.1288
B	107.4 ± 2.148	93.48 ± 1.87	73.75 ± 1.1	22.09 ± 0.4993	2.396 ± 0.2622	17.84 ± 0.4015	4.291 ± 0.1125	6.159 ± 0.2	92.97 ± 1.958	64.24 ± 2.098	2.897 ± 0.1145
C	97.05 ± 1.941	83.15 ± 1.663	75.28 ± 1.1	20.34 ± 0.4573	2.446 ± 0.2363	16.27 ± 0.3633	4.108 ± 0.1125	5.997 ± 0.2	93.46 ± 1.963	65.81 ± 2.225	2.714 ± 0.1089

APPENDIX F. COMPONENT MODELS DESCRIPTIONS

F.1 Compressor Model

The single-port vapor-injected (VI) compressor is modeled based on a compressor map provided in Tello-Oquendo et al. (2017). The map-based power consumption (in W), suction mass flow rate (in g/s) and injection mass flow rate ratio are expressed in Equations (3.7) to (3.9), where the suction dew-point temperature T_{evap}, the discharge dew-point temperature T_{cond}, and the injection dew-point temperature $T_{dew,inj}$ are in degrees Fahrenheit. In another word, they are the dew temperatures, which are the same as the saturated vapor temperatures for pure fluids. The suction pressure P_{suc} and the injection pressure P_{inj} are in kPa. The coefficients $c_1, c_2, ..., c_{11}$ are the mapped coefficients based on the experimental data (Table F.1) of Lumpkin et al. (2018) for the electrical power consumption $\dot{W}_{comp}$, the suction mass flow rate $\dot{m}_{suc}$, and the injection mass flow rate ratio $\frac{\dot{m}_{inj}}{\dot{m}_{suc}}$, as shown in Table F.2. The compressor is provided by Emerson/Copeland and has a model number ZF13KVE-TF5.

The overall isentropic efficiency is defined by ASHRAE Standard 23.1 (Standard, 2015) and can expressed by

$$\eta_{is} = \frac{\dot{m}_{suc}\left(h_{inj,is} - h_{suc}\right) + \dot{m}_{r,tot}\left(h_{dis,is} - h_{inj,mix}\right)}{\dot{W}_{comp}} \tag{F.1}$$

where $h_{inj,mix}$, the specific enthalpy of the refrigerant vapor after mixing with the intermediate pressure flow and the partially compressed flow at state $h_{inj,is}$, can be determined by

$$h_{inj,mix} = \frac{\dot{m}_{suc} h_{inj,is} + \dot{m}_{inj} h_{inj}}{\dot{m}_{tot}} \tag{F.2}$$

and $h_{dis,is}$ is defined as the specific enthalpy of refrigerant vapor at compressor discharge pressure following an isentropic compression of the refrigerant vapor from state point $h_{inj,mix}$.

Since the electrical power is known from the compressor map, so the heat transfer can be expressed as a fraction of the electrical power consumption by

$$\dot{Q}_{amb} = -f_p \dot{W}_{comp} \tag{F.3}$$

where f_p is the fraction of electrical power lost at heat transfer. Therefore, the outlet enthalpy of the compressor can be determined by

$$h_{comp,o} = \frac{h_{mix} + (h_{dis,is} - h_{inj,mix})}{\eta_{is}\,(1 + f_p)} \tag{F.4}$$

where h_{mix} is the mixed enthalpy after the first compression stage which can be determined by

$$h_{mix} = \frac{\dot{m}_{suc} h_{mix,pre} + \dot{m}_{inj} h_{inj}}{\dot{m}_{tot}} \tag{F.5}$$

Note that the enthalpy at the end of the first compression $h_{mix,pre}$ can be obtained from

$$h_{mix,pre} = h_{comp,i} + \frac{h_{dis,is} - h_{comp,i}}{\eta_{is}\,(1 + f_p)} \tag{F.6}$$

Table F.1. R-407C VI compressor performance data (Lumpkin et al., 2018).

P_{suc} kPa	P_{dis} kPa	P_{inj} kPa	T_{evap} °F	T_{cond} °F	$T_{dew,inj}$ °F	$\dot{m}_{suc}$ g/s	$\dot{m}_{inj}$ g/s	$\dot{W}_{comp}$ W
445.4	2221	859.1	30.27	130.19	66.54	64.26	18.14	4815
488.1	2221	813.6	34.99	130.19	63.31	70.31	18.90	4870
591.6	2222	935.6	45.25	130.22	71.69	86.18	18.14	5003
444	1690	661.9	30.11	110.40	51.46	65.77	12.10	3812
538.5	1686	775.7	40.17	110.23	60.52	80.13	11.34	3929
329.6	1460	584.7	15.43	100.31	44.61	48.38	9.83	3239
536.4	1459	830.8	39.96	100.26	64.55	80.13	7.56	3501
539.2	1934	915.6	40.24	120.01	70.37	79.38	13.61	4369
403.3	1938	753.6	25.26	120.16	58.84	58.97	14.36	4218
364.7	1938	704	20.30	120.16	54.94	52.92	14.36	4179
593.6	2518	1095	45.43	139.68	81.46	85.43	21.17	5588
496	2219	806.6	35.83	130.12	62.81	72.02	9.09	4580
449.5	2217	766.3	30.74	130.05	59.81	64.80	10.34	4571
596.5	2214	916.3	45.70	129.95	70.42	87.28	8.04	4680
329.9	2216	662.1	15.47	130.02	51.47	46.60	12.62	4484
328.4	1455	552.9	15.26	100.07	41.58	48.00	7.08	3154
366.9	1457	600.7	20.60	100.17	46.08	53.97	6.96	3214
402.4	1450	626.1	25.15	99.84	48.36	59.36	5.58	3209
445.5	1457	681.2	30.28	100.17	53.07	66.08	5.43	3278
492.3	1461	739.9	35.44	100.35	57.79	73.31	5.21	3353
538.5	1445	798.1	40.17	99.61	62.18	80.45	4.96	3403
494.1	1940	766.4	35.63	120.24	59.82	72.29	6.85	4085
445.8	1940	708.2	30.31	120.24	55.28	64.71	7.13	4024
404.8	1949	697.9	25.44	120.57	54.44	58.61	9.70	4081
362.5	1931	603.5	20.01	119.90	46.34	52.38	7.30	3881
327	1937	601.1	15.05	120.13	46.12	46.70	9.76	3946
590.2	2530	892.9	45.12	140.04	68.86	84.97	6.59	5093
538.2	2530	857	40.14	140.04	66.40	77.20	8.58	5099
542.3	1683	825.4	40.55	110.11	64.16	80.51	6.74	3782
490.2	1678	765.8	35.21	109.90	59.77	72.44	7.33	3712
446.6	1682	715.9	30.40	110.07	55.89	65.71	7.74	3671
543.5	1939	826.1	40.67	120.20	64.21	79.64	6.61	4149

Table F.2. Mapped coefficients of the compressor model.

	c_1	c_2	c_3	c_4	c_5	c_6	c_7	c_8	c_9	c_{10}	c_{11}	R^2
$\dot{W}_{comp}$ [W]	1	0.9805	0.998	0.3779	−0.2446	0.4547	0.03589	−0.02785	0.00799	−0.00201	1.014	0.9954
$\dot{m}_{suc}$ [g/s]	−33.54921	0.38643	1.84426	2.0399×10^{-3}	0.01081	−0.0168	1.9559×10^{-4}	-7.9688×10^{-5}	-3.1845×10^{-5}	4.8328×10^{-5}	–	0.9998
$\frac{\dot{m}_{inj}}{\dot{m}_{suc}}$ [–]	−0.4859	0.3869	–	–	–	–	–	–	–	–	–	0.7084

Table F.3. VI compressor mapping coefficients (Tello-Oquendo et al., 2017).

	c_1	c_2	c_3	c_4	c_5	c_6	c_7	c_8	c_9	c_{10}	c_{11}	R^2
$\dot{W}_{comp}$ [W]	1.003	0.9998	1.134	0.9032	−0.5003	0.5136	−0.00137	−0.00919	0.00576	−0.00156	1.053	0.9954
$\dot{m}_{suc}$ [g/s]	133.3172	0.50872	−2.1589	8.4725×10^{-3}	9.4955×10^{-3}	0.01708	3.6543×10^{-5}	6.6601×10^{-6}	-4.7197×10^{-5}	-4.6172×10^{-5}	–	1
$\frac{\dot{m}_{inj}}{\dot{m}_{suc}}$ [–]	−0.3845	0.3296	–	–	–	–	–	–	–	–	–	0.9976

F.2 Condenser Model

The condenser aim to to cool the refrigerant from superheated state at approximately constant pressure and condenses it to subcooled state. In the ideal case, refrigerant enters the condenser at supeheated stated and exit at subcooled state. However, at low charge conditions, it may result in a condenser that does not have a subcooled section, and at extreme conditions, does not have a two-phase section either. Figure F.1 shows the possible configurations for the two different cases described.

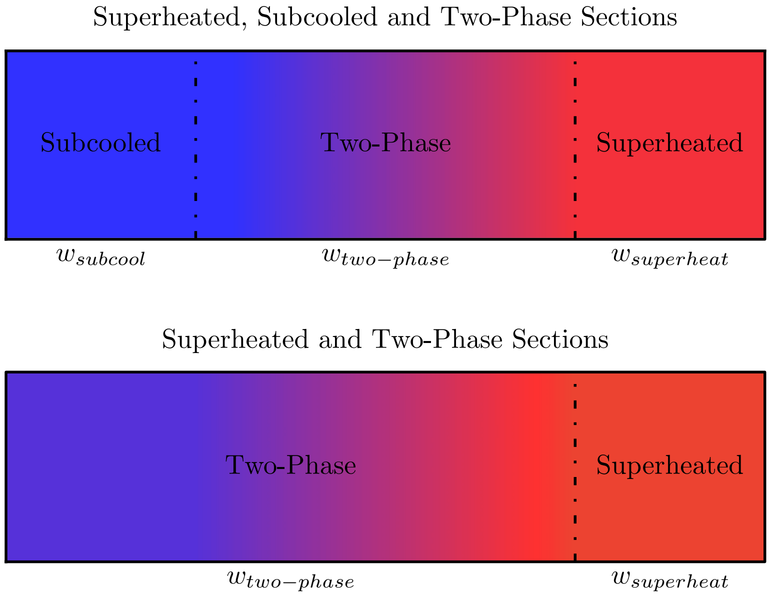
Superheated, Subcooled and Two-Phase Sections

Superheated and Two-Phase Sections

Figure F.1. Different cases for refrigerant state conditions in condenser (Bell, 2015).

In both cases, Figure F.1 represents an averaged circuit on the refrigerant side. Overall, the goal of solver for the condenser is to determine how much of the length of an averaged circuit is in the superheated, two-phase, and subcooled phases. The fraction of the circuit length in each of these sections are given by $w_{superheat}$, $w_{two-phase}$, and $w_{subcool}$, respectively. The sum of these factors must be equal to unity. In the cases where one of the sections do not exist, its circuit fraction parameter w is set to zero. Therefore, for the average length of one circuit $\overline{L_{circuit}}$, the lengths of each segment are given by

$$\begin{aligned} L_{superheat} &= w_{superheat}\overline{L_{circuit}} \\ L_{two-phase} &= w_{two-phase}\overline{L_{circuit}} \\ L_{subcool} &= w_{subcool}\overline{L_{circuit}} \end{aligned} \tag{F.7}$$

where

$$w_{superheat} + w_{two-phase} + w_{subcool} = 1 \tag{F.8}$$

The analysis on the air-side of the condenser makes a number of assumptions:

- Pure cross flow heat exchanger
- There is no condensation of moist air on the outside of the tubes since the temperature of refrigerant is above the dew-point of the air stream
- The flow is evenly balanced between all the circuits on the refrigerant side
- The flow is evenly distributed on the air-side

Because the air flow rate flow $\dot{m}_{a,total}$ is assumed to be evenly distributed across the face of the coil which has a total air-side area of $A_{a,total}$, the areas and mass flow rates for each section (Figure F.2) can be expressed as

$$\begin{aligned} A_{a,superheat} &= w_{superheat}A_{a,total} \\ A_{a,two-phase} &= w_{two-phase}A_{a,total} \\ A_{a,subcool} &= w_{subcool}A_{a,total} \end{aligned} \tag{F.9}$$

and

$$\begin{aligned} \dot{m}_{a,superheat} &= w_{superheat}\dot{m}_{a,total} \\ \dot{m}_{a,two-phase} &= w_{two-phase}\dot{m}_{a,total} \\ \dot{m}_{a,subcool} &= w_{subcool}\dot{m}_{a,total} \end{aligned} \tag{F.10}$$

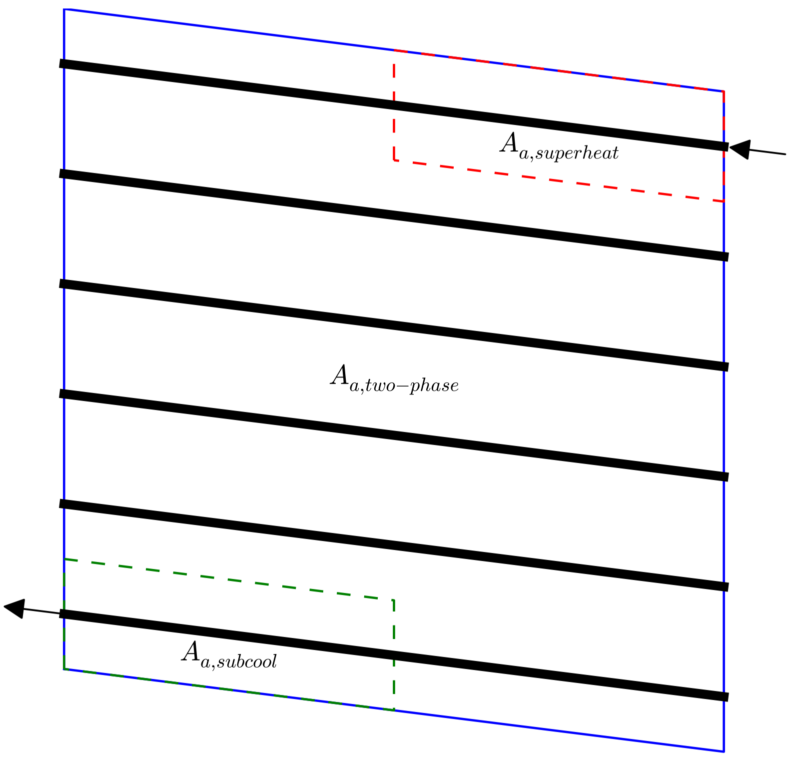

Figure F.2. Area sections on air-side of condenser (Bell, 2015).

Condenser Algorithm

The flow chart in Figure F.3 shows the algorithm used in the condenser solver. The analysis for each fraction of the circuit length w segment is described in the following sections.

Superheated Section

In the superheated section, the inlet refrigerant temperature and the outlet refrigerant saturated temperature (dew-point temperature) are known. Assuming pure

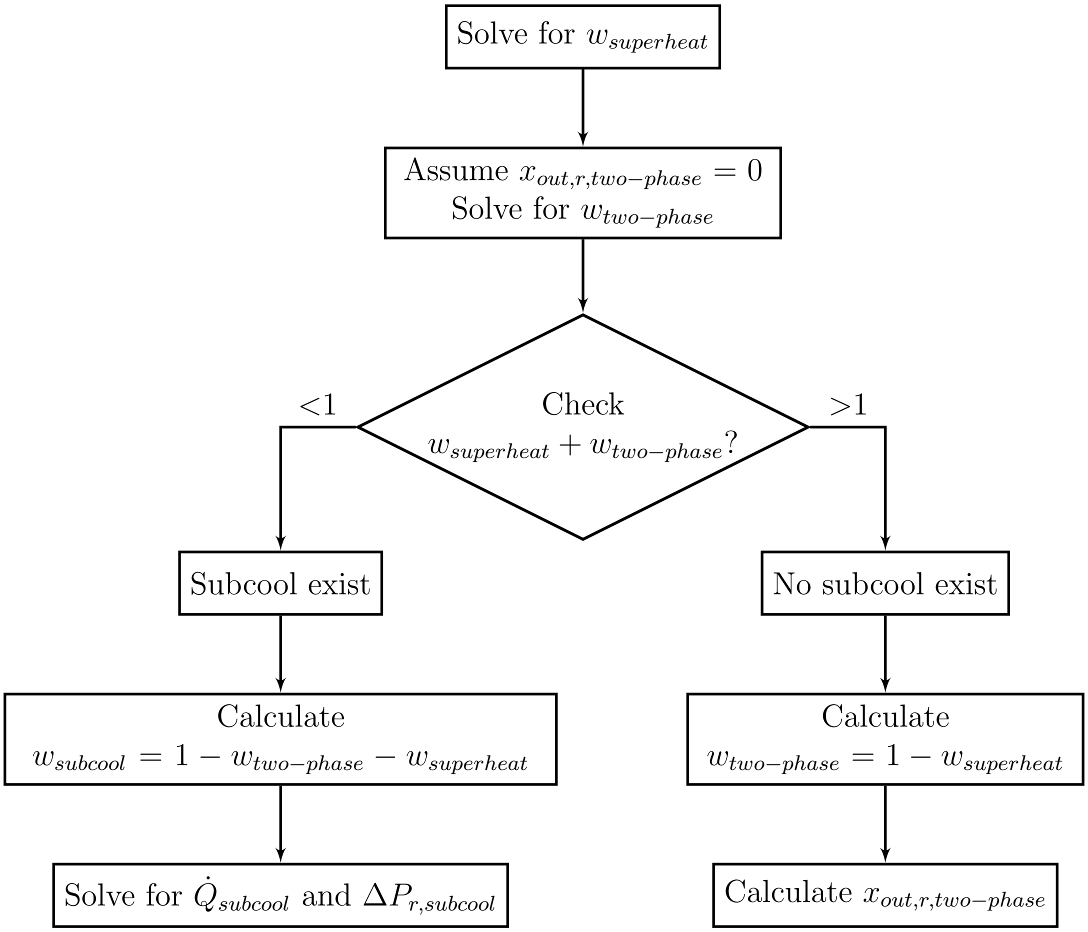

Figure F.3. Condenser algorithm flow chart.

crossflow, the fraction of the area required for the superheated section can be expressed explicitly as

$$w_{superheat} = -\frac{\ln(1-\Psi)}{\left[1 - \exp\left(\dfrac{-\mathrm{UA}_{overall}}{c_{p,a}\dot{m}_{a,total}}\right)\right]}\frac{\dot{m}_r c_{p,r}}{\dot{m}_{a,total}c_{p,a}} \tag{F.11}$$

and

$$\Psi = \frac{(T_{r,i} - T_{dew,r})}{(T_{r,i} - T_{a,i})} \tag{F.12}$$

where the derivation of this term can be obtained from *Condenser Area Derivation* section in Bell (2015). The value of $\mathrm{UA}_{overall}$ is given by

$$\mathrm{UA}_{overall} = \frac{1}{(\eta_a \alpha_a A_{a,total})^{-1} + (\alpha_{r,superheat} A_{r,wetted})^{-1} + R_w} \tag{F.13}$$

where R_w is the thermal resistance at the wall that represents the conduction heat transfer portion. The wall conduction heat transfer was not implemented in original ACHP model (Bell, 2015). The wall conduction adds more accuracy to the current model. Moreover, the analysis of the average air side heat transfer coefficient α_a can be found in *Air-Side Empirical Correlations* section in Appendix F. While the analysis of average refrigerant side heat transfer coefficient $\alpha_{r,superheat}$ is similar to that on Gnielinski (1976), in which the details are given in Appendix F.
The heat transfer rate in the superheat section can be expressed as

$$\dot{Q}_{superheat} = \dot{m}_r c_{p,r} w_{two-phase} (T_{dew,r} - T_{in,r}) \tag{F.14}$$

Moreover, the pressure drop analysis is based on Churchill (1977) for the superheated section, in which the details are available in Appendix F.

Two-phase Section

In the condenser, there are two basic possibilities. Either subcooled section exist, and therefore the outlet of the two-phase section is at a quality of 0 (saturated liquid) or subcooled section does not exist, and therefore outlet of the two-phase region is at some two-phase quality.

The first step is to assume that the outlet of the two-phase region is at a quality of 0 and calculate the required fraction of the circuit length $w_{two-phase}$. Before the length fraction can be calculated, the average refrigerant side heat transfer coefficient is required, for which the analysis can be found in *Two-Phase Condensation Heat*

Transfer section in Appendix F for micro-channel condenser. The average refrigerant-side heat transfer coefficient α_r is a function of refrigerant outlet quality.

In either configuration of the two-phase section, solving for $x_{out,r,two-phase}$ or solving for $w_{two-phasee}$, the effectiveness $\epsilon_{two-phase}$ is known. Because NTU is independent of the length fraction w, since the parameter w cancels out of the solution for NTU. Therefore, the effectiveness can be expressed as

$$\epsilon_{two-phase} = 1 - \exp\left(\frac{-\mathrm{UA}_{overall}}{\dot{m}_{a,total}c_{p,a}}\right) \tag{F.15}$$

where the value of $\mathrm{UA}_{overall}$ is determined by

$$\mathrm{UA}_{overall} = \frac{1}{(\eta_a \alpha_a A_{a,total})^{-1} + (\alpha_{r,two-phase}A_{r,total})^{-1} + R_w} \tag{F.16}$$

where the analysis of average refrigerant side heat transfer coefficient $\alpha_{r,two-phase}$ is based on Kim and Mudawar (2013), while the analysis of average air side heat transfer coefficient α_a is similar to that in superheated section.

For a given outlet quality of the two-phase section $x_{out,r,two-phase}$, the length fraction $w_{two-phase}$ can be obtained from

$$w_{two-phase} = -\frac{\dot{m}_r h_{fg}(1 - x_{out,r,two-phase})}{\dot{m}_{a,total}c_{p,a}(T_{a,i} - T_{sat,r})\varepsilon_{two-phase}} \tag{F.17}$$

The heat transfer rate in the two-phase section, since it is condensing, is given by

$$\dot{Q}_{two-phase} = \varepsilon_{two-phase}\dot{m}_{a,total}c_{p,a}w_{two-phase}(T_{i,a} - T_{dew,r}) \tag{F.18}$$

Otherwise, if the quality is being iterated for, the residual to be driven to zero by altering the outlet quality of the two phase section $x_{out,r,two-phase}$ is

$$\Delta = w_{two-phase}(x_{out,r,two-phase}) - (1 - w_{superheat}) \tag{F.19}$$

where $w_{two-phase}$ is evaluated from Equation (F.17), and $w_{superheat}$ is known from Equation (F.11). Because the value of the average refrigerant two-phase heat transfer coefficient is dependent on the two-phase section outlet quality, Brent (1973) iterative method is used.

Moreover, the refrigerant frictional pressure drop calculation is based on Kim and Mudawar (2012) analysis for the two-phase section where the details are provided in Appendix F.

Subcooled Section

If the subcooled region exists, the available area is known and therefore $w_{subcool}$ is known, as well as the inlet air and refrigerant temperatures. The inlet refrigerant temperature to the subcooled region is the saturated liquid temperature (bubble-point temperature) of the refrigerant, and the inlet air temperature is the same inlet air temperature as for all the other sections. Therefore, the UA value can be determined by

$$\mathrm{UA} = \frac{w_{subcool}}{(\eta_a \alpha_a A_{a,total})^{-1} + (\alpha_r A_{r,total})^{-1} + R_w} \tag{F.20}$$

Notice that wall's thermal resistance R_w is included to improve the accuracy of the model. The analysis for both averaged air and refrigerant heat transfer coefficients (α_a and α_r) are similar to that in superheated section.

The minimum and maximum capacitance rates of air and subcooled refrigerant can be expressed as

$$C_{min} = \min[\dot{m}_r c_{p,r}, \dot{m}_{a,total} c_{p,a} w_{subcool}] \tag{F.21}$$

and

$$C_{max} = \max[\dot{m}_r c_{p,r}, \dot{m}_{a,total} c_{p,a} w_{subcool}] \tag{F.22}$$

which give the NTU to be

$$\mathrm{NTU} = \frac{\mathrm{UA}}{C_{min}} \tag{F.23}$$

Assuming a pure cross flow, if the minimum capacitance is on the air side, the effectiveness yields

$$\epsilon_{subcool} = \frac{1}{C_r}\left\{1 - \exp(-C_r\left[1 - \exp(-\mathrm{NTU})\right])\right\} \tag{F.24}$$

where

$$C_r = \frac{C_{min}}{C_{max}} \tag{F.25}$$

On the other hand, if the minimum capacitance rate is on the refrigerant side, the effectiveness yields

$$\epsilon_{subcool} = 1 - \exp\left(-\frac{1}{C_r}\left[1 - \exp(-C_r\mathrm{NTU})\right]\right) \tag{F.26}$$

The heat transfer rate in the subcooled section can be determined by

$$\dot{Q}_{subcool} = -\varepsilon_{subcool} C_{min}(T_{bubble,r} - T_{i,a}) \tag{F.27}$$

which is negative because heat is removed from the refrigerant. Likewise, the refrigerant pressure drop analysis for subcooled section is similar to that of superheated section in which it is based on Churchill (1977) correlation (available in Appendix F).

Overall Calculation

Once all the variables are calculated in all the sections of the condenser, the overall heat transfer rate, pressure drop, and refrigerant charge in the condenser are given by

$$\begin{aligned} \dot{Q} &= \dot{Q}_{superheat} + \dot{Q}_{two-phase} + \dot{Q}_{subcool} \\ \Delta P_r &= \Delta P_{r,superheat} + \Delta P_{r,two-phase} + \Delta P_{r,subcool} \\ m_r &= m_{r,superheat} + m_{r,two-phase} + m_{r,subcool} \end{aligned} \tag{F.28}$$

If subcooled region exists, the condenser outlet subcooling is calculated by

$$\Delta T_{sc} = T_{bubble,r} - T_{out,r} \tag{F.29}$$

and if subcooled region does not exist, an effective subcooling amount is determined by

$$\Delta T_{sc} = \frac{h_{fg} x_{out,r,two-phase}}{c_{p,dew}} \tag{F.30}$$

where $c_{p,dew}$ is the specific heat of saturated liquid. This effective subcooling parameter is primarily needed to continue the iterative solver. For cycle convergence, subcooling should exist.

F.3 Micro-Channel Heat Exchanger Model

In the original ACHP model (Bell, 2015), only one type of heat exchanger is considered which is the fin-tube heat exchanger. As a contribution to the ACHP model, the micro-channel type is developed and presented in this section. The mathematical model is based on of the literature in Lee (2010).

There is some disagreement in literature as to the best way to describe the tube layouts. The arrangements used here is that there are a number of banks of heat exchangers. In practice, micro-channel heat exchanger which act as a condenser has only one bank, however, some packaged air conditioners might have several banks. To generalize the model, several banks are considered. The bank is defined as the vertical column that has several tubes when viewed end-on with the air flow passing from left to right. The heat exchanger in Figure F.4 has only one bank, with 70 tubes per bank, and 3 passes per bank. The geometrical terms of multi-louvered-fin heat exchanger are shown in Figure F.5.

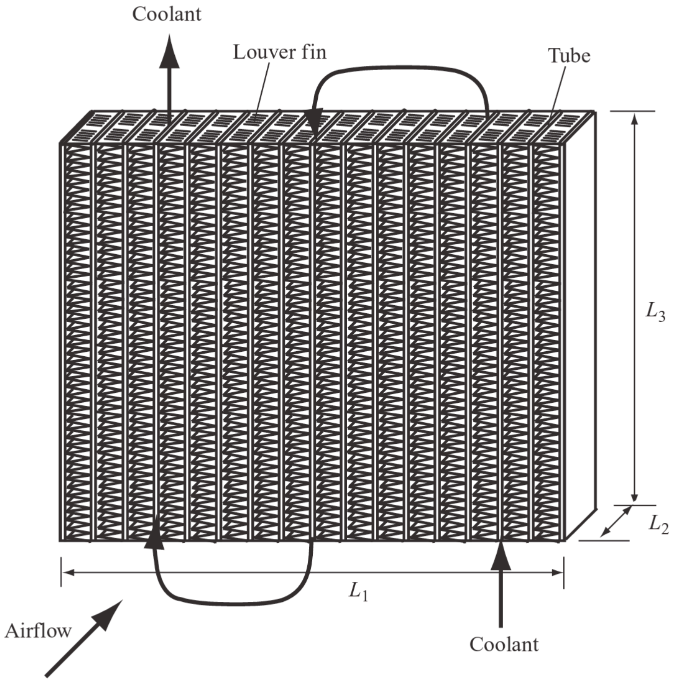

Figure F.4. Louver-fin-type plate-fin heat exchanger (Lee, 2010).

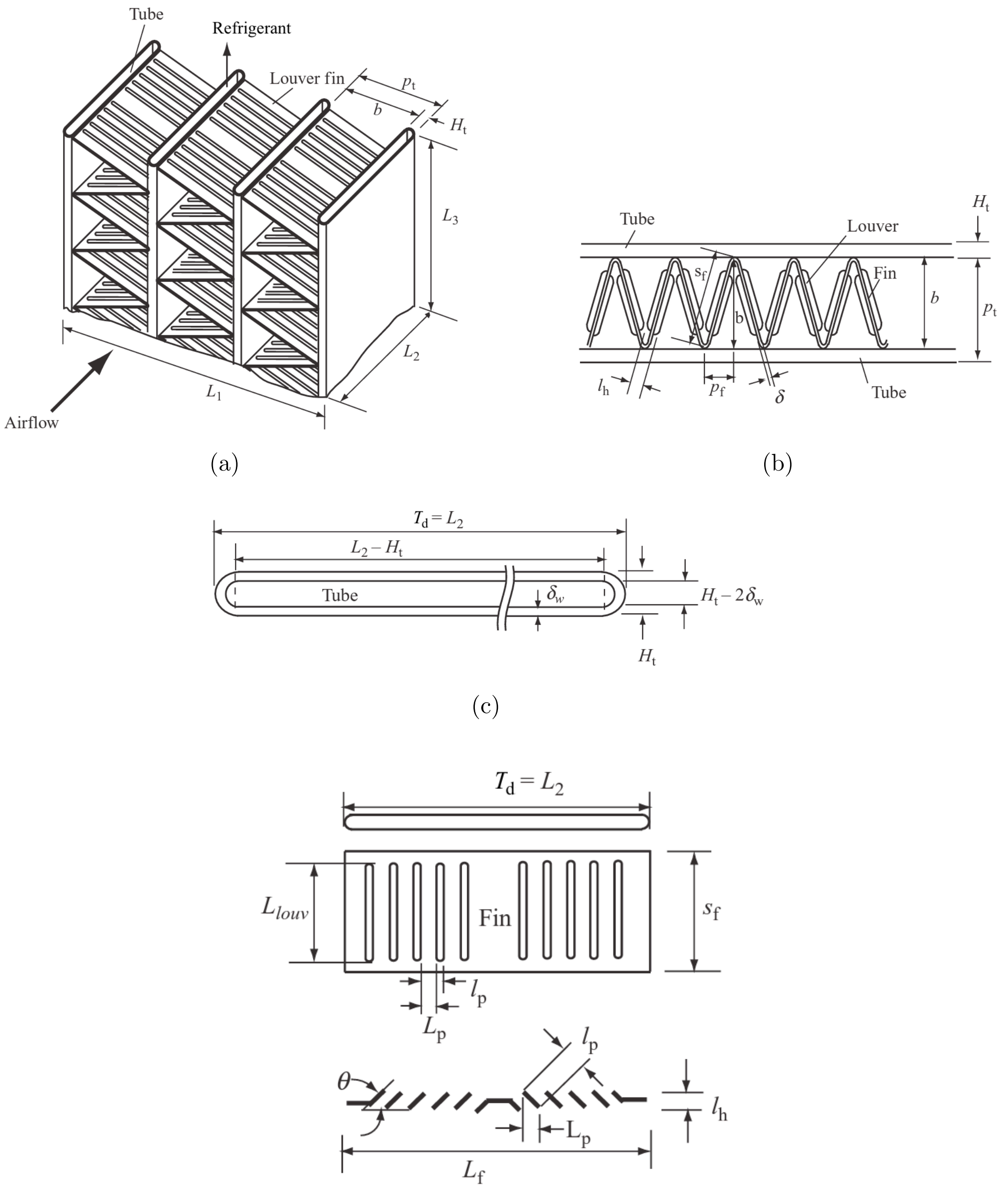

(a)

(b)

(c)

(d)

Figure F.5. Definition of geometrical parameters of corrugated louver fins (Lee, 2010).

Notice that there is certain number of tubes per bank (*e.g.,* 70 tubes per bank in Figure F.4), and Figure F.6 defines the terms which describe the heat exchanger tube spacing, major diameter (tube outside height), and tube depth (tube outside width).

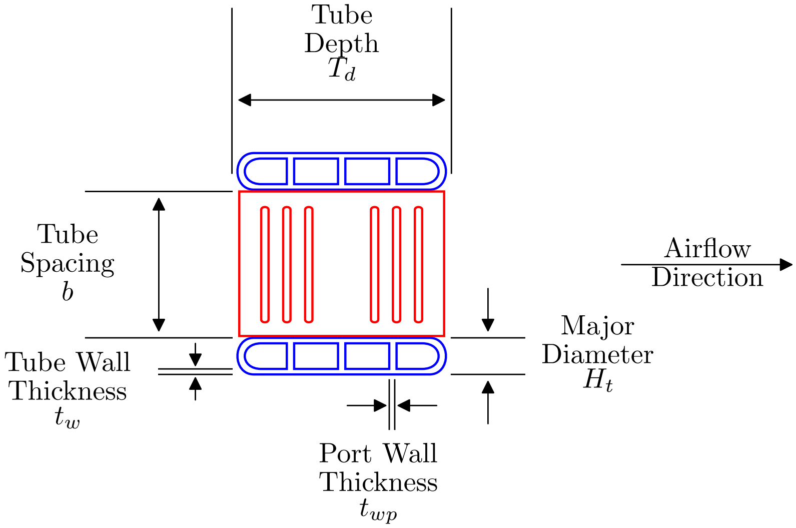

Figure F.6. Louver-fin-type micro-channel heat exchanger arrangement.

The empirical correlations for air-side heat transfer and pressure drop of louvered-fin-type heat exchangers can be found in *Air-Side Empirical Correlations* section below, and the refrigerant-side correlations can be found in *Pressure Drop and Heat Transfer in Micro-Channel Condenser* section in Appendix F.

In order to use the heat exchanger in ACHP, complexities of circuiting are neglected. In practice, micro-channel heat exchangers defined by the number of passes. As a results, some passes can have more tubes than the others. In this work, averaged number of tubes per pass is employed. For simplicity, the number of tubes per pass presents the number of circuits in the micro-channel heat exchanger. The number of circuits is give by

$$N_{circuits} = \frac{N_{tubes/bank}}{N_{pass}} \tag{F.31}$$

In practice, it is uncommon for the number of tubes per bank to be divisible by the number of circuits. As a result, some circuits can be longer than others. In this work, average circuit lengths are employed. The average circuit length is given by

$$L_{tubes,total} = N_{tubes/bank} N_{bank} L_{tube} \tag{F.32}$$

So, the effective length of a circuit can be expressed as

$$\overline{L_{circuit}} = \frac{L_{tubes,total}}{N_{circuits}} \tag{F.33}$$

This average circuit length is primarily required for the calculation of the fluid-side pressure drop. Other parameters that are required are the total refrigerant-side volume $V_{r,total}$, which can be given by

$$V_{r,total} = \left[\underbrace{(T_d - H_t)(H_t - 2t_w)}_{\text{rectangle of tube}} + \underbrace{\frac{\pi}{4}(H_t - 2t_w)^2}_{\text{circular part on sides}} - \underbrace{(H_t - 2t_w) t_{wp} (N_{ports} - 1)}_{\text{thickness between ports}} \right] \overline{L_{circuit}} N_{circuits} \tag{F.34}$$

The refrigerant-side surface area (tube wetted area) is given by

$$A_{r,wetted} = \left[\underbrace{2(T_d - H_t)}_{\text{tube straight length}} + \underbrace{\pi (H_t - 2t_w)}_{\text{circular part on sides}} - \underbrace{2t_{wp}(N_{ports} - 1)}_{\text{horizontal port thickness}} + \underbrace{2(H_t - 2t_w)(N_{ports} - 1)}_{\text{vertical thickness between ports}} \right] \overline{L_{circuit}} N_{circuits} \tag{F.35}$$

The refrigerant-side cross section area (free-flow area) is determined by

$$A_{r,c} = \left[\underbrace{(T_d - H_t)(H_t - 2t_w)}_{\text{area of rectangle tube}} + \underbrace{\frac{\pi}{4}(H_t - 2t_w)^2}_{\text{circular part on sides}} - \underbrace{t_{wp}(H_t - 2t_w)(N_{ports} - 1)}_{\text{thickness between ports}} \right] N_{circuits} \tag{F.36}$$

The hydraulic diameter on refrigerant-side can be calculated by

$$D_h = \frac{4A_{r,c}L_{circuit}}{A_{r,wetted}} \tag{F.37}$$

The refrigerant side mass flux can be found by

$$G = \frac{\dot{m}_r}{A_{r,c}} \tag{F.38}$$

In the original ACHP model (Bell, 2015), the wall conductance was neglected. However, to improve the accuracy of the model, it was implemented herein. The thermal resistance at the tube wall can be found by

$$R_w = \frac{t_w}{k_w A_w} \tag{F.39}$$

where the total wall conduction area A_w (excluding port's thickness) is determined by

$$A_w = 2\left[T_d - t_{wp}\left(N_{ports} - 1\right)\right] L_{circuit} N_{circuits} \tag{F.40}$$

Air-Side Geometric Parameters

The calculation of major geometrical parameters are discussed in this section. Fins per meter

$$\text{FPM} = \frac{\text{FPI}}{0.0254} \tag{F.41}$$

Fin pitch (distance between centerlines of fins)

$$p_f = \frac{1}{\text{FPM}} \tag{F.42}$$

Fin height

$$s_f = \sqrt{b^2 + p_f^2} \tag{F.43}$$

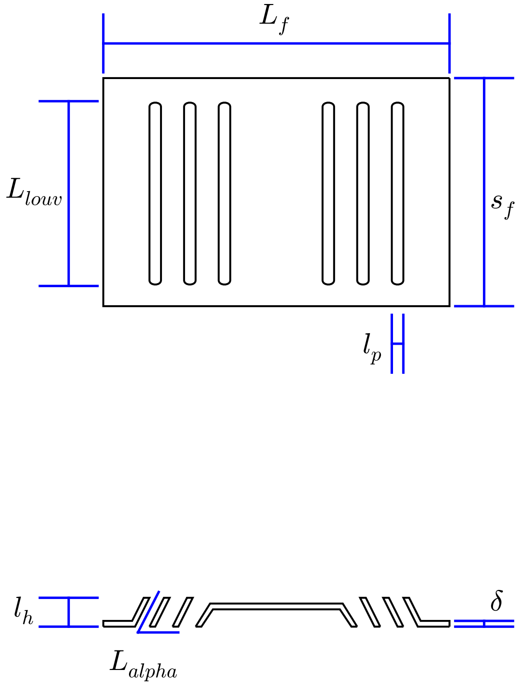

Figure F.7. Louver-fin geometrical parameters.

Louver cut length[1]

$$L_{louv} = 0.85 s_f \tag{F.44}$$

Fin pitch

$$p_t = H_t + b \tag{F.45}$$

Louver height l_h as a function of louver pitch l_p is give by

$$l_h = l_p \sin\left(\frac{\pi L_{alpha}}{180}\right) \tag{F.46}$$

Number of air passages[2]

$$N_{pg} = N_{tubes/bank} - 1 \tag{F.47}$$

---

[1] Calculated in case L_{louv} can not be physically measured

[2] If micro-channel HX has no tubes on the edges, then $N_{pg} = N_{tubes/bank} + 1$

Height of heat exchanger (core width)

$$L_1 = N_{pg}b + N_{tubes/bank}H_t \tag{F.48}$$

Total number of fins (per bank)

$$n_f = \frac{L_3}{p_f}N_{pg} \tag{F.49}$$

where L_3 is the length of single tube.

Total number of louvers (per bank)

$$n_{louv} = \left(\frac{L_f}{l_p} - 1\right)n_f \tag{F.50}$$

The primary area A_p (per bank) is calculated by subtracting the fin base areas from the tube outer surface area as

$$A_p = \underbrace{\left[2\left(L_2 - H_t\right) + \pi H_t\right]L_3 N_{tubes}}_{\text{tube outside surface area}} - \underbrace{2\delta L_2 n_f}_{\text{fin base area}} \tag{F.51}$$

where L_2 is the tube outside width (depth) T_d, while L_3 is the heat exchanger length as shown in Figure F.4.

The total fin area (per bank) is the sum of the fin area and the louver edge area as

$$A_f = \underbrace{2\left(s_f L_f + s_f\delta\right)n_f}_{\text{fin area}} + \underbrace{2L_{louv}\delta n_{louv}}_{\text{louver edge area}} \tag{F.52}$$

So, the total heat transfer surface area on air-side is obtained by

$$A_t = \left(A_f + A_p\right)N_{bank} \tag{F.53}$$

The minimum free-flow area on air-side is expressed by

$$A_c = \underbrace{bL_3N_{pg}}_{\substack{\text{area spacing}\\ \text{between tubes}}} - \underbrace{\left[\delta\left(s_f - L_{louv}\right) + L_{louv}l_h\right]n_f}_{\text{fin and louver edge area}} \tag{F.54}$$

The frontal area on air-side is given by

$$A_{fr} = L_1L_3 \tag{F.55}$$

Air-Side Heat Transfer and Pressure Drop Parameters

The air-side heat transfer and pressure drop parameters are calculated based on the following parameters:
The mass flow rate based on inlet conditions is evaluated as

$$\rho_{ha} = \frac{1+W}{v_{ha}} \tag{F.56}$$

$$\dot{m}_{ha} = \dot{V}_{ha}\rho_{ha} \tag{F.57}$$

The air mass flux through the heat exchanger can be defined by

$$G = \frac{\dot{m}_{ha}}{A_c} \tag{F.58}$$

Therefore, the maximum velocity on air-side can be calculated by

$$u_{max} = \frac{G}{\rho_{ha}}\frac{A_{fr}}{A_c} \tag{F.59}$$

Specific heat, thermal conductivity and viscosity based on humid air property correlations, so the Prandtl Number can be calculated by

$$\mathrm{Pr} = \frac{c_{p,ha}\mu_{ha}}{k_{ha}} \tag{F.60}$$

Reynolds number based on the hydraulic diameter and mass flux can found by

$$\mathrm{Re}_{D_h} = \frac{GD_h}{\mu_{ha}} \tag{F.61}$$

However, in the louver-fin-type heat exchangers, the air-side correlations are expressed as a function of Reynolds number which is based on louver pitch l_p as

$$\mathrm{Re}_{lp} = \frac{\rho_{ha} u_{max} l_p}{\mu_{ha}} \tag{F.62}$$

Air-Side Empirical Correlations

The correlations used for calculating air-side heat transfer and pressure drop of louvered-type micro-channel heat exchanger are summarized in Table F.4.

Table F.4. Summary of correlations employed in air-side of condenser model.

Parameter	Reference
Heat transfer	Kim and Bullard (2002)
Pressure drop	Chang et al. (2000)

Colburn j-factor correlation for multi-louvered fins is given by

$$j = \mathrm{Re}_{l_p}^{-0.487} \left(\frac{L_{alpha}}{90}\right)^{0.257} \left(\frac{p_f}{l_p}\right)^{-0.13} \left(\frac{b}{l_p}\right)^{-0.29} \left(\frac{L_f}{l_p}\right)^{-0.235} \left(\frac{L_{louv}}{l_p}\right)^{0.68} \left(\frac{p_t}{l_p}\right)^{-0.279} \left(\frac{\delta}{l_p}\right)^{-0.05} \tag{F.63}$$

So, air-side mean heat transfer coefficient can be calculated by

$$\alpha_a = \frac{j \rho_{ha} u_{max} c_{p,a}}{\mathrm{Pr}^{2/3}} \tag{F.64}$$

The air-side pressure drop fanning friction factor

$$f_{a,total} = f_1 f_2 f_3 \tag{F.65}$$

where

$$f_1 = \begin{cases} 14.39\mathrm{Re}_{l_p}^{\left(-0.805\frac{p_f}{s_f}\right)} \left(\log_e\left[1+\left(\frac{p_f}{l_p}\right)\right]\right)^{3.04} & \mathrm{Re}_{l_p} < 150 \\ 4.97\mathrm{Re}_{l_p}^{\left(0.6049-\frac{1.064}{L_{alpha}{}^{0.2}}\right)} \left[\log_e\left(\left(\frac{\delta}{p_f}\right)^{0.5}+0.9\right)\right]^{-0.527} & \mathrm{Re}_{l_p} \geq 150 \end{cases} \tag{F.66}$$

$$f_2 = \begin{cases} \left[\log_e\left(\left(\frac{\delta}{p_f}\right)^{0.48}+0.9\right)\right]^{-1.453} \left(\frac{D_h}{l_p}\right)^{-3.01} \left[\log_e\left(0.5\mathrm{Re}_{l_p}\right)\right]^{-3.01} & \mathrm{Re}_{l_p} < 150 \\ \left[\left(\frac{D_h}{l_p}\right)\log_e\left(0.3\mathrm{Re}_{l_p}\right)\right]^{-2.966} \left(\frac{p_f}{L_{louv}}\right)^{-0.7931\frac{p_t}{b}} & \mathrm{Re}_{l_p} \geq 150 \end{cases} \tag{F.67}$$

$$f_3 = \begin{cases} \left(\frac{pf}{L_{louv}}\right)^{-0.308} \left(\frac{L_f}{L_{louv}}\right)^{-0.308} \exp\left(-0.1167\frac{p_t}{H_t}\right) L_{alpha}{}^{0.35} & \mathrm{Re}_{l_p} < 150 \\ \left(\frac{p_t}{H_t}\right)^{-0.0446} \log_e\left(1.2+\left(\frac{l_p}{p_f}\right)^{1.4}\right)^{-3.553} L_{alpha}{}^{-0.477} & \mathrm{Re}_{l_p} \geq 150 \end{cases} \tag{F.68}$$

Air-side pressure drop including, beside friction, momentum, expansion and contraction effects yields

$$\Delta P_a = \frac{G^2}{2\rho_{in,a}}\left[\underbrace{\left(1-\sigma^2+K_c\right)}_{\text{contraction}} + \underbrace{2\left(\frac{\rho_{in,a}}{\rho_{out,a}}-1\right)}_{\text{acceleration}} + \underbrace{f_{a,total}\left(\frac{A_t}{A_c}\right)\left(\frac{\rho_{in,a}}{\rho_{m,a}}\right)}_{\text{friction}} - \underbrace{\left(1-\sigma^2-K_e\right)\left(\frac{\rho_{in,a}}{\rho_{out,a}}\right)}_{\text{expansion}}\right] \tag{F.69}$$

where air-side pressure drop is solved using nonlinear least-squares algorithm because the air-side pressure drop is a function of air inlet and outlet conditions. The parameters used to calculated the air-side pressure drop are defined as follows:

The average air density $\rho_{m,a}$ is calculated according to

$$\frac{1}{\rho_{m,a}} = \frac{1}{2}\left(\frac{1}{\rho_{in,a}}+\frac{1}{\rho_{out,a}}\right) \tag{F.70}$$

The Porosity on air-side is defined the ratio of free-flow area to frontal area as

$$\sigma = \frac{A_c}{A_{fr}} \tag{F.71}$$

In Equation (F.69), K_c is a contraction coefficient at the inlet and K_e is an expansion coefficient at the outlet. Typical values of K_c and K_e are given in Lee (2010) for multiple-triangular-channel core.

Fin Efficiency

Fin efficiency is based on analysis by Kim and Bullard (2002) and modified for wet and dry fins with multi-louvered fins. The analysis is as follows:
The m factor is given by

$$m = \sqrt{\frac{2\alpha_a(c_s/c_p)}{k_{fin}\delta}\left(1+\frac{\delta}{L_f}\right)} \tag{F.72}$$

The characteristic length is obtained by

$$L_s = \frac{s_f}{2} - \delta \tag{F.73}$$

The finned surface efficiency can be found by

$$\eta_f = \frac{\tanh(mL_s)}{mL_s} \tag{F.74}$$

Therefore, the overall surface efficiency is given by

$$\eta_a = 1 - \frac{A_f}{A_t}(1-\eta_f) \tag{F.75}$$

F.4 Evaporator Model

Refrigerant enters the evaporator at some vapor quality between 0% and 100%, and ideally exits as a superheated vapor. The analysis for the evaporator shares some features that are employed in the condenser model. However, the evaporator analysis is more complicated because it is based on moving boundaries on both the refrigerant and air sides. On the refrigerant-side, the moving boundary is between two-phase refrigerant and superheated refrigerant, and on the air-side, there is a moving boundary between wet and dry parts of the coil. The evaporator is fin-and-tube type where the air-side geometric analysis is given in *Fin-Tube Heat Exchangers* section in Bell (2015). The correlations used for calculating the air-side heat transfer and pressure drop of the fin-and-tube type evaporator are listed in Table F.5.

Table F.5. Summary of correlations employed in air-side of evaporator model.

Parameter	Reference
Heat transfer	Wang et al. (1998)
Fin efficiency	Schmidt (1945) modified by Hong and Webb (1996)

The evaporator is assumed to be cross-counter-flow, and if the two-phase and superheated region exist, the mass flow of air and total air side surface area for each of the superheated and two-phase regions can be expressed as

$$\begin{aligned} \dot{m}_{a,superheat} &= w_{superheat}\dot{m}_{a,total} \\ \dot{m}_{a,two-phase} &= w_{two-phase}\dot{m}_{a,total} \end{aligned} \tag{F.76}$$

and

$$\begin{aligned} A_{a,superheat} &= w_{superheat}A_{a,total} \\ A_{a,two-phase} &= w_{two-phase}A_{a,total} \end{aligned} \tag{F.77}$$

On the refrigerant-side, the surface area for superheated and two-phase sections are given by

$$\begin{aligned} A_{r,superheat} &= w_{superheat} A_{r,total} \\ A_{r,two-phase} &= w_{two-phase} A_{r,total} \end{aligned} \tag{F.78}$$

Evaporator Algorithm

The flow chart in Figure F.8 shows the algorithm used in the evaporator solver. The analysis for two-phase and superheat regions are described in the following sections.

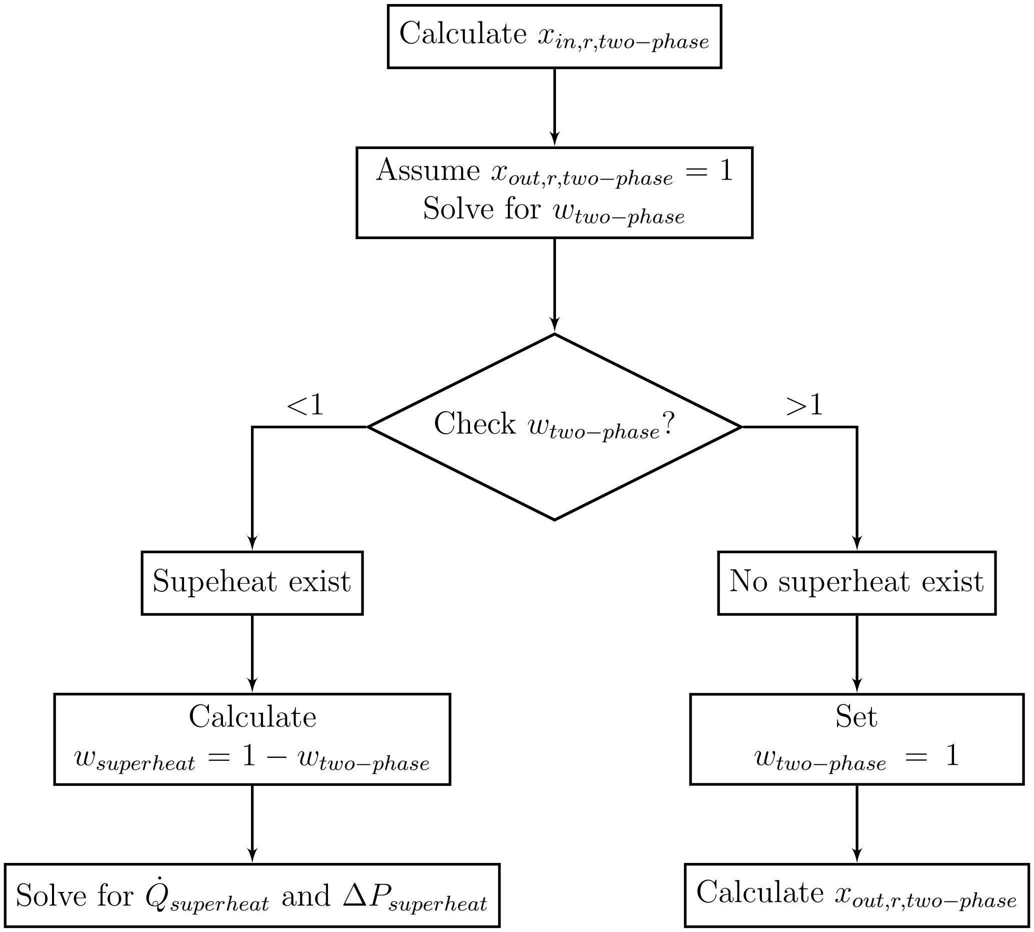

Figure F.8. Evaporator algorithm flow chart.

Two-phase Section

In the two-phase section, the target heat transfer rate is determined from

$$\dot{Q}_{target} = \dot{m}_r(x_{r,o} - x_{r,i})h_{fg} \tag{F.79}$$

and the heat transfer rate from the partially-wet/partially-dry analysis in *Heat Exchangers with and without Dehumidification* section in Bell (2015) is labeled as $\dot{Q}_{PWPD}$. Not to mention, Shah (1976) analysis is used to calculate the average refrigerant side heat transfer coefficient in the two-phase section (available in Appendix F).

Initially, it is assumed that all the heat exchanger is in the two-phase region. If using the outlet quality of saturated vapor ($x_{out,r} = 1$) with all the heat exchanger in the two-phase region, and $\dot{Q}_{PWPD}$ is greater than $\dot{Q}_{target}$, too much of the heat exchanger area was assumed to be in the two-phase section, and there must exist a superheated section. Therefore, the length fraction $w_{two-phase}$ is iteratively solved using Brent (1973) method as abounded solver ($w_{two-phase}$ is bounded between 0 and 1). The remaining area is given to the superheated section, so the superheated section circuit length fraction $w_{superheat}$ is determined by

$$w_{superheat} = 1 - w_{two-phase} \tag{F.80}$$

Moreover, the refrigerant frictional pressure drop calculation for two-phase section is based on Lockhart and Martinelli (1949) analysis and the details can be found in *Two-Phase Evaporation Pressure Drop* section in Appendix F.

Superheated Section

In the superheated section, for a given $w_{superheat}$, the analysis is given in *Heat Exchangers with and without Dehumidification* section in Bell (2015) where the refrigerant is single-phase, and the air-side surface may be fully-wet, partially-wet, or fully-dry, and all the inlet conditions for the superheated section are known. The air inlet state to the superheated section is assumed to be the same as for the two-phase section because the superheated section is typically rather small, and both superheated and two-phase portions should see approximately at the same inlet air state. The refrigerant properties are calculated using the same single-phase correlations as for the condenser, namely from Gnielinski (1976). Likewise, the refrigerant pressure drop in the superheated section is calculated using the same analysis as for the condenser, namely from Churchill (1977). Both correlations are available in Appendix F.

Overall Calculation

Once all the variables are calculated in all the sections of the evaporator, the overall heat transfer rate, pressure drop and mass of refrigerant charge are given by

$$\begin{aligned} \dot{Q} &= \dot{Q}_{two-phase} + \dot{Q}_{superheat} \\ \Delta P_r &= \Delta P_{r,two-phase} + \Delta P_{r,superheat} \\ m_r &= m_{r,two-phase} + m_{r,superheat} \end{aligned} \tag{F.81}$$

If superheated section exists, the evaporator outlet superheat is calculated by

$$\Delta T_{sh} = T_{out,r} - T_{dew,r} \tag{F.82}$$

and if superheated section does not exist, an effective superheat amount is determined by

$$\Delta T_{sh} = \frac{h_{out,r} - h_{dew,r}}{c_{p,dew}} \tag{F.83}$$

where $c_{p,dew}$ is the specific heat of saturated liquid. This effective superheat parameter is primarily needed to continue the iterative solver. In the cycle model, the superheat section should be existed for cycle model convergence.

F.5 Plate Heat Exchanger Economizer Model

The motivating factor that drives the use of plate heat exchangers (PHXs) is that they are a highly-compact heat exchanger that allows for excellent heat transfer between two fluids with very well controlled pressure drop. They tend to be slightly more expensive than equivalent coaxial type heat exchangers due to their accurate manufacturing requirements. But they can be easily altered to add more plates to give more surface area to increased heat transfer rate and lower pressure drop. The trade-off as usual is that adding plates to decrease the pressure drop also results in a decrease in heat transfer coefficient, which means that each m^2 of surface area in the PHX becomes less useful.

Geometric Parameters

In the most basic configuration of a PHX, hot and cold streams in pure counterflow alternate through the stack of plates. From the side view, a simplified schematic of the PHX is shown in Figure F.9.

In practice, it is sometimes useful to have one of the stream do multiple passes for one pass of the other stream, but this capability is not included in the PHX model as of this time. This is commonly used when the capacitance rates are very different, a sufficient heat transfer rate cannot be achieved for one fluid, or when one of the fluids is particularly sensitive to pressure drop. All of these issues are particularly strongly felt for the flow of gases.

The front view of a typical PHX heat exchanger is illustrated in Figure F.10. Robust gasketing of the plates is required to ensure that the fluid phases do not mix at the inlets and outlets of the plates. Each of the plates that form the internal surface of the PHX are formed of plates with a wavy shape, and the edge of the plate are similar to those shown in Figure F.11.

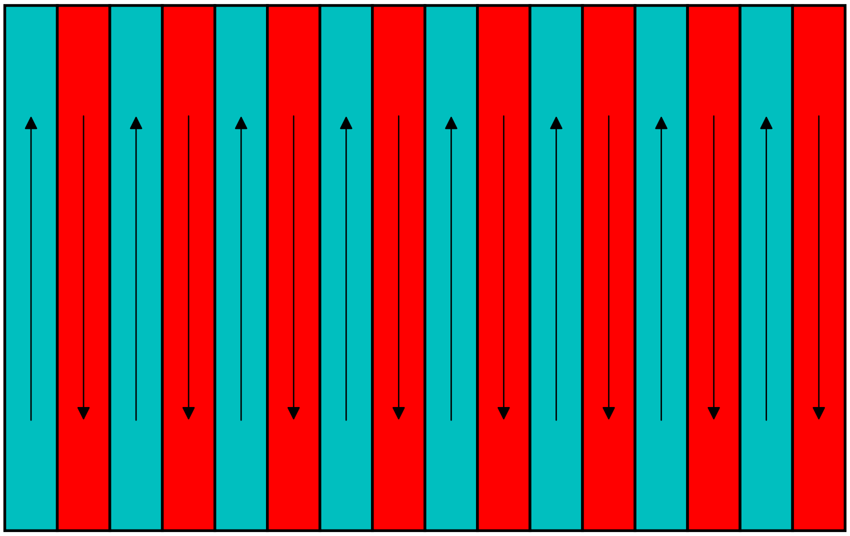

Figure F.9. Schematic of side-view for counterflow plate heat exchanger (Bell, 2015).

Based on this geometry, the hydraulic diameter d_h is defined by

$$d_h = \frac{4\hat{a}}{\Phi} \tag{F.84}$$

where the parameter Φ is the ratio of the actual area to the planar area enclosed by the edges of the plate (bounded by L and B, as shown in Figures F.10 and F.11). Typically the plates do not have exactly a sinusoidal profile, but, to a decent approximation, their profile is sinusoidal, which results in the value of Φ of

$$\Phi = \frac{1}{6}\left(1 + \sqrt{1+X^2} + 4\sqrt{1+X^2/2}\right) \tag{F.85}$$

where the wavenumber X is given by

$$X = 2\pi\hat{a}/\Lambda \tag{F.86}$$

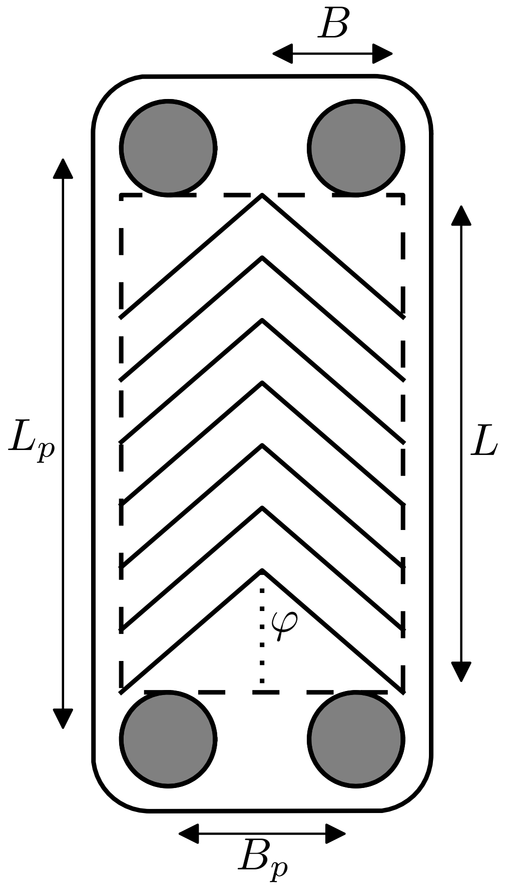

Figure F.10. Definition of geometrical parameters of plate heat exchanger (Bell, 2015).

When the plates are put together to form a stack, the plates are alternated, and as a result, chevron-shaped flow paths are formed, which have the effect of yielding highly mixed flow, resulting in good heat transfer coefficients.

A stack of N_{plates} forms the heat exchanger. There are total of $N_{channels}$ formed between the plates. If $N_{channels}$ is evenly divisible by 2, both fluids have the same number of channels. If $N_{channels}$ is not evenly divisible by 2, one stream must have one extra channel. The outer two plates do not provide any heat transfer as they are just used to maintain the channel structure for the outermost channels. Therefore, a

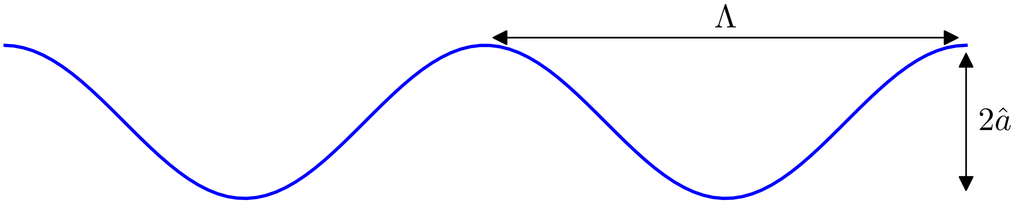

Figure F.11. Wavy profile shape for a single plate in plate heat exchanger (Bell, 2015).

total of $N_{plates} - 2$ are active plates, for which the active area of one side of one plate is equal to

$$A_{1p} = B_p L_p \Phi \tag{F.87}$$

Each channel of a fluid gets two sides of this area, which yields the cold- and hot-side wetted areas of

$$\begin{aligned} A_h &= 2N_{channels,h} A_{1p} \\ A_c &= 2N_{channels,c} A_{1p} \end{aligned} \tag{F.88}$$

and the volumes are

$$\begin{aligned} V_h &= N_{channels,h} B_p 2\hat{a} \\ V_c &= N_{channels,c} B_p 2\hat{a} \end{aligned} \tag{F.89}$$

and the mass flow rate of the hot and cold fluids per circuit are equal to

$$\begin{aligned} \dot{m}_{h,ch} &= \dot{m}_h / N_{channels,h} \\ \dot{m}_{c,ch} &= \dot{m}_c / N_{channels,c} \end{aligned} \tag{F.90}$$

Mathematical Description

With the set of required correlations defined, it is now possible to analyze the plate heat exchanger (PHX) for a range of different configurations. The PHX model is constructed to be general enough that it can handle any phase of fluids entering into the heat exchanger. The basic idea behind the PHX model is a two-step process:

1. Determine the bounding heat transfer rate (100% effectiveness) limited by taking each fluid to the inlet temperature of the other fluid. This is the maximum amount of heat transfer possible. In addition, to be aware for internal pinch points.
2. Since the heat transfer rate is now bounded between zero and the maximum, iterate to find the actual heat transfer rate in the heat exchanger in order to yield the actual size of PHX as described in the next section.

Bounds on Heat Transfer Rate

Since the PHX is pure counterflow, the lowest possible temperature that the hot stream can achieve is the inlet temperature of the cold stream, and similarly, the highest temperature that the cold stream can achieve is the inlet temperature of the hot stream. The inlet enthalpies of the hot stream $h_{h,i}$ and the cold stream $h_{c,i}$ allow to calculate a preliminary value for the upper bound on the heat transfer rate:

$$\begin{aligned} \dot{Q}_{max,h} &= \dot{m}_h \left[h_{h,i} - h(T = T_{c,i}, P = P_{h,i}, \mathrm{Ref}_h)\right] \\ \dot{Q}_{max,c} &= \dot{m}_c \left[h(T = T_{h,i}, P = P_{c,i}, \mathrm{Ref}_c) - h_{c,i}\right] \\ \dot{Q}_{max,\epsilon=1} &= \max[\dot{Q}_{max}, \dot{Q}_{min}] \end{aligned} \tag{F.91}$$

Using this preliminary bound on the heat transfer rate, it is then possible to determine the enthalpies and temperatures of both fluids at each of their phase transitions (if they exist).

In the case of an evaporator that cools a water stream (hot-side), there is no possibility of temperature inversion within the heat exchanger because the refrigerant enters at some quality greater than zero, and there is no possibility that the isobar of the refrigerant could intersect the isobar of the hot water. Figure F.12 illustrates this configuration.

Since the heat transfer rate is known, it can be determined whether any of the phase transitions can be physically reached. In the configuration shown in Figure F.12, there are two regions; In cell 1, the hot fluid (water) is single-phase and the cold fluid (refrigerant) is evaporating, and in cell 2, the hot fluid is still single-phase, and the cold fluid is now single-phase as well.

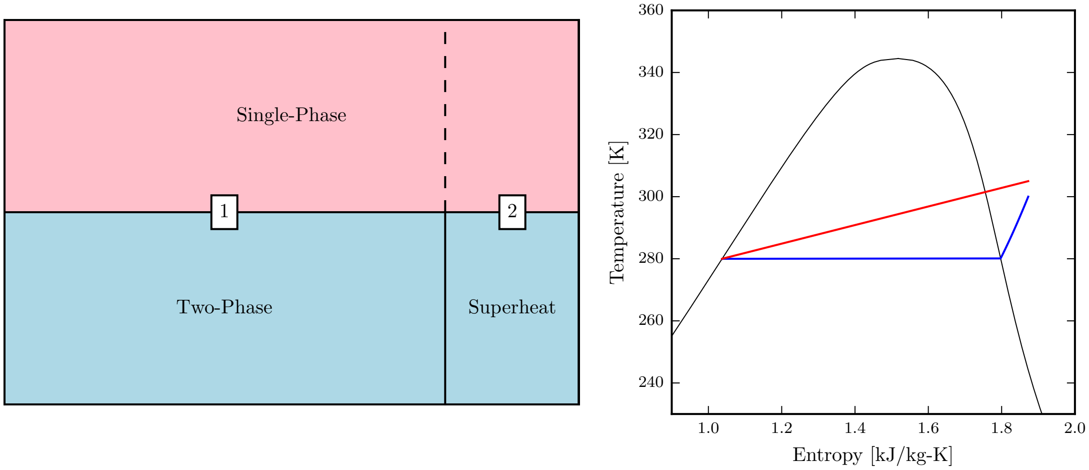

Figure F.12. Case of no internal pinching for $\dot{Q}_{max,\epsilon=1}$ where hot stream fluid is single-phase (Bell, 2015).

On the other hand, if the refrigerant were condensing, and entering at some subcooling amount greater than zero, for instance 10K, the analysis is slightly different. In this case, it is entirely possible that there could be temperature inversion at the heat transfer rate given by $\dot{Q}_{max,\epsilon=1}$, as shown in Figure F.13.

Thus, a new maximum heat transfer rate $\dot{Q}_{max}$ can be determined that is less than $\dot{Q}_{max,\epsilon=1}$ whereby the temperatures of the two streams are equated at the possible pinch point, which resembles the behavior shown in Figure F.14.

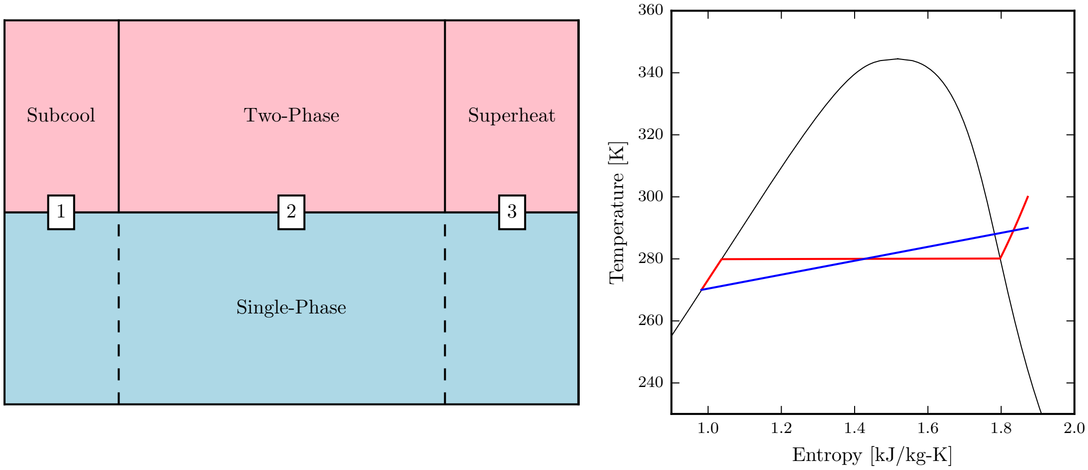

Figure F.13. Case of internal pinching for $\dot{Q}_{max,\epsilon=1}$ where cold stream fluid is single-phase (Bell, 2015).

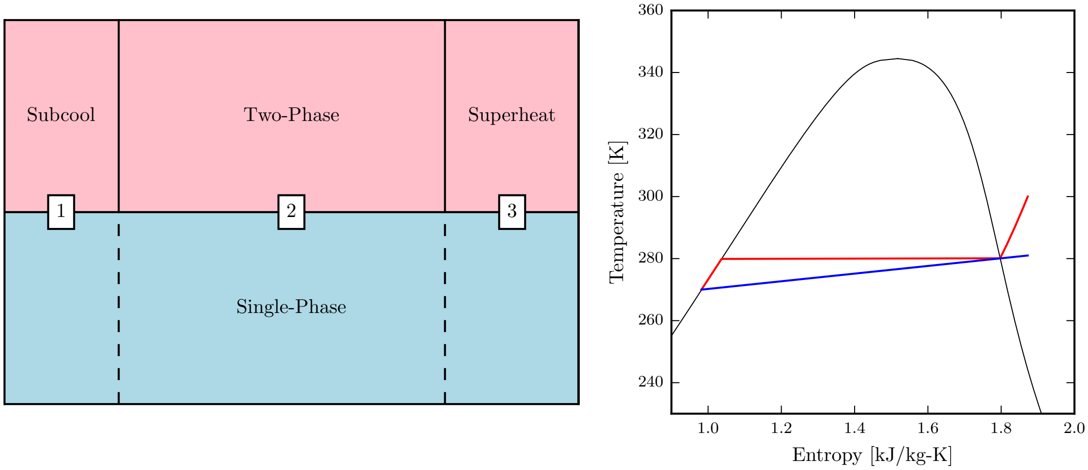

Figure F.14. Case of pinching at $\dot{Q}_{max}$ where cold stream fluid is single-phase (Bell, 2015).

In this case, the water (cold-side) is limiting the heat transfer rate, and the maximum heat transfer rate can be given by taking the water all the way to the dew-point temperature of the refrigerant (hot-side), and using the known heat transfer rate in cell 3. The cold-stream pinch enthalpy is given by

$$h_{pinch} = h(T = T_{dew,h}, P = P_c, \mathrm{Ref}_c) \tag{F.92}$$

Since the inlet enthalpy and outlet enthalpy (saturated vapor) of the hot refrigerant are known in cell 3, the heat transfer rate in cell 3 is known from

$$\dot{Q}_{cell,3} = \dot{m}_h \left[h_{h,i} - h(T = T_{dew,h}, x = 1, \mathrm{Ref}_h)\right] \tag{F.93}$$

and the new limiting heat transfer rate can be given by

$$\dot{Q}_{max} = \dot{m}_c(h_{pinch} - h_{c,i}) + \dot{Q}_{cell,3} \tag{F.94}$$

where the term $\dot{m}_c(h_{pinch} - h_{c,i})$ is from heating up the cold fluid to the pinch-point temperature.

Calculation of Heat Transfer Rate

Now that the physical bounds on the heat transfer rate in the PHX have been determined, it is now possible to finish analyzing the PHX performance. For a given $\dot{Q} < \dot{Q}_{max}$, there are a number of different cells, and in each one, at least one of the fluids has a phase transition. In the degenerate case that both fluids are single-phase throughout the PHX, there is only one cell, and no phase transitions anywhere in the heat exchanger. The discussion that follows here assumes that the heat transfer rate $\dot{Q}$ is known, but in fact, it is iteratively obtained by a bounded solver (Brent, 1973) because $\dot{Q}$ is known to be between 0 and $\dot{Q}_{max}$.

For a given $\dot{Q}$, the outlet enthalpies are known, which begins the process of building enthalpy vectors for both streams. The outlet enthalpies for each stream are given by

$$\begin{aligned} h_{h,o} &= h_{h,i} - \dot{Q}/\dot{m}_h \\ h_{c,o} &= h_{c,i} + \dot{Q}/\dot{m}_c \end{aligned} \tag{F.95}$$

which yields the initial enthalpy vectors (ordered from low to high enthalpy) of

$$\begin{aligned} \vec{h}_h &= [h_{h,o}, h_{h,i}] \\ \vec{h}_c &= [h_{c,i}, h_{c,o}] \end{aligned} \tag{F.96}$$

To these enthalpy vectors are now added any phase transitions that exist; a phase transition exists if its corresponding saturation enthalpy is between the inlet and outlet enthalpies of the fluid. With each phase transition enthalpy comes a partner enthalpy of the other stream. This set of enthalpy vectors then define the enthalpies of both streams at each cell edge. For instance, in the case shown in Figure F.12, there is one phase transition where the refrigerant transitions between two-phase and superheated vapor. The enthalpy of the cold stream at the phase transition (PT) point is given by

$$h_{PT} = h(T = T_{dew,c}, x = 1, \mathrm{Ref}_c) \tag{F.97}$$

and the enthalpy of the hot stream at the phase transition h^*_{PT} can be obtained by an energy balance over cell 2, which yields

$$\dot{m}_h(h_{h,i} - h_{PT}) = \dot{m}_c(h_{c,o} - h^*_{PT}) \tag{F.98}$$

or

$$h^*_{PT} = h_{c,o} - \frac{\dot{m}_h(h_{h,i} - h_{PT})}{\dot{m}_c} \tag{F.99}$$

and now the enthalpy vectors are given by the values

$$\begin{aligned} \vec{h}_h &= [h_{h,o}, h_{PT}, h_{h,i}] \\ \vec{h}_c &= [h_{c,i}, h^*_{PT}, h_{c,o}] \end{aligned} \tag{F.100}$$

If there are multiple phase transitions on each side, the same method is applied, where the phase transition enthalpies and their partner enthalpies are obtained by an energy balance on the new cell that is formed, working from the outer edges of the enthalpy vectors towards the inside since the outlet enthalpies of both streams are known and can be used in the energy balances to back out partner enthalpies.

For a given value of $\dot{Q}$, each of the enthalpy vectors has the same length of $N_{cell}+1$, which then form the enthalpy boundaries for the N_{cell} cells. In each cell, first the phase of each fluid must be determined. Each fluid will have the same phase throughout the entire cell which is the main idea behind this method. The average enthalpy of each fluid in the cell can be used to determine the phase of each fluid in the cell. Our goal now is to determine how much of the physical length of the heat exchanger is required to obtain the given duty in each cell. The required physical heat exchanger length of the cell w can be given by

$$L_i = w_i L \tag{F.101}$$

where all the w_i parameters must sum to unity.

In a given cell, the heat transfer rate is known because this is how the enthalpy vectors have been constructed. The heat transfer rate in the cell can be given by

$$\dot{Q}_i = \dot{m}_r(\vec{h}_{h,i+1} - \vec{h}_{h,i}) \tag{F.102}$$

So long as at least one of the fluids in the cell is single-phase, the effectiveness in the cell can be defined by

$$\epsilon = \frac{\dot{Q}_i}{C_{min}(T_{h,i,cell} - T_{c,i,cell})} \tag{F.103}$$

where $T_{h,i,cell}$ and $T_{c,i,cell}$ are the hot fluid and cold fluid inlet temperatures to the cell. The minimum capacitance rate C_{min} is by definition on the single-phase-fluid side. In the single-phase/two-phase cell case, the minimum capacitance rate is given by

$$C_{min} = \dot{m}_{\mathrm{single-phase}} c_{p,\mathrm{single-phase}} \tag{F.104}$$

and since the flow is pure counter-flow, the NTU can be obtained directly from

$$\mathrm{NTU} = -\ln(1-\epsilon) \qquad (C_r = 0) \tag{F.105}$$

If both fluids are single phase, the minimum capacitance rate can be obtained from

$$\begin{aligned} C_{min} &= \min[\dot{m}_h c_{p,h}, \dot{m}_c c_{p,c}] \\ C_{max} &= \max[\dot{m}_h c_{p,h}, \dot{m}_c c_{p,c}] \\ C_r &= C_{min}/C_{max} \end{aligned} \tag{F.106}$$

which yields the NTU for the single-phase/single-phase cell with pure counterflow of

$$\mathrm{Ntu} = \frac{1}{C_r - 1} \ln\left(\frac{\epsilon - 1}{\epsilon C_r - 1}\right) \qquad (C_r < 1) \tag{F.107}$$

and the required heat conductance can be obtained from

$$\mathrm{UA}_{req} = \mathrm{NTU}\ C_{min} \tag{F.108}$$

The actual heat transfer conductance in the call can be given by

$$\mathrm{UA}_{actual} = \frac{1}{\alpha_c A_c} + \frac{t}{kA} + \frac{1}{\alpha_h A_h} \tag{F.109}$$

where the areas are based on the total wetted area of the heat exchanger and local heat transfer coefficients (α_h and α_c) for the cell are employed (see Section *Pressure Drop and Heat Transfer in Plate Heat Exchanger Economizer* in Appendix F). The fraction of the heat exchanger that would be required for the given thermal duty in the cell can be obtained from

$$w_i = \frac{\mathrm{UA}_{req}}{\mathrm{UA}_{actual}} \tag{F.110}$$

Determination of Thermal Duty

Finally, the heat transfer rate in the PHX is obtained through an iterative scheme. The value of $\dot{Q}$ is known to be between zero and $\dot{Q}_{max}$, and the residual to be driven to zero by a numerical solver (Brent, 1973) is

$$\Delta = 1 - \sum_i w_i \tag{F.111}$$

which yields to zero if $\dot{Q}$ has been appropriately found.

F.6 Pre-Conditioner Model

In order to obtain good initial guesses for the cycle solver (*i.e.,* the dew-point temperatures of the refrigerant in the evaporator, condenser and economizer, namely T_{evap}, T_{cond}, and $T_{dew,inj}$, respectively), a pre-conditioner model is used. The pre-conditioner model developed in Bell (2015) is modified for the purpose of this work. The following assumptions are employed in the pre-conditioner model:

- Condenser air stream is the minimum capacitance rate in the condenser, and the limiting outlet state for the air in the condenser is T_{cond}
- Effectiveness of all heat exchangers is constant (*i.e.,* $\epsilon_{HX} = 0.96$)
- Compressor and economizer superheats are constant
- Compressor and economizer are adiabatic
- Evaporator is fully wet, fully dry, or a simple weighted mix of the two
- Isenthalpic expansion valves
- Line sets (*i.e.,* vapor line and liquid line) are not considered
- Air specific heat and density are constant (*i.e.,* $\rho_{da} = 1.2$ kg/m^3, and $c_{p,a} = 1.005$ kJ/kg-K)

The cycle pre-conditioner algorithm is shown in Figure 3.10 and the analysis as follows.

In the compressor, for a given set of dew-point temperatures (T_{evap}, T_{cond}, and $T_{dew,inj}$) and known superheats ($\Delta T_{sh,suc}$, $\Delta T_{sh,inj}$), the inlet, outlet and injection pressures can be computed. Hence, the compressor map (Equations (3.7) to (3.9)) can be used to predict the refrigerant mass flow rates as well as the compressor power as

$$\dot{m}_{suc} = f_{map}(T_{evap}, T_{cond}, \Delta T_{sh,suc}) \tag{F.112}$$

$$\dot{m}_{inj} = f_{map}(\dot{m}_{suc}, P_{evap}, P_{inj}) \tag{F.113}$$

$$\dot{W}_{comp} = f_{map}(T_{evap}, T_{cond}, T_{dew,inj}, \Delta T_{sh,suc}, \Delta T_{sh,inj}) \tag{F.114}$$

In the condenser, the heat transfer rate can be found by

$$\dot{Q}_{cond,a} = \epsilon_{HX}\rho_{da}\dot{V}_{ha,cond}c_{p,a}(T_{i,a,cond} - T_{cond}) \tag{F.115}$$

The condenser heat transfer rate based on the imposed subcooling can also be found by

$$\dot{Q}_{cond,r} = (\dot{m}_{suc} + \dot{m}_{inj})\,(h_{r,o,comp} - h_{r,o,cond}) \tag{F.116}$$

where $h_{r,o,cond}$ is the targeted condenser outlet enthalpy *i.e.,* $h = f(T_{cond} - \Delta T_{sc}, P_{cond})$. Theoretically, those two heat transfer rate terms should match, and consistency is imposed by the numerical solver that is employed.

Due to several cases that the evaporator could encounter (*i.e.,* coil being fully-wet, fully-dry, or partially-wet and partially-dry), it is considered the most complicated component in the system. To simplify the solver, the next steps are followed. Similarly, as in the full evaporator model, the evaporator is first considered to be fully-dry, yielding the heat transfer rate of

$$\dot{Q}_{evap,dry} = \epsilon_{HX}\rho_{da}\dot{V}_{ha,evap}c_{p,a}(T_{i,a,evap} - T_{evap}) \tag{F.117}$$

Then using the dry evaporator heat transfer analysis, it is possible to determine the surface temperature. The UA values for refrigerant-side and air-side can be expressed respectively as

$$\mathrm{UA}_r = \alpha_r A_{r,total} \tag{F.118}$$

$$\mathrm{UA}_a = \eta_a \alpha_a A_{a,total} \tag{F.119}$$

The outlet temperature on the air-side can be determined by

$$T_{o,a,evap} = T_{i,a,evap} - \frac{\dot{Q}_{evap,dry}}{\dot{m}_{a,total}c_{p,a}} \tag{F.120}$$

which yields the air-side inlet surface temperature of

$$T_{s,a,i} = \frac{\mathrm{UA}_a T_{i,a,evap} + \mathrm{UA}_r T_{evap}}{\mathrm{UA}_a + \mathrm{UA}_r} \tag{F.121}$$

and the air outlet surface temperature of

$$T_{s,a,o} = \frac{\mathrm{UA}_a T_{o,a,evap} + \mathrm{UA}_r T_{evap}}{\mathrm{UA}_a + \mathrm{UA}_r} \tag{F.122}$$

If both $T_{s,a,o}$ and $T_{s,a,i}$ are above the dew-point temperature of the entering air (*i.e.,* T_{dp}), the rate of heat transfer in the evaporator is equal to the dry-analysis heat transfer rate, and evaporator heat transfer rate is determined by Equation (F.117). If both $T_{s,a,o}$ and $T_{s,a,i}$ are below the dew-point of the entering air, the coil is entirely wet, for which the heat transfer rate can be obtained from

$$\dot{Q}_{evap,wet} = \epsilon_{HX} \rho_{da} \dot{V}_{ha,evap} (h_{a,i} - h_{a,s,evap}) \tag{F.123}$$

where $h_{a,s,evap}$ is the saturated air enthalpy at T_{evap} and $h_{a,i}$ is the enthalpy of the inlet air to the evaporator.

In the case which the dew-point of the inlet air is between $T_{s,a,o}$ and $T_{s,a,i}$, the heat transfer rate in the evaporator is given by a simple weighted sum as

$$\dot{Q}_{evap} = f_{dry} \dot{Q}_{evap,dry} + (1 - f_{dry}) \dot{Q}_{evap,wet} \tag{F.124}$$

where f_{dry} can be expressed by

$$f_{dry} = 1 - \frac{T_{dp} - T_{s,a,i}}{T_{s,a,o} - T_{s,a,i}} \tag{F.125}$$

Thus, the evaporator simple analysis can be summarized as follows:

$$\dot{Q}_{evap} = \begin{cases} \dot{Q}_{evap,dry} & T_{s,a,o} > T_{dp} \text{ and } T_{s,a,i} > T_{dp} \\ \dot{Q}_{evap,wet} & T_{s,a,o} < T_{dp} \text{ and } T_{s,a,i} < T_{dp} \\ f_{dry}\dot{Q}_{evap,dry} + (1 - f_{dry})\,\dot{Q}_{evap,wet} & T_{s,a,i} > T_{dp} > T_{s,a,o} \end{cases} \tag{F.126}$$

Considering the assumption of adiabatic economizer and isenthalpic expansion process across both expansion valves, an energy balance is then performed on the evaporator to determine the states on the economizer (*i.e.,* cold-side inlet and hot-side outlet)

$$h_{r,i,evap} = h_{r,i,comp} - \frac{\dot{Q}_{evap}}{\dot{m}_{suc}} \tag{F.127}$$

where $h_{r,i,evap} = h_{h,o,econ} = h_{c,i,econ}$.

The cold-side heat transfer rate of the economizer is calculated from

$$\dot{Q}_{econ,c} = \dot{m}_{inj}\left(h_{r,inj} - h_{c,i,econ}\right) \tag{F.128}$$

and the hot-side heat transfer rate of the economizer is given by

$$\dot{Q}_{econ,h} = \left(\dot{m}_{inj} + \dot{m}_{suc}\right)\left(h_{h,i,econ} - h_{h,o,econ}\right) \tag{F.129}$$

where $h_{h,i,econ}$ is equal to the targeted condenser outlet enthalpy (*i.e.,* $h_{r,o,cond}$).

Finally, the residuals to be driven to 0 are the overall energy balance over the system, as well as matching $\dot{Q}_{cond,a}$ with $\dot{Q}_{cond,r}$, and $\dot{Q}_{econ,h}$ with $\dot{Q}_{econ,c}$. The residual vector as a function of T_{evap}, T_{cond}, and $T_{dew,inj}$ is given in Equation (3.10). A non-linear multi-dimensional numerical solver is used to drive the norm of $\vec{\Delta}$ to sufficiently close to zero by altering T_{evap}, T_{cond}, and $T_{dew,inj}$.

F.7 Refrigerant Correlations

A model is only as good as the correlations it is based on. A number of heat transfer and pressure drop correlations are needed for condenser, evaporator and plate heat exchanger (PHX) economizer models. Tables F.6, F.7, and F.8 summarize the correlations used for micro-channel condenser, fin-and-tube evaporator, and PHX economizer models, respectively.

Table F.6. Summary of correlations employed in micro-channel condenser model.

Parameter	Reference
Single-Phase Pressure Drop	Churchill (1977)
Single-Phase Heat Transfer	Gnielinski (1976)
Two-Phase Condensation Pressure Drop	Kim and Mudawar (2012)
Two-Phase Condensation Heat Transfer	Kim and Mudawar (2013)
Two-Phase Refrigerant Charge	Zivi (1964)

Table F.7. Summary of correlations employed in fin-and-tube evaporator model.

Parameter	Reference
Single-Phase Pressure Drop	Churchill (1977)
Single-Phase Heat Transfer	Gnielinski (1976)
Two-Phase Evaporation Pressure Drop	Lockhart and Martinelli (1949)
Two-Phase Evaporation Heat Transfer	Shah (1976)
Two-Phase Refrigerant Charge	Zivi (1964)

Table F.8. Summary of correlations employed in PHX economizer model.

Parameter	Reference
Single-Phase Pressure Drop	Martin (2010)
Single-Phase Heat Transfer	Martin (2010)
Two-Phase Pressure Drop	Claesson (2004); Lockhart and Martinelli (1949)
Two-Phase Evaporation Heat Transfer	Cooper (1984)
Two-Phase Condensation Heat Transfer	Longo (2010, 2011); Longo et al. (2004)
Two-Phase Refrigerant Charge	Zivi (1964)

Pressure Drop and Heat Transfer in Micro-Channel Condenser

In the two-phase region, the pressure drop components are the frictional pressure drop, the accelerational pressure drop, and the gravitational pressure drop (assumed to be negligible). The Kim and Mudawar (2012) correlation is used to find the frictional pressure drop gradient in micro-channel condenser, but it varies with quality. The total pressure drop is then found by integrating the pressure drop gradient over the range of qualities of interest. In the micro-channel condenser, the heat transfer coefficient can be a function of flow patterns which are annular, slug or bubbly flows, and therefore Kim and Mudawar (2013) correlation is used. Zivi (1964) void fraction correlation is used to count for the charge in two-phase section of the micro-channel condenser.

Two-Phase Condensation Pressure Drop

The two-phase frictional pressure drop gradient is based on the following algorithm:

1. Find the superficial Reynolds Number for each phase based on the actual flow rate of the individual phase

$$\mathrm{Re}_g = \frac{GxD_h}{\mu_g} \tag{F.130}$$

$$\mathrm{Re}_f = \frac{G(1-x)D_h}{\mu_f} \tag{F.131}$$

2. Friction factor for each phase

$$f_k = \begin{cases} \dfrac{16.0}{\mathrm{Re}_k} & \mathrm{Re}_k < 2000 \\ \dfrac{0.079}{\mathrm{Re}_k^{0.25}} & 2000 \le \mathrm{Re}_k < 20,000 \\ \dfrac{0.046}{\mathrm{Re}_k^{0.2}} & \mathrm{Re}_k \ge 20,000 \end{cases} \tag{F.132}$$

where the subscript k denotes f or g for liquid and vapor phases, respectively. Special case for laminar flow in rectangular channel, the two-phase friction factor can be given as

$$f_k \mathrm{Re}_k = 24(1 - 1.3553\beta + 1.9467\beta^2 - 1.7012\beta^3 + 0.9564\beta^4 - 0.2537\beta^5) \quad \text{(F.133)}$$

where β is the channel aspect ratio.

3. Frictional pressure drop based on actual flow rate of each phase

$$-\left(\frac{dP}{dz}\right)_f = \frac{2f_f G^2 (1-x)^2 v_f}{D_h} \quad \text{(F.134)}$$

$$-\left(\frac{dP}{dz}\right)_g = \frac{2f_g G^2 x^2 v_g}{D_d} \quad \text{(F.135)}$$

4. Lockhart-Martinelli parameter

$$X^2 = \frac{\left(\frac{dP}{dz}\right)_f}{\left(\frac{dP}{dz}\right)_g} \quad \text{(F.136)}$$

5. Find the liquid Reynolds Number and the vapor Suratman Number based on the actual flow rate

$$\mathrm{Re}_{fo} = \frac{GD_h}{\mu_f} \quad \text{(F.137)}$$

$$\mathrm{Su}_{go} = \frac{\rho_g \sigma D_h}{\mu_g^2} \quad \text{(F.138)}$$

6. Find the Lockhart-Martinelli Constant (C-coefficient) based on liquid Reynolds Number and the vapor Suratman Number (using 2000 as the transitional Re to ensure continuity)

$$C = \begin{cases} 0.39\mathrm{Re}_{fo}^{0.03}\mathrm{Su}_{go}^{0.10}\left(\dfrac{\rho_f}{\rho_g}\right)^{0.35} & \mathrm{Re}_f \geq 2000 \ \&\ \mathrm{Re}_g \geq 2000 \\ 8.7\times10^{-4}\mathrm{Re}_{fo}^{0.17}\mathrm{Su}_{go}^{0.50}\left(\dfrac{\rho_f}{\rho_g}\right)^{0.14} & \mathrm{Re}_f \geq 2000 \ \&\ \mathrm{Re}_g < 2000 \\ 0.0015\mathrm{Re}_{fo}^{0.59}\mathrm{Su}_{go}^{0.19}\left(\dfrac{\rho_f}{\rho_g}\right)^{0.36} & \mathrm{Re}_f < 2000 \ \&\ \mathrm{Re}_g \geq 2000 \\ 3.5\times10^{-5}\mathrm{Re}_{fo}^{0.44}\mathrm{Su}_{go}^{0.50}\left(\dfrac{\rho_f}{\rho_g}\right)^{0.48} & \mathrm{Re}_f < 2000 \ \&\ \mathrm{Re}_g < 2000 \end{cases} \tag{F.139}$$

7. Two-phase multipliers for each phase

Gas multiplier

$$\phi_g^2 = 1 + CX + X^2 \tag{F.140}$$

Fluid multiplier

$$\phi_f^2 = 1 + \frac{C}{X} + \frac{1}{X^2} \tag{F.141}$$

8. Find condensing frictional pressure drop gradient for a given value of x

$$-\left(\frac{dP}{dz}\right)_{f,2\phi} = \begin{cases} -\left(\dfrac{dP}{dz}\right)_g \phi_g^2 & -\left(\dfrac{dP}{dz}\right)_g \phi_g^2 > -\left(\dfrac{dP}{dz}\right)_f \phi_f^2 \\ -\left(\dfrac{dP}{dz}\right)_f \phi_f^2 & -\left(\dfrac{dP}{dz}\right)_g \phi_g^2 < -\left(\dfrac{dP}{dz}\right)_f \phi_f^2 \end{cases} \tag{F.142}$$

9. Average frictional pressure drop gradient is calculated iteratively using Simpson's rule to carry out numerical integration

$$\overline{\Delta P_{f,2\phi}} = \frac{\displaystyle\int_{x_1}^{x_2} -\left(\frac{dP}{dz}\right)_{f,2\phi} dx}{x_2 - x_1} \tag{F.143}$$

Accelerational Pressure Drop

The accelerational pressure drop calculation is based on the consideration of two-phase flow. It is caused by the change in velocity of the vapor and liquid phases due to phase change, which in the case of condensation, reduces the vapor velocity, resulting in a pressure increase.

$$-\left(\frac{\partial P}{\partial z}\right)_{A,2\phi} = G^2 \frac{d}{dz}\left[\frac{x^2 v_g}{\varepsilon} + \frac{(1-x)^2 v_f}{1-\varepsilon}\right] \tag{F.144}$$

where ε is the refrigerant vapor void fraction[3].
Integrating over the length where the quality goes from x_1 to x_2 yields

$$\Delta P_{A,2\phi} = \int_0^L \left[-\left(\frac{\partial P}{\partial z}\right)_{A,2\phi} dz\right] \tag{F.145}$$

and thus

$$\Delta P_{A,2\phi} = G^2 L \left[\left(\frac{x_2^2 v_g}{\varepsilon_2} + \frac{(1-x_2)^2 v_f}{1-\varepsilon_2}\right) - \left(\frac{x_1^2 v_g}{\varepsilon_1} + \frac{(1-x_1)^2 v_f}{1-\varepsilon_1}\right)\right] \tag{F.146}$$

If the quality in the term

$$\left(\frac{x^2 v_g}{\varepsilon} + \frac{(1-x)^2 v_f}{1-\varepsilon}\right) \tag{F.147}$$

is 0 or 1, one part is zero and the other is an indeterminate form of 0/0. One evaluation of L'Hopital's rule can be used to show that if the quality is zero, the term in Equation (F.147) is equal to v_f, or if the quality is 1, this term is equal to v_g.

Two-Phase Condensation Heat Transfer

Since the heat transfer coefficient for micro-channel condenser is based on the flow pattern (annular flow, slug or bubbly flow) as stated in Kim and Mudawar (2013), so the average condensing heat transfer coefficient is based on the following algorithm:

---

[3] To avoid confusion with heat transfer coefficient α, ε is used for void fraction

1. Find the Lockhart-Martinelli parameter

$$X_{tt} = \left(\frac{\mu_f}{\mu_g}\right)^{0.1} \left(\frac{1-x}{x}\right)^{0.9} \left(\frac{\rho_g}{\rho_f}\right)^{0.5} \tag{F.148}$$

2. Find the modified Weber Number

$$\mathrm{We}^* = \begin{cases} 2.45 \dfrac{\mathrm{Re}_g^{0.64}}{\mathrm{Su}_{go}^{0.3} \left(1 + 1.09 X_{tt}^{0.039}\right)^{0.4}} & \mathrm{Re}_f \leq 1250 \\ 0.85 \dfrac{\mathrm{Re}_g^{0.79} X_{tt}^{0.157}}{\mathrm{Su}_{go}^{0.3} \left(1 + 1.09 X_{tt}^{0.039}\right)^{0.4}} \left[\left(\dfrac{\mu_g}{\mu_f}\right)^2 \left(\dfrac{\rho_f}{\rho_g}\right)\right]^{0.084} & \mathrm{Re}_f > 1250 \end{cases} \tag{F.149}$$

3. The heat transfer coefficient for a given quality x is given by

   for annual flow (smooth-annular, wavy-annular, and transition flows) ($\mathrm{We}^* > 7X_{tt}^{0.2}$):

$$\alpha_{2\phi} = 0.048 \frac{k_f}{D_h} \mathrm{Re}_f^{0.69} \mathrm{Pr}_f^{0.34} \frac{\phi_g}{X_{tt}} \tag{F.150}$$

   for slug and bubbly flows ($\mathrm{We}^* < 7X_{tt}^{0.2}$):

$$\alpha_{2\phi} = \frac{k_f}{D_h} \left[\left(0.048 \mathrm{Re}_f^{0.69} \mathrm{Pr}_f^{0.34} \frac{\phi_g}{X_{tt}}\right)^2 + \left(3.2 \times 10^{-7} \mathrm{Re}_f^{-0.38} \mathrm{Su}_{go}^{1.39}\right)^2\right]^{0.5} \tag{F.151}$$

4. The average condensation heat transfer coefficient between a quality of x_1 and x_2 is given by

$$\overline{\alpha_{2\phi}} = \frac{\displaystyle\int_{x_1}^{x_2} \alpha_{2\phi}(x)\, dx}{x_2 - x_1} \tag{F.152}$$

   where the integral is evaluated numerically using Simpson's rule.

Pressure Drop and Heat Transfer in Fin-and-Tube Evaporator

In the two-phase region, the pressure drop components are the frictional pressure drop, the accelerational pressure drop, and the gravitational pressure drop (assumed to be negligible). The Lockhart and Martinelli (1949) correlation is used to find the frictional pressure drop gradient in fin-and-tube evaporator, but it varies with quality. The total pressure drop is then found by integrating the pressure drop gradient over the range of qualities of interest. In the evaporator, the heat transfer coefficient can be a function of flow patterns which are annular, slug or bubbly flows, and therefore Shah (1976) correlation is used. Zivi (1964) void fraction correlation is used to count for the charge in two-phase section of the fin-and-tube evaporator.

Two-Phase Evaporation Pressure Drop

The two-phase frictional pressure drop gradient is based on the following algorithm:

1. Find the superficial Reynolds Number for each phase based on the actual flow rate of the individual phase

$$\mathrm{Re}_g = \frac{GxD_h}{\mu_g} \tag{F.153}$$

$$\mathrm{Re}_f = \frac{G(1-x)D_h}{\mu_f} \tag{F.154}$$

2. Friction factor for each phase

$$f_k = \begin{cases} \dfrac{16.0}{\mathrm{Re}_k} & \mathrm{Re}_k < 1000 \\ \dfrac{0.046}{\mathrm{Re}_k^{0.2}} & \mathrm{Re}_k > 2000 \\ (1-w)\dfrac{16.0}{\mathrm{Re}_k} + w\dfrac{0.046}{\mathrm{Re}_k^{0.2}} & 1000 < \mathrm{Re}_k < 2000 \end{cases} \tag{F.155}$$

where the subscript k denotes f or g for liquid and vapor phases, respectively, and $w = (\mathrm{Re}_k - 1000)/(2000 - 1000)$ which results in a linear interpolation for the transitional Reynolds number region.

3. Frictional pressure drop based on actual flow rate of each phase

$$-\left(\frac{dP}{dz}\right)_f = \frac{2f_f G^2(1-x)^2 v_f}{D} \tag{F.156}$$

$$-\left(\frac{dP}{dz}\right)_g = \frac{2f_g G^2 x^2 v_g}{D} \tag{F.157}$$

4. Lockhart-Martinelli parameter

$$X^2 = \frac{\left(\dfrac{dP}{dz}\right)_f}{\left(\dfrac{dP}{dz}\right)_g} \tag{F.158}$$

5. Find the Lockhart-Martinelli Constant (C-coefficient) based on the flow Re of each phase (using 1500 as the transitional Re to ensure continuity)

$$C = \begin{cases} 20 & \mathrm{Re}_f > 1500 \ \& \ \mathrm{Re}_g > 1500 \\ 12 & \mathrm{Re}_f < 1500 \ \& \ \mathrm{Re}_g > 1500 \\ 10 & \mathrm{Re}_f > 1500 \ \& \ \mathrm{Re}_g < 1500 \\ 5 & \mathrm{Re}_f < 1500 \ \& \ \mathrm{Re}_g < 1500 \end{cases} \tag{F.159}$$

6. Two-phase multipliers for each phase

   Gas multiplier

$$\phi_g^2 = 1 + CX + X^2 \tag{F.160}$$

   Fluid multiplier

$$\phi_f^2 = 1 + \frac{C}{X} + \frac{1}{X^2} \tag{F.161}$$

7. Find evaporating frictional pressure drop gradient for a given value of x

$$-\left(\frac{dP}{dz}\right)_{f,2\phi} = \begin{cases} -\left(\frac{dP}{dz}\right)_g \phi_g^2 & -\left(\frac{dP}{dz}\right)_g \phi_g^2 > -\left(\frac{dP}{dz}\right)_f \phi_f^2 \\ -\left(\frac{dP}{dz}\right)_f \phi_f^2 & -\left(\frac{dP}{dz}\right)_g \phi_g^2 < -\left(\frac{dP}{dz}\right)_f \phi_f^2 \end{cases} \tag{F.162}$$

8. Average frictional pressure drop gradient is calculated iteratively using Simpson's rule to carry out numerical integration

$$\overline{\Delta P_{f,2\phi}} = \frac{\displaystyle\int_{x_1}^{x_2} -\left(\frac{dP}{dz}\right)_{f,2\phi} dx}{x_2 - x_1} \tag{F.163}$$

Accelerational Pressure Drop

The accelerational pressure drop calculation is based on the consideration of two-phase flow. It is caused by the change in velocity of the vapor and liquid phases due to phase change, which in the case of boiling creates vapor and accelerate the vapor velocity, resulting in a pressure increase.

$$-\left(\frac{\partial P}{\partial z}\right)_{A,2\phi} = G^2 \frac{d}{dz}\left[\frac{x^2 v_g}{\varepsilon} + \frac{(1-x)^2 v_f}{1-\varepsilon}\right] \tag{F.164}$$

where ε is the refrigerant vapor void fraction[4].
Integrating over the length where the quality goes from x_1 to x_2 yields

$$\Delta P_{A,2\phi} = \int_0^L \left[-\left(\frac{\partial P}{\partial z}\right)_{A,2\phi} dz\right] \tag{F.165}$$

and thus

$$\Delta P_{A,2\phi} = G^2 L \left[\left(\frac{x_2^2 v_g}{\varepsilon_2} + \frac{(1-x_2)^2 v_f}{1-\varepsilon_2}\right) - \left(\frac{x_1^2 v_g}{\varepsilon_1} + \frac{(1-x_1)^2 v_f}{1-\varepsilon_1}\right)\right] \tag{F.166}$$

---

[4] Typically α is used for void fraction, but here it is used for heat transfer coefficient

If the quality in the term

$$\left(\frac{x^2 v_g}{\varepsilon} + \frac{(1-x)^2 v_f}{1-\varepsilon}\right) \tag{F.167}$$

is 0 or 1, one part is zero and the other is an indeterminate form of 0/0. One evaluation of L'Hopital's rule can be used to show that if the quality is zero, the term in Equation (F.167) is equal to v_f, or if the quality is 1, this term is equal to v_g.

Two-Phase Evaporation Heat Transfer

Shah (1976) correlation is used to model the heat transfer coefficient for boiling fluid in a tube. The non-dimensional groups of interest are the convection number

$$\mathrm{Co} = \left(\frac{1}{x} - 1\right)^{0.8} \sqrt{\frac{\rho_g}{\rho_f}} \tag{F.168}$$

The Froude number is

$$\mathrm{Fr}_l = \frac{G^2}{\rho_f^2 g D} \tag{F.169}$$

and the boiling number is

$$\mathrm{Bo} = \frac{q"}{G h_{fg}} \tag{F.170}$$

The pure-liquid heat transfer coefficient is given by

$$\alpha_l = 0.023 \left(\frac{G(1-x)D}{\mu_f}\right)^{0.8} \mathrm{Pr}_f^{0.4} \frac{k_f}{D} \tag{F.171}$$

If Bo > 0.0011, then F $= 14.7$, Otherwise, F $= 15.43$

If $\mathrm{Fr}_l \geq 0.04$, then N = Co, else $N = 0.38\mathrm{Fr}_l^{-0.3} Co$

$$\psi_{cb} = \frac{1.8}{N^{0.8}} \tag{F.172}$$

If N is between 0.1 and 1.0 inclusive

$$\begin{gathered}\psi_{bs} = F\sqrt{\mathrm{Bo}}\exp(2.74N^{-0.1}) \\ \psi = \max(\psi_{bs}, \psi_{cb})\end{gathered} \tag{F.173}$$

If N $<$ 0.1

$$\begin{gathered}\psi_{bs} = F\sqrt{\mathrm{Bo}}\exp(2.47N^{-0.15}) \\ \psi = \max(\psi_{bs}, \psi_{cb})\end{gathered} \tag{F.174}$$

If N is *very* small in magnitude, $\exp(2.47N^{-0.15})$ blows up to infinity, so to correct, at high vapor quality, the value for the heat transfer coefficient between quality of 0.999 and 1.0 is linearly interpolated to give better behavior at very high vapor quality, which yields very small values of N.

The pure vapor ($x = 1$) heat transfer coefficient is given by

$$\alpha_g = 0.023\left(\frac{GD}{\mu_g}\right)^{0.8}\mathrm{Pr}_g^{0.4}\frac{k_g}{D} \tag{F.175}$$

If N $>$ 1.0 and Bo $>$ 0.00003

$$\begin{gathered}\psi_{nb} = 230\sqrt{\mathrm{Bo}} \\ \psi = \max(\psi_{nb}, \psi_{cb})\end{gathered} \tag{F.176}$$

If N $>$ 1.0 and Bo $<$ 0.00003

$$\begin{gathered}\psi_{nb} = 1.0 + 46.0\sqrt{\mathrm{Bo}} \\ \psi = \max(\psi_{nb}, \psi_{cb})\end{gathered} \tag{F.177}$$

Therefore, the heat transfer coefficient as a function of quality x is given by

$$\alpha_{2\phi}(x) = \psi\alpha_l \tag{F.178}$$

The average evaporation heat transfer coefficient between a quality of x_1 and x_2 is given by

$$\overline{\alpha_{2\phi}} = \frac{\displaystyle\int_{x_1}^{x_2} \alpha_{2\phi}(x)\,dx}{x_2 - x_1} \tag{F.179}$$

where the integral is evaluated numerically using Simpson's rule.

Two-Phase Refrigerant Charge

Zivi (1964) slip flow model is used to count for the refrigerant charge in the two-phase portion. The slip ratio is equal to

$$S = \left(\frac{v_g}{v_f}\right)^{1/3} \tag{F.180}$$

which yields the void fraction for a given quality of

$$\varepsilon = \frac{1}{1 + \frac{\rho_g}{\rho_f} S \left(\frac{1-x}{x}\right)} \tag{F.181}$$

and the average void fraction between qualities of x_1 and x_2 can be found by

$$\overline{\varepsilon} = -\frac{C_\varepsilon \left[\log\left(\frac{(x_2-1)\,C_\varepsilon - x_2}{(x_1-1)\,C_\varepsilon - x_1}\right) + x_2 - x_1\right] - x_2 + x_1}{\left(C_\varepsilon^2 - C_\varepsilon + 1\right)(x_2 - x_1)} \tag{F.182}$$

where the term C_ε is obtained by

$$C_\varepsilon = \frac{\rho_g}{\rho_f} S \tag{F.183}$$

which yields the average density in the two-phase section of

$$\overline{\rho} = \rho_g \overline{\varepsilon} + \rho_f (1 - \overline{\varepsilon}) \tag{F.184}$$

Therefore, the total mass of refrigerant contained in the two-phase section is equal to

$$m = \bar{\rho} V \tag{F.185}$$

Single-Phase Pressure Drop

The Churchill (1977) correlation (based on a Darcy friction factor for which the laminar friction factor is $f = 64/\mathrm{Re}_D$) is

$$f = 8\left[\left(\frac{8}{\mathrm{Re}_D}\right)^{12} + \frac{1}{(A+B)^{1.5}}\right]^{1/12} \tag{F.186}$$

where

$$A = \left(-2.457\log\left[\left(\frac{7}{\mathrm{Re}_D}\right)^{0.9} + 0.27(\mathrm{e}/D)\right]\right)^{16} \tag{F.187}$$

and

$$B = \left[\frac{37530.0}{\mathrm{Re}_D}\right]^{16} \tag{F.188}$$

with the Reynolds number defined by

$$\mathrm{Re}_D = \frac{\rho\bar{U}D}{\mu} = \frac{4\dot{m}}{\pi\mu D} \tag{F.189}$$

With the known friction factor, the pressure gradient is given by

$$\frac{dP}{dz} = \frac{-fvG^2}{2D} \tag{F.190}$$

with the mass flux defined by

$$G = \frac{\dot{m}}{(\pi D^2/4)} \tag{F.191}$$

and assuming the gradient to be constant over the length L because averaged properties are used, the total pressure drop is

$$\Delta P = \frac{-fvG^2L}{2D} \tag{F.192}$$

Single-Phase Heat Transfer

The Gnielinski (1976) correlation is good for smooth tubes where $0.5 < \mathrm{Pr} < 2000$ and $3000 < \mathrm{Re}_D < 5 \times 10^6$. The single-phase heat transfer coefficient can be expressed by

$$\alpha = \frac{k}{D} \frac{(f/8)(\mathrm{Re}_D - 1000)\,\mathrm{Pr}}{1 + 12.7(f/8)^{1/2}(\mathrm{Pr}^{2/3} - 1)} \tag{F.193}$$

Single-Phase Refrigerant Charge

The refrigerant charge for a single-phase volume is equal to

$$m = \rho V \tag{F.194}$$

where the density ρ is based on the average temperature and pressure.

In the case that given circuit of a heat exchanger is being analyzed, the value of L is equal to the length of the circuit (or average length if there are multiple circuits). In addition, the mass flow rate $\dot{m}$ is therefore given as the mass flow rate per circuit.

Pressure Drop and Heat Transfer in Plate Heat Exchanger Economizer

Single-Phase Pressure Drop

Martin (2010) analysis is employed when there is single-phase flow on one side of the PHX. Using this analysis, the pressure drop and heat transfer coefficients for the fluid flowing between the plates can be calculated.

The Reynolds number for the flow through the channel between two plates is given by

$$\mathrm{Re} = \frac{\rho u d_h}{\mu} \tag{F.195}$$

where the velocity per channel is given by

$$u = \frac{\dot{m}_{ch}}{2\hat{a}\rho B_p} \tag{F.196}$$

The pressure drop and heat transfer coefficients are usually a function of the Reynolds number, and if the flow is laminar ($\mathrm{Re} < 2000$), the factors ζ_0 and $\zeta_{1,0}$ are given by

$$\begin{aligned} \zeta_0 &= \frac{64}{\mathrm{Re}} \\ \zeta_{1,0} &= \frac{597}{\mathrm{Re}} + 3.85 \end{aligned} \tag{F.197}$$

and if the flow is turbulent ($\mathrm{Re} \geq 2000$), the factors ζ_0 and $\zeta_{1,0}$ are given by

$$\begin{aligned} \zeta_0 &= \frac{1}{(1.8\ln(\mathrm{Re}) - 1.5)^2} \\ \zeta_{1,0} &= \frac{39}{\mathrm{Re}^{0.289}} \end{aligned} \tag{F.198}$$

The friction factor ζ is obtained from

$$\frac{1}{\sqrt{\zeta}} = \frac{\cos\varphi}{\sqrt{b\tan\varphi + c\sin\varphi + \zeta_0/\cos\varphi}} + \frac{1-\cos\varphi}{\sqrt{\zeta_1}} \tag{F.199}$$

where the factor ζ_1 is given by

$$\zeta_1 = a\zeta_{1,0} \tag{F.200}$$

and the factors a and b and c given by Martin are

$$\begin{aligned} a &= 3.8 \\ b &= 0.18 \\ c &= 0.36 \end{aligned} \tag{F.201}$$

The Hagen number is defined by

$$\mathrm{Hg} = \frac{\zeta \mathrm{Re}^2}{2} = \frac{\rho \Delta P d_h^3}{\mu^2 L_p} \tag{F.202}$$

which gives the value for the pressure drop

$$\Delta P = \mathrm{Hg}\frac{\mu^2 L_p}{\rho d_h^3} \tag{F.203}$$

Single-Phase Heat Transfer

The Nusselt number is expressed by

$$\mathrm{Nu} = c_q \mathrm{Pr}^{1/3} (\mu/\mu_w)^{1/6} [2\mathrm{Hg}\sin(2\varphi)]^q \tag{F.204}$$

where the recommended values of the constants c_q and q from Martin (2010) are 0.122 and 0.39, respectively. For simplicity, μ and μ_w are assumed to be equal.
Finally, the overall heat transfer coefficient is obtained from

$$\alpha = \frac{k\mathrm{Nu}}{d_h} \tag{F.205}$$

Two-Phase Evaporation Heat Transfer

When the fluid flow is evaporating, it is quite a bit more difficult to determine the best model to use. There are contradictory conclusions drawn in literature as to what type of heat transfer is occurring.

It seems like the most accepted view, though is open to debate, is that the flow is governed by nucleate boiling within the channels, and as a result, nucleate pool boiling relations are employed in order to calculate the heat transfer coefficient. This model has some features which are not well-suited to implementation into the PHX model. For instance, there is no quality dependence on heat transfer coefficient, which yields un-physically high values of heat transfer coefficient at high quality (should go to the saturated vapor gas heat transfer coefficient at pure vapor).

In spite of these shortcomings, the pool boiling correlation of Cooper (1984) was used. This yields a simple form of the solution for the heat transfer coefficient. The heat transfer coefficient is obtained from

$$\alpha = 55K(P^*)^{0.12-0.2\log_{10}(R_p)}\left[-\log_{10}(P^*)\right]^{-0.55}(q")^{0.67}M^{-0.5} \tag{F.206}$$

where

$$\begin{aligned} P^* &= P/P_{crit} \\ q" &= \dot{Q}/A \end{aligned} \tag{F.207}$$

and M is the molar mass (kg/kmol) of the fluid and R_p is the relative roughness of the surface and K is set to unity. However, Claesson (2004) suggested a correction of 1.5.

Two-Phase Condensation Heat Transfer

The available models for condensing flow in PHX share many of the shortcomings of the evaporating flow models. There is a paucity of good data available, since most of the know-how is controlled by the major PHX manufacturers. With that being said, many researchers have studied this topic, but the parameter space (geometrically and thermodynamically) is quite vast. This is still a topic that could do with further study.

Longo et al. (2004) and Longo (2010, 2011) conducted studies that looked at condensation in PHX, and from these studies it can be seen that at low equivalent Reynolds number ($\text{Re}_{eq} < 1750$), the j-factor is nominally constant at a value of 60, and above that, it is linear with equivalent Reynolds number, so the j-factor can be given by

$$j = \begin{cases} 60 & \text{Re}_{eq} < 1750 \\ \dfrac{75-60}{3000-1750}(\text{Re}_{eq} - 1750) + 60 & \text{Re}_{eq} \geq 1750 \end{cases} \tag{F.208}$$

where the equivalent Reynolds number is defined by

$$\text{Re}_{eq} = \frac{G\left[(1-\overline{x}) + \overline{x}\sqrt{\dfrac{\rho_f}{\rho_g}}\right] d_h}{\mu_f} \tag{F.209}$$

where $\overline{x}$ is the average quality.

Finally, the heat transfer coefficient yields

$$\alpha = \frac{jk\text{Pr}^{1/3}}{d_h} \tag{F.210}$$

Two-Phase Pressure Drop

In order to calculate the pressure drop in evaporating and condensing flow in the PHX channel, the frictional pressure drop is calculated using the Lockhart and Martinelli (1949) correlation from *Two-Phase Evaporation Pressure Drop* section with the value of the parameter C of 4.67 as recommended by Claesson (2004). The accelerational pressure change is given from the same section.

VITA

VITA

Ammar Mohammad Khalil Bahman was born in Birmingham, United Kingdom, on Nov. 29, 1984. The author received his Bachelor's degree in Mechanical Engineering in 2006 from Kuwait University, College of Engineering and Petroleum. He received his Master degree in Mechanical Engineering under the supervision of Professor Walid Chakroun in 2009 from Kuwait University, College of Engineering and Petroleum. He received another Master degree in Mechanical Engineering under the supervision of Professor Muhammad Rahman in 2011 from University of South Florida, College of Engineering. In addition, he worked for Kuwait Oil Company as a mechanical maintenance engineer from Nov. 2007 to Feb. 2008. Then, he worked as a teaching assistant for the Mechanical Engineering Department in the College of Engineering and Petroleum, Kuwait University, from Mar. 2008 to Aug. 2009. Later, he worked in the Public Authority for Applied Education and Training (PAAET), Kuwait, as a teaching assistant from Aug. 2009 to Aug. 2013. He got a scholarship for PhD in the area of HVAC from the Mechanical Engineering Department in the College of Engineering and Petroleum, Kuwait University in Aug. 2013. He started his PhD studies at the Ray W. Herrick Laboratories of Purdue University in West Lafayette, Indiana, USA in Fall 2013 and has been a PhD student since then. The author is a member of the American Society of Mechanical Engineers (ASME), and a member of the American Society for Heating, Refrigerating and Air Conditioning Engineers (ASHRAE) since 2004. He is also a member of the International Institute of Refrigeration (IIR) since 2017.